UNIVERSITY OF CALIFORNIA
RIVERSIDE

Interfacial Interactions Pertinent to Single-Molecule and Solar-Energy Applications

A Dissertation submitted in partial satisfaction
of the requirements for the degree of

Doctor of Philosophy

in

Biochemistry and Molecular Biology

by

Srigokul Upadhyayula

June 2013

Dissertation Committee:
Dr. Valentine Vullev, Chairperson
Dr. Russ Hille
Dr. Hyle Park

The Dissertation of Srigokul Upadhyayula is approved by:

_____

_____

_____

Committee Chairperson

University of California, Riverside

Acknowledgements

I am extremely grateful to Dr. Valentine Vullev for providing me with the opportunity to join his lab as a graduate student, for imparting valuable knowledge & experience, and for his patience & advise. His mentorship to continually develop my abilities, his push to believe in my dreams, enabled me with the drive to reach my aspirations. His dedication, investment, and his expectations for excellence towards his graduate students leave me with a sincere sense of gratitude. Thank you for being the kind of mentor that every graduate student hopes for! **много благодаря!**

I am thankful to my committee members: Dr. Russ Hille & Dr. Boris Hyle Park for helpful discussions, and for their constant support and helpful advice. I am thankful to Dr. Park for allowing me to attend and learn from his group's optics related meetings. Moreover, I am grateful for helpful discussions on the reflectance interference imaging setup. I would like to sincerely thank the Department of Biochemistry and Department of Microbiology and Plant Pathology for providing 12 quarters of Teaching Assistantship to support my graduate studies. I am grateful to Dean of Graduate Division for award the Dissertation Year Fellowship and for the Dissertation Research Grant. I am thankful to Lynn Scott from Riverside Public Utilities and American Public Power Association for the DEED grant. I would like to thank the Biochemistry Department faculty and the Randolph T. and Mary K. Wedding family for their generous support. Without the support and generous grants from the Wedding family, Earle C. Anthony and James and Margaret Lesley, I would not have been able to attend high-impact conferences, one where I received interviews for postdoctoral positions. I would like to acknowledge Dr.

ALN Rao for giving me my first opportunity at UC Riverside. I am grateful for the support from graduate students, faculty and staff in the Bioengineering Department.

I could not have accomplished any of this without the support of Vullev Group members. I would like to thank Dr. Duoduo Bao, for her extensive insight and assistance with organic synthesis. In addition, I am grateful to Vicente Nuñez, Jillian Larsen, and Jacob Vasquez for detailed discussions on an array of organic synthesis and microfluidic topics. I am grateful to Jaclyn Yuki Lock for keeping me inspired and motivated, and for proof reading my dissertation. I would like to thank the Dr. Bing Xia, Vicente Nuñez and Kenny Chau, for granting me permission to reprint the published journal articles. I would also like to acknowledge the many amazing undergraduates, graduates, and co-authors for their contributions to my dissertation chapters – Duoduo Bao, Vicente Nuñez, Jillian Larsen, Tim Quinata, Stephen Bishop, Sharad Gupta, Noah Jonson, Baharak Bahmani, Kliment Bozhilov, Jeremy Stubbs, Pamela Jreij, and Pratima Nallagatla, Brent Millare, Amy Ferreira, Robert Bonderer, Samih Baqai, Somaia S. Sylvia, K. M. Masum Habib, Khalid Ashraf, Adam Lin, Hong Xu, Ali Hadian, Sanghoon Shin, Prashanthi Vandrangi, and Georgi Y. Georgiev. None of this would be possible without support from Profs. Mihrimah Ozkan & Cengiz Ozkan for granting us access to their capacitance bridge; Prof. Roger Lake and his group for their extensive assistance with theoretical calculations; and would like to my academic grandfather, Prof. Guilford Jones, II.

To my undergraduate mentees, fellow graduate students, and professors: these past five years of work would not have been as much fun or educational without all of you! Thank you!

I would like to thank and dedicate this dissertation to:

My parents: Suryaprakash & Sridevi Upadhyayula

My brothers and Sister: Sriteja, Saikrishna & Sripriya Upadhyayula;
My uncle and aunt: Ramesh & Sujatha Upadhyayula;
My grandparents: Late Krishnamurthy Upadhyayula and Late VenkataRao Vadlamani (grandfathers), Lakshmi Upadhyayula and Lakshmibai Vadlamani (grandmothers);
and to:
My friends and family

For their unwavering love, support and confidence.

ABSTRACT OF THE DISSERTATION

Interfacial Interactions Pertinent to Single-Molecule and Solar-Energy Applications

by

Srigokul Upadhyayula

Doctor of Philosophy, Graduate Program in Biochemistry and Molecular Biology
University of California, Riverside, June 2013
Dr. Valentine Vullev, Chairperson

Visualizing the dynamics of nanometer-sized macromolecules presents considerable challenges that stem from non-specific interfacial interactions between the micrometer-sized probes used in those visualizations; as a result, advances in single-molecule protein interaction studies have not been extensively explored. The first part of my doctoral research sought to address this limitation by determining the capability of different surface coatings of polyethylene glycol to suppress non-specific interfacial interactions. Concurrently, we developed a magnetic puller setup capable of attaining forces between hundreds of femto-newtons and approximately one hundred pico-newtons. Magnetic pullers allow for probing thousands of single-molecule events simultaneously, providing considerable advantages over traditional magnetic tweezers. The design and application of thermally-regulated electromagnetic pullers, capable of attaining forces in the fN-to-nN dynamic range, is essential for single-molecule proteomic studies.

By applying relatively weak pulling forces (e.g., ~1.2 pN), we examined the efficacy of removing polystyrene microbeads from glass surfaces. When either the glass or the beads were not PEGylated, the adhesion between them was substantial. Furthermore, when the PEG polymers were too short or too long, we still observed substantial adhesion of the beads to the glass surfaces. Coatings of PEG with molecular weights ranging between 3 and 10 kDa proved critical for suppressing the adhesion.

My research also focused on investigating anthranilamide derivatives, as bioinspired electrets, for improving the efficiency of interfacial charge transfers that are essential for solar-energy applications. A substantial portion of these studies were directed toward understanding the fundamental electrostatic properties of amides, with a focus on carboxyamides. Carboxyamides are small polar groups that, as peptide bonds, constitute the principle structural components of proteins. The electric fields from the amide dipoles govern the electrostatic properties and activity of proteins. Therefore, we undertook a detailed study of the medium dependence of the molar polarization and of the permanent dipole moments of amides with different states of alkylation. The experimentally-measured and theoretically-calculated dipole moments of the solvated amides both manifested a dependence on the media polarity. Specifically, an increase in solvent polarity led to a subsequent increase in both the measured and calculated permanent dipole moments of the solutes. We attributed the observed enhancement of the amide dipoles to the reaction fields in the solvated cavities.

Our bioinspired approach and usage of amide dipoles as a principal field source allowed us to develop molecular electrets based on *oligo*-anthranilamides. Electrets, and specifically, dipole-polarization electrets, are the electrostatic analogues of magnets, i.e., they are systems with codirectionally ordered permanent electric dipoles. The de novo designed anthranilamides are bioinspired in the sense that, similar to protein helices, they possess permanent intrinsic dipoles resultant from the ordered orientation of amide and hydrogen bonds. Unlike the helices, however, these bioinspired oligomers have the redox properties necessary to mediating long-range charge transfer along their backbones.

Overall, the most significant contributions from my doctoral research are: (1) the optimization of polyethylene glycol surface coatings for suppressing non-specific interfacial interactions; (2) the development of an electromagnetic puller setup with a wide dynamic force range capable of simultaneously probing thousands of single-molecule protein interactions; (3) the characterization of the effects of solvent polarity on the dipole moments of amides; and (4) the demonstration of the ability of organic materials with dipole moments to rectify photoinduced charge transfer.

Contents

---Appendix---

List of Schemes

CHAPTER 1:

CHAPTER 2:

CHAPTER 3:

CHAPTER 4:

Appendix

CHAPTER 5:

List of Tables

CHAPTER 1:

CHAPTER 3:

CHAPTER 4:

Appendix

CHAPTER 5:

List of Figures

CHAPTER 1:

^{1}H-NMR spectra of the amide, N-^{1}H, region, depicting the concentration dependence of the chemical shifts of the N-^{1}H protons for samples dissolved in $CDCl_3$.

Figure 3-5 *p 171*

^{1}H-NMR spectra of the carbonyl and aliphatic proton regions of $CDCl_3$ solutions of the six amides. **(a, c, e)** Chemical shifts of the carbonyl and the aliphatic proton at two different sample concentrations. **(b, d, f)** Chemical shifts of the aliphatic protons at two different concentrations for the samples with ethylated carbonyls. **(g)** Chemical shifts of the carbonyl and the methylene protons of HHE showing the presence of two conformers. In (g), the highest peaks in the carbonyl and in the aliphatic region are normalized for clarity. **(h)** Balls and sticks structures of the two most stable HHE conformers with the corresponding atomic charges calculated for chloroform media. The singlet at 7.27 ppm was from the traces of C^1HCl_3 and was used for internal standard, and the broad singlet at 1.56 ppm was ascribed to traces of water in the solvent.

Figure 3-6 *p 173*

^{1}H-NMR spectra of TCE-d_2 solutions of five of the six amides depicting the concentration dependence (or the lack of concentration dependence) of the chemical shifts of: **(a, d)** the carbonyl protons of Hxx in the 8 – 8.5 ppm region; **(a, b, c)** the amide protons of xHx in the 5 – 6 ppm region; **(b – e)** the methylene protons of Exx and xxE in the 2 – 3.5 ppm region; and **(b – e)** the methyl protons of Exx and xxE in the 1 – 1.5 ppm region. HHE does not have sufficient solubility in TCE. The solvent peak of TCE-d_1 is at 6 ppm.

CHAPTER 4:

Figure 4-1 *p 220*

Absorption and emission properties of the anthranilamide oligomers. **(a-c)** Steady-state absorption and emission spectra (chloroform solutions; l_{ex} = 305 nm). The absorption spectra for 5 mM concentrations were scaled up by a factor of 10 for comparison with the absorption spectra for 50 mM concentrations. The emission spectra for concentrations exceeding 10^{-4} M were recorded using small-angle fluorescence spectroscopy.(Mayers, Vezenov et al. 2005; Wan, Thomas et al. 2009; Lu, Bao et al. 2010; Thomas, Clift et al. 2010; Ghazinejad, Kyle et al. 2012; Upadhyayula, Quinata et al. 2012) **(d)** Time-resolved emission decays recorded at the low-energy bands, i.e., at 545 nm for h-A-ph, and at 520 nm for h-AAA-ph (l_{ex} = 278 nm, half-height pulse width = 1 ns).

Figure 4-2 *p 222*

Concentration dependence of the emission properties of the anthranilamide oligomers. **(a)** A representative example of deconvolution of a fluorescence spectrum using a sum of two Gaussian functions. To plot the spectrum versus energy, i.e., vs. wavenumber, $\tilde{\nu}$, instead of vs. wavelength, l, we converted the fluorescence intensity accordingly, $F_{\tilde{\nu}}(\tilde{\nu}) = \lambda^2 F_{\lambda}(\lambda)$.(Valeur 2002) **(b)** Concentration dependence of the fractions of the

monomer, R_m, and aggregate, R_a, emission (eq. 1). **(c)** Concentration dependence of the monomer fractions, x (eq. 2). **(d)** Linear analysis of $\lg(C(1\text{-}x))$ vs. $\lg(Cx)$ (eq. 3). The gray circles designate the data points; and the red and blue lines – the linear data fits at low and high concentrations, respectively.

Figure 4-3 *p 224*

Dependence of **(a)** the density, r, and **(b, c)** the dielectric properties of anthranilamide solutions in chloroform on the oligomer molar fraction, c_2. **(b)** Dielectric constant, e, of h-AA-ph solutions extracted from capacitance measurements at different frequencies. **(c)** e of solutions of the three oligomers extracted from capacitance measurements at 100 kHz.

Figure 4-4 *p 226*

^{1}H-NMR spectra of the three anthranilamide oligomers with assignments of the peaks corresponding to the amide protons. (2 mM in $CDCl_3$; 400 MHz)

Figure 4-5 *p 228*

^{1}H-^{13}C gHMBC spectrum of h-AAA-ph (2 mM in $CDCl_3$; 400 MHz). **(a)** The full spectral range with ^{2}J correlations (indicated with the gray lines) between ^1H_e/$^1H_{e'}$ and $^{13}C_d$ and between $^{13}C_d$ and ^1H_d (Scheme 4-3). **(b-e)** Zoomed ^{3}J correlation peaks between the amide protons and the carbons three bonds away. The peaks at: **(b)** 12.3 ppm; **(c)** 11.9 ppm; **(d)** 11.2 ppm; and **(e)** 8.45 ppm.

Appendix

CHAPTER 5:

Figure 5-1 *p 266*

Space-domain time-resolved emission measurements. **(a)** Microscope image (16 bit) of the region of a microchannel, filled with water, illuminated at 280 nm. The imaged emission originated from autofluorescence. **(b)** Microscope image of the emission decay recorded through a band-pass filter (570-620 nm). Solution of 20 mM Eu^{3+} and 100 mM DPA was flown through the illuminated region of the channel (l_{ex} = 280 nm) at flow rate Q = 20 ml min^{-1}. Scale bars on (a) and (b) correspond to 200 mm. **(c)** Emission trace, $R^*(x)$, extracted from the decay image, (b), along with excitation trace, $L(x)$, extracted from the image of the illumination spot, (a), and the data fit of $R^*(x)$ vs. x using equations 1 and 2. **(d)** The same $R^*(x)$ and $L(x)$ as (c), in which the data fitting was limited to the decay region of the image trace with minimum interference from the autofluorescence from the excitation spot. The difference in the lifetimes from (c) and (d) was less than 10%. The inset represents the decay data and the data fit plotted against logarithmic ordinate. The use of equations 1 and 2 provided adequate data fits for the traces, $R^*(x)$, extracted from images (b). As indicated by the residuals, however, limiting the data fits to the regions of the emission-decay traces, $R^*(x)$, where the autofluorescence from the

excitation had minimum to no contribution, improved the quality of the data fits, i.e., (c) vs. (d).

Figure 5-2 *p 268*

Channel cross-section and flow-velocity profiles, $v_x(x, y, z)$, estimated from profilometry and fluorescence images for different flow rates, Q. **(a)** Surface plot of the entrance region of a mFL channel from profilometry data. **(b, c)** Uncorrected epifluorescence images (8 bit) of the entrance region of a mFL channel filled with 1 mM aqueous solution of fluorescein buffered at pH 8, at rest and at flow rate of 50 ml min^{-1}. **(d, e)** Uncorrected fluorescence traces across the channels, recorded at different flow rates, as indicated with the dotted red lines on the images, (b) and (c). **(f, g)** Channel cross-sections estimated from the fluorescence traces (d) and (e), using equations 4 and 5. **(h)** Spectral overlap between the fluorescein absorption at pH 8 and the excitation, I_0, obtained from the microscope mercury lamp as a light source, passed through the fluorescein isothiocyanate (FITC) excitation filter used for the recording of the fluorescence images. **(i, j)** Flow-velocity profiles for 10 and 50 ml min^{-1}, obtained using equation 3 and smoothed cross-sections (f) for various flow rates assuming no-slip conditions and parabolic distribution.

Figure 5-3 *p 271*

Space-domain emission decays of Tb^{3+} and Eu^{3+} chelated with DPA, recorded for different flow rates. **(a)** Emission spectra of Tb^{3+} and Eu^{3+} in the presence of DPA. **(b)** Images of the emission decays of lanthanide chelates, recorded at different flow rates. The scale bars correspond to 200 mm. The emission-decay images were recorded through band-pass filters: 510-560 nm for the terbium (III) samples, and 570-620 nm for the europium (III) samples. **(c)** Emission-decays traces, $R^*(x)$, of the three lanthanide chelates recorded at flow rate, Q = 40 ml min^{-1}, along with the corresponding data fits and fitting residuals. **(d)** Emission-decay traces of $Tb(DPA)_3$, along with the corresponding data fits and fitting residuals, recorded at flow rates, Q = 10, 30 and 50 ml min^{-1}. The traces were extracted from the middle of the imaged channels, i.e., $y = w / 2$. For $Ln(DPA)_3$, C_{Ln} = 20 mM and C_{DPA} = 100 mM; and for Tb(DPA), C_{Tb} = 50 mM and C_{DPA} = 10 mM (l_{ex} = 280 nm).

Figure 5-4 *p 273*

Time-domain measurements, with the corresponding monoexponential data fits, of emission decays of Tb^{3+} and Eu^{3+} chelated with DPA, normalized for t = 0, which correspond to the timing of the excitation laser pulse, and presented against logarithmic ordinate. For $Ln(DPA)_3$, C_{Ln} = 20 mM and C_{DPA} = 100 mM; and for Tb(DPA), C_{Tb} = 50 mM and C_{DPA} = 10 mM (l_{ex} = 266 nm; 40 fs pulse width at 800 nm prior to the second and third harmonic generators).

Preface

This dissertation covers two lines of research that focus on surface interactions essential for single-molecule force studies, and on field-induced modulation of charge transfer pertinent to interfacial processes for solar-energy conversion applications. Overall, the most significant contributions from my doctoral research are: (1) the optimization of polyethylene glycol surface coatings for suppressing non-specific interfacial interactions; (2) the development of an electromagnetic puller setup with a wide dynamic force range capable of simultaneously probing thousands of single-molecule protein interactions; (3) the characterization of the effects of solvent polarity on the dipole moments of amides; and (4) the demonstration of the ability of organic materials with dipole moments to rectify photoinduced charge transfer.

Single-molecule studies. Studies at a single-molecule level allow for exploring the stochastic nature of biological and chemical systems (inherent in the fundamental quantum mechanics principles). That is, single-molecule measurements provide access to observables that are lost in the ensemble average of traditional bulk studies. As an indispensible but nonetheless largely unexplored tool for biochemistry and cell biology, single-molecule approaches provide a means for the direct observation of rare events and of the kinetic constants of intermediates formed during an enzymatic reaction that eventually determine whether a process occurs in a step-wise fashion or in simultaneity

(Bustamante, Chemla et al. 2004; Nahas, Wilson et al. 2004; Deniz, Mukhopadhyay et al. 2008; Neuman and Nagy 2008; Walter, Huang et al. 2008; Kapanidis and Strick 2009).

Single-molecule force measurements. The ability to selectively exert force on a single molecule, and to quantify its response, provides venues for the experimental exploration of molecular mechanics. Single-molecule force measurements (SMFMs) permit direct experimental probing of the energy landscape of bimolecular processes, such as protein-ligand interactions and protein folding. Furthermore, SMFM encompasses the only experimental technique that allows for direct testing of the structural directionality of molecular interactions, which can in turn be used for the selective application of mechanical stress to macromolecules. Biomembrane force probes (BFP), atomic force microscopes (AFM), optical tweezers (OP), and magnetic tweezers (MT) constitute just a few of the examples of single-molecule force techniques (Evans 2001; Erdmann and Schwarz 2004; Neuman and Nagy 2008; Walter, Huang et al. 2008). These techniques examine nanometer-sized complexes that are immobilized on micrometer-sized probes. The probes for SMFM, such as AFM tips or microbeads, serve the dual role of acting as force transducers and as probes for visualizing molecular displacement with sub-nanometer resolution. While each of the listed force techniques has a combination of advantages and disadvantages to their use, MT is the only tool that has the potential to be optimized to achieve: (1) a wide dynamic range of forces pertinent to biochemical interactions, (2) minimum or no sample overheating, and (3) a force exertion that is orthogonal to almost all biological interactions. While MT setups utilize multiple

magnetic core setups to tweeze single beads at micrometer distances (Neuman and Nagy 2008), we focused on the development of a magnetic puller setup (a variation of MT, described in chapter 2) that allows us to study thousands of single-molecule interactions simultaneously.

Suppressing nonspecific interactions. The sensitivity of magnetic tweezers (and all single-molecule force techniques) is compromised by undesired nonspecific interactions which occur at the interfaces between adjacent micrometer-sized objects (i.e., objects that are nanometers apart from each other). Specifically, the investigated nanometer-size molecules are immobilized on micrometer-size probes and on flat surfaces or on another micrometer-size object. The separation of nonspecifically-adhered micrometer-size objects requires forces in the range of nanonewtons, andthe manipulation of single-molecule interactions requires forces in the order of piconewtons. Currently, a combination of proteins such as bovine serum albumin, detergents, emulsifiers, and/or lipid bilayers are employed to achieve the suppression of nonspecific adhesion (Leckband and Israelachvili 2001; Graneli, Yeykal et al. 2006; Zhang, Ang et al. 2011). Utilizing proteins for passivation is not an optimal approach as they may non-specifically interact, especially when studying protein-protein interactions. Detergents, emulsifiers, or surfactants are another widely used class of reagents for suppressing nonspecific interactions. Since this class of reagents is largely solution- or buffer-based, they are required in high concentration or in concentrations above their critical micelle-forming concentration to be effective. At these high concentrations, they form micelles or bilayers

that can disrupt active site interactions between proteins, ligands, and substrates—or worse, they can perturb the native protein structure (Dennis 1973; Delorme, Dhouib et al. 2011; Filice, Marciello et al. 2011). Polyethylene glycol (PEG), also referred to as polyethylene oxide when is molecular weight is above 10 or 30 kDa, provides an excellent alternative for engineering passive biocompatible coatings, as it has none of the disruptive effects listed above.

By employing straightforward considerations, such as the nonspecific van der Waal forces and the conformational properties of PEG, the first part of my doctoral research focused on developing bioinert coatings for glass slides and the superparamagnetic microbeads that: (1) keep the interfaces between the slide and the bead materials separated from each other by at least 30 nm; and (2) provide an environment at the interfaces that will not compromise the functionality of the covalently attached biomolecules. Using a six-step procedure developed in our lab—involving silanization, deprotection, reductive amination, amide coupling, carboxyl activation, and amide coupling—allows us to covalently attach PEG to silica-based surfaces and to attach proteins onto the PEG layers while maintaining their functionality (Wan, Thomas et al. 2009).

Bioinspired electrets. In addition to addressing the unwanted issues with nonspecific adhesion at force-probe interfaces, my doctoral research focused on investigating the use of anthranilamide derivatives as bioinspired electrets for improving the efficiency of

interfacial charge transfer for solar-energy applications. A substantial portion of my characterizations of these organic electrets focused on understanding the fundamental electrostatic properties of amides—the building blocks of macromolecules, such as proteins—and of the bioinspired electrets we designed. Macromolecular electrets (which possess permanent electric dipoles with ordered orientation and are thus electrostatic analogues of magnets) have the potential to control the directionality of charge transfer, and hence, to improve the efficiency of photovoltaic and other energy-conversion devices. We demonstrated that, similar to protein α-helices, oligo-anthranilamides possess considerable intrinsic dipole moments, making them highly promising macromolecular electrets (Ashraf, Millare et al. 2009). In comparison with proteins, the anthranilamides have narrower band gaps and possess considerably higher conformational stability.

Carbon-neutral energy sources. The worldwide energy consumption rate for 2005 was approximately 16 TeraWatts (1TW = 10^{12} W) and fossil fuels generated roughly 400-450 ExoJoules (1EJ = 10^{18} Joules) out of the 500 EJ consumed (United-States-Department-of-Energy 2006). Over the last six-and-a-half ice age cycles (beginning roughly 650,000 years before the present), atmospheric CO_2 levels have never exceeded 300 ppm (Siegenthaler, Stocker et al. 2005). Today's growing environmental threat (as of January 2009, CO_2 levels were at 390 ppm) has been attributed to fossil fuel energy consumption (Green, Baksi et al. 2007; Gauthier 2009). For this reason, it is imperative to establish

carbon-neutral energy sources that can sustain our needs—i.e., energy sources that do not perturb natural carbon cycles. However, hydroelectricity, geothermal electricity, tidal power, wind power, and biomass-derived energy do not possess the potential to generate energy at rates that keep up with those of our current and projected energy consumption (Isaacs and Schmitt 1980; United-States-Department-of-Energy 2006; Green, Baksi et al. 2007).

Solar energy. The sun is a sustainable source of energy that far exceeds our generation rate: With approximately 176 PetaWatts (1PW = 10^{15} W) reaching the earth's surface, the practical energy generation rate approximates 600 TW (Barnham, Mazzer et al. 2006; Lewis and Nocera 2006). However, the infrastructure needed to support mass utilization of solar energy has not yet been full developed; there are three components of the existing solar-energy infrastructure in particular that require further development before viable solar power usage can occur: (1) Light-energy harvesting; (2) energy storage and transportation; and (3) energy conversion (Barnham, Mazzer et al. 2006). Efficient forward charge transfer, and, in particular, efficient interfacial charge transfer coupled with the simultaneous suppression of undesired back charge transfer, is profoundly essential to all three components of plausibly competitive solar-energy technology. Therefore, a principal focus of our research is on increasing the efficiency of photoinduced charge separation at a molecular level while suppressing charge recombination.

Light-energy harvesting. The key process in light harvesting involves photoinduced charge separation and consequent multistep electron and hole transfers. For example, when a semiconductor junction of a photovoltaic cell or a photosynthetic reaction center absorbs sunlight, electrons are dislodged, causing charge separation. These free electrons can move back to recombine with the positive charges, thereby losing the absorbed energy in a form of heat (Peaker, Markevich et al. 2004; Lewis 2005; Kosyachenko, Grushko et al. 2006); however, the electron and the formed hole can also migrate away from each other, producing photocurrent. By utilizing macromolecules with large intrinsic dipole moments in the direction of charge transfer, i.e., molecular electrets, we aim to demonstrate an acceleration of forward charge transfer and a suppression of the undesired charge recombination.

Role of electrostatics in proteins. Amide bonds, which result in the joining of two amino acids together, are essential linkages for the building blocks of life. Amide placement and geometry in proteins and other biomolecules have an intrinsic ability to affect the function of the molecule as a whole; amide dipoles facilitate various ligands and other essential components for interactions essential to maintaining native function. Although the secondary and tertiary protein structures are well documented to implicate the relationship between structure and function, it is in fact the electronic properties that define protein functions (Suydam, Snow et al. 2006; Sigala, Fafarman et al. 2007). Since carboxyamides are small polar groups that, as peptide bonds, are principal structural components of proteins that govern their electrostatic properties, we investigated the

medium dependence of the molar polarization and of the permanent dipole moments of amides with different states of alkylation. As we show (in Chapter 3), the experimentally-measured and theoretically-calculated dipole moments manifested a solvent dependence that increased with the increase in the media polarity.

Rectification of charge transfer using protein alpha-helices. Biology offers some of the best-known examples of molecular electrets, as seen in photosynthetic machinery. Polypeptide alpha helices have large intrinsic dipole moments (Hol, Van Duijnen et al. 1978) resultant from the ordered orientation of amide and hydrogen bonds. The intrinsic dipole moments of protein alpha helices amount to approximately 4-5 Debyes per residue (Fedorova, Chaudhari et al. 2003). Galoppini and Fox demonstrated that the dipole moments generated by polypeptide alpha helices rectify photoinduced charge transfer rates (Galoppini and Fox 1996; Fox and Galoppini 1997; Yasutomi, Morita et al. 2004): Charge transfers in the direction opposite to the dipole moment are 5–27 times faster than charge transfers in the same direction as the dipole moment (Galoppini and Fox 1996; Fox and Galoppini 1997). Due to large band gaps and conformational instability, however, when taken out of their native environment, polypeptide alpha helices are not optimal materials for solar-energy-conversion applications. Therefore, we undertook the design of bioinspired electrets by utilizing polymers with extended pi-conjugation—known to facilitate long-range charge transfer along their backbone (Sikes, Smalley et al. 2001; Visoly-Fisher, Daie et al. 2006)—and with an ordered orientation of peptide and hydrogen bonds in order to generate substantial macromolecular dipole moments.

Rectification of charge transfer using bioinspired organic electrets. We utilized a bioinspired approach to develop oligo-anthranilamides, a class of organic materials that are *de novo* designed from biomolecular motifs possessing intrinsic dipole moments, which are vital to facilitating efficient long-range charge transfer (i.e., we developed materials based off of the photosynthetic machinery that evolved to efficiently utilize protein alpha helices as molecular electrets, coupling these features with conjugated polymers). X-ray structures indicate that oligo-anthranilamides have an extended planar conformation supported by hydrogen bond networks (Hamuro, Geib et al. 1996). Similar to conjugated polymers, the anthranilamides have an extensive pi-conjugation that provides pathways for efficient long-range charge transfer along their backbones. We hypothesized that these anthranilamides posses intrinsic dipoles that are attributable to the orientation of the amide bonds and the hydrogen bond network. Our lab conducted computational studies in order to examine the electronic properties of oligo-anthranilamides. Using *ab initio* functional theory calculation, we showed that: (1) anthranilamides derivatives have intrinsic dipole moments along their main axis; (2) these intrinsic dipoles increased with increasing length of the oligo-anthranilamide; (3) band gaps decreased with increasing length of the oligo-anthranilamide; and (4) each anthranilamide residue contributed approximately 3 Debyes to the axial dipole, where ~1.8 Debyes came from the amide bond and ~0.9 Debyes from a hydrogen bond (Ashraf, Millare et al. 2009).

Based on these theoretical findings, we synthesized anthranilamide-pyrene dyads and investigated their charge-transfer properties. The pyrene acted as an electron acceptor and mediated charge separation that was considerably faster when the electron moved along the dipole than when it moved against it. Furthermore, we demonstrated that the charges, i.e., holes, can localize on dialkylamino derivatives of anthranilamides. This property is essential to the hopping (or on-resonance) mechanism, which is in turn essential to attaining long-range charge transfer.

References:

Ashraf, M. K., B. Millare, et al. (2009). "Theoretical design of bioinspired macromolecular electrets based on anthranilamide derivatives." Biotechnology progress.

Barnham, K. W. J., M. Mazzer, et al. (2006). "Resolving the energy crisis: nuclear or photovoltaics?" Nature materials.

Bustamante, C., Y. Chemla, et al. (2004). "MECHANICAL PROCESSES IN BIOCHEMISTRY." Annu. Rev. Biochem. **73**(1): 705-748.

Delorme, V., R. Dhouib, et al. (2011). "Effects of surfactants on lipase structure, activity, and inhibition." Pharmaceutical research **28**(8): 1831-1842.

Deniz, A. A., S. Mukhopadhyay, et al. (2008). "Single-molecule biophysics: at the interface of biology, physics and chemistry." Journal of The Royal Society Interface.

Dennis, E. A. (1973). "Kinetic dependence of phospholipase A 2 activity on the detergent Triton X-100." Journal of lipid research **14**(2): 152-159.

Erdmann, T. and U. S. Schwarz (2004). "Stochastic dynamics of adhesion clusters under shared constant force and with rebinding." The Journal of chemical physics **121**(18): 8997-9017.

Evans, E. (2001). "Probing the relation between force--lifetime--and chemistry in single molecular bonds." Annual review of biophysics and biomolecular structure **30**: 105-128.

Fedorova, A., A. Chaudhari, et al. (2003). "Photoinduced Electron-Transfer along [alpha]-Helical and Coiled-Coil Metallopeptides." J. Am. Chem. Soc.

Filice, M., M. Marciello, et al. (2011). "Hydrolysis of fish oil by hyperactivated rhizomucor miehei lipase immobilized by multipoint anion exchange." Biotechnology Progress **27**(4): 961-968.

Fox, M. A. and E. Galoppini (1997). "Electric field effects on electron transfer rates in dichromophoric peptides: the effect of helix …." J. Am. Chem. Soc.

Galoppini, E. and M. A. Fox (1996). "Effect of the Electric Field Generated by the Helix Dipole on Photoinduced Intramolecular Electron …." J. Am. Chem. Soc.

Gauthier, M. (2009, February 23, 2009). "Earth's First video log about atmospheric CO2." CO2 Speaker's Corner. Retrieved 07/08/2009, 2009, from http://co2now.org/.

Graneli, A., C. C. Yeykal, et al. (2006). "Organized arrays of individual DNA molecules tethered to supported lipid bilayers." Langmuir : the ACS journal of surfaces and colloids **22**(1): 292-299.

Green, C., S. Baksi, et al. (2007). "Challenges to a climate stabilizing energy future." Energy Policy.

Hamuro, Y., S. Geib, et al. (1996). "Oligoanthranilamides. Non-peptide subunits that show formation of specific secondary structure." J. Am. Chem. Soc **118**(32): 7529-7541.

Hol, W. G. J., P. T. Van Duijnen, et al. (1978). "The α-helix dipole and the properties of proteins." nature.com.

Isaacs, J. D. and W. R. Schmitt (1980). "Ocean energy: forms and prospects." Science.

Kapanidis, A. N. and T. Strick (2009). "Biology, one molecule at a time." Trends in Biochemical Sciences.

Kosyachenko, L. A., E. V. Grushko, et al. (2006). "Recombination losses in thin-film CdS/CdTe photovoltaic devices." Solar Energy Materials and Solar Cells.

Leckband, D. and J. Israelachvili (2001). "Intermolecular forces in biology." Quarterly reviews of biophysics **34**(2): 105-267.

Lewis, N. S. (2005). "Chemical control of charge transfer and recombination at semiconductor photoelectrode surfaces." Inorg. Chem.

Lewis, N. S. and D. G. Nocera (2006). "Powering the planet: Chemical challenges in solar energy utilization." Proceedings of the National Academy of Sciences.

Nahas, M., T. Wilson, et al. (2004). "Observation of internal cleavage and ligation reactions of a ribozyme." Nat Struct Mol Biol **11**(11): 1107-1113.

Neuman, K. and A. Nagy (2008). "Single-molecule force spectroscopy: optical tweezers, magnetic tweezers and atomic force microscopy." Nat Meth **5**(6): 491-505.

Neuman, K. C. and A. Nagy (2008). "Single-molecule force spectroscopy: optical tweezers, magnetic tweezers and atomic force microscopy." Nature Methods **5**(6): 491-505.

Peaker, A. R., V. P. Markevich, et al. (2004). "Recombination and radiation damage in crystalline silicon solar cell material." physica status solidi (c).

Siegenthaler, U., T. F. Stocker, et al. (2005). "Stable carbon cycle-climate relationship during the late Pleistocene." Science.

Sigala, P. A., A. T. Fafarman, et al. (2007). "Do Ligand Binding and Solvent Exclusion Alter the Electrostatic Character within the Oxyanion Hole of an Enzymatic Active Site?" J. Am. Chem. Soc. **129**(40): 12104-12105.

Sikes, H. D., J. F. Smalley, et al. (2001). "Rapid electron tunneling through oligophenylenevinylene bridges." Science.

Suydam, I. T., C. D. Snow, et al. (2006). "Electric Fields at the Active Site of an Enzyme: Direct Comparison of Experiment with Theory." Science **313**(5784): 200-204.

United-States-Department-of-Energy (2006). "World Consumption of Primary Energy by Energy Type and Selected Country Groups, 1980-2004." Energy Information Administration. Retrieved Jan 20, 2007.

Visoly-Fisher, I., K. Daie, et al. (2006). "Conductance of a biomolecular wire." Proceedings of the National Academy of Sciences.

Walter, N. G., C. Y. Huang, et al. (2008). "Do-it-yourself guide: how to use the modern single-molecule toolkit." Nature Methods **5**(6): 475-489.

Walter, N. G., C. Y. Huang, et al. (2008). "Do-it-yourself guide: how to use the modern single-molecule toolkit." Nat Meth.

Wan, J., M. S. Thomas, et al. (2009). "Surface-Bound Proteins with Preserved Functionality." Annals of biomedical engineering.

Yasutomi, S., T. Morita, et al. (2004). "A molecular photodiode system that can switch photocurrent direction." Science.

Zhang, W., W. T. Ang, et al. (2011). "Minimizing nonspecific protein adsorption in liquid crystal immunoassays by using surfactants." ACS applied materials & interfaces **3**(9): 3496-3500.

Chapter 1

Coatings of Polyethylene Glycol for Suppressing Non-specific Interactions between Solid Microspheres and Flat Surfaces

TOC graph

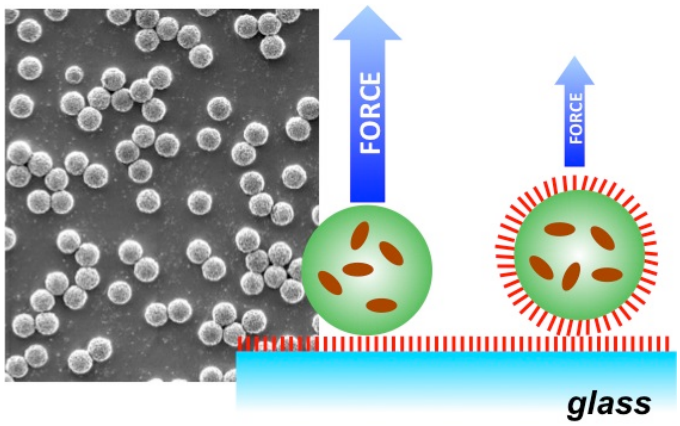

ABSTRACT

This article describes the development and the examination of surface coatings that suppress the adhesion between glass surfaces and polystyrene microspheres. Superparamagnetic doping of the microbeads allowed for exerting magnetic forces on them. The carboxyl functionalization of the polystyrene provided the means for coating the beads with polyethylene glycol (PEG) with different molecular weight. Under gravitational force, ~ 0.3 pN, the microbeads settled on glass surfaces with similar polymer coatings. We examined the efficacy of removing the beads from the glass surfaces by applying pulling force of 1.2 pN. The percent beads remaining on the surface after applying the pulling force for more than 5s served as an indication of the adhesion propensity. Coating of PEG with molecular weight ranging between 3 and 10 kDa was essential for suppressing the adhesion. For the particular substrates, surface chemistry and aqueous media we used, coatings of 5 kD manifested optimal suppression of adhesion: i.e., only 3% of the microbeads remained on the surface after applying the pulling magnetic force. When either the glass or the beads were not PEGylated, the adhesion between them was substantial. Addition of a non-charged surfactant, TWEEN, above its critical micelle concentrations (CMCs) suppressed the adhesion between non-coated substrates. The extent of this surfactant-induced improvement of the adhesion suppression, however, did not exceed the quality of preventing the adhesion that we attained by PEGylating both substrates. In addition, the use of surfactants did not significantly improve the suppression of bead-surface adhesion when both substrates were PEGylated. These findings suggest that such surfactant additives tend to be

redundant and that covalently grafted coatings of PEGs with selected chain lengths provide sufficient suppression of non-specific interfacial interactions.

KEYWORDS: PEG, TWEEN, polystyrene beads, magnetic tweezers, van der Waals interactions, non-specific interactions, protein adsorption

Introduction

Recent advances in single-molecule force measurements (SMFMs) provide the means to study and elucidate the intricacies of mechanisms and interactions within macromolecular structures.(Neuman and Nagy 2008; Kapanidis and Strick 2009) As vital techniques, SMFMs allow for probing the energy landscape of bimolecular processes such as receptor-ligand interactions(Ainavarapu, Wiita et al. 2008) and protein folding under mechanical stress.(Pum, Horejs et al. 2011) The techniques for SMFM, such as biomembrane force probes, atomic force microscopes, and optical tweezers, have varying advantages and disadvantages, Among the array of SMFM tools available, we employed a variation of magnetic tweezers for their biocompatibility and force dynamic range. Magnetic forces are orthogonal to most biological interactions, and magnetic tweezers permit a reliable access to the low piconewton and sub-piconewton force domain.

An effective way to experimentally study single-molecule mechanics is to employ force measurement on macromolecular complexes (with dimensions in the order of a few nanometers) immobilized on micrometer-size probes.(Neuman and Nagy 2008) While the diffraction limit prohibits optical imaging of single molecules in their native environment, optical methods allow for following with ångström resolution the movement of micrometer-size probes, to which the molecules are connected. These probes (e.g., microbeads or AFM tips) have a dual purpose: (1) they are the force transducers, and (2) they are the optical (imaging) probes for following mechanical displacements within the examined molecules.

Forces feasible for probing single-molecule interactions and conformational mechanics range between about 10 and 100 pN. This force domain, however, is overwhelmed by non-specific interactions involving the micrometer-size probes. Non-specific attractive forces (which result from van der Waals and other electric interactions)(Leckband and Israelachvili 2001; Israelachvili 2005) between the probes and other solid interfaces readily exceed a nanonewton at nanometer separations: i.e., separations comparable to protein dimensions. In contrast, biospecific interactions involve the same forces in a spatially regulated and cooperative manner to ensure strong non-covalent binding only upon acceptable complementarity between the structure, the charge distribution, and the hydrogen-bonding propensity of the interacting molecular species.(Israelachvili 2005) A principal challenge for SMFMs is characterizing such biospecific interactions, which are confined to a single molecule on the background of non-specific attractive forces between probes that are orders of magnitude larger than the investigated molecule.

Coatings of physisorbed proteins are frequently the choice for suppressing non-specific interactions.(Hickman, Sweryda-Krawiec et al. 2004) The hydration and the charge similarity of the protein coatings provide non-specific repellence, opposing the non-specific van der Waals attraction between coated interfaces. Using such a passivation approach, however, is not optimal because it may preclude the study of proteins, materials or macromolecules that interact with proteins.(Niedzwiecki, Grazul et al. 2010) Furthermore, the addition of surfactants may be a requirement for attaining adequate suppression of the undesired non-specific adhesion between protein-coated interfaces.(Schoenfisch, Brogan et al. 2004; Zhang, Ang et al. 2011)

Surfactants, indeed, represent another widely used class of molecules for suppressing non-specific interactions.(Danilowicz, Greenfield et al. 2005) In order to be effective, however, these amphipaths are largely required in high concentrations, i.e., in concentrations exceeding their CMCs.(Wahlgren, Welin-Klintström et al. 1995; Vullev and Jones 2002) Additionally, the presence of surfactants in such high concentrations can disrupt active sites, and hence the studied biospecific interactions; or worse, they can perturb the native protein structures.(Otzen 2011)

Therefore, it is essential to seek venues for suppressing the non-specific interactions between micrometer-size objects when connected via nanometer-size molecules. Using chemisorbed (instead of physisorbed) passivation biocompatible coatings,(Wan, Thomas et al. 2009) along with eliminating the need of additives such as surfactants, provides considerable advantages for SMFMs.

Herein, we demonstrated that covalently grafted coatings of polyethylene glycol (PEG), with a molecular weight (MW) considerably exceeding 1 kDa, suppressed the non-desired adhesion of polystyrene microspheres to glass surfaces. We examined the adhesion propensity of polystyrene micorspheres to flat glass surfaces when coated with PEGs with different length, varying from about 22 to 450 repeating units and corresponding to MW from about 1,000 to 20,000 Da. (The PEGs with different MW are designated in the text as PEG-"MW in Da", i.e., Peg-1000 to PEG-20000.) Coatings of PEGs with MW ranging between 3 kDa and 10 kDa provided optimal suppression of the non-specific adhesion. When the microbeads and the glass were coated with PEG-5000, less than 3% of the beads remained on the surface after applying 1.2 pN pulling force. When only the beads or the glass were coated (with PEG-3000), the non-specific

interactions were still prevalent. Adding a non-charged surfactant, TWEEN®20, only marginally improved the suppression of non-specific interactions. Relating our adhesion findings with the structural features of the hydrated PEGs, provided guidelines for suppressing non-specific interactions between micrometer-size objects at nanometer separation.

Results

Instrument setup and calibration. We employed a variation of magnetic tweezers, more accurately termed magnetic pullers, in order to characterize the non-specific interaction between glass surfaces and superparamagnetically doped polystyrene microspheres (Scheme 1-1). Magnetic pullers usually employ a single electromagnet that does not generate a magnetic trap. The pullers are relatively simple devices, and they allow for a well-controlled exertion of relatively weak forces on magnetic micro- and nano-objects, i.e., forces that are less than 10 pN, directed toward the magnet.

The magnetic pullers are inverted optical microscopes with electromagnets or permanent magnets above the sample focal plane (Scheme 1-1a).(Kapanidis and Strick 2009) Microbeads that contain paramagnetic material are allowed to settle under gravity on the surface of a sample slide. The surface on which the beads settle is within the depth of field of the objective (Scheme 1-1b). Magnetic field gradients, generated by the magnet above the focal plain, exert pulling forces on the beads (Scheme 1-1c). As the pulling force moves the microbeads away from the surface, and hence out of the depth of

field, the beads "disappear" from the focus of the image. By recording movies of the beads settled in the field of depth,(Vullev, Wan et al. 2006; Thomas, Clift et al. 2010) we were able to monitor the number of beads on the glass surface at each time point.

We employed superparamagnetic materials to ensure that: (1) the beads attain complete magnetization in relatedly weak fields; and (2) their magnetization would not manifest hysteretic behavior when the field was turned off. Hence, the magnitude of the force depended mostly on the field gradient, which was readily controlled by varying the current passed through the electromagnet coil or by moving the permanent magnet up and down above the focal plane.(Danilowicz, Greenfield et al. 2005; Bijamov, Shubitidze et al. 2010) Since we aimed at piconewton forces, we chose to employ an electromagnet in order to avoid moving parts and eliminate unnecessary vibrations during the measurements.

When suspended in the aqueous solution, each bead experienced 0.3 ± 0.1 pN gravitational pull downward, as we determined from direct measurements and from calculations accounting for the bead buoyancy in the used media. After allowing the beads to settle on the glass surfaces for three minutes (Scheme 1-1c), we switched the electromagnet to apply 1.2 ± 0.3 pN upward net pulling force (Scheme 1-1d). We quantified the extent of the non-desired adhesion as the percent of beads that remained on the surface after applying the magnetic force for five seconds (Figure 1-1).

In order to calibrate the magnetic puller, we moved the objective to attain a side view for the setup (Scheme 1-2). A suspension of the superparamagnetic microbeads was introduced in a square capillary under the magnet (Scheme 1-2). We recorded the

velocities with which the microbeads in the capillary moved toward the magnet and employed the Stoke's drag equation for estimating the magnetic force on the beads at different distances from the magnet, and at various voltages applied to the coil of the electromagnet.

Non-specific interfacial interactions. A range of interfacial attractive and repulsive forces governs the propensity for non-specific adhesion of micrometer-size objects to solid surfaces.(Israelachvili 1992; Vasquez, Vu et al. 2009) As encompassed by the Derjaguin–Landau–Verwey–Overbeek (DLVO) theory, the double-layer electrostatic forces, F_{DL} (which can be attractive or repulsive), between a microsphere with a radius, r, and a flat solid surface decrease exponentially with the interfacial distance, d.(Israelachvili 1992; Leckband and Israelachvili 2001) Concurrently, the integrated van der Walls forces, F_{vdW} (which are inherently attractive), between a microsphere and a surface, nanometers away from the sphere, decrease with the square of d for small separation distances, i.e., for $d << r$:(Israelachvili 1992; Leckband and Israelachvili 2001)

$$F_{vdW} = -\frac{Ar}{6d^2} \tag{1a}$$

$$F_{DL} = \kappa Z r \exp(-\kappa d) \tag{1b}$$

where A is the Hamaker constant taking into consideration the static, ε_i, and dynamic, n_i^2, dielectric properties of the materials composing the sphere (i = 1), the flat substrate (i =

2) and the media separating the sphere from the flat surface ($i = 3$). Z is a similar constant for the double-layer interactions that depends on the surface potential, ψ_0, and the valency of the electrolyte, z. The charge of the electrolyte ions, z_i, and their densities in the bulk solution, $\rho_{\infty i}$ (i.e., at infinity d), determine the Debye length, κ^{-1}, of the media with a relative dielectric constant ε:(Israelachvili 1992; Bard and Faulkner 2001; Leckband and Israelachvili 2001; Bao, Millare et al. 2009; Hu, Xia et al. 2009; Bao, Ramu et al. 2010; Upadhyayula, Bao et al. 2011)

$$A = A_{\nu=0} + A_{\nu>0} \approx$$
$$\approx \frac{3}{4} k_B T \left(\frac{\varepsilon_1 - \varepsilon_3}{\varepsilon_1 + \varepsilon_3}\right)\left(\frac{\varepsilon_2 - \varepsilon_3}{\varepsilon_2 + \varepsilon_3}\right) +$$
$$+ \frac{3}{8} h\nu_e \frac{\left(n_1^2 + n_3^2\right)\left(n_2^2 + n_3^2\right)}{\left(\sqrt{n_1^2 + n_3^2} + \sqrt{n_2^2 + n_3^2}\right)\sqrt{2\left(n_1^2 + n_3^2\right)\left(n_2^2 + n_3^2\right)}} \quad (2a)$$

$$Z \approx 64\pi\varepsilon_0\varepsilon\left(\frac{k_B T}{e}\right)^2 \tanh^2\left(\frac{ze\psi_0}{4k_B T}\right) \quad (2b)$$

$$\kappa = \sqrt{\frac{\sum_i \rho_{\infty i}\left(ez_i\right)^2}{\varepsilon_0 \varepsilon k_B T}} \quad (2c)$$

where k_B is the Boltzmann constant; T is the thermodynamic temperature; ν designates electromagnetic frequency, i.e., $A_{\nu=0}$ and $A_{\nu>0}$ are the static and dynamic components of the Hamaker constant, respectively, and ν_e is a resonance electronic transition frequency

(usually the band at the red edge of the UV/Vis absorption spectra); h is the Planck constant; ε_0 is the electric permittivity of vacuum; and e is the elementary charge.

At distances exceeding about $10\kappa^{-1}$, F_{DL} and F_{vdW} decrease to about a piconewton or less.(Israelachvili and Ninham 1977; Leckband and Israelachvili 2001) Considering, for example, the interactions between polystyrene microspheres and glass surfaces in aqueous media provided an estimate that an increase in d from about 1 nm to 30 nm decreased F_{vdW} three orders of magnitude, i.e., from nanonewtons to piconewtons (equations 1a and 2a). Thus, keeping tens of nanometers separation between the surfaces of the polystyrene microbeads and the glass may not be sufficient but is a necessary condition for preventing non-specific adhesion.

Non-charged surface coatings bring the values of ψ_0 close to zero. Therefore, for distances considerably exceeding the Debye length, $|F_{DL}| << |F_{vdW}|$. For the 100-mM phosphate buffer that we used in this study, $\kappa \approx 1.3$ nm^{-1}, allowing us to ignore the contribution of the electrostatic (double layer) interactions between non-charged surfaces should the separation between the polystyrene and the glass exceed a few nanometers (equations 1b, 2b, and 2c).

Surfaces coated with non-charged bioinert layers of *oligo*ethylene glycols (between three and six repeating units) suppress protein adsorption and cell adhesion based on protein-protein interactions.(Mrksich and Whitesides 1996; Chen, Mrksich et al. 1997; Chapman, Ostuni et al. 2000; Hu, Gao et al. 2009) Such short oligomers, however, do not provide sufficient separation between the microspheres and the surfaces. Therefore, we

focused on coatings composed of linear PEGs with MW of 1,000 Da and larger, i.e., polymers with more than 20 repeating units.

Surface derivatization and characterization. Using surface-chemistry protocols that we previously developed,(Hong, Bao et al. 2008; Millare, Thomas et al. 2008; Wan, Thomas et al. 2009; Thomas, Millare et al. 2010; Chau, Millare et al. 2011) we coated glass slides with PEGs with MW = 1, 2, 3, 5, 10 and 20 kDa. Concurrently, resorting to carboxylated polystyrene microspheres (that were superparamagnetically doped) allowed us to PEGylate them via aqueous-phase coupling protocols. FITR spectra confirmed the PEGylation of the superparamagnetically doped polystyrene beads. Furthermore, the beads manifested a positive shift in their ζ-potentials after PEGylation, consistent with the loss of negative charges from the deprotonated free carboxyl groups. Electron microscopy showed that the PEGylation did not alter the morphology of the beads on micrometer and submicrometer scales (Figure 1-2a, 1-2b), which was consistent with the formation of passivation layers with thicknesses that did not exceed a few tens of nanometers.

Spectroscopic ellipsometry revealed that the thickness of the coatings did not increase proportionally with the length of the PEG chains (Table 1-1). Furthermore, the extent of drying had a pronounced effect on the measured thickness of the PEG layers.

For each sample, we observed two "metastable" states of PEG hydration when the polymer films were left in contact with air. (The ellipsometry studies were carried in a clean-room environment with humidity maintained at 45%.) Draining the Milli Q water from the sample surfaces and letting them vent in the air led to constant thicknesses

(within 30 minutes of drying) as monitored by ellipsometry (h_{wet} in Table 1-1). The water molecules bound to the PEG chains remained in these "*wet*" films, making h_{wet} representative of the PEGylated surfaces when immersed in aqueous media.

Vigorous mechanical drying of the same samples (using a stream of dry nitrogen) decreased the thicknesses of the films (Table 1-1). Removal of most of the PEG-bound water appeared to have allowed the polymer chains to collapse and the films to thin. Although it is impossible to obtain complete dehydration of the PEG coatings under the conditions of the environment, the thicknesses of these "*dry*" films, h_{dry}, provided a handle for estimating the surface packing, γ, and the average distance, s, between the grafting sites (Table 1-1). Indeed, employing a materials model encompassing the parameters of pure PEG, provided excellent data fits for the ellipsometry spectra of the "*dry*" samples. In comparison, for the analysis of the "*wet*" samples, the data fits had higher χ^2 values than the χ^2 for the "*dry*" samples. As an alternative, we also allowed some of the optical parameters of the pure PEG film to relax in order to improve the fits.

For PEG-1000 the method of drying did not have a considerable effect on the coating thickness (Table 1-1). In contrast, while h_{wet} dropped when the PEG MW exceeded 10 kDa, while h_{dry} manifested a trend of an increase with the PEG MW (Table 1-1). For all PEG MWs, the polymer Flory radii, R_F, were larger than the separation, s, between their grafting sites (Table 1-1). This finding ($s < R_F < h_{wet}$) suggested that the PEGs in these coatings most probably existed as "brush" conformers.(Israelachvili 1992; Leckband and Israelachvili 2001)

Role of PEG length. Long-range interfacial interactions (equations 1 and 2) provide key guidelines for the thicknesses of the passivation layers. Maintaining the interfacial interaction energies at levels that are comparable with the thermal energy, k_BT, requires inert layers that keep interfacial separation of tens of nanometers between the polystyrene microspheres and the flat glass surface.

To examine this somewhat oversimplified view on suppressing interfacial non-specific interactions, we tested the dependence of the adhesion on the length of the PEGs composing the coatings on the beads and on the flat surfaces. When the microspheres and the glass substrates were coated with PEG-1000, on average about 60 % of the beads remained on the surface upon applying 1.2-pN force (Figure 1-3a). An increase in the PEG length to about PEG-5000 lead to a drastic decrease in the number of beads remaining adhered to the glass substrate in the presence of the pulling magnetic force (Figure 1-3a). Indeed, when the microspheres and the glass were coated with PEG-5000, only about 3 % of the beads remained on the surface upon applying the magnetic pulling force.

An increase in the molecular weight of the coating PEGs to 10 kDa and 20 kDa led to an opposite trend. The number of remaining adhered beads increased with the increase in the PEG molecular weight (Figure 1-3a). This finding illustrated the limits in applying models for interactions between rigid substrates (equations 1 and 2) to the mechanics of soft materials,(Drobek, Spencer et al. 2005; Jones, Yan et al. 2007) i.e., to surface coatings composed of flexible polymers.

Overall, films of linear PEGs with MW between 3 kDa and 10 kDa appeared optimal for suppressing adhesion between the microspheres and the glass surfaces. That is, for 3 Da ≤ MW ≤ 10 Da, less than $1/5^{th}$ of the beads remained adhered to the surface after applying piconewton pulling force (Figure 1-3a).

Role of PEG coatings. PEG-3000 was the shortest polymer that provided acceptable suppression of non-specific interfacial interactions between the microbeads and the flat substrate. Therefore, we employed PEG-3000 not only for investigating the interactions between PEGylated and bare surfaces, but also for analyzing the dependence of the adhesion on surfactant additives.

Coating the glass surfaces and the beads with PEG-3000 provided the means for suppressing non-specific interactions (Table 1-1 and 1-2). In contrast, when only the glass surfaces were coated with PEG-3000 and the beads were not coated, about 82% of the beads remained adhered after applying the magnetic force (Table 1-2). Similarly, when the glass was not coated and the beads were PEGylated, about 72 % of the beads remained adhered after applying the pulling force (Table 1-2). These results show the importance of having both coated beads and coated glass surfaces for effective suppression of non-specific interactions when using PEG-3000 for passivation.

Separating the microbeads from the glass surface with two PEG-3000 layers (each about 16-nm thick) provides a means to keep sufficient distance between polystyrene and the glass surfaces, which is essential for minimizing the interfacial interactions. Overlap between the PEG films induces repulsive forces essential for keeping the two substrates apart.(Kenworthy, Hristova et al. 1995; Drobek, Spencer et al. 2005) In contrast, the

presence of only one PEG-3000 layer cannot provide wide enough separation between the substrates. It is consistent with the observed elevated adhesion when either only the beads or only the surfaces were PEGylated (Table 1-2).

As an alternative, identically prepared coatings of PEG-1000 and PEG-2000, had thicknesses of 4.0 and 10 nm, respectively. Coating the glass and the beads with these relatively thin PEG films did not sufficiently suppress the adhesion of the microspheres to the surfaces, as made evident by the copious amount of beads remaining on the glass upon applying 1.2-pN force (Table 1-1).

Role of non-charged surfactant. Despite the encouraging results, PEG-3000 coatings still did not provide quantitative suppression of the non-specific adhesion: i.e., even when both substrates were PEGylated about 10-15% of the beads remained adhered to the surface after applying the magnetic forces. Defects in the PEG coatings are a plausible cause of the observed residual adhesiveness. Physisorption of PEG conjugates to coat the defects in the surface layers is a feasible venue for further suppression of the non-specific interactions. The hydrophilic components of the TWEEN® surfactants are composed of PEG chains. Therefore, we chose to use TWEEN® in order to enhance the suppression of the adhesiveness of the interfaces.

To examine the effect of a non-charged surfactant on the adhesion between the beads and the glass surfaces, we added 10 μM, 100 μM and 250 μM of TWEEN®20 to the microbead aqueous suspension prior to dropping it over the glass surfaces. The presence of 10 μM TWEEN® (that is under its CMC) had no detectable effect on suppressing the

non-specific adhesion. For most of the investigated interfaces, the adhesion-suppressing effect of the surfactant became apparent when its concentration increased to 250 μM (Figure 1-4 and Table 1-2).

Electrostatic interactions. In addition to the van der Waals interactions (along with the steric and the thermal-fluctuation and hydration interaction between the PEG layers leading to the entropic repulsion), the Coulombic interactions present another principal contributor to the non-specific forces.(Israelachvili 2005) Therefore, it is essential to consider the charged groups on the different substrates when submersed in the neutral-pH aqueous media: (1) the non-coated glass surfaces were negatively charged; (2) the non-coated polystyrene beads were also negatively charged due to their derivatization with carboxylates; (3) PEG-coated glass surfaces may possess residual positive charges buried in the PEG layers close to the glass surface because the PEG chains were grafted to aldehyde-functionalized glass via reductive amination leaving secondary amines at the PEG-glass interface;(Wan, Thomas et al. 2009) and (4) PEG-coated beads may possess residual negative charges due to non-reacted carboxylates (remaining buried under the PEG layers) after grafting the amine terminated PEGs to the carboxyl-functionalized beads via amide coupling. In addition, we prepared aminated glass slides for attaining a substrate with positively charged surfaces in which the charged groups were not buried under PEG coatings.

Non-coated beads with aminated glass surfaces provided attractive electrostatic interactions that were primarily derived from the negative charges from the deprotonated

carboxyl groups on the beads and the positive charges from the protonated amines on the glass. In this experimental scenario, about 99% of the beads remained on the glass surface upon applying 1.2-pN force for five seconds. In contrast, non-coated beads and non-coated glass surfaces provided repulsive electrostatic interactions (where both surfaces were negatively charged), and only about 2% of the beads remained on the surface after the application of the magnetic force (Table 2).

Strictly speaking, the interaction energies, which govern the observed repulsion and adhesion between charged interfaces, are entropic in nature. In aqueous solutions, the electrostatic interactions fall off with distance quite substantially beyond a few nanometers. In fact, the Debye length in the aqueous media we used (containing 100 mM phosphate buffer, pH 7) was about 6.5 Å, making the Coulombic forces significant only when the charged surfaces were practically in contact with one another. When the charged interfaces approached each other, the counterions were either: (1) forced to bind to the charged sites (if the two surfaces had the same charge) leading to a decrease in entropy (i.e., an unfavorable energy change resulting in repulsive force); or (2) expelled into the bulk solution (if the two surfaces were oppositely charged) leading to an entropy increase (i.e., a favorable energy change resulting in attractive force).

Discussion

While considering van der Waals interfacial interactions between micrometer-sized objects provided the initial guidelines for selecting the thickness of the surface coatings

that suppress non-specific adhesion, such an oversimplified view of the integrated dipole and induced-dipole interactions between two dielectric materials separated by aqueous media could not encompass the complexity of non-specific attractive forces.(Israelachvili 2005; Vullev 2005) The surface of the polystyrene beads, for example, was not smooth and homogeneous (Figure 1-2a, 1-2b), and the van der Waals analysis did not take into consideration the molecular composition of the interfaces.

For PEG-1000 and PEG-2000, the enormous error bars from the adhesion measurements (Table 1-1) reflected the pronounced local variations in the morphologies of coated surfaces, i.e., they were indicative of the heterogeneity in the coatings. While ellipsometry averaged over the relatively large beam-reflection area used for the measurements (about 1 mm^2), the pulling experiments probed the surfaces at contact areas that were considerably smaller than a square micrometer. Therefore, the discrepancies observed in the pulling measurements with PEG-1000 and PEG-2000 most probably were a corollary of the inability of the relatively short chains of these polymers to efficiently cover neighboring "pinhole" areas of exposed substrate surfaces that were not PEGylated at sufficient grafting densities.

Too well packed or too loosely packed PEG layers cannot suppress non-specific adsorption and adhesion.(Harder, Grunze et al. 1998; Majewski, Kuhl et al. 1998; Bahmani, Gupta et al. 2011) Indeed, the dense packing of PEG layers, containing PEGs in all-trans rather than helical conformation,(Harder, Grunze et al. 1998; Feldman, Hähner et al. 1999) may offer an alternative explanation for the observed inefficient suppression of adhesion by the shortest PEG. Such all-trans PEG conformers, however,

require packing densities of about 5 molecules per nm^2 (or more), corresponding to $s <$ 0.5 nm.(Harder, Grunze et al. 1998) None of the surface coatings we investigated had such a high packing density: i.e., for all of them $\gamma \leq 2.7$ nm^{-2} and $s \geq 0.7$ nm (Table 1-1). Therefore, excessively high density of packing with PEG-1000 and PEG-2000 did not contribute to their inefficiency in suppressing non-specific adhesion.

For all coatings, $s < R_F$, suggesting that they were composed of PEGs in "brush" rather than in "mushroom" morphology.(Israelachvili 1992; Leckband and Israelachvili 2001) While the increment per residue for all-trans PEG chains is about 0.36 nm, the increment per residue for PEG helical conformers (composing "brush" coatings) is about 0.28 nm.(Harder, Grunze et al. 1998) Thus, to ensure helical conformation essential for "brush" morphology, the thickness of a film composed of PEG chains of N residues cannot exceed $0.28N$ nm. For all the coatings we investigated, indeed, $h_{wet} < 0.28N$ nm.

An increase in the packing density provides a means for forcing the helical conformers in the "brush" polymer layer to extend away from the surface and increase interfacial separation between coated substrates:(Heuberger, Drobek et al. 2005) i.e., $R_F < h_{wet}$. For suppressing adhesion, therefore, the PEGs have to be packed densely but not too densely.

How dense is dense? Considering the ratio between h_{wet} and R_F as a characteristic of packing-induced steric constraint of the polymer chains, allowed for setting apart the PEGs that provided optimal adhesion suppression: i.e., for PEG-3000, PEG-5000, and PEG-10000, $h_{wet} / R_F > 10$ (Figure 1-3c). The decrease in h_{wet} / R_F as the PEG MW increased from 5 kDa to 20 kDa was consistent with the observed decrease in the efficiency of adhesion suppression (Figure 1-3c). While maintaining $s > 0.52$ nm and $h <$

0.28*N* nm,(Harder, Grunze et al. 1998) attaining $h_{wet} / R_F > 10$ could serve as a guideline for PEG coatings that suppress undesired adhesion between micrometer-size objects.

Addition of TWEEN®20 suppressed the attractive interactions between oppositely charged surfaces only when the surfactant was used in excessive concentrations, i.e., 0.25 mM (Table 1-2). A plausible explanation of the observed results is that the physisorption of the surfactant on the substrate surface led to the suppression of the electrostatic interactions by burying the charged groups and changing the structure of the double layers. Therefore, charged groups coated by the PEG layers were not expected to contribute significantly to the observed non-specific interactions. Furthermore, the counterions of such buried charged groups would be immobilized in the PEG layers, making the behavior of such trapped ion pairs closer to the behavior of dipoles than to that of individual charges.

Our findings demonstrated a dependence of the efficacy of decreasing the extent of non-specific interfacial interactions on the surfactant concentration. The results, however, revealed that complications arise if only surfactants were employed for the suppression of non-specific interactions. Since surfactants are required in considerably high concentrations, they would be capable of disrupting not only biomolecular tertiary and quaternary structures, but also sensitive electrostatic and other biospecific interactions as seen with the non-coated beads on aminated surfaces.

Are TWEEN® surfactants needed for suppressing non-specific interactions? As moderate surfactants, the different TWEEN® conjugates are widely used in biology and in biophysics, including for suppressing non-specific adhesion.(Wahlgren, Welin-

Klintström et al. 1995; Danilowicz, Greenfield et al. 2005; Hu, Gao et al. 2009; Zhang, Ang et al. 2011) Our findings, however, do not provide convincing evidence for the benefit of TWEEN® in suppressing non-specific interfacial interactions. Although addition of TWEEN®20 decreased the amount of the non-specifically adhered microbeads by a factor of two, the concentrations of the used surfactant were high enough to considerably perturb the properties of investigated biological systems, making the use of such surfactant unfeasible for SMFMs.

Why PEG? PEG is an amphipathic polymer that intercalates well in the water structure, and hence does not significantly perturb the three-dimensional molecular composition of the media.(Israelachvili 1997) The distances between the oxygens in a PEG chain match well with the hydrogen-bonding network of water, providing the means for stable hydration shells around the hydrophobic stretches of the polymer (i.e., around the ethylenes). Thus, the PEG chains form networks supporting the water structure (e.g., hydrogels) and do not interact with one another (or with other macromolecules) at temperatures and pressures under which the polymer hydration is intact. Therefore, PEG is biocompatible and coatings of PEG (in brush conformation) prevent adsorption of biological macromolecules.(Janshoff, Neitzert et al. 2000; Shang and Lee 2007; Joo, Balci et al. 2008; Hu, Gao et al. 2009; Wan, Thomas et al. 2009) While PEG is not necessarily unique and other materials are also potentially biocompatible and suppress non-specific adsorption,(Deng, Mrksich et al. 1996; Chapman, Ostuni et al. 2000; Chen, Zheng et al. 2005) the biophysics of PEG has been extensively investigated and its chemistry well developed to allow broad versatility for the preparation of robust bioinert

and biofunctional interfaces.(Harris 1992; Yu, Yang et al. 1999; Wan, Thomas et al. 2009) Overall, the PEGylation of the surfaces serves two main functions: (1) it creates a separation between the two surfaces, and (2) it introduces entropic repulsion between the surfaces,(Israelachvili and Wennerstroem 1992) as it is not energetically favorable to compress the PEG strands between the approaching interfaces when the hydrated polymer chains are in their brush conformation.(Prime and Whitesides 1991; Bergstrom, Holmberg et al. 1992; McPherson Timothy, Lee Samuel et al. 1995; Yu, Yang et al. 1999)

Conclusions

The functionality of biological molecules does not get compromised upon covalent attachment to PEG bioinert layers.(Wan, Thomas et al. 2009) This consideration, along with the ability of PEG coatings to suppress non-specific interfacial interactions, will prove immensely important and beneficial for SMFMs. Because there are more disadvantages than benefits to using TWEEN® for suppressing non-desired adhesion, we believe that the emphasis should be on improving non-adhesiveness via a rational design of surface coatings, rather than on taking "short-cuts" by using surfactants and other additives. Employing surfactants in SMFM studies, indeed, undermines the ability to study proteins with native functionality.

Nevertheless, an examination of the molecular structures of the TWEEN® surfactants revealed that the use of coatings of branched PEG derivatives might provide further

suppression of non-specific interactions. (The PEG chains in the TWEENs are branched out of a sorbitan.) Such venues for rational interfacial design at multiscale levels (from molecular to micrometer dimensions) are crucial for advancing the tools for SMFMs.

For linear PEG chains, however, we observed that the ratio between the film thickness and the Flory radius of the polymers composing the film correlated excellently with the ability of these PEG coatings to suppress non-desired adhesion. Testing this correlation in as many different applications as possible will provide the means to examine the potential universality and the limits in using the thickness-to-radius ratio for predicting resistance against non-specific interfacial interactions.

Experimental

Materials. Polymer based magnetite superparamagnetic spheres (that have carboxyl functional groups, with a mean diameter of 3 μm and 1.9 g/cm^3 density) were purchased from ProMag^{TM}. Pre-cleaned 1 mm thick microscope glass slides were purchased from VWR and cut into 25×35 mm pieces prior to use. Silicon wafers (n/phosphorous and p/boron doped, 1-10 Ω cm, one side polished, test grade, ⟨100⟩) were purchased from Silicon Sense, Inc., and cut into 25×10 mm prior to use.

The polymers, α,ω-aminomethoxy polyethylene glycol (MeO–PEG–NH_2), MW = 1, 2, 3, 5, 10, and 20 kDa, were purchased from Layson Bio. 11-aminoundecyltriethoxysilane and 11-(trietoxysilyl)un-decanaldehyde acetal were purchased from Gelest, Inc. Indium (III) chloride (99.999%), redistilled N,N-Diisopropylethylamine (DIPEA), TWEEN®20

surfactant, and sodium cyanoborohydride were purchased from Aldrich. N,N-diisopropyl-carbodiimide (DIC) and N-hydroxysuccin-imide (HOSu) were obtained from Lancaster. Hydroxybenzotriazole (HOBt) was purchased from Chem-Impex International. 1-ethyl-3-(3-dimethylaminopropyl) carbodiimide (EDC), toluene, tetrahydrofuran (THF), methanol and ethanol, all spectroscopy grade and/or anhydrous, were obtained from Fisher.

Coating and characterization of flat substrates. Using a surface chemistry protocol that we previously developed,(Wan, Thomas et al. 2009) we functionalized glass slides with varying lengths of MeO-PEG-NH_2. For ellipsometry measurements, we prepared identical coatings on silicon wavers.(Wan, Thomas et al. 2009) We monitored the completion of PEGylation reaction via surface contact angle measurements.(Millare, Thomas et al. 2008)

For the aminated control surfaces, we salinized glass slides with alkyleneamines by: (1) cleaning them as we previously described;(Wan, Thomas et al. 2009) (2) treating them with oxygen plasma;(Millare, Thomas et al. 2008; Chau, Millare et al. 2011) and (3) immersing them in an anhydrous toluene solution of 0.04% (v/v) of 11-aminoundecyltriethoxysilane and 0.02% DIPEA. The glass slides, immersed in the salanization solution, were heated on a sand bath at 110°C, and were sonicated in hot water intermittently for 60 s after the first hour. After 18 hr, the salanization bath was allowed to cool down to room temperature, the solution was discarded, and the glass

slides were doubly washed with toluene, dichloromethane, THF, ethanol, and deionized/milli Q water.

Coating and characterization of microbeads. The PEGylation of the beads involved the following principal steps:

Cleaning. 10 µl of a suspension of magnetic beads were placed in a 1 ml microfuge tube containing 250 µl solution of 0.01 M sodium hydroxide (NaOH), and gently shaken at room temperature for 10 minutes. The beads were trapped with a permanent magnet at the bottom of the tube for 5 min and the solution was decanted. This wash step was repeated twice. 500 µl of deionized water was then added to the centrifuge tube and gently shaken at room temperature for 5 minutes. The water-bead solution was decanted and the process repeated three times.

PEG coupling. In a cold room, the water was removed from the centrifuge tube and 200 µl solutions of HOSu and EDC were added to the beads, followed by addition of MeO-PEH-NH_2. The solution was gently shaken in the cold room (4°C). After overnight shaking, the solution was brought back to room temperature for 2-4 hours and washed with plenty of deionized water and decanted. Beads were stored in deionized water at 2-8°C until needed.

Verification. The presence of the PEG coatings was confirmed using FTIR as we have previously demonstrated.(Bahmani, Gupta et al. 2011) The completion of the coupling reaction was monitored by measuring the ζ-potential of the beads. The covalent

modification of the polystyrene beads with PEG led to a positive shift in the ζ-potentials, resultant from the elimination of the negatively charged carboxylic acid groups.

Ellipsometry. Spectra of the phase (Δ) and the amplitude (Ψ) were recorded between 400 and 700 nm for three angles of incidence, 60°, 70° and 80°, using Horiba Jobin Yvon UVISEL spectroscopic ellipsometer, model M200. The measurements were conducted in a class-1,000 clean room, with humidity maintained at 45 (± 1) %. The samples were mounted on an ellipsometer stage exposed to air.

For the "*wet*" PEG coatings, the samples (coated silicon wafers stored under water) were washed with Milli-Q water and kept vertically to dry over dust-free wiper tissue for at least half an hour prior to the measurements. For the ellipsometry spectra of the "*dry*" coatings, the PEGylated surfaces of the same samples were blown with copious amounts of dry nitrogen for at least 5 minutes.

The thicknesses of the PEG layers, h_{dry} and h_{wet} (Table 1-1), were obtained from global fits of the ellipsometry spectra recorded at the different angles. A two-layer model, air//PEG/SiO_2/Si,(Wan, Thomas et al. 2009) provided excellent fits for the spectra of all samples. Using models based on a single layer or on more than two layers did not yield satisfactory data fits. The fitting algorithm minimized the χ^2 values and the fitting residuals revealed the goodness of the fits. The thickness of the SiO_2 layer was about 2.2 nm and the thickness of the PEG layer varied with the MW of the polymer (Table 1-1).

Established parameters for all materials were incorporated in the data analysis software, DeltaPsi v2.4.3.158 (Horiba Jobin Yvon, Inc.). For the PEG material layer in the fitting

model, we used the default parameters provided by the Thin Film Division at HORIBA Jobin Yvon, Inc., ε_∞ = 1.0; ε_s = 1.633; ω_t = 9.723; and Γ_0 = 4.921.(Schubert 2006) For this study, we used the layer thicknesses obtained from data fits for which these parameters were fixed. Relaxing these parameters for the analyses of the "*dry*" samples did not improve the quality of the fits, and produced negative values for some of the dielectric quantities. Relaxing the parameters for the "*wet*" samples resulted in a slight improvement of the quality of the fits, and, within physically feasible values of the quantities characteristic of the PEG material, yielded layer thicknesses of 2.7, 9.1, 22, 35, and 27 nm for PEGs with MW 1, 2,3, 5, 10, and 20 kDa, respectively. Nevertheless, because we did not have a basis for judging the plausibility in the variations of the fitting dielectric and optical parameters, we used the results from the data fits with fixed parameters (i.e., using a model for pure PEG for analyzing the data from the wet PEG samples) with the understanding that the values of h_{wet}, reported in Table 1-1, might be underestimated.

Microscopy. Fluorescence microscopy images were acquired using a Nikon Ti-U inverted microscope (Nikon, Inc., Melville, NY), equipped with a 100× Nikon oil immersion objective (numerical aperture, 1.49; working distance, 120 μm) and a Hamamatsu electron multiplier charge-coupled-device digital camera (model C9100-13; Hamamatsu Corp., Bridgewater, NJ), as we previously described.(Xia, Upadhyayula et al. 2011) Suspension of superparamagnetic beads was dropped on a glass slide, placed over the objective of the microscope, and the beads were allowed to settle on the glass

surface. Using bright-field mode, the objective was focused on the settled beads, and for the imaging, it was turned into fluorescence mode utilizing the autofluorescence from the polystyrene material composing the microspheres (λ_{em} = 536 nm, bandwidth = 25 nm).

Scanning electron microscopy images were recorded using FEI XL30-FEG SEM. Prior to imaging, the superparamagnetic beads were washed with Milli Q water several times, lyophilized, spread on a sample stage, and sputter-coated with a conductive layer (80% Pt and 20% Pd).

Calibration of the magnetic puller. We built a magnetic puller setup to carryout the adhesion studies (Scheme 1-1). We designed the setup in two interchangeable configurations: (1) "work mode" for measurements of the number of beads on a flat surface of a transparent substrate (Scheme 1-1a), in which the objective is positioned below the sample slide and (2) "calibration mode" for force calibration (Scheme 1-2), in which the objective provides a side view of the suspension allowing for tracking the position of beads as they move vertically in response to the magnetic field. The two parameters used for controlling the force experienced by the paramagnetic beads are: (1) the distance from the core of the electromagnet and (2) the current flowing through the coil of the electromagnet, controlled by the applied voltage.

Stoke's drag equation allowed us to determine the forces generated on the super paramagnetic bead at different distances and different applied voltages (Figure 1-5):

$$F_d = -6\pi\mu r v \qquad (3)$$

where F_d is the drag force, μ is the viscosity of the media, and r is the radius of a bead that moves with velocity v. The viscosity of the solutions used for the force calibrations was measured using a Cannon-Fenske N 956 Size 150 viscometer.

Because the employed forces were relatively weak, we accounted for the gravitational pull on the suspended beads. The magnetic force that pulls the beads upward opposes the drag force and the gravitational force. Two different approaches allowed us to determine the gravitational force: (1) calculate it by accounting for the bead buoyancy using the Archimedes' principle, from the density of the solution (measured with a Mettler Toledo portable density meter – Densito 30PX) and from the density and the volume of the beads; and (2) estimate it from the measured velocities with which the beads settle down. Both approaches provided similar values for a gravitational force of 0.3 ± 0.1 pN that each suspended bead experienced.

The dependence of the magnetic force on the horizontal distance from the magnet core and on the vertical distance from the center of the magnet was tested using a 2-factor ANOVA as implemented by Igor Pro (version 6.22A).(Thomas, Millare et al. 2010) The side field of view of the bead suspension was separated into four vertical and three horizontal sections, and the velocities of beads in any of the 12 quadrants were measured. From the measured velocities, we calculated the magnetic forces exerted on the beads (Table 1-3). The two null hypotheses for the ANOVA test were that the magnetic pulling force did not depend on the horizontal position, x, and on the vertical position, y. The p-values obtained from the 2-factor ANOVA were $p_x = 0.44$, $p_y = 0.030$, and $p_{xy} = 0.95$, not

allowing the rejection of the lack of dependence on *x*, but allowing the rejection of the lack of dependence on *y* (assuming $\alpha = 0.05$). This finding indicated that all beads within the horizontal field of view (in work mode) experienced the same force.

Measuring desorption of beads from glass surfaces. For a typical adhesion experiment, we placed the calibrated electromagnet ~1.5 mm from the surface of the glass (Scheme 1-1a) and applied 12 V to achieve 1.5 pN of magnetic force. Accounting for the opposing gravitational force provided an estimate of 1.2 ± 0.3 pN for net force pulling upward, which each bead experienced when the magnet was turned on.

Using the magnetic puller in a work mode (Scheme 1-1a), we injected a suspension of beads into a PDMS well on the glass slide. By focusing the objective at the surface of the glass, we observed only the beads that settled on the surface, thereby disregarding the beads that had not made contact with the glass.

After allowing the beads to settle on the glass bottom of the well for 3 min, we turned on the electromagnet to exert a relatively weak net force (~1.2 pN) pulling upward, away from the glass surface. Using a CCD camera (at 10 frames per second), we recorded the beads on the surface from 3-5 seconds before the electromagnet was switched on, to 8-10 seconds after. The movies were saved as stacks of images and the number of beads remaining on the surface with respect to time was analyzed using Imaris Bitplane software.

Acknowledgment: The U.S. National Science Foundation provided funding for this research (CBET 0935995 and EEC 0649096). Dr. Kishore Uppireddi from Thin Film Division at Horiba Jobin Yvon, Inc., provided assistance with the ellipsometry modeling and analysis. The electron-microscopy studies were conducted under the supervision of Dr. Krassimir N. Bozhilov at the Central Facility for Advanced Microscopy and Microanalysis at the University of California, Riverside, established with funding from the U.S. National Science Foundation. We also thank Mr. George Ibrahim, Ms. Katie Peterson, Mr. Andrew Vu, and Mr. Jyann-Tyng Lu for the initial design and the assembly of the magnetic-puller setup.

Tables

Table 1-1. Properties of surface coatings of PEG with different molecular weight (MW).

MW_{PEG} / Da	h_{dry} / nm [a]	γ / nm^{-2} [b]	R_F / nm [c]	s / nm [d]	h_{wet} / nm [e]	% beads [f]
1,000	4.00 ± 0.01	2.65 ± 0.01	0.91	0.693 ± 0.004	4.00 ± 0.01	58.7 ± 61.0
2,000	6.07 ± 0.02	2.01 ± 0.01	1.29	0.796 ± 0.004	10.1 ± 0.34	28.4 ± 38.2
3,000	7.05 ± 0.94	1.56 ± 0.21	1.59	0.895 ± 0.093	16.3 ± 0.07	13.7 ± 5.8
5,000	11.7 ± 0.4	1.55 ± 0.05	2.08	0.906 ± 0.022	22.8 ± 0.61	2.72 ± 0.68
10,000	10.2 ± 0.4	0.675 ± 0.026	3.04	1.37 ± 0.02	33.1 ± 0.03	8.1 ± 6.1
20,000	15.4 ± 0.5	0.510 ± 0.017	4.58	1.58 ± 0.01	26.8 ± 0.94	21.5 ± 4.2

[a] Average thickness of PEG coatings blown-dried with a stream of dry N_2 (h_{dry}), obtained from spectroscopic ellipsometry.

[b] Surface packing density in PEG chains per nm^2: $\gamma = 10^{-21} N_A h_{dry} \rho_{PEG} / MW_{PEG}$, where N_A is the Avogadro number, h_{dry} is in nm, $\rho_{PEG} = 1.1$ g ml^{-1}, and MW_{PEG} is in Da.

[c] Flory radius, R_F, was estimated from the unperturbed radius of gyration, R_g: $R_F = \alpha R_g$. $R_g = l (MW_{PEG} / 6 MW_{EG})^{1/2}$, where l is length of the polymer residue ($l = 0.358$ nm, corresponding to the oxygen-oxygen distance in all *anti-staggered* conformer of 1,2-diethoxyethane from gas-phase-optimized MO structures), and MW_{EG} is the molecular weight (44 Da). The intermolecular expansion factor, α, for PEG in water was estimated from reported data on the dependence of α on MW_{PEG} and on the absolute temperature, T: $\alpha \approx -1.3 + 8.8\times10^{-6} MW_{PEG} + 760 / T$.(Özdemir and Güner 2006)

[d] Average separation between the sites covalently holding the PEG chains to the surface: $s = (4 / \pi \gamma)^{1/2}$.(Luzinov, Julthongpiput et al. 2000)

[e] Average thickness of air-dried PEG coatings (h_{wet}) in a class-1,000 cleanroom (45% humidity level), obtained from spectroscopic ellipsometry.

[f] Percent of beads remaining on the glass surface upon applying 1.2 pN pulling force for 5 s. The beads and the surfaces were coated with PEGs with the same MW.

Table 1-2. Percent paramagnetically doped polystyrene microbeads remaining adhered on glass surfaces after applying 1.2-pN net force for 5 s, in the presence of various amount of TWEEN®20.[a]

TWEEN®20 concentration	PEG-coated glass surfaces [b]		Non-coated glass surfaces		Aminated glass surfaces [c]
	PEG-coated beads [b]	Non-coated beads	PEG-coated beads [b]	Non-coated beads	Non-coated beads
0 μM	13.7 ± 5.8	82.3 ± 9.1	72.3 ± 22.1	2.2 ± 0.6	98.7 ± 0.6
10 μM	11.7 ± 2.6	85.2 ± 2.0	82.5 ± 21.6	4.6 ± 2.1	94.6 ± 2.6
100 μM	7.6 ± 2.7	84.7 ± 5.4	89.7 ± 1.6	1.6 ± 0.8	95.2 ± 4.6
250 μM	7.2 ± 1.9	14.9 ± 1.1	71.4 ± 12.5	0.2 ± 0.1	42.7 ± 1.3

[a] The beads (3-μm diameter) were suspended in 100 mM aqueous phosphate buffer pH 7, with the indicated concentrations of surfactant, and allowed to settle on the glass surfaces for ~60 s under gravity (0.3 ± 0.1 pN per bead), prior to applying the magnetic force. For each test the percentage of adhered beads was calculated from ratios between the count of the beads that were in focus at 5 s after applying the pulling force and immediately before applying the force.

[b] Coated with PEG-3000.

[c] Amine-coated via treatment with 4-butylammoniumtriethoxysilane.

Table 1-3. Forces measured at different horizontal distances, x, from the center of the electromagnet and different vertical distances, y, from the tip of the electromagnet (at 12 V).

y / mm	x / mm		
	0.0	0.25	0.50
1.00	1.8 ± 0.4	1.7 ± 0.5	2.0 ± 0.4
1.25	1.4 ± 0.2	1.3 ± 0.3	1.7 ± 0.4
1.50	1.5 ± 0.3	1.2 ± 0.5	1.3 ± 0.5
1.75	1.3 ± 0.1	1.4 ± 0.04	1.4 ± 0.03

Schemes

Scheme 1-1. Magnetic tweezers/puller

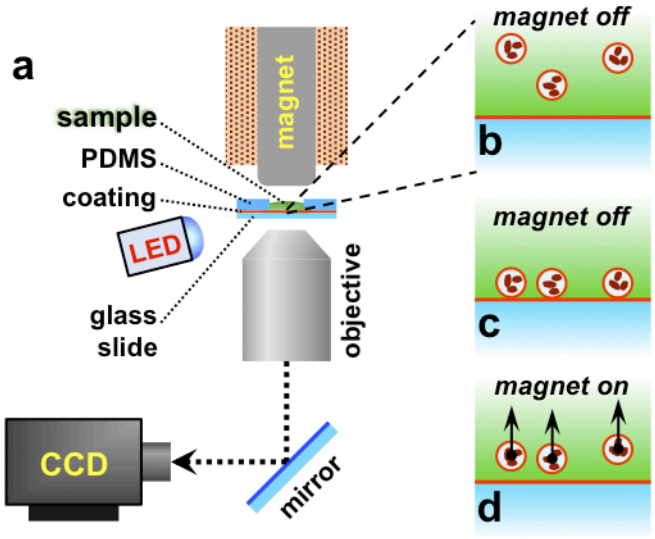

(a) setup: the sample is a suspension of superparamagnetically doped microbeads, dropped on coated glass surfaces in wells of *poly*dimethylsiloxane (PDMS); **(b)** gravity-driven settling of the beads; **(c)** beads settled on the glass surface; and **(d)** beads pulled off the surface.

Scheme 1-2. Magnetic tweezers/puller in a calibration mode.

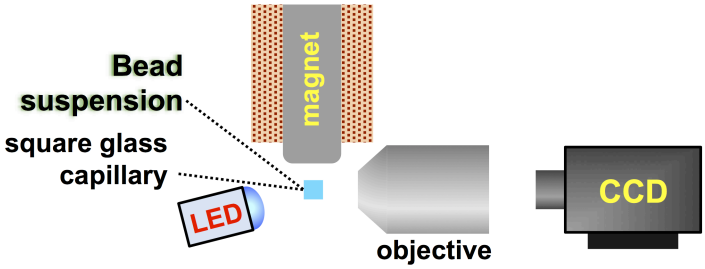

Figures

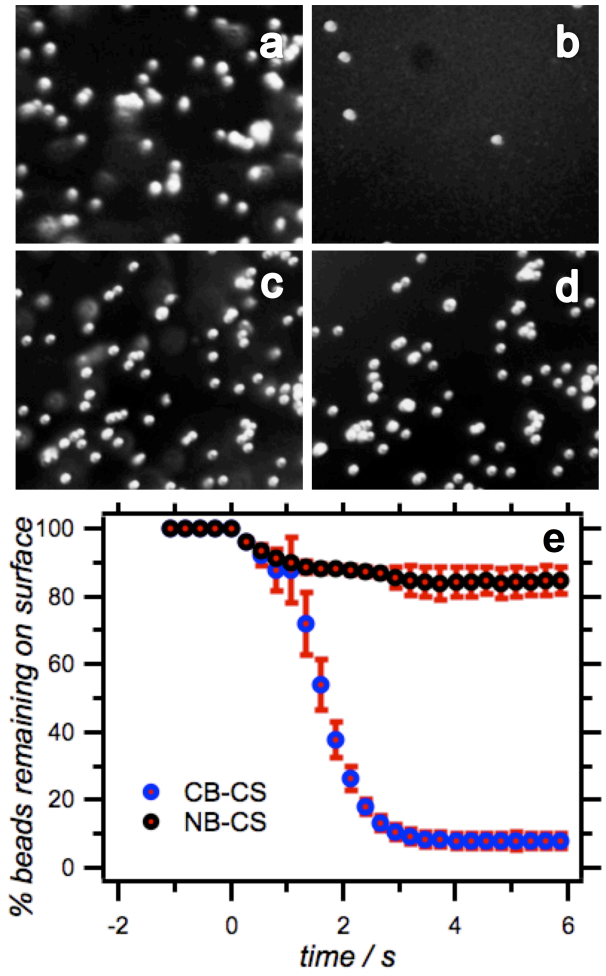

Figure 1-1

Figure 1-1. Removing of superparamagnetically doped polystyrene microbeads (3-μm diameter) from glass surfaces using 1.2-pN net force. From a suspension in an aqueous solution (100 mM phosphate buffer, pH 7), the beads were allowed to settle for ~3 min. **(a - d)** Reflection microscopy images of beads coated with PEG-3000 **(a, b)** on glass slides coated with PEG-3000, and **(c, d)** on non-coated glass slides; **(a, c)** after settling on the surface and before applying force, and **(b, d)** after applying magnetic force for 5 s. **(e)** Time course of desorption of beads from glass surfaces induced by 1.2-pN net force. (**CB-CS** designates coated beads settled on coated surfaces; and **NB-CS** designates non-coated beads settled on coated surfaces,) The beads were tracked while in focus. The depth of field of the used objective was 6 μm, exceeding the bead size. Therefore, the beads were still in focus and tracked for a few seconds after desorption from the glass surface.

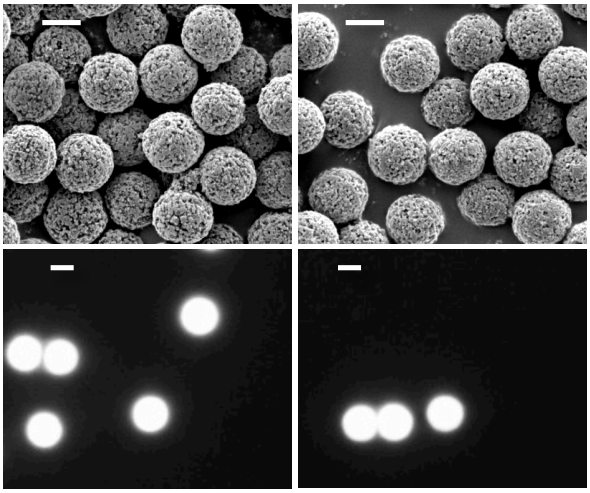

Figure 1-2

Figure 1-2. Images of superparamagnetically doped polystyrene beads (3-μm diameter) used in this study. **(a, b)** Scanning-electron micrographs and **(c, d)** epifluorescence micrographs of beads that were **(a, c)** not coated and **(b, d)** coated with PEG-3000. For the electron microscopy images, the beads were coated with platinum. The autofluorescence of the beads was used for the fluorescence imaging. The scale bars correspond to 2 μm.

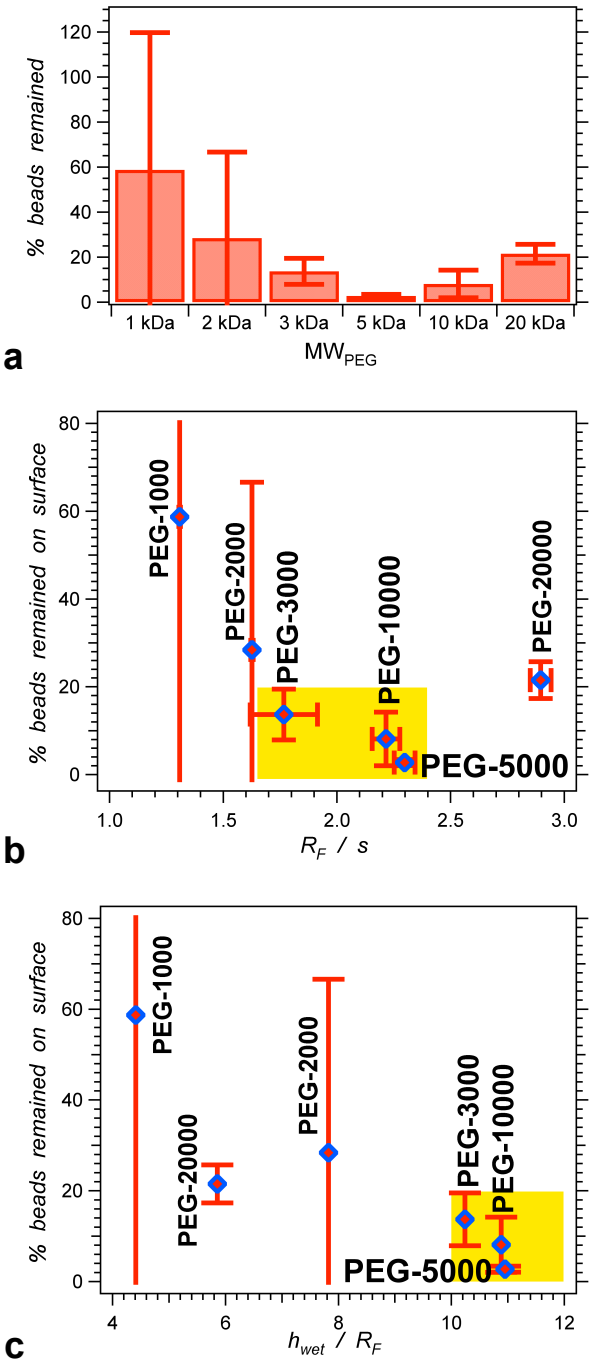
a
% beads remained
120
100
80
60
40
20
0
1 kDa
2 kDa
3 kDa
5 kDa
10 kDa
20 kDa
MW_PEG
b
% beads remained on surface
80
60
40
20
0
PEG-1000
PEG-2000
PEG-3000
PEG-10000
PEG-20000
PEG-5000
1.0
1.5
2.0
2.5
3.0
R_F / s
c
% beads remained on surface
80
60
40
20
0
PEG-1000
PEG-20000
PEG-2000
PEG-3000
PEG-10000
PEG-5000
4
6
8
10
12
h_wet / R_F

Figure 1-3

Figure 1-3. Adhesion between PEGylated superparamagnetically polystyrene microbeads (3-μm diameter) and PEGylated glass surfaces (in an aqueous solution, with 100 mM phosphate buffer, pH 7). Adhesion is expressed as % beads remaining on the surfaces after 1.2 pN pulling force for about 5 s. **(a)** Category plot representing the dependence of the adhesion on the molecular weight of the PEG, MW_{PEG}, used for coating the beads and the surfaces. **(b)** Dependence of the adhesion on the ratio between the PEG Flory radius and the average distances between the grafting sites, R_F / s. **(c)** Dependence of the adhesion on the ratio between the layer thickness and the PEG Flory radius, h_{wet} / R_F.

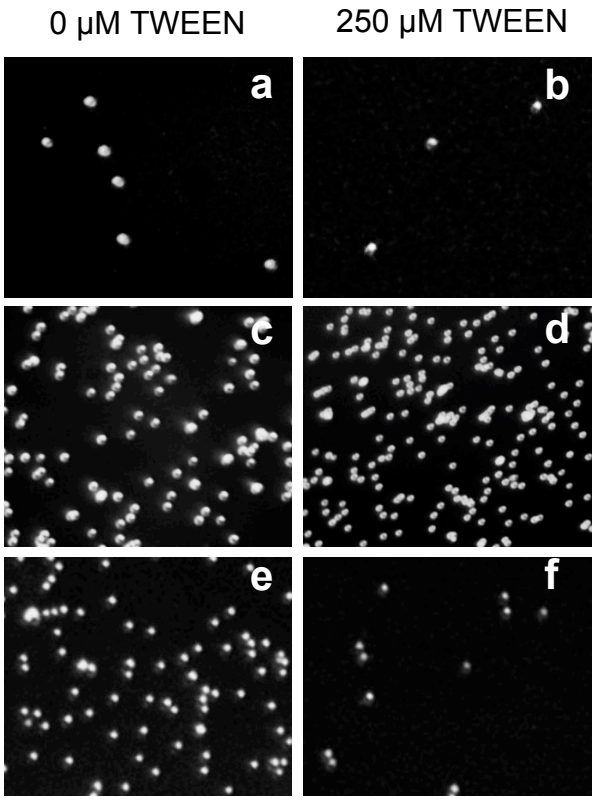

Figure 1-4

Figure 1-4. Reflection microscopy images of beads remaining on flat glass surfaces *after* applying 1.2-pN force for 5 s: **(a, c, e)** in the absence of surfactant; and **(b, d, f)** in the presence of 250 μM TWEEN®20. **(a, b)** PEG-coated beads on PEG-coated surfaces; **(c, d)** PEG-coated beads on non-coated surfaces; and **(e, f)** non-coated beads on PEG-coated surfaces. The coatings were of PEG-3000. The beads were suspended in 100 mM aqueous phosphate buffer, pH 7, in the presence or absence of surfactant as indicated, and allowed to settle for ~3 min prior to applying the pulling magnetic force.

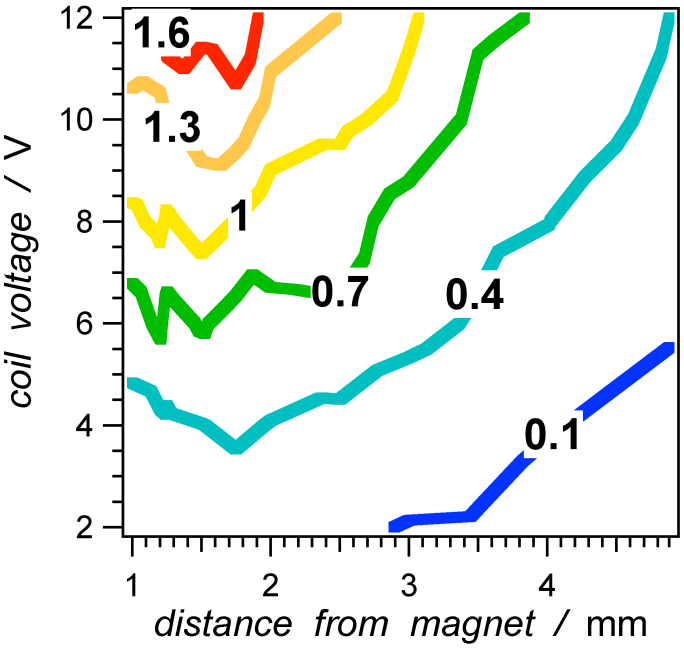
12
10
8
6
4
2
1.6
1.3
1
0.7
0.4
0.1
coil voltage / V
1
2
3
4
distance from magnet / mm

Figure 1-5

Figure 1-5. Dependence of the magnetic force, F_m, on the applied voltage and on the distance from the magnet tip, represented as a counter plot. (F_m is in pN.) The forces were extracted from the velocities of beads moving upward toward the center of the magnet (within a strip ± 0.1 mm from the central line, and maintaining constant velocity within ± 0.1 mm around the designated distance from the magnet). From the velocities, the drag forces, F_d, were calculated (equation 3). The difference between F_m and the gravitational force, F_g, opposes F_d, the magnitude of which, represents the net force, F_N, that each bead experiences: $F_m = -F_d - F_g$; and $F_N = F_m - F_g$. Each data point is an average from the measured velocities of at least three to five beads.

References:

Ainavarapu, S. R. K., A. P. Wiita, et al. (2008). "Single-molecule force spectroscopy measurements of bond elongation during a bimolecular reaction." Journal of the American Chemical Society **130**(20): 6479-6487.

Bahmani, B., S. Gupta, et al. (2011). "Effect of polyethylene glycol coatings on uptake of indocyanine green loaded nanocapsules by human spleen macrophages in vitro." J. Biomed. Opt. **16**(5): 051303/051301-051303/051310.

Bao, D., B. Millare, et al. (2009). "Electrochemical Oxidation of Ferrocene: A Strong Dependence on the Concentration of the Supporting Electrolyte for Nonpolar Solvents." J. Phys. Chem. A **113**(7): 1259-1267.

Bao, D., S. Ramu, et al. (2010). "Electrochemical Reduction of Quinones: Interfacing Experiment and Theory for Defining Effective Radii of Redox Moieties." J. Phys. Chem. B **114**(45): 14467-14479.

Bard, A. J. and L. R. Faulkner (2001). Electrochemical Methods: Fundamentals and Applications.

Bergstrom, K., K. Holmberg, et al. (1992). "Reduction of fibrinogen adsorption on PEG-coated polystyrene surfaces." Journal of biomedical materials research **26**(6): 779-790.

Bijamov, A., F. Shubitidze, et al. (2010). "Quantitative modeling of forces in electromagnetic tweezers." J. Appl. Phys. **108**(10): 104701/104701-104701/104709.

Chapman, R. G., E. Ostuni, et al. (2000). "Surveying for Surfaces that Resist the Adsorption of Proteins." J. Am. Chem. Soc. **122**(34): 8303-8304.

Chau, K., B. Millare, et al. (2011). "Dependence of the quality of adhesion between poly(dimethylsiloxane) and glass surfaces on the composition of the oxidizing plasma." Microfluid. Nanofluid. **10**(4): 907-917.

Chen, C. S., M. Mrksich, et al. (1997). "Geometric control of cell life and death." Science **276**(5317): 1425-1428.

Chen, S. F., J. Zheng, et al. (2005). "Strong resistance of phosphorylcholine self-assembled monolayers to protein adsorption: Insights into nonfouling properties of zwitterionic materials." Journal of the American Chemical Society **127**(41): 14473-14478.

Danilowicz, C., D. Greenfield, et al. (2005). "Dissociation of ligand-receptor complexes using magnetic tweezers." Analytical Chemistry **77**(10): 3023-3028.

Deng, L., M. Mrksich, et al. (1996). "Self-Assembled Monolayers of Alkanethiolates Presenting Tris(propylene sulfoxide) Groups Resist the Adsorption of Protein." J. Am. Chem. Soc. **118**(21): 5136-5137.

Drobek, T., N. D. Spencer, et al. (2005). "Compressing PEG brushes." Macromolecules **38**(12): 5254-5259.

Feldman, K., G. Hähner, et al. (1999). "Probing resistance to protein adsorption of oligo(ethylene glycol)-terminated self-assembled monolayers by scanning force microscopy." J. Am. Chem. Soc. **121**(43): 10134-10141.

Harder, P., M. Grunze, et al. (1998). "Molecular Conformation in Oligo(ethylene glycol)-Terminated Self-Assembled Monolayers on Gold and Silver Surfaces Determines Their Ability To Resist Protein Adsorption." J. Phys. Chem. B **102**(2): 426-436.

Harris, J. M. (1992). Poly(ethylene glycol) chemistry: biotechnical and biomedical applications, Plenum Press.

Heuberger, M., T. Drobek, et al. (2005). "Interaction forces and morphology of a protein-resistant poly(ethylene glycol) layer." Biophysical Journal **88**(1): 495-504.

Hickman, J. J., B. Sweryda-Krawiec, et al. (2004). "A new interpretation of serum albumin surface passivation." Langmuir **20**(6): 2054-2056.

Hong, C., D. Bao, et al. (2008). "Print-and-Peel Fabrication of Microelectrodes." Langmuir **24**(16): 8439-8442.

Hu, J., B. Xia, et al. (2009). "Long-Lived Photogenerated States of alpha - Oligothiophene-Acridinium Dyads Have Triplet Character." J. Phys. Chem. A **113**(13): 3096-3107.

Hu, K., Y. Gao, et al. (2009). "Fluorinated silicon surfaces under mixed surfactants: resistance to nonspecific protein adsorption for biosensing." Langmuir **25**(21): 12404-12407.

Israelachvili, J. (1997). "The different faces of poly(ethylene glycol)." Proceedings of the National Academy of Sciences of the United States of America **94**(16): 8378-8379.

Israelachvili, J. (2005). "Differences between non-specific and bio-specific, and between equilibrium and non-equilibrium, interactions in biological systems." Quarterly Reviews of Biophysics **38**(4): 331-337.

Israelachvili, J. N. (1992). Intermolecular and Surface Forces, Academic Press.

Israelachvili, J. N. and B. W. Ninham (1977). "Intermolecular forces - the long and short of it." Journal of Colloid and Interface Science **58**(1): 14-25.

Israelachvili, J. N. and H. Wennerstroem (1992). "Entropic forces between amphiphilic surfaces in liquids." Journal of Physical Chemistry **96**(2): 520-531.

Janshoff, A., M. Neitzert, et al. (2000). "Force Spectroscopy of Molecular Systems-Single Molecule Spectroscopy of Polymers and Biomolecules." Angewandte Chemie **39**(18): 3212-3237.

Jones, G., II, D. Yan, et al. (2007). "Photoinduced Electron Transfer in Arylacridinium Conjugates in a Solid Glass Matrix." J. Phys. Chem. B **111**(24): 6921-6929.

Joo, C., H. Balci, et al. (2008). "Advances in single-molecule fluorescence methods for molecular biology." Annual review of biochemistry **77**: 51-76.

Kapanidis, A. N. and T. Strick (2009). "Biology, one molecule at a time." Trends in Biochemical Sciences **34**(5): 234-243.

Kenworthy, A. K., K. Hristova, et al. (1995). "Range and Magnitude of the Steric Pressure between Bilayers Containing Phospholipids with Covalently Attached Poly(Ethylene Glycol)." Biophysical Journal **68**(5): 1921-1936.

Leckband, D. and J. Israelachvili (2001). "Intermolecular forces in biology." Quarterly Reviews of Biophysics **34**(2): 105-267.

Luzinov, I., D. Julthongpiput, et al. (2000). "Polystyrene layers grafted to epoxy-modified silicon surfaces." Macromolecules **33**(3): 1043-1048.

Majewski, J., T. L. Kuhl, et al. (1998). "X-ray Synchrotron Study of Packing and Protrusions of Polymer-Lipid Monolayers at the Air-Water Interface." Journal of the American Chemical Society **120**(7): 1469-1473.

McPherson Timothy, B., J. Lee Samuel, et al. (1995). Analysis of the Prevention of Protein Adsorption by Steric Repulsion Theory. Proteins at Interfaces II, American Chemical Society. **602:** 395-404.

Millare, B., M. Thomas, et al. (2008). "Dependence of the quality of adhesion between polydimethyl siloxane and glass surfaces on the conditions of treatment with oxygen plasma." Langmuir **24**(22): 13218-13224.

Mrksich, M. and G. M. Whitesides (1996). "Using self-assembled monolayers to understand the interactions of man-made surfaces with proteins and cells." Annual Review of Biophysics and Biomolecular Structure **25**: 55-78.

Neuman, K. C. and A. Nagy (2008). "Single-molecule force spectroscopy: optical tweezers, magnetic tweezers and atomic force microscopy." Nature Methods **5**(6): 491-505.

Niedzwiecki, D. J., J. Grazul, et al. (2010). "Single-Molecule Observation of Protein Adsorption onto an Inorganic Surface." J. Am. Chem. Soc. **132**(31): 10816-10822.

Otzen, D. (2011). "Protein-surfactant interactions: A tale of many states." Biochim. Biophys. Acta, Proteins Proteomics **1814**(5): 562-591.

Özdemir, C. and A. Güner (2006). "Solution thermodynamics of poly(ethylene glycol)/water systems." Journal of Applied Polymer Science **101**(1): 203-216.

Prime, K. and G. Whitesides (1991). "Self-assembled organic monolayers: model systems for studying adsorption of proteins at surfaces." Science **252**(5009): 1164-1167.

Pum, D., C. Horejs, et al. (2011). "Single-molecule Force Spectroscopy Reveals the Individual Mechanical Unfolding Pathways of a Surface Layer Protein." Journal of Biological Chemistry **286**(31): 27416-27424.

Schoenfisch, M. H., K. L. Brogan, et al. (2004). "Influence of surfactants and antibody immobilization strategy on reducing nonspecific protein interactions for molecular recognition force microscopy." Langmuir **20**(22): 9729-9735.

Schubert, M. (2006). "Another century of ellipsometry." Ann. Phys. **15**(7-8): 480-497.

Shang, H. and G. U. Lee (2007). "Magnetic tweezers measurement of the bond lifetime-force behavior of the IgG-protein A specific molecular interaction." Journal of the American Chemical Society **129**(20): 6640-6646.

Thomas, M. S., J. M. Clift, et al. (2010). "Print-and-Peel Fabricated Passive Micromixers." Langmuir **26**(4): 2951-2957.

Thomas, M. S., B. Millare, et al. (2010). "Print-and-peel fabrication for microfluidics: what's in it for biomedical applications?" Ann Biomed Eng **38**(1): 21-32.

Upadhyayula, S., D. Bao, et al. (2011). "Permanent Electric Dipole Moments of Carboxyamides in Condensed Media: What Are the Limitations of Theory and Experiment?" J. Phys. Chem. B **115**(30): 9473-9490.

Vasquez, J. M., A. Vu, et al. (2009). "Fluorescence enhancement of warfarin induced by interaction with beta -cyclodextrin." Biotechnol. Prog. **25**(4): 906-914.

Vullev, V. I. (2005). "Modulation of dissociation kinetics by external force: examination of the Bell model." J. Biol. Sci. **5**(6): 744-758.

Vullev, V. I. and G. Jones (2002). "Photoinduced electron transfer in alkanoylpyrene aggregates in conjugated polypeptides." Tetrahedron Lett. **43**(47): 8611-8615.

Vullev, V. I., J. Wan, et al. (2006). "Nonlithographic Fabrication of Microfluidic Devices." J. Am. Chem. Soc. **128**(50): 16062-16072.

Wahlgren, M., S. Welin-Klintström, et al. (1995). "Competition between fibrinogen and a non-ionic surfactant in adsorption to a wettability gradient surface." Colloids and Surfaces B: Biointerfaces **4**(1): 23-31.

Wan, J., M. S. Thomas, et al. (2009). "Surface-bound proteins with preserved functionality." Ann. Biomed. Eng. **37**(6): 1190-1205.

Xia, B., S. Upadhyayula, et al. (2011). "Amyloid histology stain for rapid bacterial endospore imaging." J. Clin. Microbiol. **49**(8): 2966-2975.

Yu, H. U., Z. H. Yang, et al. (1999). "Protein interactions with poly(ethylene glycol) self-assembled monolayers on glass substrates: Diffusion and adsorption." Langmuir **15**(24): 8405-8411.

Zhang, W., W. T. Ang, et al. (2011). "Minimizing nonspecific protein adsorption in liquid crystal immunoassays by using surfactants." ACS applied materials & interfaces **3**(9): 3496-3500.

Chapter 2

The Design of Magnetic Pullers for Proteomic Applications

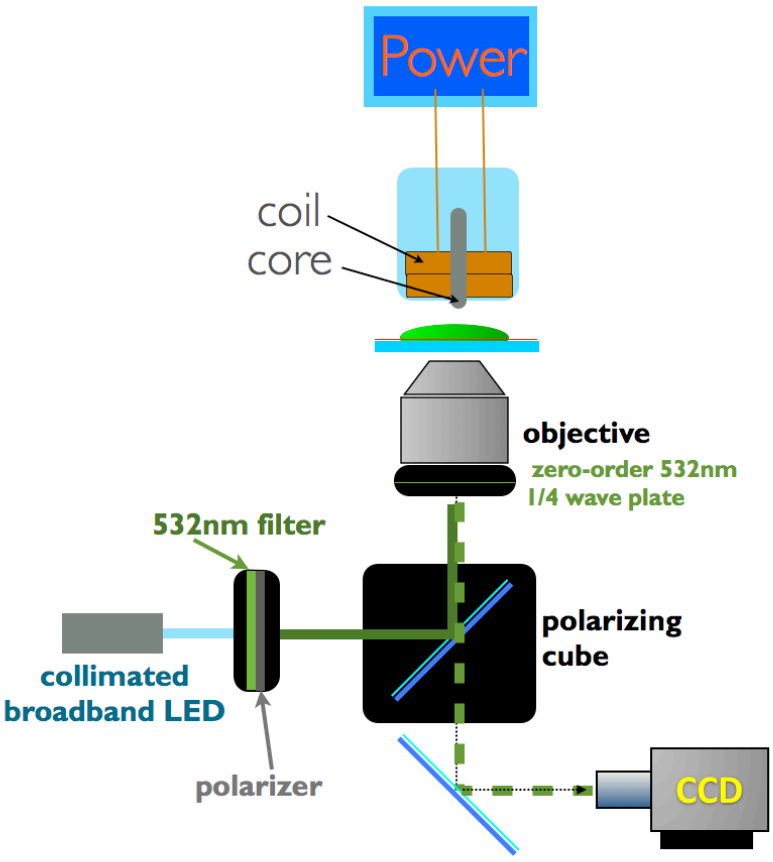

Abstract

This article describes the design and implementation of a thermally-regulated electromagnetic pullers setup capable of attaining forces between hundreds of fN and approximately 100 pN. Such range of dynamic force is essential for single-molecule proteomic studies, as the use of magnetic pullers allows us to probe thousands of single-molecule events simultaneously, making them preferential to traditional magnetic tweezers. The magnetic pullers setup utilizes an inverted microscope with a single electromagnet above the sample stage. The electromagnet's coil dimensions and the core setup were optimized to prevent generation of excess heat while retaining the ability to maintain large magnetic field gradients and forces at millimeter distances. The undesired heat generation was suppressed via convection cooling, i.e., by immersing the electromagnetic coil in silicone oil and a dry ice mixture. The simultaneous use of ceramic heaters and a temperature process controller allowed for regulating the temperature at the tip of the core with a ± 2˚C accuracy, which is essential for maintaining the integrity of biological samples. Microbeads densely packed with magnetite (specifically, ProMag beads from Bangs Laboratory and DynaBeads® from Invitrogen) were used to complement the optimized parameters of the magnetic pullers in order to generate higher and consistent forces.

Introduction

Recent technological advances have permitted the observation of single-molecule events with sufficient signal-to-noise ratios (Bustamante, Chemla et al. 2004; Deniz, Mukhopadhyay et al. 2008; Neuman and Nagy 2008). Despite their relatively low sensitivity, single-molecule measurements provide key information that is lost in traditional bulk (or ensemble-average) studies due to property averaging over an immense number of molecular species. Unlike ensemble-average studies that indirectly provide information about conformational and dynamic properties of biochemical systems, single-molecule experiments enable direct observations of: (1) the stochastic nature of molecular events (inherent from the fundamental quantum mechanics principles); (2) the formation of intermediates; and (3) rare events (Bustamante, Chemla et al. 2004; Nahas, Wilson et al. 2004; Walter, Huang et al. 2008; Kapanidis and Strick 2009).

Force measurements bring additional key and unique features to the single-molecule studies that are still largely unexplored: (1) they are the only experimental technique that directly tests the structural directionality of molecular interactions; and (2) they allow for the selective application of mechanical stress to macromolecules. In cellular environments, many proteins and macromolecular assemblies exist and function under stress (e.g. microtubules and intermediate filaments) (Wang, Butler et al. 1993). Therefore, *in vitro* biochemical assays, where the macromolecules are conformationally relaxed, may not always represent the true natural state of the investigated systems.

The application of external forces to dissociating complexes changes the energy landscape of the studied system and, hence, alters the kinetics of dissociation (Figure 2-1) (Bongrand 1999; Evans 2001; Guthold, Superfine et al. 2001). Only dissociation processes that are oriented in the direction of the applied external force experience this perturbation effect on their kinetics. Therefore, we postulate that this phenomenon provides a means for examining the dissociation processes of protein systems. Despite its immense potential for use in both biochemistry and chemistry, the capability of using force techniques for the investigation of protein-protein interactions at a single-molecule level still remains largely unexplored.

About 30 years ago, Bell introduced a simple linear model that quantified the force-induced perturbation of dissociation kinetics (Bell 1978):

$$E_a(F) = E_a^{(0)} - F\gamma \tag{1}$$

where $E_a(F)$ and $E_a^{(0)}$ are the activation energies of dissociation in the presence and absence of force, F, respectively. The distance between the equilibrium minimum and the transition state of the complex (Figure 2-1b) is represented by an empirical parameter γ. Therefore, the rate constant of dissociation can be readily represented as:

$$k_d(F) = \nu_d \exp\left(-\frac{E_a^{(0)} - \gamma F}{k_B T}\right) = k_d^{(0)} \exp\left(\frac{\gamma F}{k_B T}\right) \tag{2}$$

where the pre-exponential factor, ν_d, represents the frequency at which the transition state is reached before dissociation, $k_d^{(0)}$ is the dissociation rate constant in the absence of an external force, k_B is the Boltzmann constant, and T is the absolute temperature in Kelvin.

The Bell model (eq. 1 and 2) has proved an immense advancement in the field and has been widely employed for the interpretation of force-modulated phenomena. Despite these contributions and despite its attractive simplicity, however, we believe that the Bell model is flawed. The model assumes that the value of γ does not depend on applied external force, which is an assumption that we believe to be incorrect. We thus conclude that the Bell model can only be accurately used for force measurements: (1) at relatively weak forces where $\gamma(F)$ can be approximated to its value in the absence of force, $\gamma(0)$; (2) at a relatively narrow force dynamic range within which changes in $\gamma(F)$ are negligible and the linearity of eq. 1 and 2 is acceptable; and (3) of two-state processes where only one transition state is available. Only force techniques coupled with the use of non-linear models (when the dissociation occurs through intermediates and is not a two-state process) directly provide the mechanistic information necessary to constructing potential-energy profiles of dissociation processes (Evans 1999; Guthold, Superfine et al. 2001; Vullev 2005).

Employing surface-engineering methodologies developed in our laboratory (Upadhyayula, Quinata et al. 2012), we aim to demonstrate the utility of using magnetic pullers for single-molecule proteomics research. In comparison with other widely used force techniques, such as atomic force microscopy and optical tweezers (Kapanidis and Strick 2009), magnetic pullers offer the following key advantages: (1) they allow for

recording hundreds of single-molecule events during a single measurement; (2) they eliminate the possibility of sample property perturbation during measurement, as magnetic forces are orthogonal to most biological interactions; and (3) they eliminate the need for considering loading rates (*dF/dt*) due to their ability to conduct measurements at constant force

We differentiate in this study between magnetic pullers and magnetic tweezers. Traditional magnetic tweezers are widely used for the investigation of molecular systems with lengths larger than the diffraction limit of optical microscopy, such as DNA and RNA (Haber and Wirtz 2000; Assi, Jenks et al. 2002; Gosse and Croquette 2002). Numerous reports for different force magnitudes (Chiou, Huang et al. 2006; Neuman and Nagy 2008; Walter, Huang et al. 2008; Kapanidis and Strick 2009) focus on relatively narrow ranges (0.01 pN to tens of pN or less) while using complex multi-magnet setups at sub-millimeter distances to study one single-molecule interaction at a time.

Although the term "magnetic tweezers" has become widely used due to its utility in contrasting the system with "optical tweezers," the phrase is not truly descriptive. The applied magnetic fields do not generate traps where they "tweeze" objects—in fact, the trap of the magnetic field lies within the magnet itself. Rather, the method utilizes magnetic field gradients that apply forces on an object (with magnetic susceptibility) by pulling them toward the magnet. Moreover, the traditional experimental design using magnetic tweezers with multiple magnets employs trapping a single bead, thereby facilitating the study of one single-molecule interaction at a time. However, by

employing "magnetic pullers," we propose to study thousands of single-molecule events in parallel.

Herein, we describe the parameters and components of a robust electromagnetic pullers setup with a dynamic force range from about 0.1 to 100 pN. We expect to readily broaden the upper limit of the dynamic range to about 1 nN by using densely packed superparamagnetic beads, which will allow us to explore a broad range of molecular interactions. Such a setup will have the attractive features of the other single-molecule force techniques alongside all the advantages that magnetic pullers have to offer.

Results & Discussion

Coil design. Electromagnetic coil, or solenoid, is one of the two major components comprising the electromagnet. Forces generated by an electromagnet are proportional to the magnetic field gradient:

$$F = m\nabla|B| \tag{3}$$

where F is the force, m is the magnetic moment or magnetic dipole moment, and ∇B is the magnetic field gradient. Thus it is important to design a coil capable of generating large magnetic fields and, subsequently, large gradients. The coil, powered with tightly controlled direct current, generates magnetic fields along the axis of the loop as described by the Biot-Savart Law:

$$B_z = \frac{\mu_0}{2} \frac{r^2 I}{\left(z^2 + r^2\right)^{\frac{3}{2}}} \tag{4}$$

where B is the magnetic field, μ_0 is the magnetic constant, r is the radius of a single coil loop, and z is the height, i.e., the distance from the center of the loop's axis to the top or the bottom. In this expression, B_z represents the magnetic field that is generated along the solenoid's central axis, z, of the solenoid. Summing the B_z from equation 4 for all loops allows for an estimation of the change in magnitude of the magnetic field (i.e., the field gradient) along z. The magnitude and the gradient of the field, therefore, strongly depend on: (1) the wire thickness, which governs resistance, and hence the current and the amount of produced heat; (2) the height of the coil; and (3) the diameter or the radius, r. In an effort to identify the diameter and the height of coil that would produce the largest field gradient while minimizing the amount of heat generated, we employed Wavemetrics Igor Pro V.6 analysis software to generate three simulations optimizing each of the three parameters listed above (Figure 2-1). Since power, or the generated heat, is proportional to the resistance and the square of the current in the coils, it is critical to determine the optimal coil configuration for generating the largest magnetic fields for a given length and thickness of wire.

From the three simulations (Figure 2-1), we determined that an increase in two of the examined parameters led to an asymptotic approach of a constant maximum value for B_z, i.e., an increase above a certain value did not significantly affect the generated magnetic fields at the tip of the magnet. First, the wire thickness of approximately 0.6

mm showed the best generated field; increasing the wire thickness to 0.8 mm did not significantly increase the field strength (Figure 2-1a). It is important to optimize the wire thickness to reduce the amount of generated heat. i.e., thicker wire yields lower resistance than thinner wire, but takes up more space and thus reduces the number of loops wound around the axis for a given coil volume. Second, the height of the coil presented a similar limitation, where increasing the height beyond 30 mm did not significantly increase the magnetic field generated at the tip of the magnet (Figure 2-1b). Therefore, in order to prevent the generation of excessive heat, we limited the height of the coils to between 15-30 mm. Third, the diameter of the coil did not present a limitation in the generated magnetic field, i.e., as we increased the diameter of the coil, the magnetic field increased proportionally (Figure 2-1c). Based on these findings, we prepared our coils using copper wire with a thickness of 0.5 mm, a height of 20 mm, and a diameter of 50 mm for all subsequent core optimization tests.

Core design. In order to generate the largest magnetic fields and field gradients, we needed to identify the core assembly with optimal configurations for achieving this state; to this end, we investigated several core assemblies ranging from a single core with different tip configurations to double and triple cores (Scheme 2-2, 2-3, 2-4).

For the single core setup, we investigated four tip configurations, where the 2 mm flat-tip with rounded edges generated the largest fields and the most stable gradient (Scheme 2-2, Figure 2-2a). The other configurations proved markedly less suitable for our study. The 4 mm flat-tip with rounded edges generated magnetic fields lower than the 2 mm flat-tip, and the unrounded flat-tip generated the smallest magnetic field and

gradient. The sharp V shaped tip generated a relatively large field and gradient; however, it produced the smallest working area wherein the applied forces are homogenous and is therefore disadvantageous for applying homogenous forces on thousands of superparamagnetic beads in a given area or field of view.

For the double core electromagnet setup, we employed three different variations (Scheme 2-3): (1) the "Double Flat" variation holds two cores flat on the same plane, where 10 mm of the edges on the sides of each core are tapered to maintain a 110˚ angle between them; (2) the "Double V Shaped Orientation Flat" variation holds the two cores at a 65˚ angle; and (3) the "Double V Shaped Orientation Arrow" variation is comprised of two cores with sharp V shaped tips tapered to look like an arrow, where the two cores are held together at a 65˚ angle. The "Double Flat" cores were held in place in two configurations (North dipole facing North dipole and North dipole facing South dipole), both of which produced the weakest magnetic fields. The "Double V Shaped Orientation Flat" proved the most suitable of the double core electromagnet setups for our study, as it produced the largest magnetic field and gradient among all two-core configurations (Figure 2-2b).

The triple core setup consisted of three cores arranged in a 'V' shape, inclined at approximately 50˚, and separated from each other by a 120˚ angle (Scheme 2-4). For this setup, we used three configurations: one configuration with all North dipoles facing each other and two configurations with one South dipole facing two North dipoles. As was anticipated, the two configurations with one South dipole facing two North dipoles exhibited similar magnetic fields and gradients, both of which were lower than the fields

and gradients exhibited by the configuration wherein all North dipoles faced each other (Figure 2-2c).

Among all the tested configurations under identical power conditions, i.e., between single, double and triple cores with alternating dipoles, a single core with a 2 mm flat-tip with rounded edges produced the largest magnetic field and magnetic gradients (Figure 2-2d). For this reason, we employed the single core, 2 mm flat-tip with rounded edges for all subsequent magnetic field and force calibrations.

Magnetic field and force calibrations. We calibrated the electromagnet, composed of a coil (5 cm diameter and 2 cm height) and a single core (2 mm flat-tip with rounded edges), at 1.8 A of current using a guassmeter to profile the magnetic fields at varying *x*- and *y*- coordinates (Figure 2-3a); subsequently, we derived the magnetic field gradients (Figure 2-3b). As expected, a 2 mm flat-tip with rounded edges produced smooth concave magnetic fields and generated a constant magnetic field gradient. Due to the rounded tip, fringe effects at distances of less than 1 mm were not observed. The symmetric nature of the fields (Figure 2-3a) and of the gradients (Figure 2-3b) reflects both the symmetry of the tip of the core and the precision with which we can measure these fields. From the gradient profile, it is apparent that in a given field of view, the magnetic particles will experience symmetric horizontal forces that cause them to move in only a vertical direction; these magnetic beads exhibit an exponential dependence on force relative to their vertical distance from the tip of the core, as documented in Figure 2-3b. Furthermore, we performed *y*- coordinate field profiling of the electromagnet at

varying levels of current passing through the coil (Figure 2-4), which showed a decrease in both the field and the gradient strength with decreasing levels of current. We were thus able to modulate the magnetic forces exerted on superparamagnetic beads with precision by changing only the current and by using a stationary electromagnet (i.e., by using an assembly with no moving parts).

Once we employed the temperature regulation system, we repeated our force calibrations, dividing the field of view into four-by-four quadrants in order to determine if the force is dependent on the location of the bead along the *x*- or along the *y*- axis (data that we confirmed using ANOVA). The forces generated from the electromagnet reached upwards of ~70pN at a distance of 4 mm from the tip and exponentially decreased as distance increased (Figure 2-5). In contrast, five square 1 cm x 1 cm neodymium permanent magnets generated lower forces at these distances, and, moreover, did not decay at the same rate.

Temperature regulation system. The need to maintain the temperature of an electromagnetic coil proves the biggest limitation of the magnetic pullers setup. Controlling the temperature at the tip of the core is essential, since temperature has the ability to greatly affect biological samples. When the electromagnet is run at 1.8 A or greater without a cooling system, an immense amount of heat is generated; the core temperature increases by 80˚C within five minutes (Figure 2-6a) and is capable of reaching over 200˚C within ten minutes. This increase in temperature is amplified exponentially as current levels increase—the magnetic fields and generated gradients are thereby diminished (Figure 2-7), resulting in fluctuating forces. Oscillations in

temperature during the course of our experiments (which lasted between 5 and 10 minutes) were significant enough to cause changes in the exerted forces. These changes in the exerted forces, resulting from the propagation of heat-transfer between the tip of the core and the capillary, also caused changes in the solution's viscosity, and were observed during force calibration analysis.

We employed a constant-cooling strategy by submerging the electromagnet in a PTFE beaker containing silicone oil and a dry ice mixture. PTFE material is inert (and thus does not interfere with the magnetic fields), is non-toxic, and has a relatively high melting point of 327˚C; silicone oil is non-conductive (and thus does not short the electrical components), nonflammable, and non-toxic, and has a working temperature range of -73˚C to 260˚C (Gelest, Inc.). We added the dry ice in order to facilitate mixing via its sublimation process. By regulating the temperature of the tip using this cooling approach, we were able to prevent the electromagnet from over-heating. We were initially unsuccessful, however, at preventing the tip from over-cooling (Figure 2-6b). We adjusted for this result by employing a stepwise heating of the tip as it cooled in the silicone oil and dry ice mixture; we chose this approach because, from a design standpoint, it is easier to over-cool the electromagnet and apply short bursts of heat in order to regulate the temperature at the tip than it is to cool the electromagnet in a controlled manner. Our use of this technique allowed us to regulate and maintain the temperature of the probe within a 2-3˚C range and to maintain a constant current, thus attaining reliable fields and gradients.

Superparamagnetic beads. In addition to optimizing the electromagnet components (critical for generating large forces homogenously over relatively large areas), it is essential to choose the correct type of microparticle for single-molecule experiments on a massively parallel scale. In this section, we will briefly discuss the five different types of microparticles we employed with the magnetic pullers.

Silicon magnetic particles are just that—particles (from Chemicell, Inc., Figure 2-8a,b); these are generally available in sub-micrometer sizes, i.e., hundreds of nanometers. While the sizes of the particles and their loading of the magnetite are generally homogenous, the shape of each particle varies drastically, which proves disadvantageous to single-molecule studies. Moreover, the particles are not spherical, and hence forces exerted on them cannot be calculated using the Stokes-Einstein equation. Thus, while the use of these particles may be advantageous to trap or separate cells in a magnetic microfluidic setup, they present severe disadvantages in single-molecule studies.

Using polystyrene beads with magnetite coating on the outside (from Spherotech, Inc., Figure 2-8c,d) produces microbeads with varying loading levels, thus causing fluctuations in the forces exerted between these microbeads. As shown in the scanning electron microscope image (Figure 2-8b,c), we see an array of non-homogeneous microbeads with varying levels of magnetite covering their surface—i.e., bald beads to beads with relatively large amounts of magnetite. Furthermore, functionalizing proteins on surfaces with magnetite adjacent to the functional groups can be detrimental to the protein function, resulting in the study of inactive proteins or protein in an unnatural state. Using these beads for single-molecule proteomics measurements is not

recommended since (1) precise forces exerted on the microbeads are unknown; and (2) coatings of magnetite may interfere with the native function of proteins.

The use of polymer non-fluorescent (Figure 2-8e,f) or fluorescent beads (Figure 2-8g,h) from Bangs Laboratories, Inc. facilitated point specific chemistry for immobilizing components essential to single-molecule studies (such as poly-ethylene glycol, and subsequent proteins or ligands), in addition to exerting precise forces on the microbeads. Visualization of these non-fluorescent beads is difficult even with a reflectance interference contrast microscope (RICM) setup, since there is no significant difference between the refractive index of the media the microbeads are suspended in and the surface of these microbeads—therefore we also investigated fluorescent microbeads (Figure 2-8g,h) where the dye is confined inside the polymer coating of the magnetite. We employed a fluorescence microscope setup with an FITC filter set to visualize the fluorescence of the dye in the beads. Our ability to visualize and track the beads was impaired after roughly 60 minutes of collimated LED excitation (Figure 2-9).

The polystyrene beads (DynaBeads®) from Invitrogen, Inc. produced the most consistent forces of all the microbeads tested (Figure 2-8i,j). Moreover, the combination of the beads' smooth outer surfaces and their composition presented with a sufficient change of refractive index (between the bead surface and the surrounding solution), enabling us to readily visualize these beads with the RICM setup. While the densities of all the microbeads vary by batch within the same company (Bangs Laboratory), DynaBeads®, have the highest density (capable of comparatively large forces) in the ~3

μm size range and are the only commercially available beads to present the clean, smooth surface essential for point specific surface chemistry.

Conclusions

We designed a magnetic pullers setup capable of exerting upwards of 100 pN forces at 3 mm away from the electromagnet. Theoretical considerations demonstrated that the diameter, rather than the height of the coil, is the most essential parameter for optimizing and maximizing the magnetic gradient that is generated. The optimization of coil dimensions further contributed to the overall setup by preventing unnecessary heat generation. Moreover, of the tested core configurations, we found that the largest magnetic field gradients were generated from a single 2 mm flat-tip core, rather than from double or triple cores. The temperature regulation setup readily cooled the electromagnet coil, while maintaining the temperature at the tip within 2˚C of the preset temperature for the experiment.

Experimental

Magnetic pullers setup. The magnetic pullers setup is comprised of an inverted microscope with an electromagnet (or permanent magnet) apparatus on top. A custom machine-fabricated setup consisting of a magnet stage and a sample holder was built around a hollow Zeiss Axiovert S100 TV frame. The microscope frame was used to hold

optics such as objectives and mirrors to project the image into a Spot Insight QE Model 4.2 charge-coupled camera (Diagnostic Instruments). Since bright field microscopy is not a reliable method for visualizing beads with the electromagnetic setup on top, fluorescence microscopy, or reflectance interference contrast microscopy (RICM), was employed. Fluorescent superparamagnetic beads (from Bangs Laboratory, COMPEL™ Magnetic COOH modified, 3 μm) were used with an FITC filter set for fluorescence visualization. Subsequently, RICM was employed for non-fluorescent beads, with a collimated white LED light source passing through a 532 bandpass filter, a polarizer, a polarizing beamsplitter, and a 532nm zero-order quarter waveplate before hitting and reflecting back from the beads.

Thermally regulated electromagnetic setup. The electromagnet is comprised of a coil (5 cm diameter and 2 cm height) and a single 2 mm flat-tip rounded edge core. The single core is custom-machined to be a two part setup consisting of: (1) a steel core with tapped threads, and (2) a 2 mm flat rounded tip that is lathed from the same metal rod to form a screw. These two parts screw-fit each other, forming a complete core-tip configuration. To fit the electromagnet into the polytetrafluoroethylene (PTFE) beaker (purchased from Dynalon Labware with dimensions of 8 cm diameter and 10.6 cm height), the beaker's base was lathed down to ~2 mm thickness and drilled at the center to allow for the screw component of the tip to slip in from the outside and access the hollow core with tapped threads inside the beaker. The tip is screwed to the core, thereby holding the PTFE beaker

firmly between the two parts. The coil is placed in the beaker around the core, and is completely submerged in silicone oil.

The temperature at the tip of the core was monitored using Vernier's LabQuest temperature probe. The beaker-and-electromagnet setup was placed on an aluminum stage with a hole drilled at the center to allow access to the protruding tip. Two ceramic insulated strip heaters, connected to a solid state relay and temperature process controller (purchased from Omega: Temperature & Process Controller CNI16D44-C4EI-AL; ceramic insulated strip heaters, HSC series; solid-state relay SSRL240DC50; T-type copper constantan thermocouple 5TC-TT-T-30-36), were placed on either side of the beaker in order to heat the stage (which was in contact with the tip of the core) and were regulated using a T-type thermocouple in contact with the tip.

Magnetic field profiling. The magnetic field profiling of different coils and cores was carried out using a Lakeshore 425 Gaussmeter. A transverse probe was connected to the gaussmeter and anchored to a micromanipulator (HS-6 by Märzhäuser Wetzlar); measurements in the *y*- direction were recorded with micrometer precision and repeated twice. To power the electromagnet, we used a DC power supply (Mastech DC Power Supply HY3020MR, capable of generating up to 20 Amps of current with 30 Volts) with a microprocessor controller to maintain fixed current or fixed voltage.

Force calibrations. Using previously developed protocol (Upadhyayula, Quinata et al. 2012), force calibrations of the electromagnet setup were performed on non-fluorescent Bangs Laboratory superparamagnetic beads of diameter 2.99μm in Microcells (0.5 mm or 1 mm) square ID capillary tubes filled with 60% or 80% glycerol solutions. The dynamic viscosity of the glycerol solutions was measured using Cannon-Fenske N 956 Size 150 viscometer (viscosities of 39.3 ± 0.24 cP and 68.2 ± 0.04 cP were measured for the 60% and 80% glycerol-bead mixture solutions, respectively). The superparamagnetic beads were allowed to settle in the capillary tube before we powered on the electromagnet. The square capillary was positioned below the electromagnet-beaker setup and adjacent to a 3 mm 45˚ mirror positioned above the objective. (Due to the size of the electromagnet setup, a 3 mm mirror was needed to reflect the light passing through the capillary to the objective.) The subsequent video was captured at 5 frames/sec for 30 seconds. We then analyzed the videos to determine the velocity with which the beads were moving and subsequently determined the values of the forces using the Stokes-Einstein equation (Upadhyayula, Quinata et al. 2012).

Schemes

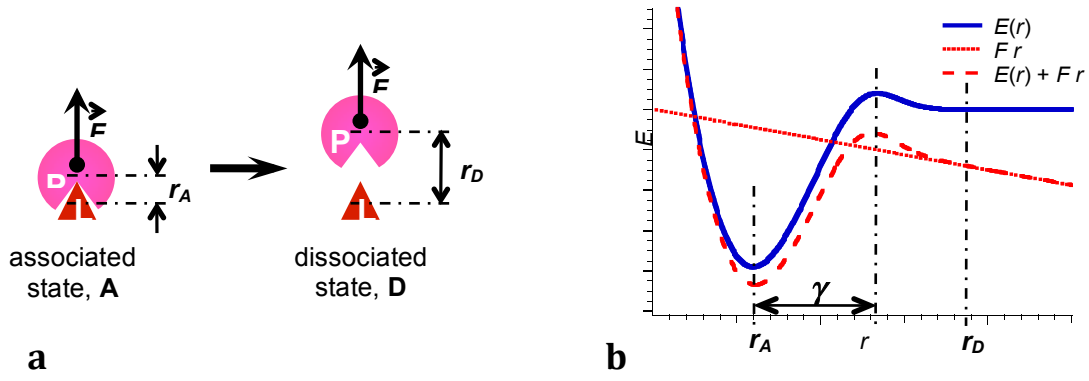

Scheme 2-1. A two-state model of dissociation of the complex between **P** and **L** under applied force, *F*: **(a)** a schematic representation of the process of dissociation; **(b)** dependence of the energy of the system, *E*, on the distance of separation between **P** and **L**, *r*.

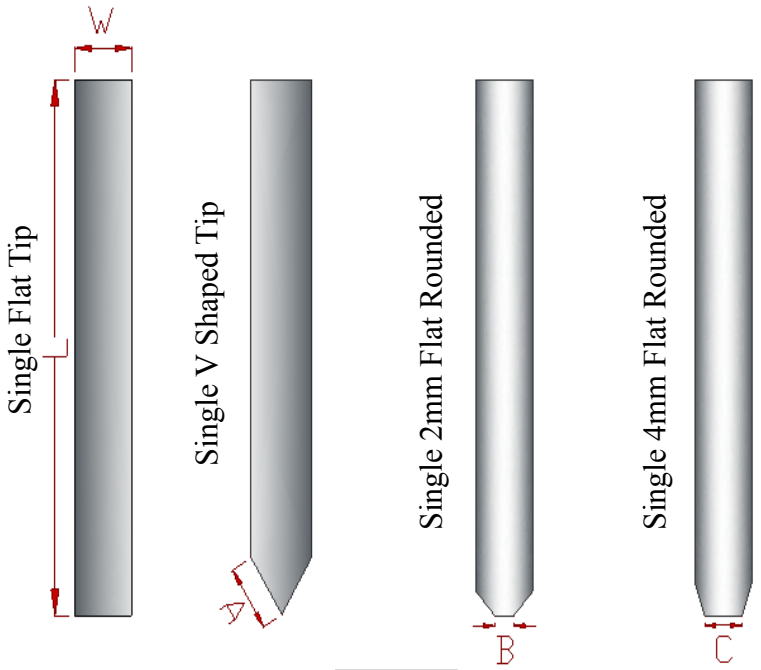

L	140mm
W	6mm
A	6mm
B	2mm
C	4mm

Scheme 2-2. Single electromagnetic core configurations

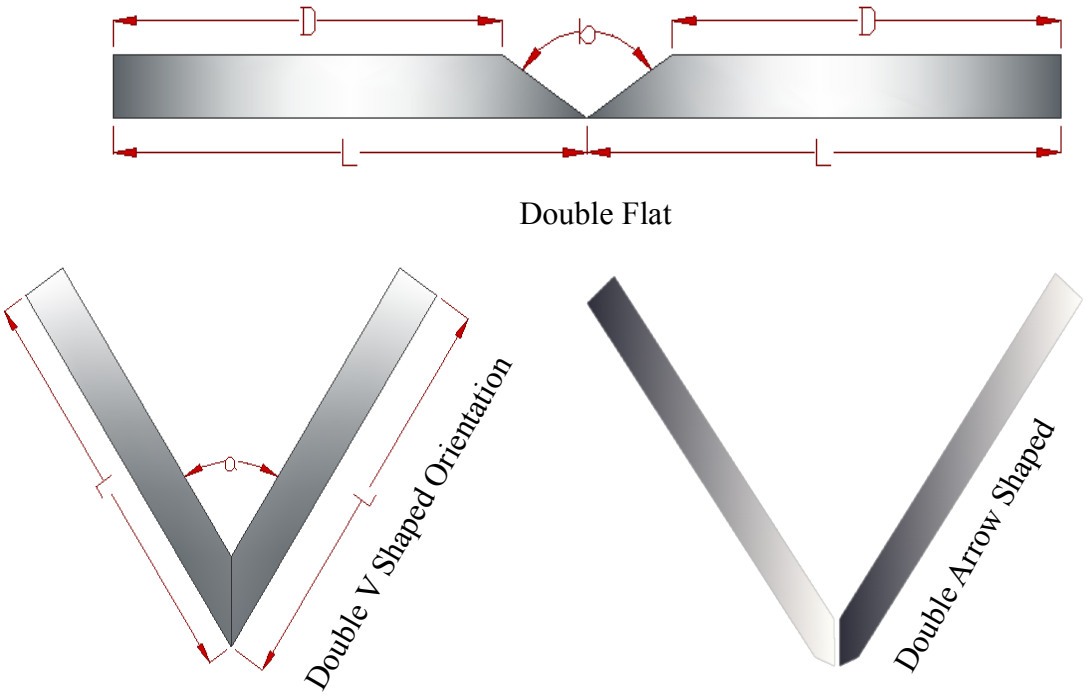

L	140mm
W	6mm
a	65°
b	110°

Scheme 2-3. Double electromagnetic core configurations

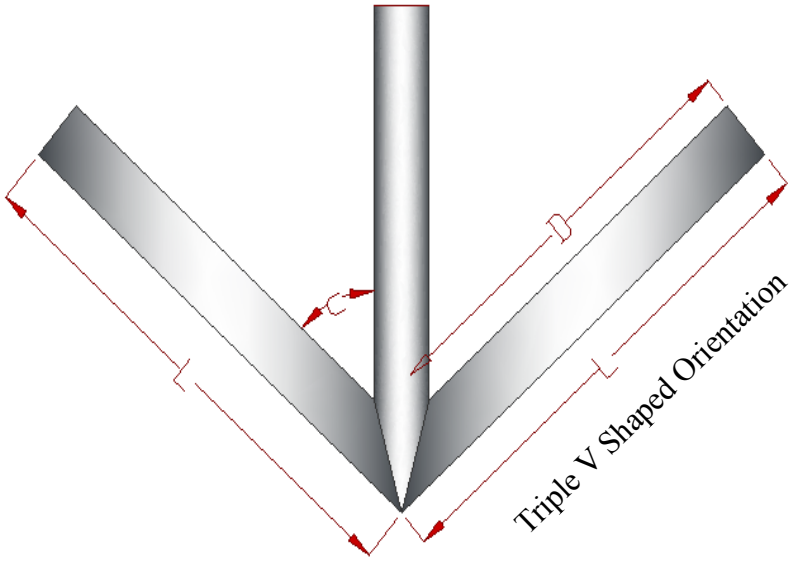

L	140mm
D	130mm
c	50°

Scheme 2-4. Triple electromagnetic core setup

Figures

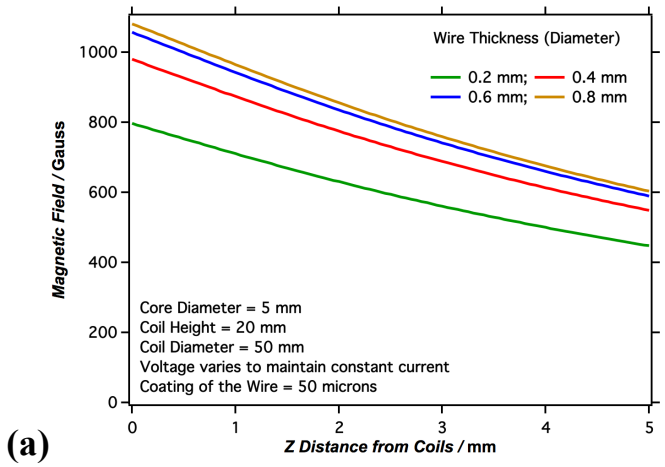

(a)

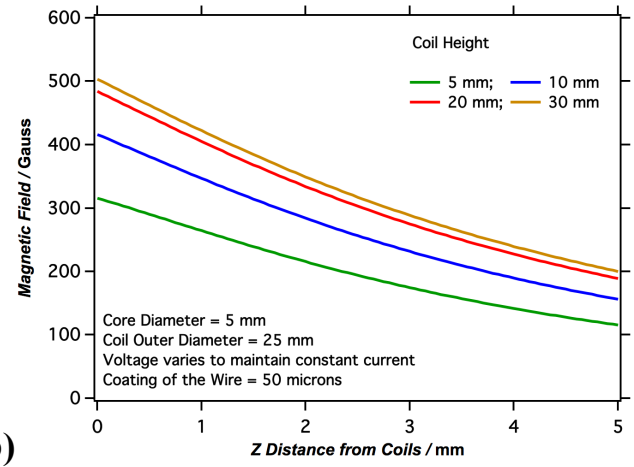

(b)

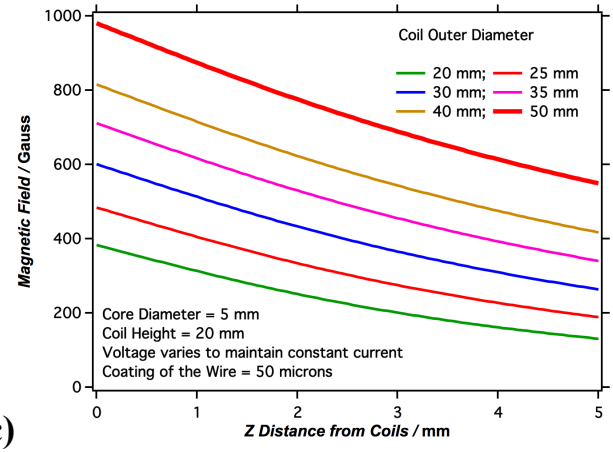

(c)

Figure 2-1

Figure 2-1. Magnetic field dependence on (a) wire thickness; (b) coil height; (c) coil diameter. This theoretical analysis was carried out by optimizing the parameters described in the Biot-Savart law (equation 4).

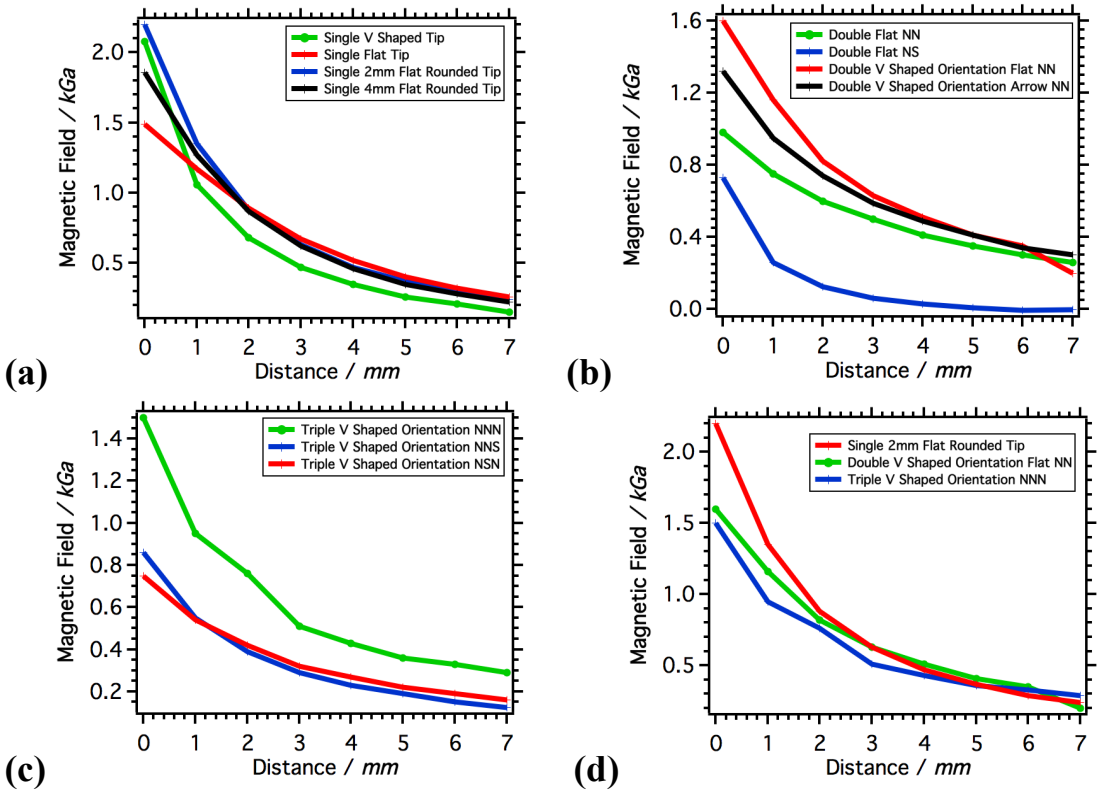
(a)
Single V Shaped Tip
Single Flat Tip
Single 2mm Flat Rounded Tip
Single 4mm Flat Rounded Tip
Magnetic Field / kGa
Distance / mm
(b)
Double Flat NN
Double Flat NS
Double V Shaped Orientation Flat NN
Double V Shaped Orientation Arrow NN
Magnetic Field / kGa
Distance / mm
(c)
Triple V Shaped Orientation NNN
Triple V Shaped Orientation NNS
Triple V Shaped Orientation NSN
Magnetic Field / kGa
Distance / mm
(d)
Single 2mm Flat Rounded Tip
Double V Shaped Orientation Flat NN
Triple V Shaped Orientation NNN
Magnetic Field / kGa
Distance / mm

Figure 2-2

Figure 2-2. Comparision of magnetic fields generated using (a) single core; (b) double core; and (b) triple core configurations. The single core with the 2 mm tip configuration generated the largest magnetic fields when compared to the highest field generating configurations in double and triple core setups (d). All fields were generated using a coil with 5 cm diameter and 2 cm height at 1.8A.

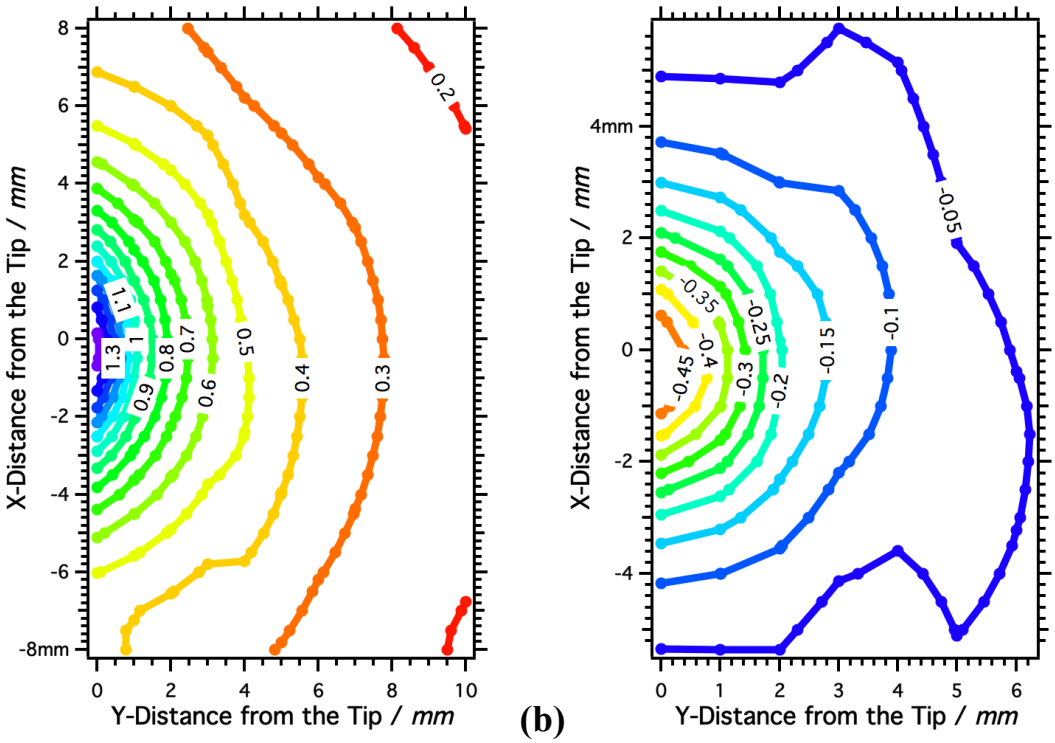
X-Distance from the Tip / mm
Y-Distance from the Tip / mm
8
6
4
2
0
-2
-4
-6
-8mm
0
2
4
6
8
10
0.2
0.3
0.4
0.5
0.6
0.7
0.8
0.9
1
1.1
1.3
(a)
X-Distance from the Tip / mm
Y-Distance from the Tip / mm
4mm
2
0
-2
-4
0
1
2
3
4
5
6
-0.05
-0.1
-0.15
-0.2
-0.25
-0.3
-0.35
-0.4
-0.45
(b)

Figure 2-3

Figure 2-3. Profiling the (a) magnetic field and (b) magnetic gradient in x- and y-direction using a single 2 mm flat-tip with rounded edges and a coil with 5 cm diameter by 2 cm height at 1.8A. The intensity (z- dimension) in the contour plots has kiloGauss units.

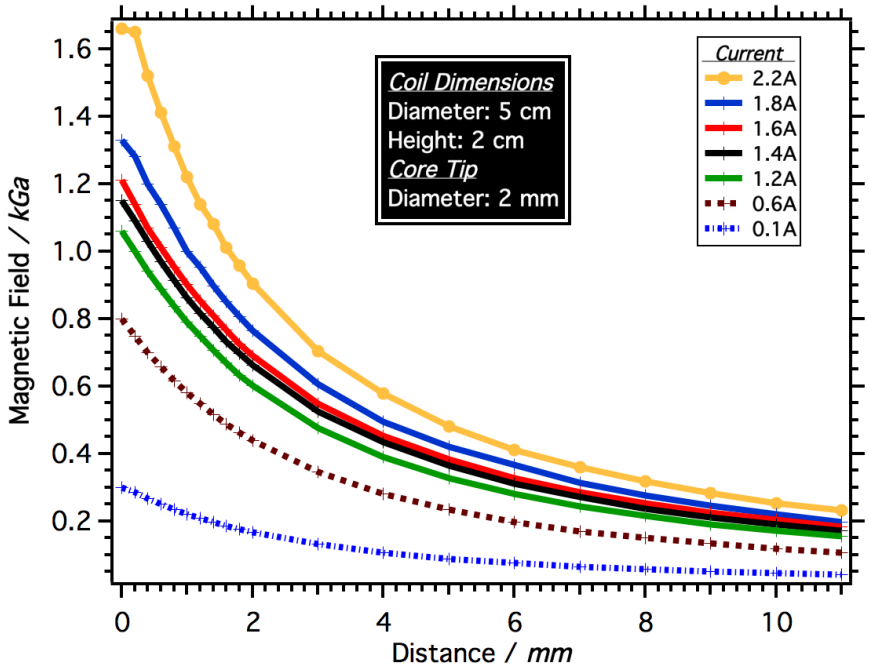
Coil Dimensions
Diameter: 5 cm
Height: 2 cm
Core Tip
Diameter: 2 mm
Current
2.2A
1.8A
1.6A
1.4A
1.2A
0.6A
0.1A
Magnetic Field / kGa
Distance / mm
1.6
1.4
1.2
1.0
0.8
0.6
0.4
0.2
0
2
4
6
8
10

Figure 2-4

Figure 2-4. Varying the current changes the magnetic fields produced by the electromagnetic setup. All fields were generated using a coil with 5 cm diameter and 2 cm height.

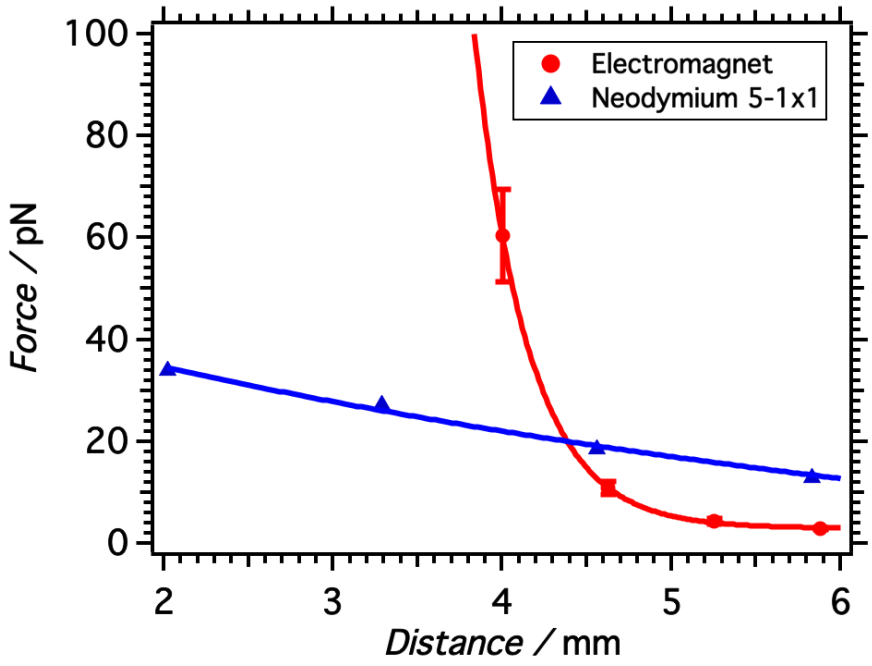
Electromagnet
Neodymium 5-1x1
Force / pN
Distance / mm
100
80
60
40
20
0
2
3
4
5
6

Figure 2-5

Figure 2-5. Force calibrations using Bangs Laboratory microbeads with a temperature-regulated electromagnetic setup consisting of a single 2 mm flat-tip and a coil with dimensions at 1.8A (red line). In comparision, the forces generated by five 1 cm by 1 cm neodymium magnets is shown in blue.

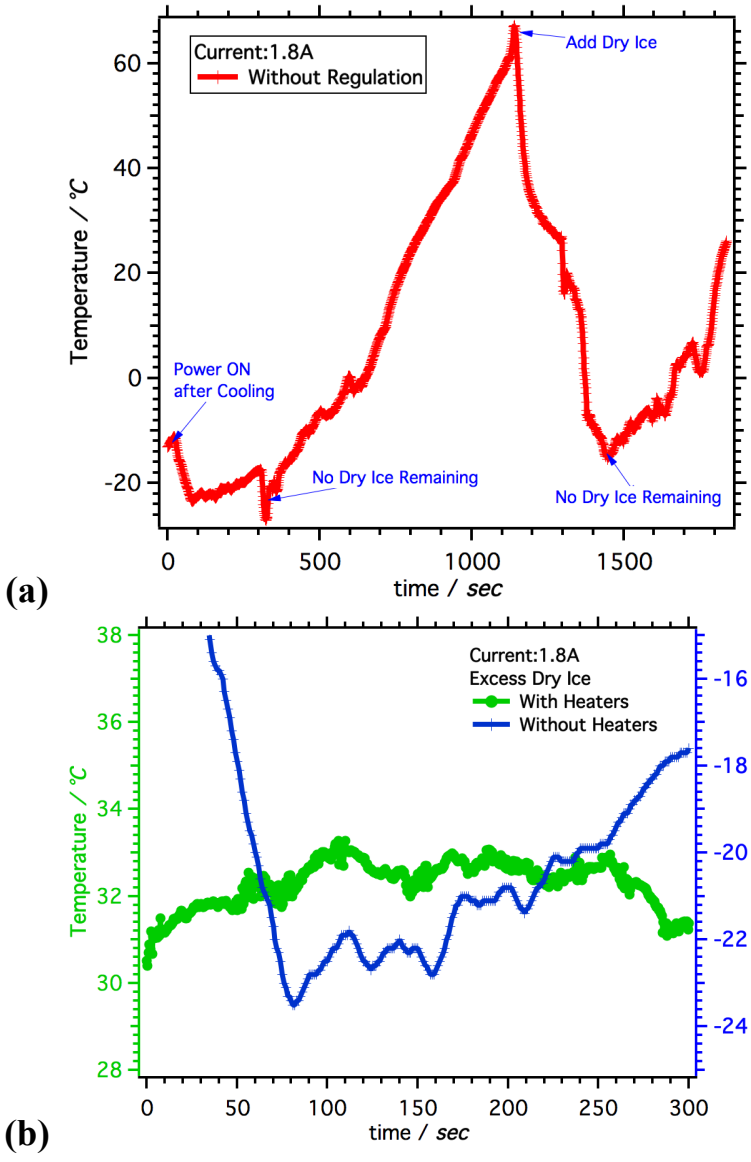
Current:1.8A
Without Regulation
Add Dry Ice
Power ON
after Cooling
No Dry Ice Remaining
No Dry Ice Remaining
Temperature / °C
time / sec
(a)
Current:1.8A
Excess Dry Ice
With Heaters
Without Heaters
Temperature / °C
time / sec
(b)

Figure 2-6

Figure 2-6. (a) Cycling of core tip temperature with the addition and complete sublimation of dry ice. (b) The constant cooling of the electromagnet with and without the use of heaters (set to 32˚C) to regulate the temperature at the tip. All fields were generated using a coil with 5 cm diameter and 2 cm height at 1.8 A.

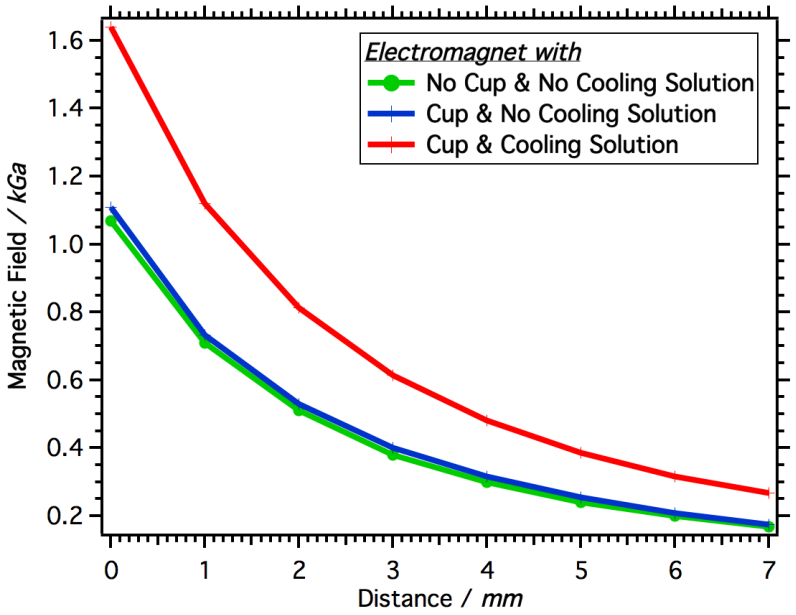
Electromagnet with
No Cup & No Cooling Solution
Cup & No Cooling Solution
Cup & Cooling Solution
Magnetic Field / kGa
Distance / mm
1.6
1.4
1.2
1.0
0.8
0.6
0.4
0.2
0
1
2
3
4
5
6
7

Figure 2-7

Figure 2-7. The heating of the electromagnet setup causes a discernable decrease in the magnetic fields that are generated. All fields were generated using a coil with 5 cm diameter and 2 cm height at 1.8 A.

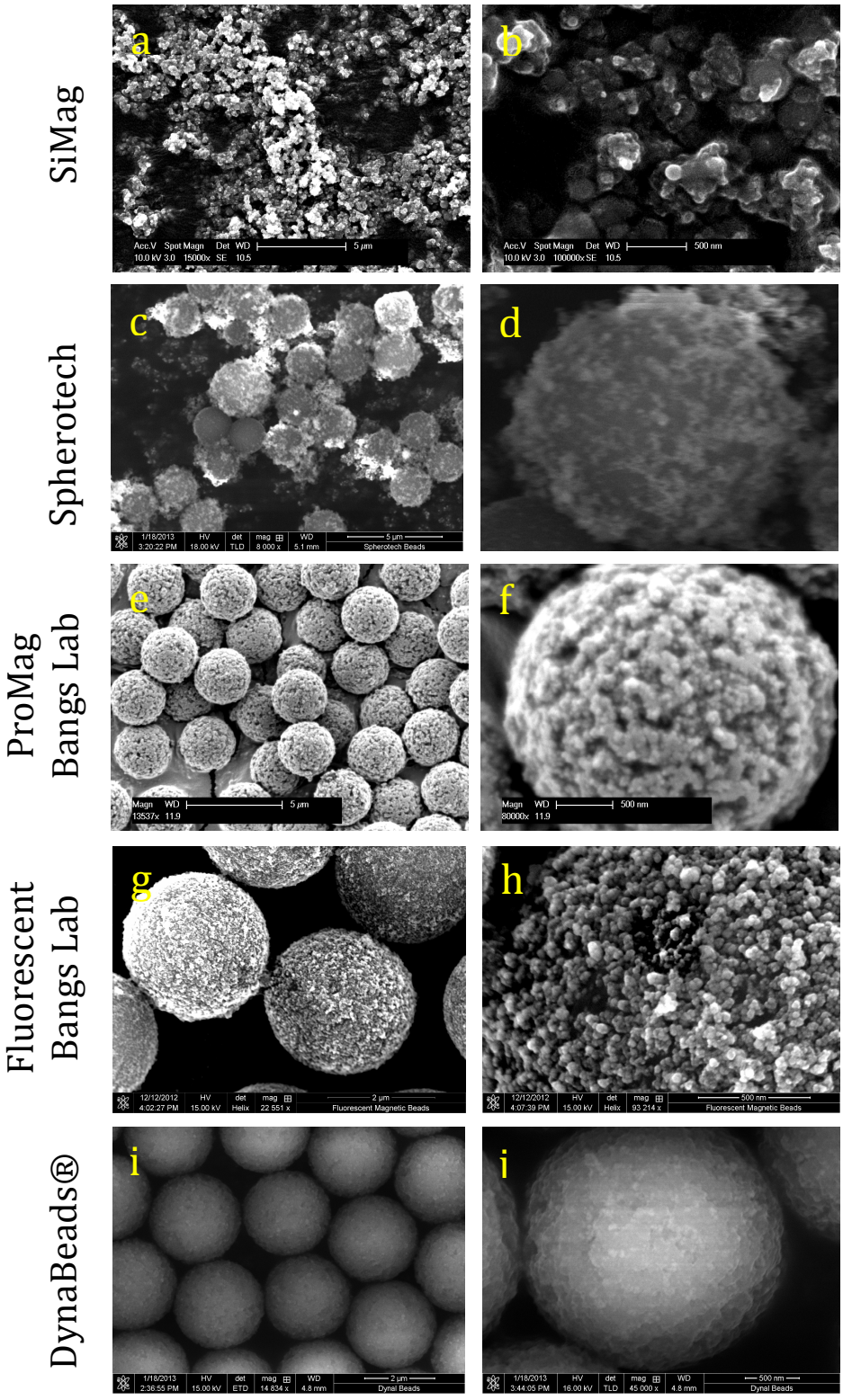
SiMag
Spherotech
ProMag Bangs Lab
Fluorescent Bangs Lab
DynaBeads®
a
b
c
d
e
f
g
h
i
i

Figure 2-8. Scanning electron microscope pictures of superparamagnetic microbeads/particles from commercially available sources. Spherotech beads (c,d), fluorescent Bangs Lab beads (g,h) and DynaBeads® (i,j) were imaged without being sputter coated with conducting material. SEM was performed using Philips XL30 FEG and Nova NanoSEM 450 (Detectors: CONCENTRIC BACKSCATTERED DETECTOR (CBS); EVERHART THORNLEY DETECTOR (ETD); THROUGH LENS DETECTOR (TLD)).

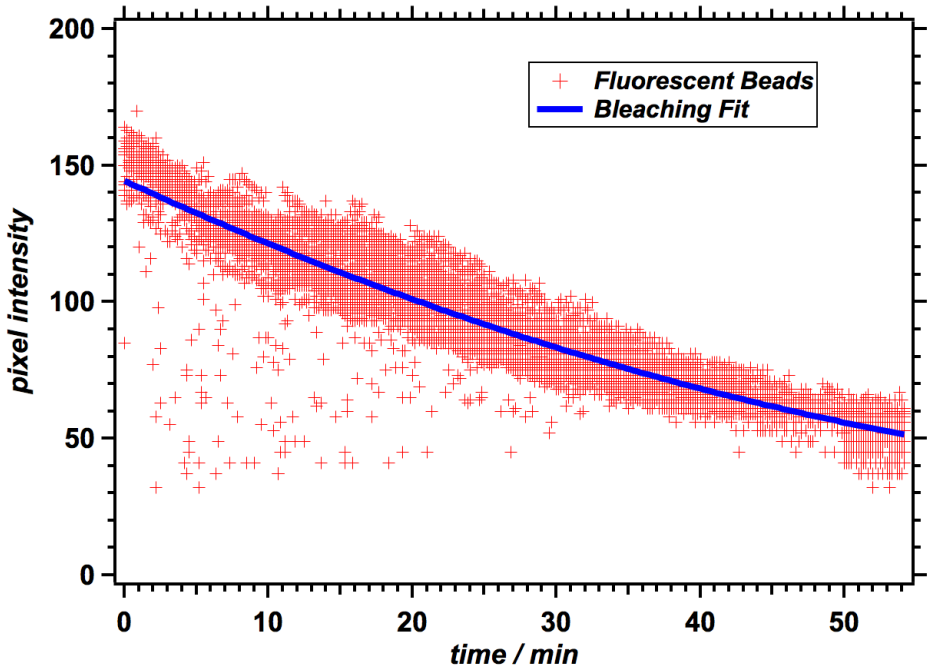
Fluorescent Beads
Bleaching Fit
pixel intensity
time / min
200
150
100
50
0
0
10
20
30
40
50

Figure 2-9

Figure 2-9. Intensity of ~50 fluorescent Bangs Laboratory microbeads tracked as a function of time with constant excitation using FITC filter set.

References

Assi, F., R. Jenks, et al. (2002). "Massively parallel adhesion and reactivity measurements using simple and inexpensive magnetic …." Journal of applied physics.

Bell, G. (1978). "Models for the specific adhesion of cells to cells." Science **200**(4342): 618.

Bongrand, P. (1999). "Ligand-receptor interactions." Reports on Progress in Physics.

Bustamante, C., Y. Chemla, et al. (2004). "MECHANICAL PROCESSES IN BIOCHEMISTRY." Annu. Rev. Biochem. **73**(1): 705-748.

Chiou, C., Y. Huang, et al. (2006). "New magnetic tweezers for investigation of the mechanical properties of single DNA molecules." Nanotechnology **17**(5): 1217-1224.

Deniz, A. A., S. Mukhopadhyay, et al. (2008). "Single-molecule biophysics: at the interface of biology, physics and chemistry." Journal of The Royal Society Interface.

Evans, E. (1999). "Looking inside molecular bonds at biological interfaces with dynamic force spectroscopy." Biophysical Chemistry.

Evans, E. (2001). "P ROBING THE R ELATION B ETWEEN F ORCE-L IFETIME- AND C HEMISTRY IN S INGLE M OLECULAR B ONDS." Annual Review of Biophysics and Biomolecular Structure **30**(1): 105-128.

Gosse, C. and V. Croquette (2002). "Magnetic tweezers: micromanipulation and force measurement at the molecular level." Biophysical Journal **82**(6): 3314-3329.

Guthold, M., R. Superfine, et al. (2001). "… : Force measurements on single molecules and how they relate to bulk reaction kinetics and energies." Biomedical Microdevices.

Haber, C. and D. Wirtz (2000). "Magnetic tweezers for DNA micromanipulation." Review of Scientific Instruments.

Kapanidis, A. N. and T. Strick (2009). "Biology, one molecule at a time." Trends in Biochemical Sciences.

Nahas, M., T. Wilson, et al. (2004). "Observation of internal cleavage and ligation reactions of a ribozyme." Nat Struct Mol Biol **11**(11): 1107-1113.

Neuman, K. and A. Nagy (2008). "Single-molecule force spectroscopy: optical tweezers, magnetic tweezers and atomic force microscopy." Nat Meth **5**(6): 491-505.

Upadhyayula, S., T. Quinata, et al. (2012). "Coatings of polyethylene glycol for suppressing adhesion between solid microspheres and flat surfaces." Langmuir : the ACS journal of surfaces and colloids **28**(11): 5059-5069.

Vullev, V. (2005). "Modulation of Dissociation Kinetics by External Force: Examination of the Bell Model." Journal of Biological Sciences **5**(6): 744-758.

Walter, N. G., C. Y. Huang, et al. (2008). "Do-it-yourself guide: how to use the modern single-molecule toolkit." Nat Meth.

Wang, N., J. P. Butler, et al. (1993). "Mechanotransduction across the cell surface and through the cytoskeleton." Science.

Chapter 3

Permanent Electric Dipole Moments of Carboxyamides in Condensed Media: What Are the Limitations of Theory and Experiment?

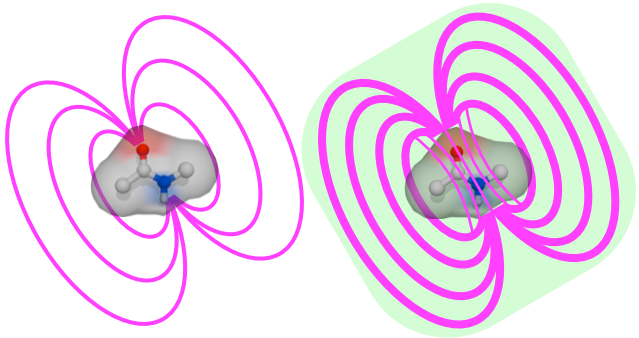

ABSTRACT

Electrostatic properties of proteins are crucial for their functionality. Carboxyamides are small polar groups that, as peptide bonds, are principal structural components of proteins that govern their electrostatic properties. We investigated the medium dependence of the molar polarization, and of the permanent dipole moments of amides with different state of alkylation. The experimentally measured and theoretically calculated dipole moments manifested a solvent dependence that increased with the increase in the media polarity. We ascribed the observed enhancement of the amide polarization to the reaction fields in the solvated cavities. Chloroform, for example, caused about a 25% increase in the amide dipole moments determined for vacuum, as the experimental and theoretical results demonstrated. Another chlorinated solvent, 1,1,2,2-tetrachloroethane, however, caused an "abnormal" increase in the experimentally measured amide dipoles, which the theoretical approaches we used could not readily quantify. We showed and discussed alternatives for addressing such discrepancy between theory and experiment.

KEYWORDS: amides, peptides, polarity, polarizability, dielectric, reaction field

Introduction

This article describes a comparative study of the ground-state electric dipole moments of six aliphatic carboxyamides (Scheme 3-1). From experimentally obtained values for the molar polarizations, extrapolated to infinite dilutions, we estimated the permanent electric dipoles of the amides for different solvent media. Concurrently, we determined the amide dipoles theoretically using *ab initio* calculations for vacuum and for condensed media. For chloroform, the independently obtained experimental and theoretical results manifested identical solvent effect on the amide dipoles. For other solvents, however, we observed discrepancy between theory and experiment, which pointed to certain limitations of the used theoretical and experimental approaches.

As vital components of life, proteins have a broad spectrum of functional capacities. Proteins not only provide structural support,(Petrasek and Schwarzerova 2009; Launey, Buehler et al. 2010) but also drive mechanical movements.(Hackney 2007; van den Heuvel and Dekker 2007; Sowa and Berry 2009) Proteins mediate active and passive transport,(Dolezal, Likic et al. 2006; Alber, Dokudovskaya et al. 2007; Trinkle-Mulcahy and Lamond Angus 2007) as well as signaling;(Knoblich 2006; Slessareva and Dohlman 2006; Hardie 2007) and they act as enzymatic entities.(Petricoin, Belluco et al. 2006; Barglow and Cravatt 2007; Rexach, Clark et al. 2008; Weerapana, Simon et al. 2008) In addition to the three-dimensional structures, the electrostatic properties of proteins define their reactivity and govern their structure-function relations.(Suydam, Snow et al. 2006; Sigala, Fafarman et al. 2007) Local electric fields within the protein environment alter the

pK_a values of ionizable functional groups,(Kundrotas and Alexov 2006) and enable binding selectivity for different types of substrates and for other proteins.(Dudev and Lim 2003)

Peptide bonds, which are essentially α-carboxyamides between amino-acid residues, are the most essential linkages in proteins. In addition to their role as structural building blocks, peptide bonds contribute significantly to the protein electrostatics. Indeed, amides are small polar groups with permanent electric dipoles exceeding ~3 D.(Prasad and Sundaram 1979; Makarenko, Makovetskii et al. 1991)

A polypeptide α-helix, for example, supported by a network of hydrogen bonds, is a template for amide bonds with an ordered orientation. The co-directionally oriented amide dipoles, along with the shift in the electron density upon the creation of the hydrogen bonds, generate substantial permanent electric dipole moments for this class of protein conformers, i.e., protein α-helices possess dipole moments amounting to 3 – 5 D per residue.(Wada 1959; Hol 1985) Such electrostatic properties, however, are not unique solely for protein α-helices. Protein 3_{10}-helices possess permanent dipole moments of similar magnitude.(Shin, Newton et al. 2003) (3_{10}-helices can be viewed as "tightly wound" α-helices. In fact, α-helices are 3.6_{13}-helices with 3.6 residues per turn and 13-bond loops constrained between every two neighboring hydrogen bonds.(Doig 2002)) Although polyprolines cannot form intramolecular hydrogen bond, the ordered orientation of peptide bonds in polyproline type I and type II helices also results in considerable permanent electric dipoles that are oppositely oriented for these two types of conformers.(Shin, Newton et al. 2003)

Nature employs such protein electrets for a range of vital functions. (Electrets are materials with ordered electric dipole moments: i.e., they are the electrostatic analogues of magnets.(Mopsik and Broadhurst 1975; Qiu 2010)) The electric field generated by helix dipoles drives protein binding of charged species,(Hol, Van Duijnen et al. 1978) and facilitates the charge-selectivity of ion channels.(Doyle, Cabral et al. 1998; Dutzler, Campbell et al. 2002) In the vicinity of polypeptide helices, the dipole electric fields rectify the directionality of electron transfer.(Galoppini and Fox 1996; Shin, Newton et al. 2003; Yasutomi, Morita et al. 2004) Employing oriented amide arrangements in synthetic oligomers allowed for the design of bioinspired electrets.(Ashraf, Pandey et al. 2009; Vullev 2011) Overall, as principal linkers in biological and synthetic polymers,(Jones, Lu et al. 1995; Jones, Vullev et al. 2000; Jones and Vullev 2002; Vullev and Jones 2002; Vullev and Jones 2002; Jones, Zhou et al. 2003; Wan, Ferreira et al. 2008) the amides and the amide dipoles define the electrostatic properties of macromolecules and govern their functionality.

From readily measurable dielectric quantities, the Debye relation allows for an experimental estimation of the magnitudes of permanent electric dipole moments, μ, of polar molecules:(Debye 1945)

$$\mu^2 = \frac{9\varepsilon_0 k_B T}{N_A} P_{2\mu}^{(0)} \qquad (1)$$

where $P_{2\mu}^{(0)}$ is the molar polarization resultant from the field-induced orientation of the molecular dipoles, T is the temperature (in K), and the rest of the quantities are well-known physical constants, i.e., ε_0 – the dielectric permittivity of vacuum, k_B – the Boltzmann constant, and N_A –Avogadro's number.

In order to extract intramolecular characteristics from bulk quantities of a solute, the intermolecular interactions in the samples have to be negligible. Hence, gas-phase measurements taken under low-pressure conditions provide the ideal experimental source for estimating molar polarizations for dipole-moment calculations.(Hurdis and Smyth 1942; Nace and Nealey 1966; Steimle, Nachman et al. 1987; Canagaratna, Ott et al. 1997; Jraij, Allouche et al. 2006) Such experimental requirements, however, present challenges and are implausible for a broad range of molecular species of biological and chemical importance.

As an alternative to gas-phase settings, dielectric and density measurements of binary liquid solutions offer the means for estimating molar polarizations.(Breitung, Vaughan et al. 2000; Tjahjono, Davis et al. 2007) Using non-polar solvents as major components of such binary solutions, provides the means for close to gas-phase microenvironment for the molecular species of interests (which are introduced as the minor components of the binary systems).

To further avoid intermolecular interactions, such as aggregation, the molar polarizations are extracted from diluted solutions. Such dilutions of the analyte, however, decrease the signal-to-noise ratios and places demands on the precisions of the measurements. Extrapolation to infinite dilutions, developed initially by

Hedestrand(Hedestrand 1929) and consequently by Halverstadt and Kumler,(Halverstadt and Kumler 1942) provides the means for accessing bulk quantities that reliably characterize intramolecular properties.(Taylor 1975)

The extrapolation of dielectric and density characteristics to zero-solute concentrations yields the total molar polarization, $P_2^{(0)}$. The pronounced difference between the time scales of the various modes of polarization allows for an approximation of the total molar polarization, $P_2^{(0)}$, as an additive quantity of the orientation or dipole, $P_{2\mu}^{(0)}$, vibrational or atomic, $P_{2\nu}^{(0)}$, and electronic, $P_{2e}^{(0)}$, molar polarizations:

$$P_2^{(0)} = P_{2\mu}^{(0)} + P_{2\nu}^{(0)} + P_{2e}^{(0)} \qquad (2)$$

Assuming that $P_{2\mu}^{(0)}$ is the principal component of $P_2^{(0)}$, and that $P_{2\nu}^{(0)}$ and $P_{2e}^{(0)}$ are solely correction terms, permits the use of the values of the total polarization as an approximation for the orientation polarization. Implementing such an approximation, i.e., $P_{2\mu}^{(0)} \approx P_2^{(0)}$, for dipole-moment calculations from experimental measurements (equation 1), has proven quite acceptable, especially when the solute dipoles are considerably larger than the solvent dipoles.(Halverstadt and Kumler 1942; Breitung, Vaughan et al. 2000) Alternatively, the polarizability of the solute, obtained from its refractivity at off-resonance excitation with visible light, can account for its molar electronic polarization.(Hedestrand 1929; Breitung, Vaughan et al. 2000) Therefore, high-frequency excitation allows for an estimation of the fast-response electronic polarization, while low-

frequency excitation yields the cumulative effect of the total polarization. Decoupling the estimation of the vibrational from the orientation polarization, however, is still an experimental challenge.

Despite a strong preference for nonpolar solvents that do not exhibit specific interactions with the analyte molecules, the use of nonpolar media presents significant experimental drawbacks, such as limited solubility. Furthermore, idealized gas-phase conditions (or condensed-phase conditions that imitate gas phase) are not truly representative of a condensed-phase environment – important, for example, for biological and materials systems.(Leontyev and Stuchebrukhov 2011) Accounting for media polarization is essential for analyzing the effects of the microenvironment on ions and dipoles in proteins and other biological systems.(Leontyev and Stuchebrukhov 2011)

While an increase in the solvent polarity may address the above issues, it introduces effects due to electrostatic solute-solvent interactions that can be prevalent even in the absence of specific intermolecular bonding.(Bao, Millare et al. 2009) Polar and/or polarizable solvent molecules, when surrounding a polar solute molecule, react to the electric field from the permanent electric dipole of the solute. As a result, the ordered solvent molecules produce a reaction field in the solvated cavity, enhancing the dipole moment of the solute.(Onsager 1936)

By accounting for the reaction field in a cavity of a solvated polar molecule, Onsager's theory has provided an excellent foundation for relating molecular dipoles to bulk dielectric properties of continuous media.(Onsager 1936) As Onsager has pointed out, his theory operates on certain assumptions which undermine its applicability, such as: (1) the

assumption of spherical molecular shapes; (2) the assumption of incompressibility, i.e., the sum of the molecular volumes equals to the total sample volume; and (3) the assumption of weak short-distance intermolecular interactions, i.e., short-distance interaction energies do not exceed k_BT. Despite these shortcomings, further developments of the Onsager's theory for non-spherically shaped molecules in non-polar media,(Myers and Birge 1981; Vlassiouk and Smirnov 2003) hydrogen-bonding environments,(Kirkwood 1939) and approximations for polar binary solutions(Malecki, Nowak et al. 1984) have proven promising for the analysis of experimental results.

Herein, we experimentally estimated the electric dipole moments of six amides (Scheme 3-1) from zero-concentration extrapolations for three solvents with different polarities: 1,4-dioxane (DO), chloroform ($CHCl_3$) and 1,1,2,2-tetrachloroethane (TCE). The solvent effects on the estimated dipole moments correlated with dielectric properties of the media. Using density functional theory (DFT), we also theoretically obtained the dipole moments of the same amides for vacuum and for five solvents: DO, $CHCl_3$, and dimethylsulfoxide (DMSO), as well as tetrachloroethene (C_2Cl_4), which has similar polarizability to TCE, and dichloromethane (CH_2Cl_2), which has similar static dielectric permittivity to TCE. The effects of the condensed media on the *ab initio* calculations were introduced as cavity reaction fields, based on Onsager's solvation theory. Similarly to the experimental result, the theoretically obtained dipole moments increased with the increase in the media polarity. The values of the vacuum theoretical dipole moments showed some similarity with the experimentally obtained dipoles for DO, which is relatively nonpolar. The theoretically and the experimentally obtained dipole values for

chloroform, conversely, were in an excellent agreement, which demonstrates the role of the reaction field in modulating the electronic properties of polar moieties in condensed media. The effect of the most polar solvents on the *ab-initio* computed dipoles, however, were not as pronounced as the experimentally obtained dipoles for TCE (i.e., the most polar solvent we used for the experimental aspects of this study). To elucidate this discrepancy, we reviewed the limitations of the experimental and the theoretical approaches used for estimations of permanent molecular dipoles.

Results and Discussion

Polarization, polarizability and permanent dipoles. How do measurable bulk dielectric properties depend on the electronic characteristics of the composing molecules? Media polarization, **P**, under external electric field, **E**, involves orientation of permanent molecular dipoles, μ_i, and induced displacement of electron density and nuclei as characterized by molecular polarizability, α_i.(Böttcher 1973) Therefore, the electric field that each molecule experiences within a solvation cavity in a media with dielectric constant ε, comprises two principal components: (1) internal field, $\mathbf{E}^{(i)}$, that polarizes the molecule; and (2) the directing field, $\mathbf{E}^{(d)}$, that exerts force to turn the molecule and align the molecular dipole.(Böttcher 1973) Similarly, the polarization in the presence of external field has two components: (1) induced polarization, $\mathbf{P}_\alpha$, that encompasses the vibrational and electronic polarization, $\mathbf{P}_\alpha = \mathbf{P}_v + \mathbf{P}_e$; and (2) orientation polarization, $\mathbf{P}_\mu$

.(Böttcher 1973) For ideal solutions composed of *H* different types of molecules, these polarization components are:(Böttcher 1973)

$$\mathbf{P}_{\alpha} = 4\pi\varepsilon_0 \sum_{i=1}^{H} N_i \alpha_i \mathbf{E}_i^{(i)} \tag{3a}$$

$$\mathbf{P}_{\mu} = \sum_{i=1}^{H} N_i \frac{\boldsymbol{\mu}_i^2}{3k_B T} \mathbf{E}_i^{(d)} \tag{3b}$$

The relation between the total polarization and the applied electric field, $\mathbf{P} = \varepsilon_0 \left(\varepsilon - 1\right)\mathbf{E}$, yields:(Böttcher 1973)

$$\left(\varepsilon - 1\right)\mathbf{E} = \sum_{i=1}^{H} N_i \left(4\pi\alpha_i \mathbf{E}_i^{(i)} + \frac{\boldsymbol{\mu}_i^2}{3\varepsilon_0 k_B T} \mathbf{E}_i^{(d)} \right) \tag{3c}$$

where N_i is the molecular density (i.e., number of molecules per unit volume) for the i^{th} type of molecules. Considering the reaction field from the solvating media, which allows for relating $\mathbf{E}_i^{(i)}$ with $\mathbf{E}_i^{(d)}$ and with the applied external electric field, **E**, transforms equation 3c into the various forms of the Onsager equation.(Onsager 1936)

Alternatively, approximating the internal and the directing field to the Lorentz's field, $\mathbf{E}_L$, for an interior of a spherical cavity exposed to external field, **E**, i.e., $\mathbf{E}_i^{(i)} \approx \mathbf{E}_i^{(d)} \approx \mathbf{E}_L = \mathbf{E}\left(\varepsilon + 2\right)/3$, simplifies equation 3 to the Debye equation:(Onsager 1936; Debye 1945; Böttcher 1973)

$$\frac{\varepsilon-1}{\varepsilon+2}=\sum_{i=1}^{H}N_i\left(\frac{4\pi}{3}\alpha_i+\frac{\mu_i^2}{9\varepsilon_0 k_B T}\right) \tag{4a}$$

which for pure liquid transforms into:

$$P=N_A\left(\frac{4\pi}{3}\alpha+\frac{\mu^2}{9\varepsilon_0 k_B T}\right)=P_\alpha+P_\mu \tag{4b}$$

The additivity of molar polarization, i.e., $P=\sum_i \chi_i P_i$, where χ_i is the mole fraction of the i^{th} component of a mixture, allows for converting the Debye equation into equation 1. For binary isotropic solutions, H = 2, therefore, in which the dipole of one of the components is considerably larger than the dipole of the other component, $\mu_2^2 >> \mu_1^2$ (that is equivalent to $N_2\mu_2^2 >> N_1\mu_1^2$ for comparable concentrations N_1 and N_2), the predominant term in equation 4a that governs the orientation molar polarization is $\mu_2^2/3\varepsilon_0 k_B T$, permitting to ignore the term with μ_1 for the less polar compound. Extrapolation to infinite dilutions of the more polar component of such a binary mixture, and using $P_{2\mu}^{(0)}$ instead of $P_{2\mu}$, allows for approaching idealized conditions, for which the Debye theory is applicable, as depicted in equation 1.

Apparently, at infinite dilution, $\chi_2 \to 0$, the inequality condition, $N_2\mu_2^2 >> N_1\mu_1^2$, cannot hold because $\lim_{x_2\to 0}(N_2) = 0$. Conversely, the inequality $N_2\mu_2^2 >> N_1\mu_1^2$ needs to be valid under the conditions of the experimental measurements of the dielectric properties

of the binary mixtures. The extrapolation to zero concentration allows for the following approximations for the dielectric and density properties of the binary solutions: $\lim_{x_2 \to 0}(\varepsilon) = \varepsilon_1$, $\lim_{x_2 \to 0}(\rho) = \rho_1$, $\lim_{x_2 \to 0}(x_1) = 1$, and $\lim_{x_2 \to 0}(P_2) = P_1^{(0)}$.[50] Therefore, $P_2^{(0)}$ and P_2 are not identical: $P_2^{(0)}$ encompasses the solvent effects of the measurements as this study reveals for the dipole moments of the aliphatic amides.

Another important consideration involves the unfeasibility to carry any of the measurements at close-to-equal concentrations of the two components of the binary mixtures. At $N_1 \approx N_2$ in condensed phase, the interactions between the molecules of the polar component make it prohibitively unfeasible to apply the Debye theory. Therefore, experimental studies are usually conducted at $N_1 >> N_2$, which allows validity of $N_2\mu_2^2 >> N_1\mu_1^2$ only if the molecules of the solvent (the predominant component) have no or negligible permanent electric dipole moment, i.e., $\mu_1 \approx 0$. Nevertheless, a number of examples of reliable estimation of the dipole moments of small polar molecules from dilute solutions in solvents with permanent dipoles, such as toluene (μ_1 = 0.36 D), 1,4-dioxane (μ_1 = 0.45 D) and acetone (μ_1 = 2.9 D),[48] illustrate that equation 1 is applicable to cases of $N_1 >> N_2$ and $\mu_1 > 0$. That is, the extrapolations to zero concentrations, $\chi_2 \to 0$, from diluted solutions yield $P_2^{(0)}$ values that are representative of the extrapolations from concentrated binary solutions with assumingly idealized no intermolecular interactions between their polar components.

Strictly speaking, polarization represents dipole density, i.e., number of dipoles per unit volume aligned or induced by the applied field. As such a quantity, therefore, **P** has the dimensions of charge time distance over volume, or charge over area, as depicted in equations 3a and 3b. Similarly, polarizability represents the dipole induced in a molecule by the field, and its dimensions should be dipole over field strength, or dipole time distance over potential. As most frequently written in different forms of the Debye equation, the polarizability, α, has dimensions of μ^2/k_BT, which, indeed, has the units of dipole time distance over potential. Conventionally, however, polarizability is expressed in units of volume and the molar polarization, P, in units of volume per mole, as depicted in equations 1 and 4b.

Lorentz-Lorenz equation (i.e., Clausius-Mossetti expression involving the dynamic dielectric constants) relates the bulk dielectric properties of a substance with the polarizability of its molecules with radii, r:

$$\alpha_i = \frac{\varepsilon_i(\omega_\alpha)-1}{\varepsilon_i(\omega_\alpha)+2} r_i^3 = \frac{3}{4\pi}\frac{\left(\varepsilon_i(\omega_\alpha)-1\right)}{\left(\varepsilon_i(\omega_\alpha)+2\right)} v_i \tag{5a}$$

$$P_{i\alpha}^{(0)} = \frac{\left(\varepsilon_i(\omega_\alpha)-1\right)}{\left(\varepsilon_i(\omega_\alpha)+2\right)}\frac{M_i}{\rho_i} = \frac{4\pi}{3} N_A \alpha_i \tag{5b}$$

where, for samples composed of molecular species i, v_i is the molecular volume, assuming spherical shape, M_i is the molecular weight, ρ_i is the density, and $\varepsilon_i(\omega_\alpha)$ is the dynamic dielectric constant measured at frequency, ω_α. (Equation 5b represents the

transformation from 4a to 4b.) The field polarization frequency, ω_α, is high enough so that the molecular permanent dipoles remain stationary (i.e., the molecules cannot turn fast enough to reorient their dipoles along the oscillating electric field); and yet, ω_α is low enough so that the electron density and nuclei of the molecules can reorganize in phase with the oscillating field. That is, $\varepsilon_i(\omega_\alpha)$ represents the dielectric properties under condition where the orientation polarization is negligible and the total polarization is governed by its vibrational and electronic components.

Experimental determination of $\varepsilon_i(\omega_\alpha)$ at such intermediate frequencies, however, is somewhat challenging. Most frequently, the experimental polarizabilities are estimated from dynamic dielectric properties recorded at optical frequencies where only the electronic polarization is prevalent:

$$\alpha_{ie} = \frac{3}{4\pi}\frac{\left(n_i^2-1\right)}{\left(n_i^2+2\right)}\frac{M_i}{\rho_i N_A} \tag{6a}$$

$$P_{ie}^{(0)} = \frac{\left(n_i^2-1\right)}{\left(n_i^2+2\right)}\frac{M_i}{\rho_i} \tag{6b}$$

where n_i is the index of refraction of molecular species i, recorded at off-resonance optical frequency, ω_e, i.e., for non-magnetic compounds, $n_i^2 = \varepsilon_i(\omega_e)$.

In general, the electronic polarization is the prevalent component of the induced polarization, i.e., usually $\varepsilon_i(\omega_\alpha) \approx 1.05\varepsilon_i(\omega_e)$. Therefore, equations 6a and 6b provide a

reasonable approximation of equations 5a and 5b for estimation of the induced polarization and polarizability from experimentally readily measurable quantities.

Theoretical dipole moments of amides. For this study, we selected six aliphatic amides with different extent of alkylation (Scheme 3-1), i.e., with a hydrogen (Hxx) or an ethyl (Exx) attached to the carbonyl carbon, and with no ethyl (xHH), one ethyl (xHE) or two ethyl substituents (xEE) on the amide nitrogen (where "x" designates "H" or "E"). We calculated the ground-state electric dipole moments of the amides using *ab initio* density functional theory (DFT) as implemented by Gaussian (Figure 3-1).(Frisch, Trucks et al. 2004; Bao, Ramu et al. 2010)

The implemented computational tools allowed for a separate analysis of the *cis* and *trans* conformers of each of the N-monoethylated amides, HHE and EHE (Figure 3-1b, c, f, g). The *cis*-HHE and *trans*-EHE were viewed as analogous because the nitrogen-bonded ethyls and the carbonyl oxygens were on the same side of the axis of the C-N amide bond (Scheme 3-1). Similarly, the *trans*-HHE and the *cis*-EHE were analogous because their carbonyl oxygens and N-bonded ethyls were on the opposite sides of the axis of the C-N amide bonds (Scheme 3-1).

The theoretical values of the dipoles for vacuum, $\mu^{(0)}$, of the eight species ranged from about 3.3 to 3.8 D (Table 3-1). The values of the dipoles for HHH, HEE, and EHH were in a good agreement with the previously reported values for these amides.(Bates and Hobbs 1951; Kurland and Wilson 1957; Sit, Dutta et al. 2000) The amide dipoles pointed from the carbonyl oxygens to the nitrogens (Figure 3-1) (i.e., the direction of electric

dipoles is from their negative to their positive poles). Alkylation of the carbonyl carbons yielded an approximate 3–10 % decrease in the magnitude of the dipole moments. Conversely, the monoalkylation of the amide nitrogens had the most pronounced effect on the dipole moments. Placing the N-bonded ethyls and the carbonyl oxygens at opposing positions, i.e., *trans*-HHE and *cis*-EHE (Scheme 3-1), substantially increased the magnitude of the amide dipoles (Table 3-1). We ascribed these substituent effects to the electron-donating properties of the ethyls. Alkylation of the carbonyl carbons decreased the polarity of the C=O bond. The polarization of the ethyls extended the separation between the centers of the positive and negative charges of the molecules, and hence increased their dipole moments (for *trans*-HHE and *cis*-EHE).

To examine the solvent effect on the dipole moments, we modified the *ab initio* calculations of the eight amide structures to account for condensed media (Figure 3-1). The polarization effects of the solvents were taken into account by using the Self-Consistent Isodensity Polarizable Continuum Model (SCI-PCM).(Foresman, Keith et al. 1996) Each amide solute, represented by a charge distribution, was embedded in a cavity and was surrounded by the solvent, which was a continuous infinite polarizable dielectric. The cavity was defined based on an isosurface of the total electron density.(Miertus, Scrocco et al. 1981; Foresman, Keith et al. 1996)

In order to examine the polarization effects of the solvent media, molecules were relaxed in the presence of the solvent as implemented by the SCI-PCM and the dipole moments were calculated again. The SCI-PCM model provides a plausible explanation for the differences between the dipole moments in vacuum, $\mu_2^{(0)}$, and in condensed media,

μ_2*.(Miertus, Scrocco et al. 1981; Foresman, Keith et al. 1996) An increase in the solvent polarity enhanced the solvent effect as indicated by the μ_2*/$\mu_2^{(0)}$ ratios, which ranged from 1.1 to 1.4 and was the most pronounced for *cis*-HHE (Table 3-1).

The molecular charge distribution induces a reaction potential in the condensed solvent media, which acts back on the molecular charge distribution changing the molecular dipole moments.(Miertus, Scrocco et al. 1981; Foresman, Keith et al. 1996) The effect of the dielectric can be viewed in terms of image charges. The molecular charges induce image charges of the opposite signs in the dielectric. These image charges further polarize the molecular charges, resulting in increased amide dipole moments. An increase in the media polarity and polarizability enhances these image-charge effects, explaining the trends in the solvent effect (Table 3-1).

Experimental dipole moments for amides in nonpolar media. We used the Hedestrand approach for extrapolating the molar polarizations to infinite dilution from concentration-dependent dielectric and density measurements:(Hedestrand 1929; Breitung, Vaughan et al. 2000; Hu, Xia et al. 2009)

$$P_2^{(0)} = \frac{3aM_1}{\rho_1(\varepsilon_1+2)^2} + \frac{(\varepsilon_1-1)}{\rho_1(\varepsilon_1+2)}\left(M_2 - \frac{bM_1}{\rho_1}\right) \qquad (7)$$

where M_i, ρ_i and ε_i are molecular weights, densities and static dielectric constants. The subscript "1" designates the quantities for the major component of the binary mixture –

the solvent, and "2" – the minor component – the solute, i.e., the amide. The superscript "(0)" designates quantity extrapolated to infinite dilution, i.e., to zero concentration.

While the empirical parameters *a* and *b* are extracted from linear fits of the dependence of measured quantities on the moles fraction of the analyte, χ_2 (equation 8a, 8b), they represent the first derivatives of the dielectric constant and of the density, respectively (equation 8c, 8d), of the binary solutions at infinite dilutions (Figure 3-2):

$$\varepsilon = \varepsilon_1 + a\chi_2 \tag{8a}$$

$$\rho = \rho_1 + b\chi_2 \tag{8b}$$

$$a = \left(\frac{\partial \varepsilon}{\partial \chi_2}\right)_{\chi_2=0} \tag{8c}$$

$$b = \left(\frac{\partial \rho}{\partial \chi_2}\right)_{\chi_2=0} \tag{8d}$$

where the quantities without subscript are for the binary solutions. The coefficients *a* and *b* differ from the original Hedestrand coefficients α and β, which were for linear fits normalized to unity intercepts, i.e., $a = \varepsilon_1\alpha$ and $b = \rho_1\beta$.(Hedestrand 1929) Nevertheless, a facile rearrangement of the original Hedesrtrand expression yields equation 7, which accommodates the use of *a* and *b* instead of α and β.

Ideally, solvents for such studies should be non-polar, non-hygroscopic, non-volatile and non-polarizable. In addition, solvents with propensities for hydrogen bonding, complexation and other relatively strong interactions with the solute should be avoided.

Therefore, saturated hydrocarbons with high boiling points, and some of their perhaloginated derivatives, present an excellent choice for simulating gas-phase conditions in condensed media.

Our initial studies, employing *n*-hexadecane ($C_{16}H_{34}$) and tetrachloromethane (CCl_4), revealed an important practical issue with the use of such non-polar solvents. A principal challenge with hydrocarbon solutions proved to be the limited solubility of some of the investigated amides.

For example, from dielectric and density measurements of amide solutions in $C_{16}H_{34}$, the determined dipole moments of HEE and EHE were 3.88±0.15 D and 3.40±0.13 D, respectively, which were in an excellent agreement with the calculated values for vacuum, $\mu_2^{(0)}$, in the absence of solvent effect (Table 3-1). Conversely, HHH and EHH did not manifest sufficient solubility in $C_{16}H_{34}$ to attain high enough concentrations necessary for measurements with acceptable signal-to-noise ratios. Concurrently, HHE and EEE had acceptable solubility in $C_{16}H_{34}$. The experimentally obtained dipoles for these two amides in $C_{16}H_{34}$, however, were 1.86±0.14 D and 4.59±0.52 D for HHE and EEE, respectively. We ascribed this discrepancy between the experimental dipoles and the corresponding theoretical $\mu_2^{(0)}$ values to the pronounced propensity for aggregation of the amides in non-polar media. Depending on the size of the aggregates and on the alignment of the amide dipoles in these aggregates, the apparent dipole values, extracted from experimental data, would exceed or be smaller than $\mu_2^{(0)}$.

To address these solubility issues, we explored the use of alternative nonpolar solvents. Due to the symmetry of its molecule, 1,4-dioxane (DO) is one of the least polar ethers

with its static and dynamic dielectric constants close in value, i.e., $\varepsilon_1 \approx n_1^2$. In fact, the dielectric constants of DO resembling those of *n*-hexadecane, i.e., for DO, $\varepsilon_1 = 2.28$ and $n_1^2 = 2.02$; and for *n*-$C_{16}H_{34}$, $\varepsilon_1 = 2.23$ and $n_1^2 = 2.05$.

From concentration-dependent density and dielectric measurements of amide-DO solutions (Figure 3-2), we obtained $P_2^{(0)}$ for the six amides (equation 7, 8). Approximating $P_{2\mu}^{(0)}$ to $P_2^{(0)}$ allowed us to use equation 1 to calculate the magnitudes of their dipole moments, μ_2** (Table 3-2). (While "*" indicates the theoretically calculated dipoles for solvent media, "**" designates amide dipoles for different solvents obtained from experimental measurements.)

We further corrected the experimental dipole moments, μ_2**, by the use of a somewhat improved approximation for the orientation polarizations, $P_{2\mu}^{(0)} \approx P_2^{(0)} - P_{2e}^{(0)}$ (equation 2). We estimated the electronic polarization using the dynamic dielectric properties of each amide (equation 6b).(Breitung, Vaughan et al. 2000) The molar electronic polarizations of the six amides, $P_{2e}^{(0)}$, were about 8 to 23 times smaller than the total molar polarizations, $P_2^{(0)}$ (Table 2). Therefore, the values of the corrected experimentally obtained dipole moments, μ_{2C}**, obtained using $P_{2\mu}^{(0)} \approx P_2^{(0)} - P_{2e}^{(0)}$, did not differ significantly from the corresponding dipoles, μ_2**, obtained using $P_{2\mu}^{(0)} \approx P_2^{(0)}$.

To compare the experimentally and theoretically obtained amide dipoles, we employed Student's *t*-tests. The obtained *p*-values manifested a lack of trends of identifying similarities between the measured dipoles for DO and the theoretical dipoles for vacuum

or for DO (Table 3-2). Comparison between the experimentally obtained dipoles for DO, μ_{2C}** (Table 3-2), and the theoretical dipoles for vacuum, $\mu_2^{(0)}$ (Table 3-1), yielded $p > 0.01$ for all amides except EHE, which prevented us from rejecting the null hypothesis, H_0, (with 99% confidence) about the identity between these experimental and theoretical values (Table 3-2). Concurrently, comparisons between the measured, μ_{2C}**, and the theoretically calculated, μ_2*, dipoles for DO of the N-monoalkylated amides, HHE and EHE, yielded $p > 0.01$. These results appeared encouraging, indicating that for these two amides, the DO solvent effect, as implemented by the PCM, correlated well with the experimental findings. We believe, however, that the interpretation of the statistical results did not provide straightforward answers, and hence required caution in drawing the conclusions. While $p > 0.01$ did not provide the basis for rejecting H_0, $p < 0.1$ was not necessarily a strong evidence for accepting H_0. Therefore, it was essential to examine closely the experimental and theoretical setups.

Experimentally, the limited solubility in non-polar solvents justified the need for carrying the analysis with DO. The improved solubility of the six aliphatic amides in this cyclic diether, suggested that DO provides solvation interactions that solubilize the polar analytes. Thus, DO is not truly non-interacting solvent, and it would be unacceptable reason to expect identity between the dipole moments measured for DO, μ_2** and/or μ_{2C}**, and the "true" amide dipoles, $\mu_2^{(0)}$, calculated for vacuum. Therefore, the similarities between the theoretical dipoles in vacuum, $\mu_2^{(0)}$, and the experimental dipoles in DO, μ_{2C}**, were most probably a serendipitous balance between enhancing and reducing solvent effects.

Theoretically, PCM model provides an excellent means for implementation of the Onsager formalism on solvation of molecules with arbitrary shapes. As a continuum model, however, PCM suffers from some deficiencies. The size of the DO solvent molecules is comparable with the sizes of the analyzed amides. Therefore, the arrangement of the DO molecules around the solvation cavity may introduce local effects on the reaction field, for which PCM does not account. DO, indeed, is a nonpolar ether. Its molecule, however, comprises two oxygens that polarize the six-member saturated ring, i.e., the DO molecule contains two oppositely oriented permanent dipoles. The exact effects of these dipoles on the reaction field in the solvation cavity cannot be predicted without vigorous analysis of the arrangement of the DO molecules around the amides.

Furthermore, the PCM model does not account for strong specific interactions, such as intermolecular hydrogen bonding. While DO is a non-interacting liquid, i.e., the DO molecules do not form hydrogen bonds with one another, DO is a hydrogen-bond acceptor. Four of the amides we studied have amide N-H hydrogens that can readily bond with the free electron pairs on the DO oxygens. Such hydrogen bonding between the DO solvent and the solvated amides causes shifts in the electron density, and hence chances in the solute polarization.

Dipole moments of amides in moderately polar media. Due to solubility issues, nonpolar media limits the type of polar molecules that are possible to examine. While nonpolar ethers, such as DO, may address the solubility issues, they introduce complexity of local solvation interactions that computationally are not readily implementable.

Therefore, we extended our studies to two chlorinated solvents, chloroform ($CHCl_3$) and 1,1,2,2-tetrachloroethane (TCE), which are known for their excellent dissolving properties for organic substances without being hydrogen-bond donors or acceptors.

Although chloroalkane solvents cannot hydrogen bond with solutes, the formation of halogen bonds (X-bonds) with hydrogen-bonded carbonyl oxygens presents a concern.(Voth, Khuu et al. 2009) In order for such X-bonding to occur, the solute itself has to form intermolecular hydrogen bonds (which is possible for the four amides that contain nitrogen-bonded hydrogens, i.e., N-H bonds).(Voth, Khuu et al. 2009) Avoiding amide aggregation via dilutions ensures avoiding such hydrogen bonding, and hence avoiding X-bonding with the solvent.

The six amides exhibited excellent solubility in $CHCl_3$, and, with the exception of HHE and EHE, the concentration dependence of the dielectric constants was linear for $\chi_2 < 0.01$ (Figure 3-3a). For the non-linear trends, we extrapolated the derivatives to zero-concentrations by fitting the data to a power function, i.e., $\varepsilon = \varepsilon_1 + a\,\chi_2 + c\,\chi_2^{\,d}$, and hence $\left(\partial\varepsilon/\partial\chi_2\right)_{\chi_2=0} = a$ for $d \neq 1$. We, however, limited our analysis to sufficiently diluted solutions (i.e., $\chi_2 < 10^3$) and avoided concentration ranges where the apparent non-linearity suggested for intermolecular interactions that caused binary solutions to deviate from ideality (Figure 3-3b).

Using the Debye-Hedestrand relations (equations 1, 2, 7, and 8), we obtained the values of the dipole moments of the six amides for $CHCl_3$, which were notably larger than the corresponding dipoles for nonpolar media obtained theoretically, $\mu_2^{(0)}$, and

experimentally, μ_2** for DO (Table 3-1 and 2). Introducing the correction for the molar electronic polarization of the amides resulted in a reduction of the dipole values by less than 5% of the uncorrected dipoles (Table 3-2). Because the values of $P_2^{(0)}$ for chloroform were larger than the corresponding $P_2^{(0)}$ values for 1,4-dioxane, the corrections for $P_{2e}^{(0)}$ were less significant for this more polar media.

The solvent effect on the amide dipoles for TCE media was even more pronounced than the solvent effect we observed for $CHCl_3$. (TCE is a more polar solvent than $CHCl_3$.) With the exception of HHE, the amides were quite soluble in TCE. The dielectric constants of the amide TCE solutions exhibited linear concentration dependence for $\chi_2 < 10^3$ (Figure 3-3c). The extrapolated $P_2^{(0)}$ values were notably larger than the $P_2^{(0)}$ values we obtained for DO and $CHCl_3$, i.e., five- to ten-fold larger (Table 3-2). Therefore, the correction for the molar electronic polarization, $P_{2e}^{(0)}$, had even lesser effect on the experimental dipole values for TCE than for DO or $CHCl_3$, i.e., for TCE, μ_{2C}** $\approx \mu_2$** (Table 3-2).

For all six amides, the *t*-tests on the identity between the experimental dipoles for chloroform, μ_{2C}**, and the theoretical dipoles for vacuum, $\mu_2^{(0)}$, yielded *p*-values smaller than 0.01, allowing for an indiscriminate rejection of $H_0 : \left(\mu_{2C}** \equiv \mu_2^{(0)}\right)$ with 99% confidence for the $CHCl_3$ measurements (Table 3-2). For TCE, identical *t*-tests yielded $p << 0.01$ for the identity between μ_{2C}** and $\mu_2^{(0)}$, which was apparent from the excessively large TCE solvent effect (Table 3-1 and 2). Indeed, the corrections for molar electronic

polarization (equation 6b) did not account for the discrepancies between the experimental dipoles, μ_2**, for the chlorinated solvents and the corresponding theoretical values for vacuum, $\mu_2^{(0)}$ (Table 3-1 and 2).

For $CHCl_3$, applying the same statistics for comparing the experimental amide dipoles with the corresponding theoretical dipoles yielded $p > 0.01$ for five of the amides, and $p > 0.10$ for μ_2** or μ_{2C}** of four of these five amides. For EHH, $p < 0.01$. Nevertheless, for EHH, the theoretically calculated value of μ_2* (for $CHCl_3$) underestimated its experimentally determined dipole moment, μ_{2C}**, with only about 10% (Table 3-1 and 2). These results allowed us to conclude that, within the inherent uncertainty of the used methods, the experimentally obtained amide dipoles for $CHCl_3$, μ_2** or μ_{2C}**, are identical with the theoretically calculated dipoles for the same solvent, μ_2*, and different from the theoretically obtained dipoles for vacuum, $\mu_2^{(0)}$.

The agreement between theory and experiment for $CHCl_3$, suggested that the reaction field exerted in the solute cavity was the underlying reason for the observed solvent effect on the amide dipoles in chloroform. Furthermore, the results demonstrated that implementation of the solvating media as a continuous dielectric into *ab initio* calculations allowed for quantification of the solvent effect of $CHCl_3$ on the amide dipoles.

The PCM model, however, did not account for the pronouncedly large solvent effects on the amide dipoles experimentally obtained from TCE solutions. We carried SCI-PCM *ab initio* calculations on the six amides, solvated by chlorinated solvents with polarity

(i.e., dichloromethane, CH_2Cl_2) and polarizability (i.e., tetrachloroethene, C_2Cl_4) similar to the polarity and polarizability of TCE (Table 3-3). The theoretically calculated solvent effects, $\mu_2^*/\mu_2^{(0)}$, for CH_2Cl_2 and C_2Cl_4 ranged between about 10% and 30% (Table 3-1). The experimentally measured solvent effect, $\mu_2^{**}/\mu_2^{(0)}$, for TCE, however, ranged between 100% and 250%. This dramatic discrepancy suggested either (1) for experimental shortcomings in use of TCE for solvent media (such as analyte aggregation); (2) for limitations in the Debye-Hedestrand formalism for analyzing TCE binary mixtures; or (2) for limitations in the theoretical treatment of TCE as a dielectric continuum as implemented with the PCM model.

Aggregation. Discrepancies in dipole moment measurements, along with non-linear concentration dependence of the dielectric constants of binary solutions, are often ascribed to aggregation. We employed ^{1}H-NMR spectroscopy to examine the aggregation propensity of the six amides in chloroform and in TCE.(Jones and Vullev 2001) (The working concentration range for the dielectric measurements is within the dynamic range of NMR spectroscopy.(Jones and Vullev 2001))

For HHH, HEH, EHH and EHE in $CHCl_3$, the concentration increase from 4×10^{-4} to 8×10^{-3} caused 0.15 to 0.3 ppm downfield shifts in the signals from their amide protons (Figure 3-4). Ascribing the deshielding (which causes such downfield shifts) to intermolecular hydrogen bonding and to an increase in the dipole-induced polarization of the N-H bonds, indicated that aggregation, and specifically, hydrogen-bonding-assisted

aggregation, was plausibly the cause for the observed changes in the chemical shifts of the amide protons.

Although the concentration dependence of the dielectric properties of the HHH and EHH solutions manifested linearity within a relatively broad concentration range, i.e., $\sim 10^{-4} < \chi_2 < \sim 10^{-2}$ (Figure 3-3a), the concentration-induced changes of the N-H chemical shifts (Figure 3-5a, b) were evidence for amide aggregation. These findings were in agreement with the reported propensity of HHH for intermolecular hydrogen bonding.(Sunners, Piette et al. 1960; Saito, Tanaka et al. 1971; Vaara, Kaski et al. 1997) Conversely, the observed concentration-dependence of the amide chemical shifts of HHE and EHE (Figure 3-4c, d), reflected the measured dielectric nonlinearity for $\chi_2 > \sim 2 \times 10^{-3}$ (Figure 3-3a).

In addition, the N-H chemical shifts of the N-monoalkylated amides, HHE and EHE, revealed an important trend regarding the conformer distribution of these two conjugates. The broad NMR peak of the amide proton of HHE had a shoulder at its downfield side (Figure 3-4c), consistent with the presence of at least two conformers, i.e., *cis* and *trans* (Scheme 3-1). Conversely, the amide signal for EHE was a singlet for the investigated concentration range, indicating the detectable presence of only one conformer (Figure 3-4d). This observation was consistent with the calculated energies of the conformers of these two amides in chloroform (Table 3-1, footnotes d and g). While the energy difference between the *cis* and *trans* conformers of HHE was 0.03 eV (comparable with k_BT for room temperature), the *cis-trans* energy difference for EHE was 0.1 eV. Therefore, the HHE samples contained two principle conformers "locked" by the partial

π-conjugation of the C-N bond, and the EHE samples were composed predominantly of the *trans*-amide (Scheme 3-1): i.e., assuming the Boltzmann distribution for room temperature, more than 98% of EHE existed in its *trans* form.

The concentration-induced changes in the chemical shifts of the methylene, $-CH_2-$, methyl, $-CH_3$, and carbonyl, -C(=O)-H, protons were not as extensive as the changes in the signals from the amide protons (Figure 3-5). The chemical shifts of the carbonyl protons (between 8.0 and 8.3 ppm) remained independent of the amide concentrations (Figure 3-5a, c, e). Conversely, the protons of the carbonyl-bound methylenes (in the region between 2 and 2.5 ppm), along with the corresponding methyl protons (in the 1 – 1.3 ppm region), exhibited slight concentration-induced upfield shifts that did not exceed about 0.02 ppm (Figure 3-5b, d, f).

The alterations in the shapes of some of the peaks, however, were a conspicuous indication of concentration-induced changes in the molecular microenvironment. For EHH, for example, the concentration increase caused a quadruplet-to-pentaplet conversion of the $-CH_2-$ proton signal and a triplet-to-quadruplet transformation of the $-CH_3$ proton signal (Figure 3-5b). The changes in peak appearance were not limited to the signals from protons of the carbonyl-bound ethyls. For EEE, for example, upon the concentration increase, the proton signals from the nitrogen-bound methylenes (in the 3 – 3.5 ppm region), along with the other signals of the other alkyl protons, broadened and manifested an increase in multiplicity (Figure 3-5e). The significance of the latter observation is that even though EEE cannot undergo intermolecular hydrogen bonding (i.e., EEE is not a hydrogen-bond donor), it still aggregates at elevated concentrations.

Therefore, in addition to hydrogen bonding, electrostatic attraction is also a driving force for amide aggregation, even in chlorinated solvents with moderate polarity.

The carbonyl proton of HHE exhibited a strong singlet, at 8.16 ppm, and a weak upfield doublet, at 8.09 ppm (Figure 3-5c, g), which provided additional information about the distribution of the *cis* and *trans* conformers of this amide. As predominantly governed by the Fermi contact mechanism, the coupling of the carbonyl proton is significantly stronger with the N-H proton located at the *trans* position than with the N-H proton located at the *cis* position.(Vaara, Kaski et al. 1997) For HHH, for example, the reported through-three-bond coupling constant for the *trans* and *cis* protons are, respectively, $^{3}J_{trans\text{-HH}} \approx 13$ Hz and $^{3}J_{cis\text{-HH}} \approx 2$ Hz.(Piette, Ray et al. 1958; Sunners, Piette et al. 1960; Vaara, Kaski et al. 1997)

For the carbonyl proton doublet of HHE (representing the minor component of the mixture), we determined $J = 12$ Hz (Figure 3-5g), which allowed us to plausibly ascribe it to the *trans* conformer. The signal from the carbonyl proton of the major component of the HHE mixture, however, appeared as a singlet with a half-height width of ~ 6 Hz. The peak broadening was the most plausible reason for masking the doublet that resulted from the coupling of the carbonyl proton with the *cis* N-H proton, for which the expected $^{3}J_{\text{HH}}$ would be in the order of 2 Hz.(Vaara, Kaski et al. 1997) Therefore, we assigned the major component to the *cis*-HHE conformer.

The estimated proton deshielding further supported the above NMR assignments for the HHE *cis* and *trans* conformers. The calculated atomic charges of the carbonyl and methylene protons of the *cis*-HHE were more positive than the charges of the same

protons of the *trans* conformer (Figure 3-5h). Therefore, the downfield shifted signals, representing the major component of HHE (Figure 3-5c, g), belonged to its *cis* conformer.

The areas under the carbonyl and methylene NMR proton peaks, assigned to the two HHE conformers, revealed that at room temperature in chloroform the *cis*/*trans* concentration ratio was: C_{cis}/C_{trans} = 3.7 (Figure 3-6g). Employing the Boltzmann distribution, we estimated the energy difference between the two conformers, i.e., $\Delta\mathscr{E} = \mathscr{E}_{trans} - \mathscr{E}_{cis} = 0.033$ eV.

In this analysis, however, we did not take under consideration the energy fluctuations induced by conformational changes in the ethyl groups of the *cis*- and *trans*-HHE structures. The NMR measurements represent the ensemble average from all thermally accessible ethyl conformations that are separated by relatively small energy barriers allowing fast exchange between them within the millisecond duration of signal recording. Conversely, the theoretical values reflected solely the energy differences between the relaxed *cis*- and *trans*-HHE structures (Figure 3-1).

Nevertheless, these findings regarding the *cis-trans* distributions of HHE and EHE, which were independently delivered by our theoretical and experimental analyses, have an important implication for viewing the factors that govern the conformations of amides, and especially, the conformations of peptide bonds in proteins and polypeptides. While the intramolecular steric hindrance may provide intuitive guidelines about the relative stability of *cis* versus *trans* amides, the steric hindrance is not the sole driving force in determining the preference of one conformer over another. In the preferred, *trans*,

conformer of EHE, the bulkiest groups, i.e., the two ethyls, are on the opposite sides of the C-N bond (Scheme 3-1; Table 3-1, footnote g), which is, indeed, intuitively expected. For HHE, however, the preferred conformer is *cis*, in which the two large substituents, i.e., the ethyl and the carbonyl oxygen, are on the same side of the C-N bond (Scheme 3-1). Indeed, the carbonyl oxygen is not as large as an ethyl, and hence the steric hindrance in *cis*-HHE is not as pronounced as it is in *cis*-EHE. Nevertheless, for a range of torsion angles, the ethyl and the oxygen of *cis*-HHE have a considerable van der Waals overlap. Therefore, other factors, such as the amide electronic structure, govern the preference of the seemingly less favorable *cis*-HHE over the *trans*-HHE.

NMR studies of the amides, employing deuterated 1,1,2,2-tetrachloroethane (TCE-d_2), revealed trends similar to the trends we observed for $CDCl_3$ (Figure 3-6). For $\chi_2 > 0.001$, which was above the working concentration range for the dielectric studies (Figure 3-3c, d), we observed 0.1 – 0.13 ppm downfield shifts of the signals from the amide, N-H, protons (Figure 3-6a, b, c). Peak broadening accompanied these shifts. The broadening of the amide peaks revealed a conspicuous distinction between the NMR spectra for $CDCl_3$ and TCE-d_2 solvents. For HHH, for example, the spectra recorded for $CDCl_3$ samples showed a distinct triplet or a multiplet for the amide protons in the 5 – 6 ppm region (Figure 3-4a). Conversely, the spectra for TCE-d_2 showed solely a broad singlet for the same amide protons (Figure 3-6a), an indication for a relatively fast exchange mediated in this solvent.

Overall, the concentration-dependent NMR spectra suggested for amide aggregation at χ_2 exceeding about 0.001. HEE was the only one of the six amides for which we did not

observe evidence for aggregation in either of the two chlorinated solvents, i.e., we did not detect concentration-induced changes in NMR shifts of its protons. Thus, the NMR findings validated our choice for conducting the dielectric linear analysis at $\chi_2 < 0.001$ (Figure 3-3b and c).

Solvent properties. The solvent effects on the ground-state amide electric dipoles reflect the enhancements from the reaction fields in the solvated cavities. As expected, an increase in the static, ε_1, and dynamic, n_1^2, dielectric constant of the solvent media (Table 3-3), caused an increase in the magnitude of the amide dipoles (Table 3-1, 2).

The excellent agreement between the experimental and theoretical dipole values for $CHCl_3$, indeed, reflects the plausibility of using continuous-medium models, with the corresponding n_1^2 and ε_1, for *ab initio* analysis of electrostatic properties of polar moieties. The solvent bulk properties, however, did not intuitively reflect the experimentally observed pronouncedly large dipole enhancement induced by TCE. While doubling ε_1 (from DO to $CHCl_3$) increased the amide dipoles with about 20 – 25 %, an additional doubling of ε_1 (from $CHCl_3$ to TCE) caused a dipole increase that amounted to three-to-four fold (Table 3-2 and 4). Similarly, the TCE-induced dipole enhancement did not follow the linear increments with the increase in n_1^2 between the three solvents (Table 3-3).

Limitations in the Debye-Hedestrand procedures for extracting dipole moments from experimentally obtained bulk dielectric data may prove to be a plausible reason for the "abnormally" large amide dipoles measured for TCE media. A principal constrain of this

formalism is its sole applicability to diluted polar analytes in nonpolar solvents. Limited solubility of many polar solutes in nonpolar solvents, however, presents important experimental limitations. Hence, how polar the nonpolar solvents can be?

A principal reason for the validity of the Debye theory solely for nonpolar solvents is its limitation imposed by the Clausius-Mossetti expression with static dielectric constants, *CM*, which cannot have values larger than unity (equation 4a).(Hill, Vaughan et al. 1969) According to the Debye theory, therefore, a nonpolar solvent should have polarity and polarizability that will yield $CM < 1$:(Hill, Vaughan et al. 1969)

$$CM^* = \frac{\rho_1 N_A}{M_1}\left(\frac{4\pi}{3}\alpha_1 + \frac{\mu_1^2}{9\varepsilon_0 k_B T}\right) < 1 \qquad (9a)$$

where,

$$CM^* \approx CM = \frac{\varepsilon - 1}{\varepsilon + 2} \qquad (9b)$$

According to this expression, the Curie temperature at which $CM^* = CM = 1$ (i.e., $\varepsilon = \infty$), is unrealistically high for polar materials, implying that they are ferroelectric at room temperature. Furthermore, for such polar materials, the equality between *CM* and *CM** as expected from their known dipoles and polarizabilities, $CM^* \approx CM$ (equation 9b), fails making the Debye formalism inapplicable for them. For DO, $CHCl_3$ and TCE at room temperature, $CM^* < 1$, and within about 20%, $CM \approx CM^*$ (Table 3-3). Conversely, CH_2Cl_2 and DMSO exhibited $CM^* > 1$, suggesting for their inapplicability for studies that require Debye-Hedestrand analysis. (DMSO, furthermore, is a hydrogen-bond

acceptor.) This criterion readily rejected the use of DMSO and CH_2Cl_2 in such line of experimental studies. TCE, however, appeared to be a borderline choice. Although for neat TCE, *CM** does not exceed unity, its values for some of the conformers were larger than ~ 0.8 (Table 3-3). Therefore, an inclusion of the contribution of a polar solute (with $\mu_2 > 4$ D) in equation 9a, causes *CM** to exceed unity for $\chi_2 > 0.05$, which is more than an order of magnitude larger than the concentration range we used in this study (Figure 3-3c, d).

The polarities, γ_1, of $CHCl_3$ and TCE are quite similar (Table 3-3). Furthermore, the magnitudes of the dielectric constants of the six amides exceed several fold the dielectric constants of any of the used solvents. Therefore, the bulk dielectric properties of the solvents do not appear to be a truly discerning criterion between the chloroform-induced and TCE-induced enhancements observed for the amide dipoles.

In addition to the *CM* criterion (equation 9), considering the molecular electrostatic (e.g., μ_1), electrodynamic (e.g., α_1), and structural properties of the solvents offers a means for elucidating the "abnormal" TCE effect on the measured amide dipoles. Equation 1 was derived from the Debye equation on the assumption that the solvent dipole term, $\mu_1^2/3\varepsilon_0 k_B T$, can be neglected (equation 4a): i.e., $(\mu_1^{(0)})^2 << (\mu_2^{(0)})^2$ or $(\mu_1^{(0)} / \mu_2^{(0)})^2 << 1$. For the six aliphatic amides, $(\mu_2^{(0)})^2$ ranged from about 12 to 16 D^2 (Table 3-1). Concurrently, $(\mu_1^{(0)})^2$ of $CHCl_3$ was about 1.1 D^2, and $(\mu_1^{(0)})^2$ of TCE ranged between about 0 and 2.5 D^2, depending on the molecular conformation (Table 3-1). Therefore, the square dipole ratios, $(\mu_1^{(0)} / \mu_2^{(0)})^2$, for the amides ranged between 0.07 and 0.09 for chloroform, and between 0 and 0.21 for TCE. (Herein, we did not discuss the

approximation of the Langevin function, $L(y) \approx y/3$ for $y^{-1} << 1$, leading to the Debye equation, because of the relatively small field strengths we used for the dielectric measurements, ensuring $\boldsymbol{\mu}\mathbf{E}^{(d)}/k_BT << 1$.(Hill, Vaughan et al. 1969))

It should be noted that due to conformational flexibility, DO and TCE media comprise mixtures of molecular conformers (Scheme 3-2).(Ramsay 1947; Mark and Sutton 1972) The calculated dipole moments of DO and TCE showed a pronounced dependence on their molecular conformations (Table 3-3). Overall, while the dipole of TCE was able to assume values close to 1.6 D, the dipoles of DO and $CHCl_3$ could not considerably exceed about 1.4 D. Therefore, TCE had the capability to generate slightly stronger reaction fields than either DO and $CHCl_3$. The polar conformers of DO and TCE, e.g., *boat* and *gauche* (Scheme 3-2), however, are not energetically the most favorable. Therefore, the permanent solvent dipoles were not able account by themselves for the pronounced TCE effect.

The polarizabilities of DO and TCE, on the other hand, had a marginal dependence on their molecular conformations (Table 3-3). Therefore, generating relatively large induced dipoles in the solvent molecules (needed for noticeable reaction fields in the solute cavities) did not require energetically unfavorable conformations. Furthermore, the wide distribution of the values of the elements of the $[\alpha_{ij}]$ tensor indicated a strong dependence of the solvent polarizabilities on their molecular orientation.

The polarizabilities of $CHCl_3$ and DO were quite comparable. The polarizability of TCE, conversely, exceeded the polarizabilities of $CHCl_3$ and DO (Table 3-3). These trends in the experimental, α_{1e}, and theoretical, α_{ii} and $\langle\alpha\rangle$, values of the polarizability of

the three solvents, provided a plausible explanation for the relatively large TCE effect on the amide dipoles.

What are the limitations of theory and experiment? For experimental estimation of dipole moments of polar moieties in liquid media, it is essential to select non-interacting nonpolar solvents. Conversely, for dissolving a solute even in a nonpolar solvent, that solvent has to be interacting in order to provide sufficient solvation stabilization, and prevent aggregation and/or phase separation. Strictly speaking then, all solvents are interacting to some extent. Therefore, for each particular study, the selected solvents ought to be interacting enough to provide sufficient solubility and prevent aggregation, and at the same time, non-interacting enough so that the media polarization around the solvated cavities does not perturb significantly the electronic properties of the analytes.

Assuming that chloroform is one of the most polar solvents applicable for the experimental estimation of the permanent dipoles of aliphatic amides (using the Debye-Hedestrand formalism), revealed the following potential requirement: (1) $CM < 1$ (equation 9); (2) $(\mu_1^{(0)} / \mu_2^{(0)})^2 < 0.1$; and (3) $\alpha_{1ii} < 10$ Å^3 for solvent molecular volume, v_1, larger than 50 or 100 Å^3. Even when these requirements were met, however, the Debye-Hedestrand analysis of the experimental data produced dipole values that encompassed the enhancement from the reaction field of the solvation cavity (Table 3-2).

Experiments do not provide means for measuring dipole moments directly. It is the Debye-Hedestrand formalism that allowed us to extract the values of the dipole moments from dielectric and density measurements (equation 1, 2, 7, 8). Like many theories and

formalisms developed in the beginning of the 20th century or earlier, the Debye theory approximates the "real systems" to idealized solutions, composed of spherical solute molecules, and nonpolar solvents that pack closely around the solute spheres. Due to its simplicity, however, the Debye theory has been widely used and preferred for relating experimentally obtained bulk dielectric characteristics of materials to the molecular electronic properties of the comprising molecules. Indeed, Debye-Hedestrand analysis of experimental data of relatively simple molecules has produced results in an excellent agreement with theoretical *ab initio* predictions.(Breitung, Vaughan et al. 2000; Tjahjono, Davis et al. 2007) Spherical approximation of the solvated cavities, have yielded theoretical results for complex molecules that agreed well with the experimental findings.(Cave, Burke et al. 2002) Such spherical approximations for molecules with heterogeneous distribution of electron density, however, result in significant discrepancies.(Bao, Ramu et al. 2010) Adopting non-spherical representations (with increased complexity) that are representative of the molecular shapes, has the ability to provide a means for agreement between theory and experiment.(Böttcher and Bordewijk 1978; Bao, Ramu et al. 2010)

For the analysis of the amide experimental dielectric data, we tested a model for solvated molecules with ellipsoidal shapes, which is an approximation for nonpolar media, based on the Onsager theory and the Böttcher formalism:(Myers and Birge 1981)

$$\left(\mu_2^{(0)}\right)^2 = \frac{M_2 \varepsilon_0 k_B T}{4\pi\rho_2 N_A} \frac{\left(\varepsilon_1 + \left(n_2^2 - \varepsilon_1\right)A_1\right)^2 \left(2\varepsilon_1 + 1\right)}{\left(1 + \left(n_2^2 - 1\right)A_1\right)^2 \left(\varepsilon_1 + \left(1 - \varepsilon_1\right)A_1\right)\varepsilon_1^2} \left(\left(\frac{\partial \varepsilon}{\partial \chi_2}\right)_{\chi_2 = 0} + \frac{3\varepsilon_1\left(\varepsilon_1 - n_2^2\right)}{2\varepsilon_1 + n_2^2} \right) \qquad (10)$$

where A_1 represents the distortion of the spherical shape of the solvated cavity: i.e., A_1 depends on the ratios between the ellipsoid semiaxes, r_1:r_2:r_3, where the permanent dipole is oriented along r_1.(Myers and Birge 1981)

For the five amides, soluble in TCE, this ellipsoid model yielded dipoles that ranged 3.9 and 5.5 D (Table 3-4), which were closer to the theoretical values of $\mu_2^{(0)}$ (Table 3-1) than the dipoles extracted using the Debye-Hedestrand analysis (Table 3-2). The same ellipsoid model applied to the $CHCl_3$ data, however, underestimated the amide dipoles (Table 3-4). A principal shortcoming of the Onsager theory, on which the ellipsoid model was based (equation 10), encompasses the assumption of incompressibility.(Onsager 1936) We estimated the volumes of the solvated cavity from density of the pure amides, ρ_2. Due to differences in solvation, the volumes of the solvated amide cavities should vary in different media. Furthermore, the molecules of $CHCl_3$ and TCE have different sizes and shapes (Scheme 3-2). Hence, most likely the solvated cavities differ in size and shape for the two solvents. Nevertheless, the results from the ellipsoid analysis revealed that deviating from the widely used spherical approximation for the solute shapes has the potential to encompass the experimentally observed solvent effects on the amide dipoles.

On the theoretical side of this study, PCM encompasses the arbitrary shapes of the solute molecules.(Tomasi, Mennucci et al. 2005) PCM, however, adopts a spherical approximation of the shapes of the solvent molecules needed for estimation of solvent accessibility.(Tomasi, Mennucci et al. 2005) Furthermore, should the solvent and solute molecules have comparable dimensions, the continuum dielectric approximation for the

cavity solvation may fail. Therefore, interpretation of the results from calculations for DO, C_2Cl_4 and DMSO media (Table 3-1), ought to be approached with caution.

Improved multiscale models, such as the QM/MM/continuum computational formalism, indeed, offer the potential to address some of the above issues and to provide insight about the structural and electronic properties of solvated cavities.(Sato 2003; Woods and Mulholland 2008) The relative complexity and the computational demand of such multiscale models, however, still prevents their wide implementation as a routine formalism for analysis of experimental findings. In fact, PCM is a multi- or bi-scale, QM/continuum model,(Tomasi, Mennucci et al. 2005) and its successful implementation and agreement with the experimental findings for amides solvated by chloroform is quite encouraging (Table 3-1 and 2).

Conclusions

How to quantify the solvent effects on the dipoles of polar species in condensed media? The simplest and well-tested models frequently impose approximations that are unfeasible for the systems to which they are applied. Conversely, by eliminating the approximations, an increase in the complexity of the models has the potential for bringing agreement between experiment and theory. The rational of such an agreement of theoretical models with experiment, however, does not guaranty that the models describe the underlying phenomena that govern the experimental results. For example, the use of ellipsoid approximation (equation 10) was arbitrary and it demonstrated trends of improvement in the analysis of the TCE experimental results. It does not claim, however,

that the aliphatic amides should fit into ellipsoid solvation cavities. Therefore, an experimental design that produces theoretically testable results with least approximations and assumptions provides the optimal venues toward understanding the investigated phenomena. In this study, the dielectric measurements and the *ab initio* calculations for the amides in chloroform-condensed media, demonstrated an optimal agreement between experiment and theory. Indeed, the many assumptions in the used analysis and formalism did not compromise this agreement.

Experimental

Materials. The six amides were purchased from TCI America. High purity chloroform, 1,4-dioxane and 1,1,2,2-tetrachloroethane were purchased from Fischer Scientific and Sigma-Aldrich. *Caution: 1,1,2,2-tetrachloroethane is a proven carcinogen (consult with its MSDS). Avoid skin contact and/or inhalation of its vapors.*

The binary amide solutions were freshly prepared prior to each measurement and kept at room temperature. We employed amide concentrations that ranged from 1 mM to 100 mM. Using the measured densities of the amide solutions, ρ (e.g., in g l^{-1}), we converted their molarity concentrations, C_2, into mole fraction concentrations, χ_2:

$$\chi_2 = \frac{C_2}{C_1 + C_2} \tag{11a}$$

$$C_1 = \frac{\rho - M_2 C_2}{M_1} \qquad (11b)$$

where M_1 and M_2 are the molecular weights of the solvent and the solute, respectively, and C_1 is the molarity concentration of the solvent.

Dielectric measurements. For the dielectric measurements, we used: (1) AH2700A ultra-precision capacitance bridge (Andeen-Hagerling, Inc., Cleveland, OH); and an ultra-high precision Wheatstone bridge, incorporated into HP 4284A LCR precision meter. Both instruments were connected to a three-terminal capacitance sample cell,(Sanabria, Miller et al. 2006; Hu, Xia et al. 2009) and the corrections for the connecting cables with up to of 4-m length were enabled.

The cell was filled with about 2 ml sample solution, the electrode separation was set at 400 μm, and the capacitance measurements were carried at frequencies ranging from 10^3 Hz to 10^6 Hz. (Due to the relatively large dissipation factor for the TCE samples, they were measured at frequencies that did not exceed 10^4 Hz) In addition to the amide binary solutions, for controls, we measured the capacitance of the neat solvents and of air (i.e., of an empty dry cell).(Hong, Bao et al. 2008) The dielectric constants of the binary amide solutions were calculated from the parallel capacitance values, corrected for dissipation.(Breitung, Vaughan et al. 2000)

The experimentally determined dielectric values presented in the tables and figures correspond to averages of at least five repeats, where the error bars represent plus/minus

one standard deviation. Except for EEE in $CHCl_3$, the multiple repeats were recorded by two or more operators at different times of year, and the samples were using solvents from different bottles. (The relatively small error bars for EEE in $CHCl_3$ reflected the fact that all repeats were carried on samples prepared by the same person from the same solvent source.)

Density measurements. The densities of the amide solutions were measured with a calibrated Mettler Toledo portable density meter (Densito 30PX). Each measurement (recorded collected at 21°C ± 0.5 °C) required about 1 ml freshly prepared sample solution. Immediately prior to each measurement, the densitometer was washed several times with the corresponding sample solution. After each measurement, the densitometer was washed with the corresponding neat solvent and nitrogen dried.

NMR spectroscopy. Proton nuclear magnetic resonance (^{1}H-NMR) spectra were recorded on a Varian Inova 400 MHz spectrometer (Varian Inova 400, CA, USA). Chemical shifts for protons are reported in parts per million and are referenced to residual protium in the deuterated NMR solvents, $CDCl_3$ and DCl_2C-$CDCl_2$ (Cambridge Isotope Laboratories, MA, USA) as an internal indicator ($CHCl_3$: δ = 7.27 ppm; and DCl_2C-$CHCl_2$: δ = 6.00 ppm).

To examine the aggregation propensity of the amides in chloroform and in 1,1,2,2-tetrachloroethane, ^{1}H-NMR spectroscopy of five concentrations of amides, 5 mM, 10 mM, 20 mM, 50 mM and 100 mM were recorded (for conversion to mole fractions, we

used equation 11). For the analysis, the NMR data were imported in Igor Pro, version 6 (WaveMetrics, Inc.) on MacOS and WindowsXP workstations.(Jones and Vullev 2002; Jones and Vullev 2002; Jones, Yan et al. 2007; Millare, Thomas et al. 2008; Vasquez, Vu et al. 2009; Chau, Millare et al. 2011)

Computational. We calculated the ground-state electric dipole moments and polarizabilities of the six amides and of the three solvents using *ab initio* DFT as implemented by Gaussian 03 and Gaussian 09.(Frisch, Trucks et al. 2004) Geometry optimizations were performed at the DFT level using the Restricted PBE(Perdew, Burke et al. 1996) exchange correlation functional and the 6-31G(d, p)(Petersson, Bennett et al. 1988; Petersson and Allaham 1991) basis set with a relaxation criterion of 4.5×10^{-4} eV $Å^{-1}$.

The polarization effects of $CHCl_3$ were taken into account by using Self-Consistent Isodensity Polarizable Continuum Model (SCI-PCM) as implemented by Gaussian.(Foresman, Keith et al. 1996) In this model, the solvent was a continuous unstructured infinite polarizable dielectric with a given dielectric constant. Each amide solute, represented by a charge distribution, was embedded in a cavity and was surrounded by the solvent. The cavity was defined based on an isosurface of the total electron density.(Miertus, Scrocco et al. 1981; Foresman, Keith et al. 1996)

The polarizabilities were calculated in Gaussian for optimized structures in vacuum using static frequencies (i.e., zero-frequency, static electric fields) as a derivative of

dipole moment at the DFT level using the Restricted PBE exchange correlation functional and 6-31G++(3df,3pd) basis set.

Acknowledgement: This research was supported by the National Science Foundation (CBET 0935995, DBI 0731660, and EEC 0649096), and by the Semiconductor Research Corporation Focus Center Research Program on Nano Materials (FENA).

Tables:

Table 3-1. Electric dipole moments and polarizabilities, α, of aliphatic amides determined theoretically for vacuum and for solvent media with different polarities.[a]

amide	$\mu_2^{(0)}$ / D	μ_2* / D					α_2 [b] / Å^3			
		DO ($\varepsilon_1 = 2.2$)	C_2Cl_4 ($\varepsilon_1 = 2.5$)	$CHCl_3$ ($\varepsilon_1 = 4.8$)	CH_2Cl_2 ($\varepsilon_1 = 8.9$)	DMSO ($\varepsilon_1 = 47$)	α_{xx}	α_{yy}	α_{zz}	$\langle\alpha_2\rangle$ [c]
HHH	3.74	4.19	4.20	4.49	4.63	4.80	3.08	4.40	5.65	4.38
HHE	3.72 [d]	4.41 [d]	4.43 [d]	4.70 [d]	4.80 [d]	4.96 [d]				8.14 [e]
cis	3.69	4.36	4.37	4.69	4.84	5.02	6.16	8.12	10.1	8.13
trans	3.98	4.46	4.47	4.93	4.75 [f]	4.87	6.11	7.76	10.7	8.18
HEE	3.78	4.20 [f]	4.21 [f]	4.49 [f]	4.63 [f]	4.79 [f]	9.80	12.3	13.6	11.9
EHH	3.51	3.97	3.99	4.32	4.47	4.67	6.33	8.23	9.60	8.05
EHE	3.36 [g]	3.79 [g]	3.85 [g]	4.24 [g]	4.31 [g]	4.49 [g]				12.0 [e]
trans	3.36	3.78	3.84	4.23	4.27 [f]	4.47 [f]	9.95	11.0	14.9	12.0
cis	3.76	4.24	4.25	4.58	4.74	4.91	9.13	11.6	15.2	12.0
EEE	3.67	4.16	4.17	4.52	4.69	4.89	11.7	16.0	19.2	15.6

[a] Theoretical values for the magnitudes of the dipole moments from DFT calculations: $\mu_2^{(0)}$ – vacuum or gas-phase calculations; and μ_2* – calculations that include the solvent effect using the Onsager formalism: DO = 1,4-dioxane; C_2Cl_4 = tetrachloroethene; $CHCl_3$ = chloroform; CH_2Cl_2 = dichloromethane; and DMSO = dimethylsulfoxide.

[b] The non-zero components of the diagonalized polarizability tensor, α_{ii}, were the eigenvalues of the $\boldsymbol{\alpha}_2 = [\alpha_{ij}]$ matrices obtained from DFT calculations of relaxed structures in vacuum.

[c] Average polarizability: $\langle \alpha_2 \rangle = (\alpha_{xx} + \alpha_{yy} + \alpha_{zz})/3$.

[d] Obtained from weighed sums of the calculated dipoles of the *cis* and *tans* conformers: $(\chi_{cis}\mu_{cis} + \chi_{trans}\mu_{trans})/(\chi_{cis} + \chi_{trans})$; $\chi_{trans}/\chi_{cis} = \exp(-\Delta\mathscr{E}/k_BT)$; $\Delta\mathscr{E} = \mathscr{E}_{trans} - \mathscr{E}_{cis}$; where the DFT-calculated total energies for the HHE conformers are: (1) $\mathscr{E}_{trans}$ = – 6754.39 eV and $\mathscr{E}_{cis}$ = – 6754.44 eV for vacuum; (2) $\mathscr{E}_{trans}$ = – 6754.50 eV and $\mathscr{E}_{cis}$ = – 6754.50 eV for DO; (3) $\mathscr{E}_{trans}$ = – 6754.51 eV and $\mathscr{E}_{cis}$ = – 6754.50 eV for C_2Cl_4; (4) $\mathscr{E}_{trans}$ = – 6754.50 eV and $\mathscr{E}_{cis}$ = – 6754.57 eV for $CHCl_3$; (5) $\mathscr{E}_{trans}$ = – 6754.60 eV and $\mathscr{E}_{cis}$ = – 6754.60 eV for CH_2Cl_2; and (6) $\mathscr{E}_{trans}$ = – 6754.63 eV and $\mathscr{E}_{cis}$ = – 6754.64 eV for DMSO.

[e] Obtained from weighed sums of the calculated average polarizabilities of the *cis* and *tans* conformers for vacuum, $(\chi_{cis}\langle\alpha_{cis}\rangle + \chi_{trans}\langle\alpha_{trans}\rangle)/(\chi_{cis} + \chi_{trans})$.

[f] These amide structures did not relax in the solvent media. Therefore, we took the relaxed amide structures for vacuum and placed it in the corresponding solvent in order to calculate the dipole moment (single-point calculation). Our comparisons between the results for other amides that were (1) relaxed in the selected solvent and (2) relaxed in vacuum and then subjected to single-point calculation in the same solvent, however, showed that the values of the dipole moment obtained by either of these two methods do not differ significantly.

[g] Obtained from weighed sums of the calculated dipoles of the *cis* and *tans* conformers, where the DFT-calculated total energies for the EHE conformers are: (1) $\mathscr{E}_{trans}$ = – 8891.27 eV and $\mathscr{E}_{cis}$ = – 8891.16 eV for vacuum; (2) $\mathscr{E}_{trans}$ = – 8891.36 eV and $\mathscr{E}_{cis}$ = – 8891.26 eV for DO; (3) $\mathscr{E}_{trans}$ = – 8891.36 eV and $\mathscr{E}_{cis}$ = – 8891.26 eV for C_2Cl_4; (4) $\mathscr{E}_{trans}$ = – 8891.42 eV and $\mathscr{E}_{cis}$ = – 8891.32 eV for $CHCl_3$; (5) $\mathscr{E}_{trans}$ = – 8891.45 eV and $\mathscr{E}_{cis}$ = – 8891.39 eV for CH_2Cl_2; and (6) $\mathscr{E}_{trans}$ = – 8891.48 eV and $\mathscr{E}_{cis}$ = – 8891.39 eV for DMSO.

Table 3-2. Electric dipole moments and molar polarizations of aliphatic amides determined experimentally from dielectric measurements for solvents media with different polarity.[a]

amide	$P_2^{(0)}$ [b] / cm^3 mol^{-1}			μ_2** / D			n_2 [c]	$P_{2e}^{(0)}$ [d]	μ_{2C}** / D		
	DO	$CHCl_3$	TCE	DO [P_0; p_{DO}] [e]	$CHCl_3$ [P_0; p_{CHCl_3}] [e]	TCE		[α_{2e}] [f]	DO [P_0; p_{DO}] [e]	$CHCl_3$ [P_0; p_{CHCl_3}] [e]	TCE
HHH	255	407	3550	3.51 ± 0.20 [0.10; 0.007]	4.43 ± 0.27 [0.002; 0.55]	13.1 ± 0.7	1.446	11 [4.2]	3.44 ± 0.20 [0.055; 0.005]	4.38 ± 0.27 [—; 0.28]	13.1 ± 0.7
HHE	382	465	— [g]	4.29 ± 0.29 [0.03; 0.47]	4.74 ± 0.57 [0.001; 0.84]	— [g]	1.430	20 [7.9]	4.18 ± 0.28 [0.047; 0.20]	4.64 ± 0.54 [0.003; 0.76]	— [g]
HEE	236	418	1580	3.37 ± 0.32 [0.08; 0.014]	4.50 ± 0.17 [—; 0.87]	8.76 ± 0.11	1.433	29 [12]	3.16 ± 0.30 [0.026; 0.006]	4.34 ± 0.16 [—; 0.036]	8.68 ± 0.11
EHH	271	488	1110	3.62 ± 0.15 [0.24; 0.018]	4.86 ± 0.16 [—; —]	7.34 ± 0.35	1.432[h]	18 [7.2]	3.50 ± 0.15 [0.90; 0.007]	4.77 ± 0.16 [—; —]	7.28 ± 0.35
EHE	442	501	1870	4.62 ± 0.31 [0.004; 0.013]	4.92 ± 0.70 [—; 0.029]	9.52 ± 0.73	1.434	29 [11]	4.47 ± 0.29 [0.005; 0.020]	4.78 ± 0.68 [—; 0.060]	9.45 ± 0.72
EEE	332	454	1810	4.01 ± 0.07 [0.002; 0.023]	4.69 ± 0.18 [—; 0.032]	9.35 ± 0.27	1.440	38 [15]	3.78 ± 0.07 [0.045; 0.001]	4.49 ± 0.17 [—; 0.32]	9.25 ± 0.27

[a] Experimental dipole moments, μ_2**, for the different solvents were calculated using equation 1, in which $P_{2\mu}^{(0)} \approx P_2^{(0)}$. For the corrected experimental dipole moments, μ_{2C}**, we used $P_{2\mu}^{(0)} \approx P_2^{(0)} - P_{2e}^{(0)}$.

[b] Molar polarizations were calculated from experimental data for binary solutions of the amides in different solvents using equations 7 and 8.

[c] Amide refractive indexes: measured for the pure compounds that are liquid at room temperature.

[d] Molar electronic polarization, in $cm^3\ mol^{-1}$, calculated from experimental n_2 values using equation 6b ($i = 2$).

[e] p-values from t-tests of the hypotheses, H_0, that the experimentally determined dipole moments are identical with the theoretically calculated dipoles for vacuum, $p_0 = p\left(\mu_2{}^{**} \equiv \mu_2^{(0)}\right)$, for DO, $p_{DO} = p\left(\mu_2{}^{**} \equiv \mu_2{}^{*}(DO)\right)$, and for $CHCl_3$, $p_{CHCl_3} = p\left(\mu_2{}^{**} \equiv \mu_2{}^{*}(CHCl_3)\right)$, where $p(\xi \equiv \zeta)$ is the probability for ξ and ζ to be identical. Dashes, —, in these columns indicate $p < 0.001$. Arbitrarily, for 99% confidence, we reject H_0 when $p < 0.01$.

[f] Molecular polarizability, in $Å^3$, calculated from experimental n_2 values using equation 6a ($i = 2$).

[g] Lack of sufficient solubility.

[h] EHH is solid at room temperature: we used a published value for its index of refraction, n_2, rather than measuring it as we did for the other five amides.

Table 3-3. Solvent dielectric bulk properties with the corresponding molecular electrostatic characteristics.

solvent	experimental						conformer	theoretical [a]					
	ε_1	n_1^2	γ_1 [b]	μ_1** / D	α_{1e} [c]/Å^3	*CM*/CM* [d]		$\mu_1^{(0)}$/D	$\boldsymbol{\alpha_1}$ [e] / Å^3				*CM** [g]
									α_{xx}	α_{yy}	α_{zz}	$\langle\alpha_1\rangle$ [f]	
DO	2.2	2.011	0.059	0.0 - 0.45 [h]	8.51	0.30 / 0.29	*chair*	0.00	8.21	8.75	10.1	9.01	0.30
							boat	1.44	8.11	8.47	10.1	8.89	0.81
C_2Cl_4	2.5	2.267	0.041	0.0 [i]	12.0	0.30 / 0.33	—	0.00	7.99	14.5	15.7	12.7	0.39
$CHCl_3$	4.8	2.083	0.27	1.0 - 1.2 [j]	8.43	0.64 / 0.56	—	1.04	6.72	9.71	9.71	8.71	0.59
TCE	8.4	2.227	0.33	1.3 - 1.7 [k]	12.1	0.86 / 0.71	*anti*	0.00	9.42	13.7	15.0	12.7	0.36
							gauche	1.58	11.4	12.1	14.3	12.6	0.84
CH_2Cl_2	8.9	2.028	0.38	1.5 - 1.7 [l]	6.46	1.1 / 0.72	—	1.61	5.23	5.86	8.48	6.53	1.2
DMSO	47	2.187	0.44	3.7 - 4.4 [m]	7.98	6.0 / 0.94	—	3.82	7.20	8.86	9.15	8.40	4.6

[a] From DFT *ab initio* calculations of relaxed structures in vacuum (Scheme 3-2).

[b] The polarities of the solvents, γ_1, were estimated from their static and dynamic dielectric constants: $\gamma_1 = n_1^{-2} - \varepsilon_1^{-1}$.

[c] The experimental solvent polarizabilities, α_{1e}, were calculated from the solvent indexes of refraction, n_1, using equation 6a ($i = 1$).

[d] From experimental measurements: *CM** from equation 9a for room temperature, using μ_1** and α_{1e}; and *CM* from equation 9b, using ε_1.

[e] The non-zero components of the diagonalized polarizability tensor, α_{ii}, were the eigenvalues of the $\boldsymbol{\alpha_1} = [\alpha_{ij}]$ matrices obtained from DFT calculations.

[f] Average polarizability: $\langle \alpha_1 \rangle = \left(\alpha_{xx} + \alpha_{yy} + \alpha_{zz}\right)/3$.

[g] From theoretical calculations: from equation 9a for room temperature, using $\mu_1^{(0)}$ and α_{zz}.

[h] Ref. (Williams 1930; Smyth and Walls 1931; Hunter and Partington 1933; Aminabhavi and Gopalakrishna 1995); [i] Ref. (Dotremont, Goethaert et al. 1993); [j] Ref. (Antony and Smyth 1964; Reinhart, Williams et al. 1970; Sato, Ohkubo et al. 1978); [k] Ref. (Thomas and Gwinn 1949; Kiyohara and Higasi 1969); [l] Ref. (Makosz 1994); [m] Ref. (Pekary 1974; Lumbroso, Cure et al. 1983; Aminabhavi and Gopalakrishna 1995).

Table 3-4. Electric dipole moments of aliphatic amides, determined experimentally from solutions in chlorinated solvents using ellipsoidal approximation of the solvation cavity (equation 10).

amide	r_1:r_2:r_3	$\mu_2^{(0)}$** / D	
		$CHCl_3$	TCE
HHH	3:1:1	1.5	5.5
HEE	2:3:1	2.1	4.5
EHH	4:2:1	2.2	3.9
EHE	2:2:1	3.0	5.4
EEE	2:3:1	2.4	5.3

Scheme 1. Amides with various extent of ethylation.

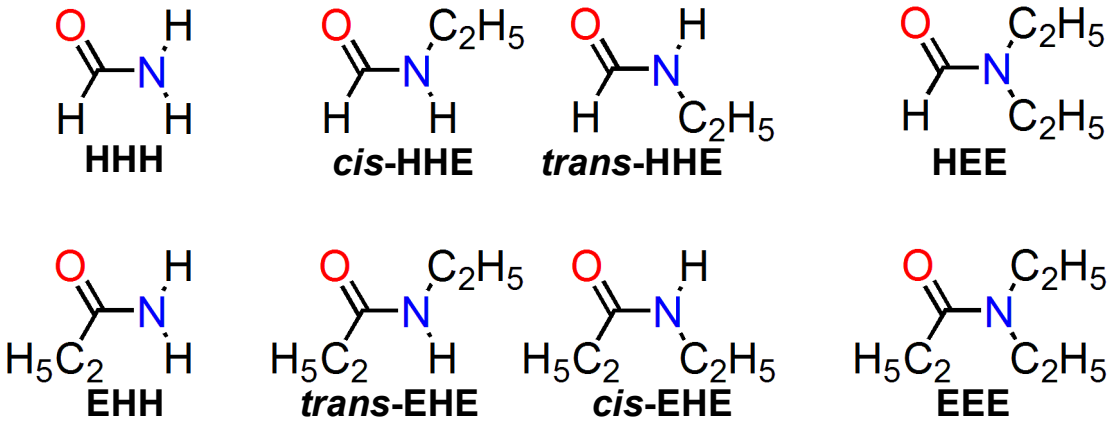

Scheme 2. Solvent molecular structures.

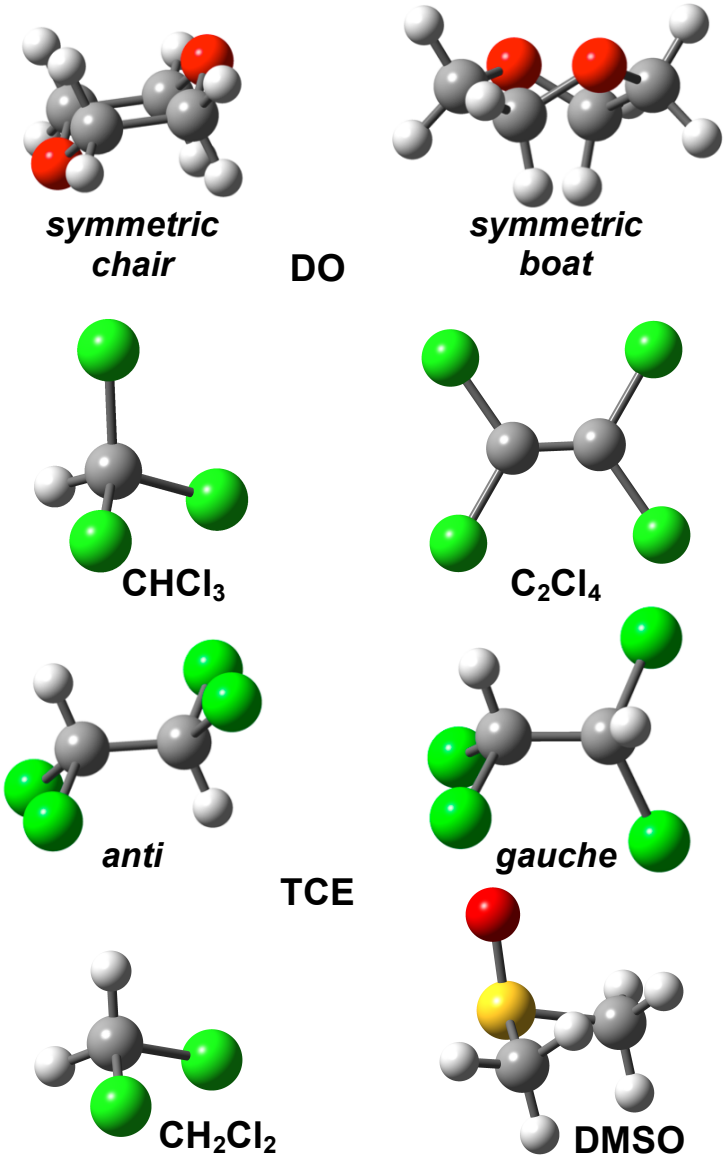

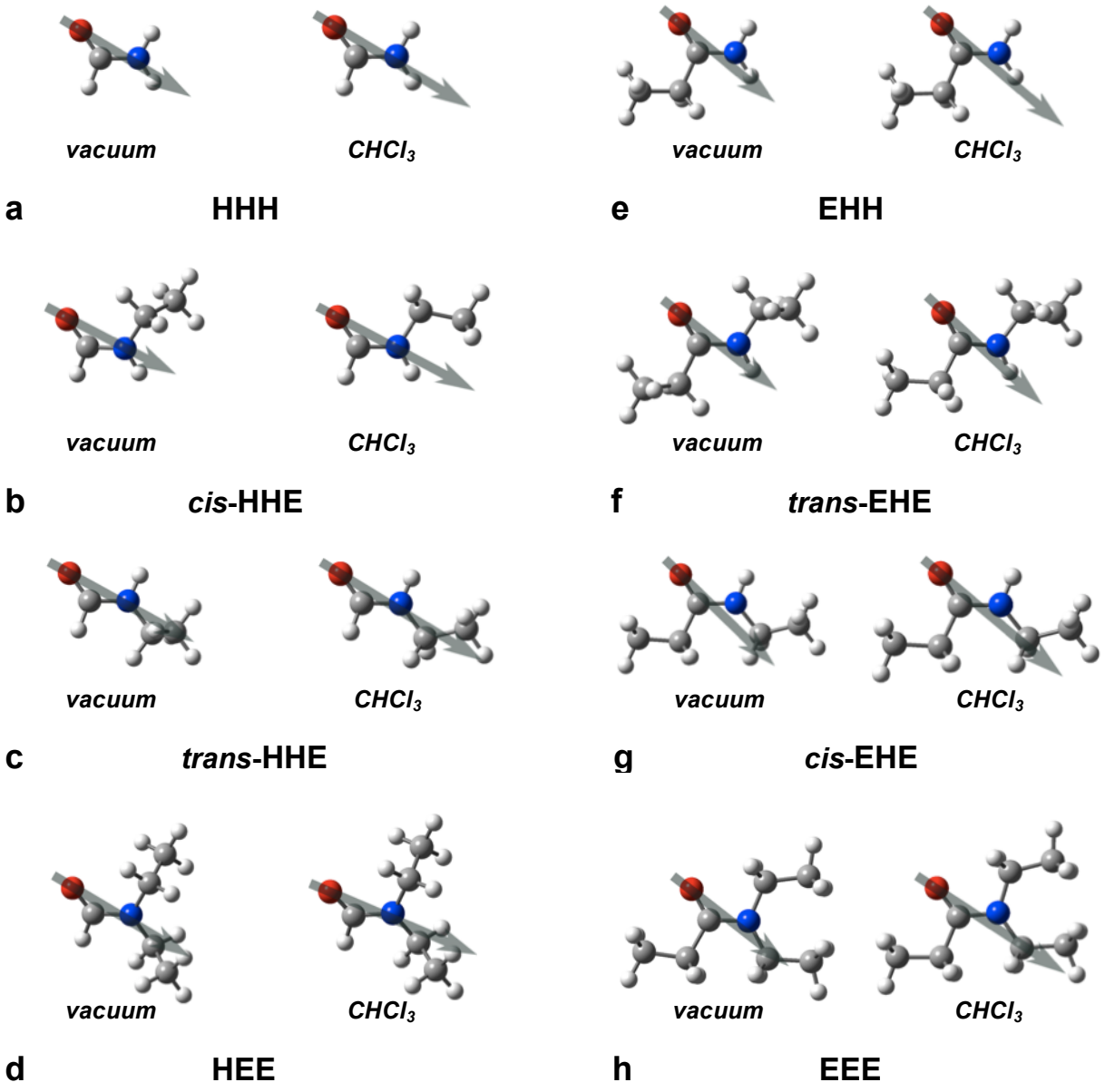
vacuum
CHCl3
a HHH
vacuum
CHCl3
e EHH
vacuum
CHCl3
b cis-HHE
vacuum
CHCl3
f trans-EHE
vacuum
CHCl3
c trans-HHE
vacuum
CHCl3
g cis-EHE
vacuum
CHCl3
d HEE
vacuum
CHCl3
h EEE

Figure 3-1

Figure 3-1. Balls and sticks models of the amide structures, optimized in vacuum and in chloroform ($CHCl_3$). The gray arrows designate the magnitudes and directions of the calculated permanent dipole moments. The direction of the dipole vectors is from their negative to their positive poles.

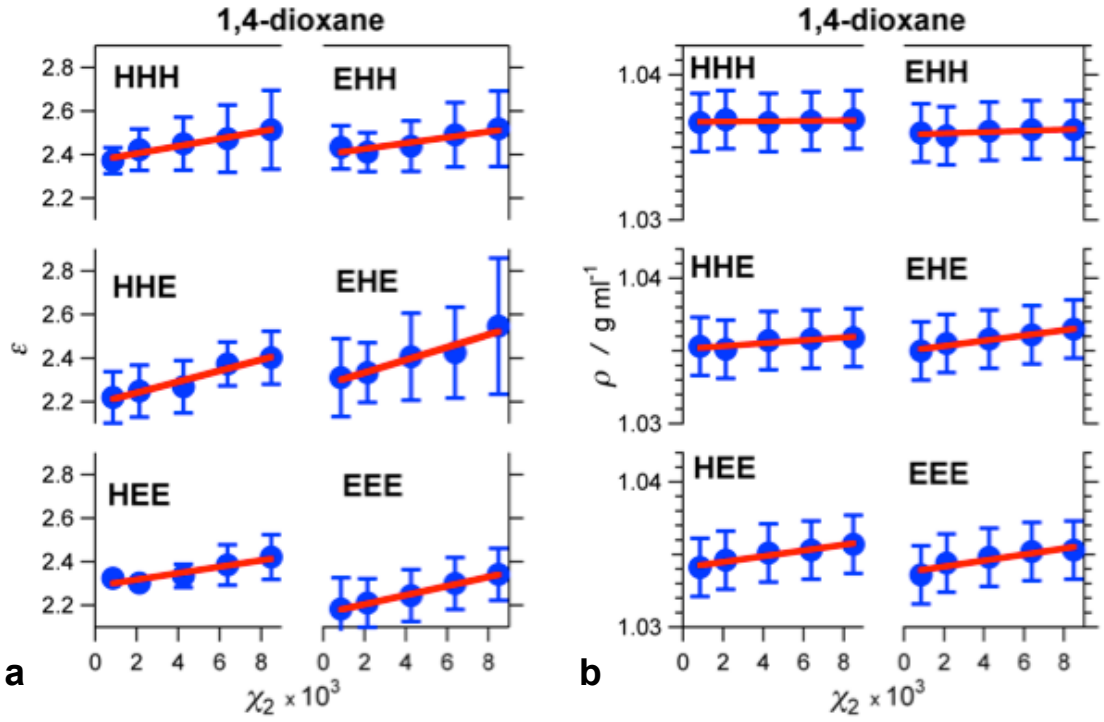
1,4-dioxane
HHH
EHH
HHE
EHE
HEE
EEE
ε
2.8
2.6
2.4
2.2
0 2 4 6 8
χ2 x 10^3
a
1,4-dioxane
HHH
EHH
HHE
EHE
HEE
EEE
ρ / g ml^-1
1.04
1.03
0 2 4 6 8
χ2 x 10^3
b

Figure 2

Figure 3-2. Dielectric and density properties of diluted amide solutions in 1,4-dioxane (DO). Concentration dependence of **(a)** the solution static dielectric constants, ε, obtained from capacitance measurements; and **(b)** the solution densities, ρ. The amide concentration is expressed in mole fractions, χ_2. The blue markers represent the experimental data and the red lines show the linear fits of the data (equation 8).

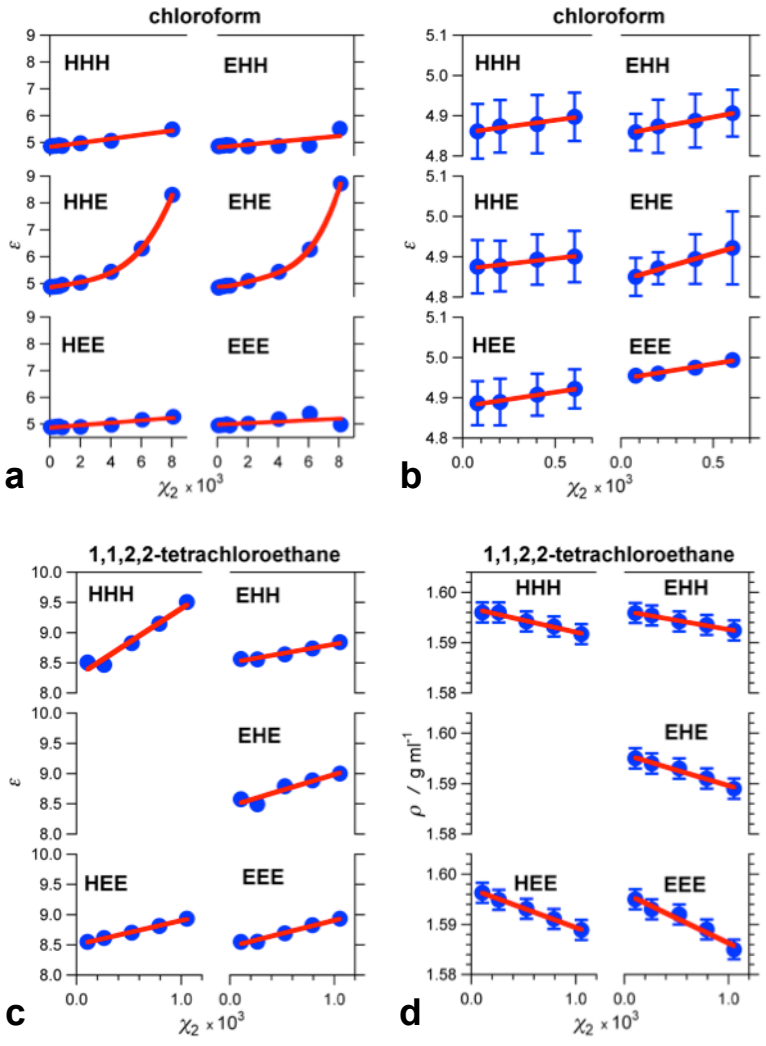
chloroform
HHH
EHH
HHE
EHE
HEE
EEE
ε
$\chi_2 \times 10^3$
a
b
1,1,2,2-tetrachloroethane
c
d
ρ / g ml⁻¹

Figure 3

Figure 3-3. Dielectric and density properties of diluted amide solutions in chlorinated solvents. **(a, b, c)** Static dielectric constant, *e*, obtained from capacitance measurements of amide solutions in **(a, b)** chloroform ($CHCl_3$), and **(c)** 1,1,2,2-tetrachloroethane (TCE). **(d)** Densities of amide solutions in TCE. The concentration of the amides, c_2, is expressed in mole fractions. The blue markers represent the experimental data and the red lines represent the data fits.

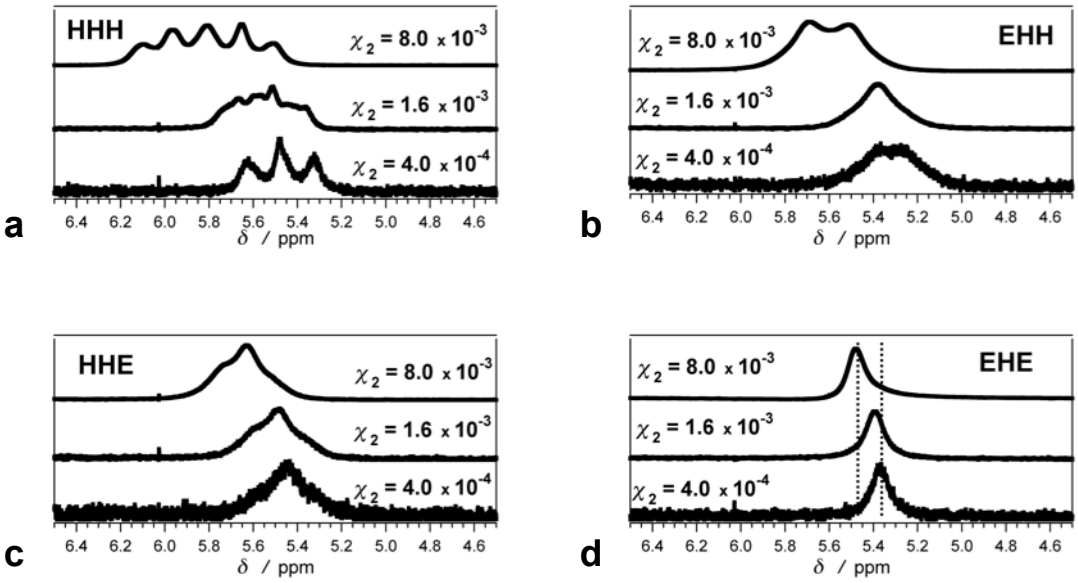
HHH
χ_2 = 8.0 x 10^{-3}
χ_2 = 1.6 x 10^{-3}
χ_2 = 4.0 x 10^{-4}
6.4 6.2 6.0 5.8 5.6 5.4 5.2 5.0 4.8 4.6
δ / ppm
a
EHH
b
HHE
c
EHE
d

Figure 4

Figure 3-4. ^{1}H-NMR spectra of the amide, N-^{1}H, region, depicting the concentration dependence of the chemical shifts of the N-^{1}H protons for samples dissolved in $CDCl_3$.

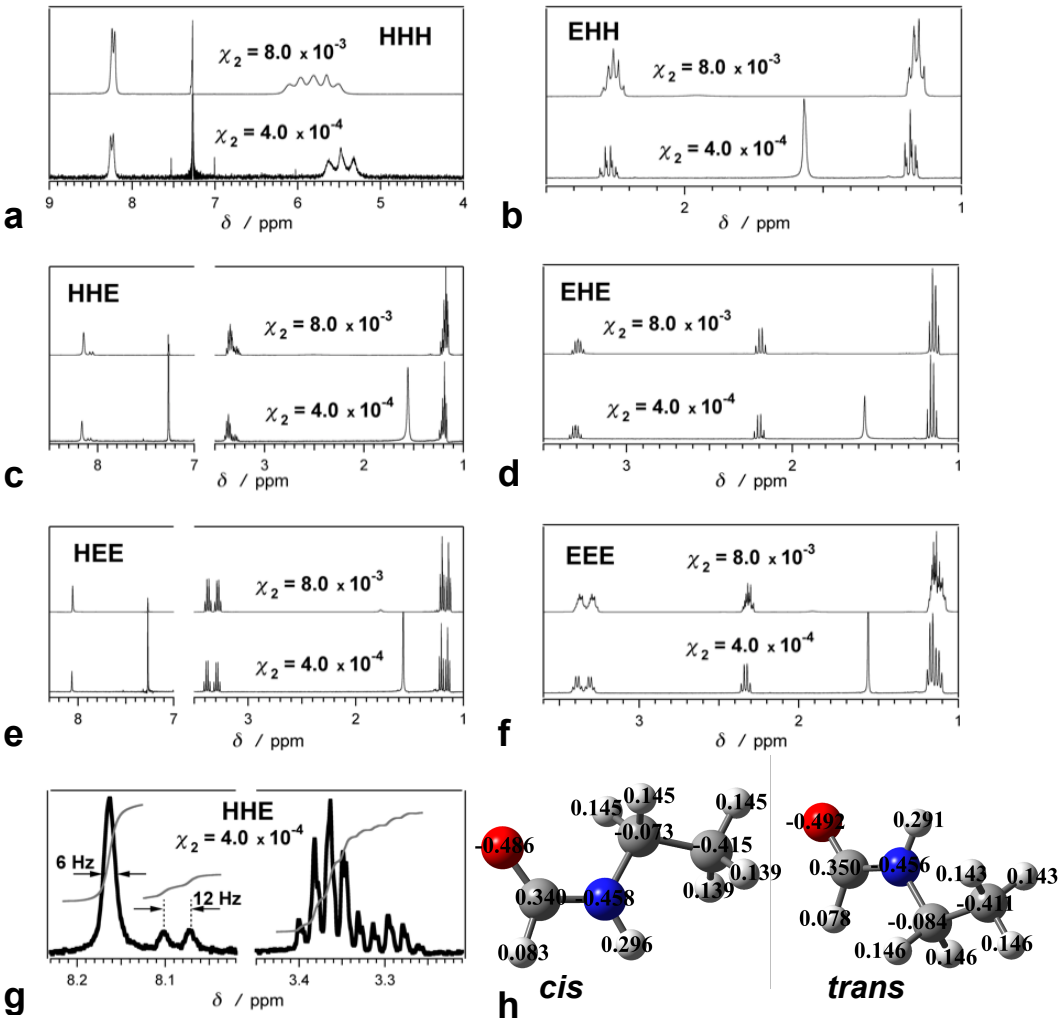
a
HHH
χ_2 = 8.0 x 10^{-3}
χ_2 = 4.0 x 10^{-4}
δ / ppm
b
EHH
χ_2 = 8.0 x 10^{-3}
χ_2 = 4.0 x 10^{-4}
δ / ppm
c
HHE
χ_2 = 8.0 x 10^{-3}
χ_2 = 4.0 x 10^{-4}
δ / ppm
d
EHE
χ_2 = 8.0 x 10^{-3}
χ_2 = 4.0 x 10^{-4}
δ / ppm
e
HEE
χ_2 = 8.0 x 10^{-3}
χ_2 = 4.0 x 10^{-4}
δ / ppm
f
EEE
χ_2 = 8.0 x 10^{-3}
χ_2 = 4.0 x 10^{-4}
δ / ppm
g
HHE
χ_2 = 4.0 x 10^{-4}
6 Hz
12 Hz
δ / ppm
h
0.145
0.145
0.145
-0.073
-0.486
-0.415
0.139
0.139
0.340
-0.458
0.083
0.296
cis
-0.492
0.291
0.350
-0.456
0.143
0.143
-0.411
0.078
-0.084
0.146
0.146
0.146
trans

Figure 5

Figure 3-5. ^{1}H-NMR spectra of the carbonyl and aliphatic proton regions of $CDCl_3$ solutions of the six amides. **(a, c, e)** Chemical shifts of the carbonyl and the aliphatic proton at two different sample concentrations. **(b, d, f)** Chemical shifts of the aliphatic protons at two different concentrations for the samples with ethylated carbonyls. **(g)** Chemical shifts of the carbonyl and the methylene protons of HHE showing the presence of two conformers. In (g), the highest peaks in the carbonyl and in the aliphatic region are normalized for clarity. **(h)** Balls and sticks structures of the two most stable HHE conformers with the corresponding atomic charges calculated for chloroform media. The singlet at 7.27 ppm was from the traces of $C^{1}HCl_3$ and was used for internal standard, and the broad singlet at 1.56 ppm was ascribed to traces of water in the solvent.

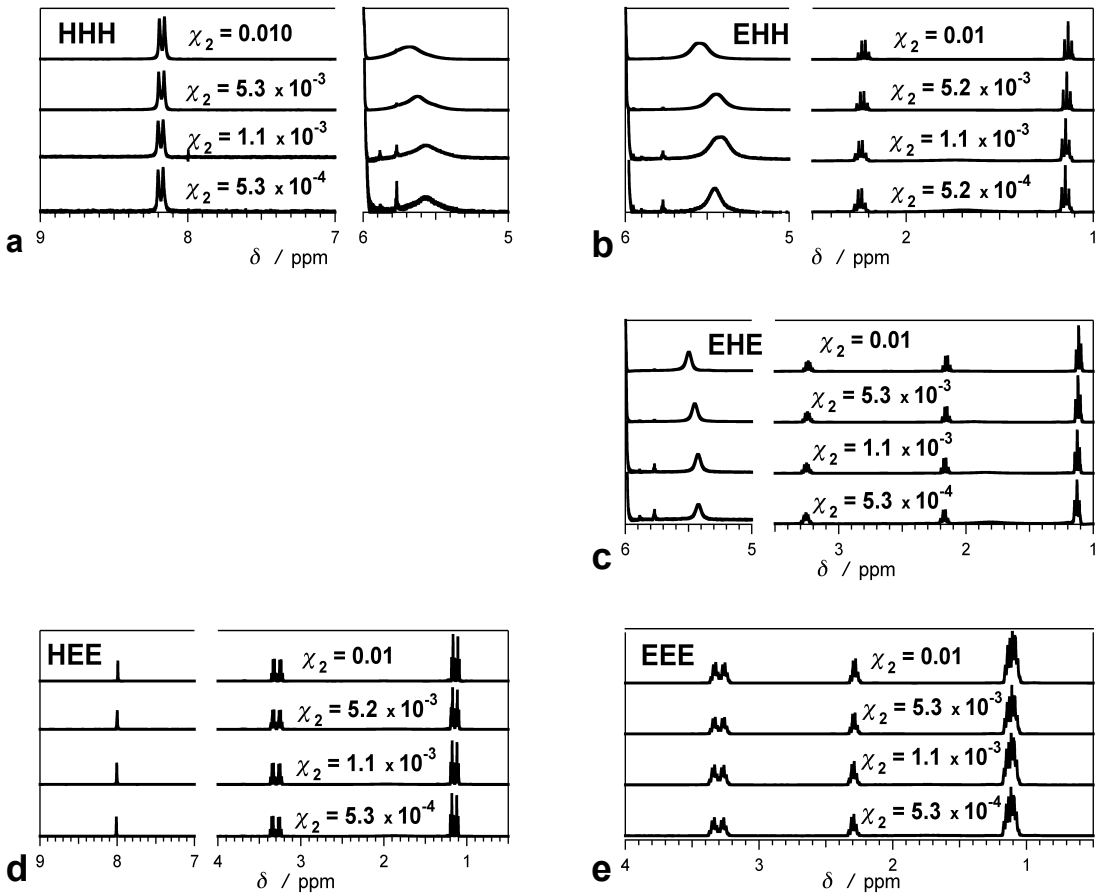
HHH
χ_2 = 0.010
χ_2 = 5.3 x 10^{-3}
χ_2 = 1.1 x 10^{-3}
χ_2 = 5.3 x 10^{-4}
a
δ / ppm
EHH
χ_2 = 0.01
χ_2 = 5.2 x 10^{-3}
χ_2 = 1.1 x 10^{-3}
χ_2 = 5.2 x 10^{-4}
b
δ / ppm
EHE
χ_2 = 0.01
χ_2 = 5.3 x 10^{-3}
χ_2 = 1.1 x 10^{-3}
χ_2 = 5.3 x 10^{-4}
c
δ / ppm
HEE
χ_2 = 0.01
χ_2 = 5.2 x 10^{-3}
χ_2 = 1.1 x 10^{-3}
χ_2 = 5.3 x 10^{-4}
d
δ / ppm
EEE
χ_2 = 0.01
χ_2 = 5.3 x 10^{-3}
χ_2 = 1.1 x 10^{-3}
χ_2 = 5.3 x 10^{-4}
e
δ / ppm

Figure 6

Figure 3-6. ^{1}H-NMR spectra of TCE-d_2 solutions of five of the six amides depicting the concentration dependence (or the lack of concentration dependence) of the chemical shifts of: **(a, d)** the carbonyl protons of Hxx in the 8 – 8.5 ppm region; **(a, b, c)** the amide protons of xHx in the 5 – 6 ppm region; **(b – e)** the methylene protons of Exx and xxE in the 2 – 3.5 ppm region; and **(b – e)** the methyl protons of Exx and xxE in the 1 – 1.5 ppm region. HHE does not have sufficient solubility in TCE. The solvent peak of TCE-d_1 is at 6 ppm.

References

Alber, F., S. Dokudovskaya, et al. (2007). "The molecular architecture of the nuclear pore complex." Nature **450**(7170): 695-701.

Aminabhavi, T. M. and B. Gopalakrishna (1995). "Density, Viscosity, Refractive-Index, and Speed of Sound in Aqueous Mixtures of N,N-Dimethylformamide, Dimethyl-Sulfoxide, N,N-Dimethylacetamide, Acetonitrile, Ethylene-Glycol, Diethylene Glycol, 1,4-Dioxane, Tetrahydrofuran, 2-Methoxyethanol, and 2-Ethoxyethanol at 298.15 K." Journal of Chemical and Engineering Data **40**(4): 856-861.

Antony, A. A. and C. P. Smyth (1964). "Microwave Absorption and Molecular Structure in Liquids .LIII. Hydrogen Bonding and Dielectric Properties in Chloroform Mixtures." Journal of the American Chemical Society **86**(2): 152-156.

Ashraf, M. K., R. R. Pandey, et al. (2009). "Theoretical design of bioinspired macromolecular electrets based on anthranilamide derivatives." Biotechnol. Prog. **25**(4): 915-922.

Bao, D., B. Millare, et al. (2009). "Electrochemical Oxidation of Ferrocene: A Strong Dependence on the Concentration of the Supporting Electrolyte for Nonpolar Solvents." J. Phys. Chem. A **113**(7): 1259-1267.

Bao, D., S. Ramu, et al. (2010). "Electrochemical Reduction of Quinones: Interfacing Experiment and Theory for Defining Effective Radii of Redox Moieties." J. Phys. Chem. B **114**(45): 14467-14479.

Barglow, K. T. and B. F. Cravatt (2007). "Activity-based protein profiling for the functional annotation of enzymes." Nat. Methods **4**(10): 822-827.

Bates, W. W. and M. E. Hobbs (1951). "The Dipole Moments of Some Acid Amides and the Structure of the Amide Group." Journal of the American Chemical Society **73**(5): 2151-2156.

Böttcher, C. J. F. (1973). Theory of Electric Polarization, Elsevier Scientific Publishing Company.

Böttcher, C. J. F. and P. Bordewijk (1978). Theory of Electric Polarization, Elsevier Scientific Publishing Company.

Breitung, E. M., W. E. Vaughan, et al. (2000). "Measurement of solute dipole moments in dilute solution: A simple three-terminal cell." Rev. Sci. Instrum. **71**(1): 224-227.

Canagaratna, M., M. E. Ott, et al. (1997). "Determination of the dipole moment of H3N-SO3 in the gas phase." Chem. Phys. Lett. **281**(1,2,3): 63-68.

Cave, R. J., K. Burke, et al. (2002). "Theoretical Investigation of the Ground and Excited States of Coumarin 151 and Coumarin 120." J. Phys. Chem. A **106**(40): 9294-9305.

Chau, K., B. Millare, et al. (2011). "Dependence of the Quality of Adhesion between Poly(dimethylsiloxane) and Glass Surfaces on the Composition of the Oxidizing Plasma." Microfluidics and Nanofluidics: in press.

Debye, P. J. W. (1945). Polar Molecules, Dover Publications, Inc., NY.

Doig, A. J. (2002). "Recent advances in helix-coil theory." Biophys. Chem. **101-102**: 281-293.

Dolezal, P., V. Likic, et al. (2006). "Evolution of the molecular machines for protein import into mitochondria." Science **313**(5785): 314-318.

Dotremont, C., S. Goethaert, et al. (1993). "Pervaporation behaviour of chlorinated hydrocarbons through organophilic membranes." Desalination **91**: 177-186.

Doyle, D. A., J. M. Cabral, et al. (1998). "The structure of the potassium channel: molecular basis of K+ conduction and selectivity." Science **280**(5360): 69-77.

Dudev, T. and C. Lim (2003). "Principles Governing Mg, Ca, and Zn Binding and Selectivity in Proteins." Chem. Rev. **103**(3): 773-787.

Dutzler, R., E. B. Campbell, et al. (2002). "X-ray structure of a ClC chloride channel at 3.0 Å reveals the molecular basis of anion selectivity." Nature **415**(6869): 287-294.

Foresman, J. B., T. A. Keith, et al. (1996). "Solvent effects .5. Influence of cavity shape, truncation of electrostatics, and electron correlation ab initio reaction field calculations." Journal of Physical Chemistry **100**(40): 16098-16104.

Frisch, M. J., G. W. Trucks, et al. (2004). Gaussian 03, Revision C.02, Wallingford, CT:Gaussian, Inc.

Galoppini, E. and M. A. Fox (1996). "Effect of the Electric Field Generated by the Helix Dipole on Photoinduced Intramolecular Electron Transfer in Dichromophoric alpha -Helical Peptides." J. Am. Chem. Soc. **118**(9): 2299-2300.

Hackney, D. D. (2007). "Processive Motor Movement." Science **316**(5821): 58-59.

Halverstadt, I. F. and W. D. Kumler (1942). "Solvent polarization error and its elimination in calculating dipole moments." J. Am. Chem. Soc. **64**: 2988-2992.

Hardie, R. C. (2007). "Dynamic platforms." Nature **450**(7166): 37-39.

Hedestrand, G. (1929). "Calculation of the molecular polarization of dissolved substances at infinite dilution." Z. physik. Chem. **2**(Abt. B): 428-444.

Hill, N. E., W. E. Vaughan, et al. (1969). Dielectric Properties and Molecular Behavior (The Van Nostrand Series in Physical Chemistry), Van Nostrand Reinhold Company Ltd.

Hol, W. G. J. (1985). "Effects of the alpha -helix dipole upon the functioning and structure of proteins and peptides." Adv. Biophys. **19**: 133-165.

Hol, W. G. J., P. T. Van Duijnen, et al. (1978). "The alpha -helix dipole and the properties of proteins." Nature **273**(5662): 443-446.

Hong, C., D. Bao, et al. (2008). "Print-and-Peel Fabrication of Microelectrodes." Langmuir **24**(16): 8439-8442.

Hu, J., B. Xia, et al. (2009). "Long-Lived Photogenerated States of alpha -Oligothiophene-Acridinium Dyads Have Triplet Character." J. Phys. Chem. A **113**(13): 3096-3107.

Hunter, E. C. E. and J. R. Partington (1933). "Studies in dielectric polarisation Part V Benzene solutions of pyrones, thiopyrones, and thioketones dtoxan soluttons of ureas and thioureas." Journal of the Chemical Society: 87-90.

Hurdis, E. C. and C. P. Smyth (1942). "Dipole moments in the vapor state and resonance effects in some substituted benzenes." J. Am. Chem. Soc. **64**: 2212-2216.

Jones, G., II, L. N. Lu, et al. (1995). "Photoactive peptides. 6. Photoinduced electron transfer for pyrenesulfonamide conjugates of tryptophan-containing peptides. Mitigation of fluoroprobe behavior in N-terminal labeling experiments." Bioorg. Med. Chem. Lett. **5**(20): 2385-2390.

Jones, G., II, V. Vullev, et al. (2000). "Multistep Photoinduced Electron Transfer in a de Novo Helix Bundle: Multimer Self-Assembly of Peptide Chains Including a Chromophore Special Pair." J. Am. Chem. Soc. **122**(2): 388-389.

Jones, G., II and V. I. Vullev (2001). "Contribution of a Pyrene Fluorescence Probe to the Aggregation Propensity of Polypeptides." Org. Lett. **3**(16): 2457-2460.

Jones, G., II and V. I. Vullev (2001). "Ground- and Excited-State Aggregation Properties of a Pyrene Derivative in Aqueous Media." J. Phys. Chem. A **105**(26): 6402-6406.

Jones, G., II and V. I. Vullev (2002). "Medium effects on the photophysical properties of terbium(III) complexes with pyridine-2,6-dicarboxylate." Photochem. Photobiol. Sci. **1**(12): 925-933.

Jones, G., II and V. I. Vullev (2002). "Medium Effects on the Stability of Terbium(III) Complexes with Pyridine-2,6-dicarboxylate." J. Phys. Chem. A **106**(35): 8213-8222.

Jones, G., II and V. I. Vullev (2002). "Photoinduced Electron Transfer between Non-Native Donor-Acceptor Moieties Incorporated in Synthetic Polypeptide Aggregates." Org. Lett. **4**(23): 4001-4004.

Jones, G., II, D. Yan, et al. (2007). "Photoinduced Electron Transfer in Arylacridinium Conjugates in a Solid Glass Matrix." J. Phys. Chem. B **111**(24): 6921-6929.

Jones, G., II, X. Zhou, et al. (2003). "Photoinduced electron transfer in alpha -helical polypeptides: dependence on conformation and electron donor-acceptor distance." Photochem. Photobiol. Sci. **2**(11): 1080-1087.

Jraij, A., A. R. Allouche, et al. (2006). "Electric dipole, polarizability and structure of cesium chloride clusters with one-excess electron." Chem. Phys. **322**(3): 298-302.

Kirkwood, J. G. (1939). "The dielectric polarization of polar liquids." Journal of Chemical Physics **7**(10): 911-919.

Kiyohara, O. and K. I. Higasi (1969). "Dipole Moments of 1,2-Dihalogeno- and 1,1,2,2-Tetrahalogenoethanes in Aromatic and Non-Aromatic Solvents." Bulletin of the Chemical Society of Japan **42**(4): 1158-1159.

Knoblich, J. A. (2006). "Sara Splits the Signal." Science **314**(5802): 1094-1096.

Kundrotas, P. J. and E. Alexov (2006). "Electrostatic properties of protein-protein complexes." Biophys. J. **91**(5): 1724-1736.

Kurland, R. J. and E. B. Wilson (1957). "Microwave Spectrum, Structure, Dipole Moment, and Quadrupole Couplin Constants of Formamide." Journal of Chemical Physics **27**(2): 585-590.

Launey, M. E., M. J. Buehler, et al. (2010). "On the mechanistic origins of toughness in bone." Annu. Rev. Mater. Res. **40**: 25-53.

Leontyev, I. and A. Stuchebrukhov (2011). "Accounting for electronic polarization in non-polarizable force fields." Phys. Chem. Chem. Phys. **13**(7): 2613-2626.

Lumbroso, H., J. Cure, et al. (1983). "The Polarity of the Oxy Sulfur Bond in Dimethylsulfoxide and Sulfone, Alkylphenyl and Alkyl-2-Pyrazinyl Sulfones." Journal of Molecular Structure **98**(3-4): 277-295.

Makarenko, V. E., V. P. Makovetskii, et al. (1991). "Electronic structure of some amides from dipole moment measurements and quantum-chemical calculations." Ukr. Khim. Zh. **57**(4): 444-448.

Makosz, J. J. (1994). "Dipole moment of molecules determined from dielectric measurements in very dilute solutions of a dipole liquid in a nondipole liquid." J. Mol. Liq. **59**(2-3): 103-113.

Malecki, J., J. Nowak, et al. (1984). "Extrapolation Method for the Determination of Electric-Dipole Moments from Solutions in Polar-Solvents." Journal of Physical Chemistry **88**(18): 4148-4152.

Mark, J. E. and C. Sutton (1972). "Dipole-Moments and Conformational Energies of Chloroethanes." Journal of the American Chemical Society **94**(4): 1083-1090.

Miertus, S., E. Scrocco, et al. (1981). "Electrostatic Interaction of a Solute with a Continuum - a Direct Utilization of Abinitio Molecular Potentials for the Prevision of Solvent Effects." Chemical Physics **55**(1): 117-129.

Millare, B., M. Thomas, et al. (2008). "Dependence of the quality of adhesion between polydimethyl siloxane and glass surfaces on the conditions of treatment with oxygen plasma." Langmuir **24**(22): 13218-13224.

Mopsik, F. I. and M. G. Broadhurst (1975). "Molecular dipole electrets." Journal of Applied Physics **46**(10): 4204-4208.

Myers, A. B. and R. R. Birge (1981). "The Experimental-Determination of Ground-State Dipole-Moments from Dielectric-Constant Measurements Using Ellipsoidal Cavity Correction Factors." Journal of Chemical Physics **74**(6): 3514-3521.

Nace, H. R. and R. H. Nealey (1966). "Dipole moment and conformation of substituted cyclohexanols." J. Am. Chem. Soc. **88**(1): 65-68.

Onsager, L. (1936). "Electric moments of molecules in liquids." J. Am. Chem. Soc. **58**: 1486-1493.

Pekary, A. E. (1974). "Dipole moment and far-infrared studies on the dimethyl sulfoxide-iodine complex." J. Phys. Chem. **78**(17): 1744-1746.

Perdew, J. P., K. Burke, et al. (1996). "Generalized gradient approximation made simple." Physical Review Letters **77**(18): 3865-3868.

Petersson, G. A. and M. A. Allaham (1991). "A Complete Basis Set Model Chemistry .2. Open-Shell Systems and the Total Energies of the 1st-Row Atoms." Journal of Chemical Physics **94**(9): 6081-6090.

Petersson, G. A., A. Bennett, et al. (1988). "A Complete Basis Set Model Chemistry .1. The Total Energies of Closed-Shell Atoms and Hydrides of the 1st-Row Elements." Journal of Chemical Physics **89**(4): 2193-2218.

Petrasek, J. and K. Schwarzerova (2009). "Actin and microtubule cytoskeleton interactions." Curr. Opin. Plant Biol. **12**(6): 728-734.

Petricoin, E. F., C. Belluco, et al. (2006). "The blood peptidome: a higher dimension of information content for cancer biomarker discovery." Nat. Rev. Cancer **6**(12): 961-967.

Piette, L. H., J. D. Ray, et al. (1958). "Analysis of the Proton Nuclear Magnetic Resonance Spectrum of Formaide by the Double Resonance Technique." Journal of Molecular Spectroscopy **2**(1): 66-72.

Prasad, C. V. and K. Sundaram (1979). "On the polarity of the amide group and its impact on dipeptide conformation." Int. J. Quantum Chem. **15**(6): 783-792.

Qiu, X. (2010). "Patterned piezo-, pyro-, and ferroelectricity of poled polymer electrets." J. Appl. Phys. **108**(1): 011101/011101-011101/011119.

Ramsay, D. A. (1947). "The Vibration Spectrum and Molecular Configuration of 1:4-Dioxane." Proceedings of the Royal Society of London Series a-Mathematical and Physical Sciences **190**(1023): 562-574.

Reinhart, P. B., Q. Williams, et al. (1970). "Microwave Measurements of Dipole Moments of Cfcl3 and Chcl3 and Their Pressure-Broadened Spectra." Journal of Chemical Physics **53**(4): 1418-&.

Rexach, J. E., P. M. Clark, et al. (2008). "Chemical approaches to understanding O-GlcNAc glycosylation in the brain." Nat. Chem. Biol. **4**(2): 97-106.

Saito, H., Y. Tanaka, et al. (1971). "Hydrogen Bond Studies by Nitrogen-14 Nuclear Magnetic Resonance .3. Study of Electron Redistribution Associated with Hydrogen Bonding and Metal-Complex Formation of Formamide and N-Methylacetamide." Journal of the American Chemical Society **93**(5): 1077-&.

Sanabria, H., J. H. Miller, et al. (2006). "Impedance spectroscopy of alpha-beta tubulin heterodimer suspensions." Biophysical Journal **90**(12): 4644-4650.

Sato, H. (2003). "Electronic structure and chemical reaction in solution." Understanding Chem. React. **24**(Molecular Theory of Solvation): 61-99.

Sato, K., Y. Ohkubo, et al. (1978). "Far-Infrared Absorption Intensities and Dipole-Moments of Some Molecules in Solutions." Bulletin of the Chemical Society of Japan **51**(9): 2493-2495.

Shin, Y.-G. K., M. D. Newton, et al. (2003). "Distance Dependence of Electron Transfer Across Peptides with Different Secondary Structures: The Role of Peptide Energetics and Electronic Coupling." J. Am. Chem. Soc. **125**(13): 3722-3732.

Sigala, P. A., A. T. Fafarman, et al. (2007). "Do Ligand Binding and Solvent Exclusion Alter the Electrostatic Character within the Oxyanion Hole of an Enzymatic Active Site?" J. Am. Chem. Soc. **129**(40): 12104-12105.

Sit, S. K., K. Dutta, et al. (2000). "Double relaxation times, dipole moments, energy parameters and molecular structures of some aprotic polar molecules from relaxation phenomena." Journal of Molecular Liquids **89**(1-3): 111-126.

Slessareva, J. E. and H. G. Dohlman (2006). "G Protein Signaling in Yeast:New Components, New Connections, New Compartments." Science **314**(5804): 1412-1413.

Smyth, C. P. and W. S. Walls (1931). "Electric moment and molecular structure. IV. The glycols." Journal of the American Chemical Society **53**(2): 2115-2122.

Sowa, Y. and R. M. Berry (2009). "The bacterial flagellar motor." Single Mol. Biol.: 105-142.

Steimle, T. C., D. F. Nachman, et al. (1987). "Laboratory measurement of the permanent electric dipole moment of gas-phase copper oxide (CuO) in its X2Pi state." J. Chem. Phys. **87**(10): 5670-5673.

Sunners, B., L. H. Piette, et al. (1960). "Proton Magnetic Resonance Measurements of Formamide." Canadian Journal of Chemistry-Revue Canadienne De Chimie **38**(5): 681-688.

Suydam, I. T., C. D. Snow, et al. (2006). "Electric Fields at the Active Site of an Enzyme: Direct Comparison of Experiment with Theory." Science **313**(5784): 200-204.

Taylor, W. J. (1975). "Apparent and Partial Molar Polarizations in Solutions and Halverstadt-Kumler and Hedestrand Equations." Journal of Physical Chemistry **79**(17): 1817-1820.

Thomas, J. R. and W. D. Gwinn (1949). "The Rotational Configuration and Dipole Moments of 1,1,2-Trichloroethane and 1,1,2,2-Tetrachloroethane." Journal of the American Chemical Society **71**(8): 2785-2790.

Tjahjono, M., T. Davis, et al. (2007). "Three-terminal capacitance cell for stopped-flow measurements of very dilute solutions." Rev. Sci. Instrum. **78**(2): 023902/023901-023902/023906.

Tomasi, J., B. Mennucci, et al. (2005). "Quantum Mechanical Continuum Solvation Models." Chem. Rev. **105**(8): 2999-3093.

Trinkle-Mulcahy, L. and I. Lamond Angus (2007). "Toward a high-resolution view of nuclear dynamics." Science **318**(5855): 1402-1407.

Vaara, J., J. Kaski, et al. (1997). "NMR properties of formamide: A first principles and experimental study." Journal of Physical Chemistry A **101**(28): 5069-5081.

van den Heuvel, M. G. L. and C. Dekker (2007). "Motor Proteins at Work for Nanotechnology." Science **317**(5836): 333-336.

Vasquez, J. M., A. Vu, et al. (2009). "Fluorescence enhancement of warfarin induced by interaction with beta -cyclodextrin." Biotechnol. Prog. **25**(4): 906-914.

Vlassiouk, I. and S. Smirnov (2003). "Electric polarization of dilute polar solutions: Revised treatment for arbitrary shaped molecules." Journal of Physical Chemistry A **107**(38): 7561-7566.

Voth, A. R., P. Khuu, et al. (2009). "Halogen bonds as orthogonal molecular interactions to hydrogen bonds." Nature Chemistry **1**(1): 74-79.

Vullev, V. I. (2011). "From Biomimesis to Bioinspiration: What's the Benefit for Solar Energy Conversion Applications?" J. Phys. Chem. Lett. **2**(5): 503–508.

Vullev, V. I. and G. Jones (2002). "Photoinduced electron transfer in alkanoylpyrene aggregates in conjugated polypeptides." Tetrahedron Lett. **43**(47): 8611-8615.

Vullev, V. I. and G. Jones, II (2002). "Photoinduced charge transfer in helical polypeptides." Res. Chem. Intermed. **28**(7-9): 795-815.

Wada, A. (1959). "Dielectric properties of polypeptide solutions. II. Relation between the electric dipole moment and the molecular weight of the alpha -helix." J. Chem. Phys. **30**: 328-329.

Wan, J., A. Ferreira, et al. (2008). "Solvent dependence of the charge-transfer properties of a quaterthiophene-anthraquinone dyad." J. Photochem. Photobiol., A **197**(2-3): 364-374.

Weerapana, E., G. M. Simon, et al. (2008). "Disparate proteome reactivity profiles of carbon electrophiles." Nat. Chem. Biol. **4**(7): 405-407.

Williams, J. W. (1930). "The dielectric constants of binary mixtures. X. The electric moments of simple derivatives of cyclohexane and of dioxan." Journal of the American Chemical Society **52**: 1831-1837.

Woods, C. J. and A. J. Mulholland (2008). "Multiscale modelling of biological systems." Chem. Modell. **5**: 13-50.

Yasutomi, S., T. Morita, et al. (2004). "A Molecular Photodiode System That Can Switch Photocurrent Direction." Science (Washington, DC, U. S.) **304**(5679): 1944-1947.

Chapter 4

Anthranilamides as Bioinspired Molecular Electrets: Experimental Evidence for Permanent Ground-State Electric Dipole Moment

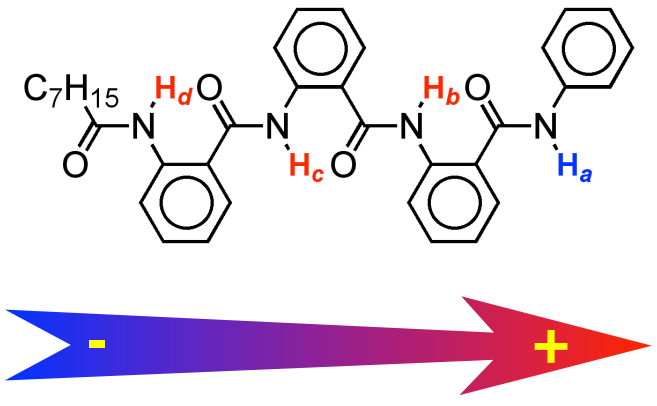

ABSTRACT

As electrostatic equivalents of magnets, organic electrets offer unparalleled properties for impacting energy-conversion and electronic applications. While biological systems have evolved to efficiently utilize protein alpha helices as molecular electrets, the synthetic counterparts of these conjugates still remain largely unexplored. This article describes a study of the electronic properties of anthranilamide oligomers, which proved to be electrets based on their intrinsic dipole moments as evident from their spectral and dielectric properties. NMR studies provided the means for estimating the direction of the intrinsic electric dipoles of these conjugates. This study sets the foundation for the development of a class of organic materials that are *de novo* designed from biomolecular motifs and possess unexplored electronic properties.

Introduction

Electrets are materials and macromolecules with ordered electric dipoles, i.e., electrets are the electrostatic analogues of magnets.(Kepler 1978; Erhard, Lovera et al. 2010) Due to the substantial electric-field gradients that their dipoles generate, electrets have an enormous potential for unprecedented applications in energy conversion, electronics and photocatalysis applications.(Garcia 2011; Suzuki 2011; Vullev 2011)

Protein helices present an important class of natural electrets. The ordered co-directional orientation of the amide and the hydrogen bonds in these protein conformers results in permanent electric dipoles amounting to about five Debyes per residue.(Hol, Van Duijnen et al. 1978; Shin, Newton et al. 2003) For example, electric fields from protein α-helices stabilize weakly solvated ions in the interiors of the potassium, KcsA, and chloride, ClC, ion channels, permitting them to function efficiently.(Doyle, Cabral et al. 1998; Dutzler, Campbell et al. 2002)

Employing polypeptide helices, derivatized with an electron donor and acceptor, Galoppini and Fox demonstrated for the first time the preferential directionality of the photoinduced electron transfer toward the positive pole of the dipole.(Galoppini and Fox 1996; Fox and Galoppini 1997) This charge-transfer rectification was ascribed to the stabilization of the charge-transfer states, in which the electrons were transduced toward the positive poles of the helix dipoles.(Shin, Newton et al. 2003) Employing this approach to gold interfaces coated with polypeptide helices provided a means for controlling the directionality of photocurrent.(Yasutomi, Morita et al. 2004)

The studies described above share the corresponding electronic properties of helical peptides as the common theme for rectifying charge transfer. Indeed, these biomimetic polypeptide conjugates have proven immensely instrumental for bringing the concept of electrets to charge transfer. Such polypeptides, however, pose some challenging limitations: (1) the conformational integrity of polypeptide α-helices is often compromised when taken out of their natural environment, thus, limiting the scopes of their applications;(Jones, Zhou et al. 2003) and (2) polypeptides composed of natural α-amino acids are wide-band-gap materials with an optical band gap of approximately 5.6 eV, which limits the distance of efficient charge transfer to less than two nanometers. Charge transfer through such polypeptides is attained solely via electron tunneling.(Beratan, Onuchic et al. 1992; Jones, Lu et al. 1995; Jones, Vullev et al. 2000; Vullev and Jones 2002; Gray and Winkler 2005) Hopping mechanism, involving multiple discreet electron-transfer steps along precisely arranged cofactors or redox residues, such as tryptophan, is essential for extending the charge-transfer distances beyond the intrinsic limits of the protein backbone chains.(Shih, Museth et al. 2008)

To address these issues, we undertook a bioinspired approach to attain organic electrets, which have the structural and functional advantages over their biological counterparts, and do not suffer the disadvantages of the biological macromolecules.(Ashraf, Pandey et al. 2009; Vullev 2011) Similar to protein α-helices, we aimed at ordered amide and hydrogen bonds to generate intrinsic electric dipoles along the backbones of the bioinspired conjugates. Unlike proteins, however, our goal was to place aromatic moieties as a part of the macromolecular backbones, in order to

attain extended π-conjugation and hence pathways for long-range efficient charge transfer. Anthranilamides proved to be excellent candidates for this bioinspired approach (Scheme 4-1).(Ashraf, Pandey et al. 2009)

Anthranilamide oligomers are known structures existing in extended conformations stabilized by intramolecular hydrogen bonding.(Hamuro, Geib et al. 1996; Hamuro and Hamilton 2001) In fact, anthranilic acid, i.e., *o*-aminobenzoic acid, is vitamin L_1. To date, the electronic properties of anthranilamides oligomers and their derivatives have not been investigated. Recently, using *ab initio* calculations, we demonstrated for the first time that these anthranilamide oligomers have intrinsic dipole moments. The vectorial sum of the dipoles from the amide bonds, along with the dipoles generated from the shift in the electron density upon the formation of hydrogen bonds, resulted in total electric ground-state dipole moments of about three Debyes per residue (Scheme 4-1).(Ashraf, Pandey et al. 2009) Unlike in protein α-helices, the intrinsic dipoles of the anthranilamide oligomers were oriented from their N- to their C-termini (Scheme 4-1).(Ashraf, Pandey et al. 2009)

Herein, we experimentally demonstrate that anthranilamides possess intrinsic dipole moments. We used relatively small conjugates, i.e., monomer, dimer and trimer, for this investigation (Scheme 4-2). Even in organic solvents, such as chloroform, in which these anthranilamide conjugates had pronounced solubility, they exhibited a strong propensity for aggregation. This self-assembly, however, was not electrostatically driven and the aggregates themselves had intrinsic dipoles as it became evident from dielectric studies of their solutions: i.e., at least partial co-directional arrangement of the anthranilamides

within the aggregates. Analysis of ^{1}H chemical shifts, as determined using NMR spectroscopy, allowed us to determine that the direction of the intrinsic dipole was from the N- to the C-termini of the anthranilamides, which confirmed our theoretical findings.

Results and Discussion

We prepared monoanthranilamide (h-A-ph), dianthranilamide (h-AA-ph) and trianthranilamide (h-AAA-ph) derivatives, in which the C-termini were capped with phenyl and the N-termini with heptyl groups (Scheme 4-2). For these studies, the solvent of choice was chloroform. It provided the needed sample solubility and concurrently, it was non-polar enough to ensure that the effects from the permanent dipoles were readily detectable.(Upadhyayula, Bao et al. 2011)

Previously reported structural data indicate that anthranilamides have a preference for an extended conformation. X-ray and NMR studies demonstrated that anthranilamide oligomers assume an extended conformation with a coplanar arrangement of the aromatic rings.(Hamuro, Geib et al. 1996; Hamuro and Hamilton 2001) Hydrogen bonding between amides attached to the same aromatic ring supports this coplanar extended conformation (Scheme 4-1).(Hamuro, Geib et al. 1996; Hamuro and Hamilton 2001) Such coplanar conformations, supported by hydrogen-bond networks, are not unusual for polymers of aromatic amides and esters in organic solvents.(Zhu, Wang et al. 2004; Gong 2008; Colombo, Coluccini et al. 2010; Coluccini, Mazzanti et al. 2010) Furthermore, structure relaxation of a range of anthranilamide oligomers, using computational

methods, constantly led to coplanar extended conformations supported by hydrogen bonds between amides attached to the same aromatic residue (Scheme 4-1).(Ashraf, Pandey et al. 2009)

The UV/visible emission spectra of all three conjugates exhibited two peaks, the intensity of which was concentration dependent (Figure 4-1). A decrease in the concentration of these conjugates in chloroform caused a decrease in the intensity of the red-shifted band, and an increase in the intensity of the high-energy peaks. These findings were an indication for aggregation of the anthranilamides in the investigated concentration range. The emission peak at about 400 nm was due to fluorescence from the monomeric forms of the anthranilamide oligomers; and the broad band at around 520 nm was ascribed to the emission of their aggregated forms. Especially for h-AAA-ph, the intensity decrease in the aggregate emission band was less substantial than the increase in the fluorescence intensity of the 400-nm monomer emission. This finding suggested that the aggregation of the anthranilamides caused a decrease in their emission quantum yields.

Possible origins of the low-energy emission band include: (1) the formation of ground-state aggregates and their direct excitation; and (2) excited-state aggregation (excimer formation), where photoexcited molecule aggregates with a ground-state molecule, were possible origins of the aggregate emission. Close examination of the absorption spectra showed a slight increase in the extinction coefficient as the concentrations increased; a case, which was most pronounced for h-AA-ph (Figure 4-1a - c). These small spectral

changes, however, cannot be conclusive for claiming or ruling out ground-state aggregation.

To address this issue, we resorted to time-resolved emission spectroscopy. The emission-decay curves, measured at the 520-nm aggregate bands, for each of the three oligomers showed a rise within the excitation pulse, followed by immediate nanosecond decay (Figure 4-1d). The lack of a slow post-excitation rise (characteristic for excimer formation), along with the fast emission decay kinetics, was indicative that the low-energy bands resulted primarily from ground-state aggregates.(Jones and Vullev 2001; Vullev, Jiang et al. 2005)

Addition of electrolyte and the use of a solvent media with higher polarity did not prevent the aggregation of the oligomers. Thus, electrostatic interactions (between the anthranilamide dipoles) were not the principal driving force for the aggregate formation. Due to the abundance of aromatic moieties in each of the oligomers, the aggregation could be plausibly ascribed to π-π stacking.

The concentration dependence of the fluorescence properties of the anthranilamides provided a means for evaluating their aggregation behavior.(Jones and Vullev 2001; Jones and Vullev 2002; Jones and Vullev 2002; Vasquez, Vu et al. 2009) Deconvolution of the fluorescence spectra (Figure 4-2a) allowed us to estimate the relative contribution to the emission from the monomer and the aggregate bands, i.e., R_m and R_a, respectively:

$$R_m = \frac{S_m}{S_m + S_a} \tag{1a}$$

$$R_a = \frac{S_a}{S_m + S_a} \tag{1b}$$

where S_m and S_a represent the integrated emission under the monomer and aggregate bands, respectively, i.e., $S = \int F(\tilde{\nu}) d\tilde{\nu}$, and $F(\tilde{\nu})$ is the fluorescence intensity at wavenumber $\tilde{\nu}$.(Jones and Vullev 2001; Jones and Vullev 2002; Vullev and Jones 2002)

As expected, an increase in the total concentration, C, of the anthranilamides, A, caused a decrease in S_m and an increase in S_a (Figure 4-2b). For h-A-ph, this change in the ratios, S, between the aggregate and monomer fluorescence bands occurred at $C < 10^{-4}$ M. For h-AA-ph and h-AAA-ph, the largest changes in S_m and S_a occurred in the sub-μM concentration range (Figure 4-2b).

The aggregation led to fluorescence quenching, and the emission quantum yields, Φ, of the aggregates were about 2 to 20 times smaller than Φ of the monomeric forms of the anthranilamides (Table 4-1). Therefore, R_m and R_a, as defined in eq. 1, did not directly represent the equilibrium concentrations [A] and [A_n] of the anthranilamide monomers and aggregates, respectively. Considering that $S_m \propto \Phi_m [\mathrm{A}]$ and $S_a \propto \Phi_a [\mathrm{A}_n]$, along with $C = [\mathrm{A}] + n[\mathrm{A}_n]$, yields:

$$[\mathrm{A}] = \frac{\phi R_m}{1 - (1 - \phi) R_m} C = \xi C \tag{2}$$

where $\phi = \Phi_a / \Phi_m$, and ξ is the fraction of the anthranilamides that are in the form of monomers, i.e., $\xi = [\mathrm{A}] / C$ (Figure 4-2c). Substituting eq. 2 in the expression for the

equilibrium constant, $K = [A_n] / [A]^n$, representing the aggregation process, n A $\rightleftharpoons$ A_n, yields:

$$\lg\left(C\left(1-\xi\right)\right) = n\lg\left(C\xi\right) + \lg\left(nK\right) \quad (3)$$

The slopes of the linear fits of lg(C(1-ξ)) vs. lg($C\xi$) provided a means for estimating of the state of aggregation, n, for the different anthranilamides (Figure 4-2d). For each of the anthranilamides, however, autocorrelation analysis revealed that a single linear fit over the whole concentration range did not yield statistically significant representations of the prelateship between lg(C(1-ξ)) and lg($C\xi$). The Durbin-Watson statistics (d) was smaller than 1 for all fits covering the full concentration ranges (Table 4-2),(Eaton 1990; Hisamatsu and Maekawa 1994; Rutledge and Barros 2002; Xia, Upadhyayula et al. 2011) indicating for possible positive autocorrelations that were not accounted for by the linear model, eq. 3. As an alternative, linear fits limited to the concentration ranges, where the biggest changes in R_m and R_a occurred, provided excellent linear correlations with $d \approx 2$ (Table 4-2).

The slopes of the linear fits, limited to the low μM and sub-μM ranges, were about 1.7, 4.1 and 2.2 for h-A-ph, h-AA-ph, and h-AAA-ph, respectively (Table 4-2). Therefore, the observed concentration-dependent changes in the fluorescence of h-A-ph and h-AAA-ph corresponded to the formation of predominantly dimers, and of h-AA-ph – tetramers. The linear fits in the concentration ranges extending to 10 mM yielded slopes of about unity, $n \approx 1$ (Table 4-2). Assuming that any aggregation, including between a monomer and an

aggregate and between two aggregates, would affect the emission properties of the anthranilamides, the unity slopes for $C > 10^{-4}$ M indicated that no detectable aggregation took place in that concentration range.

The zero-to-zero energies (E_{00}),(Bao, Millare et al. 2009) extracted from the absorption and the emission spectra, correspond to the optical gaps between their highest occupied molecular orbitals (HOMOs) and their lowest unoccupied molecular orbitals (LUMOs), i.e., the optical HOMO-LUMO gaps of the anthranilamide conjugates (Table 4-1). The optical gaps, however, do not quantitatively represent the HOMO-LUMO energy differences. Instead, the optical HOMO-LUMO gaps of the anthranilamides characterize the direct transitions between the ground and the lowest singlet excited states; i.e., transitions that do not involve nuclear reorganization, and that are between closed-shell ground states and states with singly-occupied molecular orbitals. Conversely, the calculated HOMO-LUMO gaps (ΔE) represent the theoretically estimated differences between the HOMOs and LUMOs of the ground states of the anthranilamides.(Ashraf, Pandey et al. 2009)

For the anthranilamides, E_{00} was between 0.6 and 1.3 eV smaller than ΔE (Table 4-1). Two considerations could account for the differences between E_{00} and ΔE. (1) Optically-determined HOMO-LUMO gaps tend to be underestimated due to the charge-charge stabilization between the electron in LUMO and the hole in the HOMO. (2) Density functional theory (DFT), which we used for calculating ΔE,(Ashraf, Pandey et al. 2009) cannot provide feasible predictive power for the energies of unoccupied orbitals, such as LUMOs. That is, DFT can provide estimates of trends in the energies of the LUMOs

within series of analogous molecules, but the absolute values of these estimates should be approached with caution.

A noticeable feature for these oligomers was the lack of considerable spectral shifts when the number of anthranilamide residues increased. While the molar extinction coefficients extrapolated to zero concentration, ε_0, increased substantially with the number of residues, the shifts in the spectral maxima did not exceed 25 nm (Table 4-1). In fact, the spectral maxima of h-AA-ph and h-AAA-ph were practically identical. These observations indicated that the excited states, involved in the optical transitions, were localized.(Bao, Ramu et al. 2010)

To experimentally test for permanent ground-state electric dipole moments, we used the Hedestrand approach employed with the Debye solvation theory, as we have previously described.(Hedestrand 1929; Debye 1945; Hill, Vaughan et al. 1969; Böttcher 1973; Böttcher and Bordewijk 1978; Breitung, Vaughan et al. 2000; Upadhyayula, Bao et al. 2011) Linear analysis of the concentration dependence of the dielectric constant and the density of diluted solutions of polar solutes in relatively non-polar solvents, provides the means for estimating the molecular dipole moments of the solutes (Figure 4-3).(Breitung, Vaughan et al. 2000; Tjahjono, Davis et al. 2007; Upadhyayula, Bao et al. 2011)

In the mM concentration range, required for this set of studies, the anthranilamides existed as aggregates. Nevertheless, an increase in the concentration of the anthranilamides caused an increase in the dielectric constant of the chloroform solutions as determined at different frequencies from capacitance measurements with a three-

terminal cell (Figure 4-3b, c).(Breitung, Vaughan et al. 2000) Because only small fraction of the anthranilamides existed as monomers at concentrations exceeding about 0.5 mM (Figure 4-2c), the observed increase in the dielectric constant was ascribed to permanent dipole moments of the aggregates. That is, the aggregation did not cancel the permanent dipoles of these conjugates, indicating that they assembled, at least partially, in a co-directional manner.

Using the Hedestrand approach, we extracted the molar polarizations, P_{2H} (per mole oligomer), from the experimental measurements that revealed the effect of the dipole moments on the dielectric properties of the solutions (Table 4-3). For comparison, we calculated the orientation polarization, $P_{2\mu}$, from the theoretically determined values of the dipole moments, μ_0, of similar anthranilamide oligomers in gas phase (Table 4-3).(Ashraf, Pandey et al. 2009) The magnitude of the measured polarization, P_{2H}, indeed, increased with an increase in the oligomer size, and theoretically predicted $P_{2\mu}$ followed the same trend.

Although a fraction of the anthranilamides existed as monomers in the mM concentration range of the dielectric measurements (Figure 4-2c),(Hong, Bao et al. 2008) we could not ascribe the experimentally obtained polarizations, P_{2H}, solely to the dipoles of the non-aggregated oligomer molecules that were free in solution. Assuming that the oligomer aggregates did not have ground-state dipoles and considering the fractions of the monomers, ξ, we estimated that the measured polarizations, P_{2H}, should result in dipole values of 38 D, 22 D, and 34 D for h-A-ph, h-AA-ph, and h-AAA-ph, respectively, which were unfeasibly large, exceeding about 3 to 9 times the theoretically

determined dipoles, μ_0 (Table 4-3). Conversely, assuming that the dipoles of the monomeric anthranilamide derivatives had values close to the theoretically estimated values of μ_0, we estimated that the non-aggregated oligomers contributed about 1.4%, 11% and 8.5% of the measured polarizations, P_{2H}, of A-ph, h-AA-ph, and h-AAA-ph, respectively. Therefore, it was the dipole moments of the aggregates that predominantly contributed to the experimentally determined polarizations, P_{2H}.

For h-A-ph, the experimentally obtained value of P_{2H} was slightly higher than $P_{2\mu}$ (Table 4-3). In the mM concentration range of the dielectric measurements only about 2% of h-A-ph existed as a monomer (Figure 4-2c), and indeed it was the aggregate that contributed to the dielectric properties of the solutions. Considering the dimerization behavior of h-A-ph (Table 4-2), we estimated that the permanent dipole moment of its aggregate was 7.5 D. Assuming that each anthranilamide molecule contributes about 4.5 D to the aggregate total dipoles (Table 4-3), the maximum dipole expected for these dimers was 9 D. That is, the experimentally obtained value was about 83% of the theoretically expected maximum value for the dimers, indicating that h-A-ph has a strong preference for aggregating in a co-directional manner.

This propensity for co-directional self-assembly of h-A-ph could be ascribed to the asymmetry in the terminal capping groups. Upon dimerization the C-terminal phenyl would have stronger aggregation propensity with another aromatic moiety, due to π-π stacking, for example, rather than for the N-terminal heptyl. Similarly, the N-terminal heptyl group would have a stronger propensity for aggregating with another alkyl, rather than with an aromatic moiety.

Considering that h-AA-ph exhibited an aggregation behavior leading to tetramers (Figure 4-2d, Table 4-2), from the measured polarization we estimated the dipole moment of its aggregate to be in the order of 13 D. Based on the calculated μ_0, the maximum possible value of the dipole of h-AA-ph tetramers was about 30 D. Similarly, the estimated value from the experimentally measured polarization for the dipole of the h-AAA-ph dimer was about 9.9 D, which was about half of the maximum possible value of 20 D for this aggregate, based on the theoretical estimate for μ_0 (Table 4-3). These findings indicated that h-AA-ph and h-AAA-ph also had propensity for aggregating in a co-directional manner that, however, was not as pronounced as the propensity exhibited by h-A-ph. The reason for this decrease in the preference of h-AA-ph and h-AAA-ph toward co-directional aggregation could be ascribed to the increase in their size. The larger number of aromatic rings in the longer oligomers would provide a means for more interactions between aromatic moieties, decreasing the relative contribution of the N-terminal heptyls toward the aggregation interactions, and hence decreasing the preference for the N-termini to aggregate with the N-termini of the other molecules, and the C-termini with C-termini.

Trends in the deshielding of the amide protons, $H^{(N)}$, as observed from their NMR chemical shifts, provided a means for estimation of the orientation of the anthranilamide dipoles. The C-terminal amide protons, H_a, which were not hydrogen-bonded, exhibited chemical shifts in the "aromatic" region, i.e., about 8 ppm (Figure 4-4). The hydrogen bonding of the rest of the amide protons, H_b, H_c, and H_d, caused deshielding and a

downfield shift in their signals, placing them in the "acid" region between 10.5 and 12.5 ppm (Figure 4-4).

Although at the concentrations we used for the NMR studies the anthranilamides existed as aggregates, each of the amide protons exhibited a single peak with a narrow Lorentzian shape. Two-dimensional (2D) NMR experiments utilizing intramolecular couplings revealed that each of these different singlets exhibited different correlation patterns, indicating that each of the peaks corresponded to only one amide proton. These findings suggested that the same amide proton, from the different molecules in an aggregate, had identical microenvironment.

To examine the effect of the anthranilamide intrinsic dipoles, we compared the chemical shifts of amide protons that belonged to the same molecule and that had identical bonding environment (i.e., identical within about one-residue radius comparable with the intramolecular NMR coupling effects we measured). The hydrogen-bonded amide protons, H_b and H_c of h-AAA-ph, were the choice for this comparison (Scheme 4-2). Both protons were in the middle of the oligomer, and each one of them was surrounded by three aromatic moieties with identical bonding pattern and orientation (Scheme 4-2). Despite their close similarity, H_b and H_c had distinctly different chemical shifts as evident from the three singlets separated from one another in the 11-13-ppm region (Figure 4-4). The difference in their chemical shifts could be ascribed to: (1) effects from the permanent electric dipole moments; and (2) differences in the microenvironments within the aggregates. The latter is not plausible because non-specific aggregation is very unlikely to provide unique microenvironment for the same proton

from different molecules in an aggregate. Therefore, it would be the intramolecular effects, along with the permanent electric dipoles, that govern the observed NMR chemical shifts.

To avoid ambiguities due to aggregation, we used only intramolecular correlations to assign the chemical shifts of the hydrogen-bonded amide protons, H_b, H_c, and H_d. Gradient-selected heteronuclear multiple bond correlation (gHMBC) allows for detecting ^{1}H-^{13}C coupling through several bonds, including through heteroatoms, such as the amide nitrogens.(Martins, Biesemans et al. 2000; Araya-Maturana, Pessoa-Mahana et al. 2008)

For acceptable signal-to-noise ratio, we carried the HMBC and the other 2D NMR measurements at about 50 mM sample concentrations. The chemical shifts of all protons except H_a, did not exhibit concentration dependence in the range from about 1 to 50 mM. The shift of the non-hydrogen bonded proton, H_a, however, moved downfield by about 0.45 ppm as the concentration increased to 50 mM (Figure 4-4, 5). Changes in the state of aggregation should affect the chemical shifts of all protons.(Jones and Vullev 2001; Jones and Vullev 2001) H_a was the most labile proton in h-AAA-ph, making it sensitive to changes in the activity of traces of water in the deuterated chloroform upon increasing the molar fraction of the anthranilamide. Therefore, this downfield shift of the signal from H_a is not an indication for changes in the state of aggregation. This observation, along with the fluorescence concentration-dependence trends (Figure 4-1c), implied that the aggregation occurred in the μM and sub-μM range.

The signal from the most downfield-shifted aliphatic protons, H_e and $H_{e'}$ at 2.4 ppm (Scheme 4-3), correlated with only one peak in the carbonyl carbon region on the HMBC

spectra (Figure 4-5a). This correlation allowed the assignment of the N-terminal carbonyl carbon C_d (Figure 4-5a). Concurrently, the N-terminal carbonyl carbon correlated with only one of the amide proton signals, at 11.2 ppm, which thus we assigned to H_d, (Scheme 4-2, 4-3)

To assign the chemical shifts of H_b and H_c of h-AAA-ph, we majorly resorted also to gHMBC (Figure 4-5). In the HMBC spectrum of h-AAA-ph, we compared the correlation peaks of the assigned terminal amide protons with the aromatic carbons in the region around 115 – 130 ppm (Figure 4-5a). The C-terminal amide proton, H_a, which was not hydrogen bonded, exhibited correlation peak with a maximum that spread between 120.9 and 121.4 ppm of the carbon shifts (Figure 4-5e). Concurrently, the N-terminal amide proton, H_d, exhibited two overlapping correlation peaks with maxima spreading between 120.5 and 121.0 ppm, and between 121.4 and 122.0 ppm (Figure 4-5d).

We examined the correlation peaks from the other two amide protons for patterns of connectivity with carbons that were about three bonds away from the H_a and H_d. The correlation peak that corresponded to the amide ^1H at 11.96 ppm, had a maximum that extended between 121.9 and 122.7 ppm (Figure 4-5c). Hence, this proton had some cross-correlation overlap with H_d, i.e., the 11.96-ppm proton and H_d could be coupled to the same carbon. Concurrently, the 11.96-ppm amide proton had no cross-correlation with H_a, i.e., no common carbon to which both of them would be coupled (Figure 4-5c, e). Therefore, we assigned the proton at 11.96 ppm to H_c (Scheme 4-2, Figure 4-4). The amide proton at 12.25 ppm had a correlation peak with a maximum intensity that spread widely between 121.1 to 122.4 ppm over the carbon shift region (Figure 4-5b). This

proton had cross-correlation with both H_a and with the proton at 11.96 ppm that we assigned to H_c. Conversely, due to the close overlap of the aromatic carbon peaks, we could not readily rule out cross-correlation between the 12.25-ppm proton and H_d. The lack of cross-correlation between the 11.96-ppm proton and H_a, however, made it implausible to assign the 11.96-ppm peak to H_b. Therefore, considering all possible coupling patterns, we assigned the peak at 11.96 ppm to H_c, and the peak at 12.25 ppm to H_b (Figure 4-4).

Because everything in the bonding patterns of H_b and H_c was identical within nearest residue range, we could ascribe the difference between the chemical shifts of these two protons to effects from the local electric field generated by the anthranilamide dipole (Scheme 4-1). As observed for polypeptide α-helices, positive polarization from the dipole electric field lowers the pK_a of protic groups, i.e., increases their acidity and causes a downfield shift in the signals from their protons.(Lockhart and Kim 1993) For h-AAA-ph, H_b is the most downfield shifted proton, i.e., about 0.3 ppm downfield from H_c. This difference in the chemical shifts indicated for more positive electric-field potential around H_b than around H_c. Because of the identity in the bonding microenvironment around these two protons, the anthranilamide dipole moment was the most plausible source for the difference in the electric potentials around H_b and H_c. Considering that the downfield shift in the H_b signal was consistent with a more positive potential than the potential around H_c, we could assign the direction of the anthranilamide dipole moment to be from the N- to the C-terminus: i.e., the negative pole of the dipole was oriented

toward the N-terminus and the positive pole – toward the C-terminus, consistent with the findings from our *ab initio* theoretical findings.(Ashraf, Pandey et al. 2009)

Conclusions

Anthranilamides possess intrinsic dipole moments and manifest a large propensity for self-assembly. The estimated dielectric properties of solutions of these conjugates, along with the lack of pronounced dependence of their spectral wavelength features on their molecular size, indicated for co-directional arrangements of these oligomers within their aggregates. NMR data elucidated that the orientation of the intrinsic dipoles is from the N- to the C-termini of the trianthranilamide oligomer. These findings demonstrate the anthranilamides as organic molecular electrets.

Experimental

Materials. Palladium (10%) on activated carbon powder was purchased from Sigma-Aldrich, 2-amino-N-phenylbenzamide (95 %), octanoyl chloride (99 %), pyridine (99.5+%), 2-nitrobenzoyl chloride (97 %), and all other reagents, including spectroscopic grade and anhydrous solvents dichloromethane (>99.8%) and N,N-Dimethylformamide (DMF, 99.8%) were used as supplied by commercial vendors.

Synthesis. The anthranilamide oligomers were synthesized from the C- to the N-termini by consequential addition of 2-nitrobenzoyl chloride and reduction of the nitro

groups to amines, preparing it for the next coupling step.(Hamuro, Geib et al. 1996) We started with 2-amino-N-phenylbenzamide as a phenyl-capped N-terminus.

General information. Proton (^{1}H) NMR spectra were recorded at 400 MHz at ambient temperature using $CDCl_3$ as solvent unless otherwise stated. Chemical shifts are reported in parts per million relative to $CDCl_3$ (^{1}H, δ 7.24; ^{13}C, δ 77.23). Data for ^{1}H NMR are reported as follows: chemical shift, integration, multiplicity (s = singlet, d = doublet, t = triplet, q = quartet, m = multiplet), integration and coupling constants. High-resolution mass-spectra were obtained on a Q-TOF mass spectrometer.(Wu, Becerril et al. 2011) Analytical thin layer chromatography was performed using 0.25 mm silica gel 60-F plates. Flash chromatography was performed using 60Å, 32-63 μm silica gel. Yields refer to chromatographically and spectroscopically pure materials, unless otherwise stated.(Jones, Yan et al. 2007) All reactions were carried out in oven-dried glassware under an argon atmosphere unless otherwise noted.

The purity of the anthranilamide oligomers was examined using TLC (normal phase), HPLC-MS (reverse phase) and melting point. For the HPLC tests, the mobile phase, 10% to 98% acetonitrile in water (+0.1 % trifluoroacetic acid), was applied as linear gradients between 0.5 and 2 ml min^{-2}, at flow rate 0.9 ml min^{-1}. The stationary phase in the column was 3 μm C8(2), 100 Å, packed in a 30×3.00 mm column (Phenomenex Luna®). Melting points were recorded using an electrothermal capillary melting point apparatus and are uncorrected. Combustion elemental analysis for carbon, hydrogen and nitrogen was conducted by Atlantic Microlab, Inc. (Norcross, GA). The samples were dried *in vacuo* for two to four hours prior to the analysis. The weight percentages for carbon, hydrogen

and nitrogen were reported. The expected values for the weight percentages were calculated from the empirical formulas using the known atomic weights.(Wieser and Coplen 2011)

2-octanamido-N-phenylbenzamide (h-A-Ph). To an ice-chilled 10 ml CH_2Cl_2 solution of 2-amino-N-phenylbenzamide (200 mg, 0.94 mmol) and pyridine (190 mg, 0.20 ml, 2.4 mmol) was added octanoyl chloride (310 mg, 1.9 mmol). The mixture was stirred at 0^{o}C to room temperature for 2 h. The reaction mixture was diluted with 50 ml CH_2Cl_2, then washed with 1N HCl (50 ml × 2), saturated $NaHCO_3$ (70 ml), and brine (50 ml). The organic layer was dried over Na_2SO_4, and concentrated *in vacuo* to afford white powder. Purification *via* flash chromatography on silica gel (100% CH_2Cl_2 to 1% MeOH in CH_2Cl_2) afforded 300 mg (0.88 mmol, 94%) of h-A-Ph (CAS# 881768-10-1), white solid: m.p. 115-118 ^{o}C. Elemental analysis, expected for $C_{21}H_{26}N_2O_2$: C, 74.52%; H, 7.74%; N, 8.28%; measured: C, 74.52%; H, 7.74%; N, 8.30%. ^{1}H NMR (400 MHz, $CDCl_3$) δ 10.65 (1 H, s), 8.55 (1 H, d, *J* = 8.4 Hz), 8.04 (1 H, s), 7.57 (3 H, t, *J* = 8.4 Hz), 7.45 (1 H, t, *J* = 8.4 Hz), 7.39 (2 H, t, *J* = 7.6 Hz), 7.19 (1 H, td, *J* = 7.6, 1.2 Hz), 7.08 (1 H, t, *J* = 7.6 Hz), 2.36 (2 H, t, *J* = 7.2 Hz), 1.70 (2 H, m), 1.40-1.20 (8 H, m), 0.84 (3 H, t, 7.2 Hz) ppm; ^{13}C NMR (100 MHz, $CDCl_3$) δ 172.69, 167.56, 139.41, 137.73, 132.73, 129.41, 127.09, 125.27, 122.99, 122.19, 121.65, 120.92, 38.63, 31.90, 29.43, 29.23, 25.70, 22.82, 14.28 ppm. HRMS m/z calculated for $C_{21}H_{26}N_2O_2Na$ (M+Na) 361.1892, found 361.1891 (M+Na).

2-nitro-N-(2-(phenylcarbamoyl)phenyl)benzamide. To an ice-chilled 100 ml CH_2Cl_2 solution of 2-amino-N-phenylbenzamide (5 g, 24 mmol) and pyridine (4.7 g, 4.8 ml, 59

mmol) was added 2-nitrobenzoyl chloride (8.7 g, 47 mmol). The mixture was stirred at 0^oC to room temperature for 2 h. The reaction mixture was diluted with 500 ml CH_2Cl_2, then washed with 1N HCl (300 ml × 2), saturated $NaHCO_3$ (300 ml), and brine (300 ml). The organic layer was dried over Na_2SO_4, and concentrated *in vacuo* to afford white solid (8.1 g, 22 mmol, 95 %). ^1H NMR (400 MHz, $CDCl_3$) δ 11.30 (1 H, s), 8.71 (1 H, d, J = 8.4 Hz), 8.04 (1 H, d, J = 8.0 Hz), 7.93 (1 H, s), 7.66 (3 H, m), 7.57 (2 H, m), 7.50 (2 H, t, J = 8.0 Hz), 7.36 (2 H, td, J = 8, 1.2 Hz), 7.19 (3 H, m) ppm.

2-octanamido-N-(2-(phenylcarbamoyl)phenyl)benzamide (h-AA-Ph). A 45 ml DMF solution of 2-nitro-N-(2-(phenylcarbamoyl)phenyl)benzamide (5 g, 14 mmol) was hydrogenated in the presence of 10% Pd/C (0.44 g) at 1 atm room temperature for 18 h. The reaction mixture was filtered through Celite. 300 ml CH_2Cl_2 was added to the filtrate which was washed with saturated $NaHCO_3$ (100 ml), and brine (100 ml). The organic layer was dried over Na_2SO_4, then concentrated in *vacuo* to afford 2-amino-N-(2-(phenylcarbamoyl)phenyl)benzamide as brown solid (3.7 g). This compound was used in the next step without any further purification.

To a 10 ml DMF solution of 2-amino-N-(2-(phenylcarbamoyl)phenyl)benzamide (1.0 g) and pyridine (0.6 ml, 7.4 mmol) was added 20 ml CH_2Cl_2 solution octanoyl chloride (1.0 g, 6.0 mmol). The mixture was stirred at room temperature for 2 h. The reaction mixture was diluted with 100 ml CH_2Cl_2, then washed with 1N HCl (50 ml × 2), saturated $NaHCO_3$ (70 ml), and brine (50 ml). The organic layer was dried over Na_2SO_4, and concentrated *in vacuo* to afford white powder. Purification *via* flash chromatography on silica gel (100% CH_2Cl_2 to 5% MeOH in CH_2Cl_2) afforded 1.2 g (2.6 mmol, 70 %

overall yield for the two steps) of h-AA-Ph, white solid: m.p. 169-171 ^{o}C. Elemental analysis, expected for $C_{28}H_{31}N_3O_3$: C, 73.50%; H, 6.83%; N, 9.18%; measured: C, 72.60%; H, 6.64%; N, 9.00%. ^{1}H NMR (400 MHz, $CDCl_3$) δ 11.81 (1 H, s), 11.20 (1 H, s), 8.66 (2 H, dd, *J* = 8.0, 8.8 Hz), 7.98 (1 H, s), 7.80 (1 H, d, *J* = 8.0 Hz), 7.67 (1 H, d, *J* = 7.6 Hz), 7.57 (3 H, m), 7.49 (1 H, t, *J* = 7.6 Hz), 7.39 (2 H, t, *J* = 8.0 Hz), 7.22 (3 H, m), 2.40 (2 H, t, *J* = 8.0 Hz), 1.72 (2 H, m), 1.40-1.20 (8 H, m), 0.84 (3 H, t, *J* = 6.4 Hz) ppm; ^{13}C NMR (100 MHz, $CDCl_3$) δ 172.42, 168.08, 167.50, 140.72, 139.47, 137.28, 133.37, 133.15, 129.46, 127.50, 127.05, 125.62, 123.91, 123.32, 122.50, 121.99, 121.65, 121.14, 120.23, 38.88, 31.90, 29.41, 29.22, 25.79, 22.82, 14.28 ppm. HRMS m/z calculated for $C_{28}H_{31}N_3O_3Na$ (M+Na) 480.2263, found 480.2284 (M+Na).

2-octanamido-N-(2-((2-(phenylcarbamoyl)phenyl)carbamoyl)phenyl)benzamide (h-AAA-Ph). To 25 ml DMF solution of 2-amino-N-(2-(phenylcarbamoyl)phenyl)benzamide (2.5 g, 7.5 mmol) and pyridine (1.5 ml, 19 mmol) was added 15 ml DMF solution of 2-nitrobenzoyl chloride (2.8 g, 15 mmol). The mixture was stirred at room temperature for 3 h. Large amount of white solid precipitated out. The solid was collected by filtration, and then washed with 1N HCl, saturated $NaHCO_3$, and water. The dried solid, 2-nitro-N-(2-((2-(phenylcarbamoyl)phenyl)carbamoyl)phenyl)benzamide (2.2 g), was used directly for the next step without further purification.

DMF solution (50 ml) of 2-nitro-N-(2-((2-(phenylcarbamoyl)phenyl)carbamoyl)phenyl)benzamide (2.2 g, 4.6 mmol) was hydrogenated in the presence of 10% Pd/C (0.5 g) at 1 atm room temperature for 48 h.

The reaction mixture was filtered through Celite. 500 ml CH_2Cl_2 was added to the filtrate, which was washed with saturated $NaHCO_3$ (200 ml), and brine (200 ml). The organic layer was dried over Na_2SO_4, then concentrated in *vacuo* to afford 2-amino-N-(2-((2-(phenylcarbamoyl)phenyl) carbamoyl) phenyl)benzamide as brown solid (0.8 g). This compound was used in the next step without any further purification.

To a 15 ml DMF solution of 2-amino-N-(2-((2-(phenylcarbamoyl)phenyl)carbamoyl)phenyl) benzamide (0.5 g, 1.1 mmol) and pyridine (0.2 g, 0.2 ml, 2.7 mmol) was added octanoyl chloride (0.36 g, 2.2 mmol). The mixture was stirred at room temperature for 3 h. The reaction mixture was diluted with 150 ml CH_2Cl_2, and washed with 1N HCl (70 ml × 2), saturated $NaHCO_3$ (100 ml), and brine (70 ml). The organic layer was dried over Na_2SO_4, and concentrated *in vacuo* to afford white powder. Purification *via* flash chromatography on silica gel (100% CH_2Cl_2 to 10% MeOH in CH_2Cl_2) afforded 0.48 g (0.8 mmol, 18% overall yield for the three steps) of h-AAA-Ph, white solid: m.p. 198-200 ^oC. Elemental analysis, expected for $C_{35}H_{36}N_4O_4$: C, 72.90%; H, 6.29%; N, 9.72%; measured: C, 72.87%; H, 6.23%; N, 9.77%. ^1H NMR (400 MHz, $CDCl_3$) δ 12.23 (1 H), 11.93 (1 H), 11.19 (1 H), 8.66 (2 H, m), 8.04 (1 H, s), 7.87 (2 H, t, J = 9.2 Hz), 7.65 (1 H, d, J = 8.0 Hz), 7.57 (4 H, m), 7.45 (1 H, t, J = 8.0 Hz), 7.28 (2 H, t, J = 7.6 Hz), 7.20 (4 H, m), 2.39 (2 H, t, J = 8.0 Hz), 1.71 (2 H, m, J = 7.6 Hz), 1.40-1.20 (8 H, m), 0.84 (3 H, t, 6.4 Hz) ppm; ^{13}C NMR (100 MHz, $CDCl_3$) δ 172.5, 168.0, 167.9, 167.6, 140.6, 140.1, 139.1, 137.4, 133.3, 133.1, 133.0, 132.7, 129.5, 127.8, 127.3, 127.2, 125.6, 124.3, 124.0, 123.2, 122.5, 122.1, 122.0, 121.7, 121.3, 120.8, 38.8,

31.9, 29.4, 29.2, 25.7, 22.8, 14.3 ppm. HRMS m/z calculated for $C_{35}H_{37}N_4O_4$(M+H) 577.2815, found 577.2819 (M+H).

Absorption and emission UV/visible spectroscopy. Steady-state UV/visible absorption spectra were recorded in a transmission mode. Steady-state and time-resolved emission measurements were conducted using a spectrofluorometer with double-grating monochromators and a single-photon-counting detector.(Wan, Ferreira et al. 2008; Bahmani, Gupta et al. 2011) For steady-state emission measurement, a long-pass glass filter was placed on the emission pathway to prevent the appearance of Rayleigh scattered excitation light at $2\times\lambda_{ex}$.(Jones and Vullev 2002; Jones and Vullev 2002; Vullev, Wan et al. 2006) For time-resolved emission measurements, a NanoLED was used for an excitation source (λ_{ex} = 278 nm; half-height pulse width, $W_{1/2}$ = 1 ns). For recording the profile of the excitation pulse (i.e., the instrument response function), we used deionized water as a scatterer, setting $\lambda_{em} = \lambda_{ex}$ = 278 nm. The fluorescence decays of anthranilamides were recorded at two emission maxima, high-energy bands (λ_{em} = 400 nm for all three anthranilamides), and red-shifted bands (λ_{em} = 545 nm for h-A-ph, λ_{em} = 520 nm for h-AA-ph and h-AAA-ph).

The fluorescence quantum yields, Φ, for different contraptions of the anthranilamide oligomers in chloroform were determined by comparing the integrated emission intensities of the samples with the integrated fluorescence of a reference sample with a known fluorescence quantum yield, Φ_0.(Demas and Crosby 1971; Valeur 2002; Wan, Ferreira et al. 2008) Extrapolations to zero and to infinity concentrations yielded,

respectively, the estimates for the quantum yields of the monomeric and aggregated forms of the oligomers. For references, we used solutions of coumarin 151 in ethanol (Φ_0 = 0.49) and phenanthrene in ethanol (Φ_0 = 0.13).(Dawson and Windsor 1968; Nad and Pal 2001; Montalti, Credi et al. 2006; Thomas, Millare et al. 2010; Brouwer 2011)

Dielectric measurements. We followed procedures as described previously to calculate the dielectric values.(Upadhyayula, Bao et al. 2011) Three-terminal capacitance sample cell connected to an ultrahigh precision Wheatstone bridge, incorporated into a precision meter via connecting cables with up to of 4-m length were used to collect capacitance data. The three-terminal sample cell electrodes were separated to 400 μm, and filled with 1.5 ml of freshly prepared sample solution. The capacitance measurements were carried at frequencies ranging from 10^4 Hz to 10^6 Hz. The capacitance of the neat solvent and of air was measured in an empty dry cell as controls.(Upadhyayula, Bao et al. 2011)

The experimentally determined dielectric values presented in the tables and figures correspond to averages of at least five repeats, where the error bars represent plus/minus one standard deviation.

Density measurements. The densities of freshly prepared anthranilamide solutions were measured with a calibrated portable density meter, recorded at 21 °C (± 0.5 °C). Before and after each measurement, the densitometer was washed several times with neat solvent, nitrogen dried, and washed with the corresponding sample solution.

Acknowledgments: This work was supported by the National Science Foundation (CBET 0935995 and CBET 0923408); the Riverside Public Utilities; and the American Public Power Association. We thank Dr. Shugeng Cao (Harvard Medical School), Dr. Yu Chen and Dr. Xiang Liu (Boston University) for helpful discussions.

Supporting Information. Copies of ^{13}C NMR spectra of h-A-ph, h-AA-ph, and h-AAA-ph. This material is available free of charge via the Internet at http://pubs.acs.org

Tables:

Table 4-1. Photophysical properties of the anthranilamide oligomers.[a]

	λ_{abs} / nm	ε_0 / M^{-1} cm^{-1} [b]	λ_{em} / nm	τ / ns [c]	Φ_m ($\times 10^2$) [d]	Φ_a ($\times 10^2$) [d]	E_{00} / eV [e]	ΔE / eV [f]
h-A-ph	305; 260	4,300	390; 545	0.594	10 ± 1	0.45 ± 0.14	3.6	4.9
h-AA-ph	320; 262	11,000	400; 520	1.27	0.94 ± 0.08	0.51 ± 0.04	3.5	4.3
h-AAA-ph	325; 260	24,000	400; 520	1.36	1.7 ± 0.7	0.54 ± 0.22	3.5	4.1

[a] Experimental data from UV/visible absorption and emission measurements of chloroform solutions of anthranilamides.

[b] Extinction coefficients, extrapolated to zero concentration, from nonlinear fits of the absorption at the low-energy maxima (305 and 320 nm) vs. concentration.

[c] Lifetimes from time-correlated single-photon-counting measurements, samples excited at 278 nm and emission monitored at the low-energy aggregate bands (545 for h-A-ph; and 520 nm for h-AA-ph and h-AAA-ph).

[d] Φ_m and Φ_a are the emission quantum yields of monomeric and aggregated forms of the anthranilamide conjugates, respectively, obtained from extrapolation to zero and infinity concentrations.

[e] Zero-to-zero energies were estimated from the cross-points of normalized absorption and emission spectra at lowest attainable concentrations.

[f] Theoretically calculated HOMO-LUMO gaps, i.e., molecular "band gaps," from reference (Ashraf, Pandey et al. 2009).

Table 4-2. Linear analysis of lg($C(1-\xi)$) vs. lg($C\xi$), implementing eq. 3.

	Fitting range [a]	n [b]	d [c]	*Accept* H_0? [d]
h-A-ph	0.5 μM – 10 mM	1.29 ± 0.14	0.823	no
	0.5 μM – 25 μM	1.65 ± 0.39	2.08	yes
	25 μM – 10 mM	1.02 ± 0.16	2.36	yes
h-AA-ph	0.1 μM – 10 mM	1.27 ± 0.12	0.406	no
	0.1 μM – 1 μM	4.10 ± 0.89	1.95	yes
	1 μM – 10 mM	1.05 ± 0.07	2.01	yes
h-AAA-ph	0.1 μM – 10 mM	1.30 ± 0.11	1.02	inconclusive
	0.1 μM – 25 μM	2.16 ± 0.42	2.15	yes
	25 μM – 10 mM	1.10 ± 0.12	1.92	yes

[a] Concentration ranges of the linear fits: (1) the whole concentration range; (2) the range of low concentrations, and (3) the range of the high concentrations.

[b] State of aggregation from the slopes of the linear fits (eq. 3).

[c] Durbin-Watson statistics: $d = \frac{\sum_{i=1}^{n-1}(\delta_{i+1} - \delta_i)^2}{\sum_{i=1}^{n}\delta_i^2}$, where δ_i are the residuals from the data fits, and d can assume values between 0 and 4. Values of d close to 2 signifies no autocorrelation, d close to 0 or 4 indicates a positive or negative autocorrelation, respectively.

[d] Results from testing of the null hypothesis, H_0: no autocorrelation between the residuals from the data fits. The testing of H_0 involved comparison of d with the upper and lower critical limits, $d_{U,\alpha}$ and $d_{L,\alpha}$, respectively, for $\alpha = 0.05$. If $d_{U,0.5} < d < (4 - d_{U,0.5})$, H_0 was accepted. If $d < d_{L,0.5}$ or $d > (4 - d_{L,0.5})$, the counter hypothesis was accepted. If $d_{L,0.5} \leq d \leq d_{U,0.5}$ or $(4 - d_{U,0.5}) \leq d \leq (4 - d_{L,0.5})$, the test was inconclusive.

Table 4-3. Measured and calculated molar polarizations, P_2, of the anthranilamide oligomers.

	P_{2H} / $cm^3\ mol^{-1}$ [a]	μ_0 / D [b]	$P_{2\mu}^{(0)}$ / $cm^3\ mol^{-1}$ [c]
h-A-ph	580 ± 90	4.5	421
h-AA-ph	800 ± 50	7.5	1,170
h-AAA-ph	1,020 ± 310	10	2,080

[a] Experimental estimated polarizations, using Hedestrand (H) approach, from dielectric and density data for chloroform solutions of anthranilamides. The values are reported per mole of oligomer.(Hu, Xia et al. 2009; Upadhyayula, Bao et al. 2011)

[b] Theoretically calculated dipole moments for gas phase from reference (Ashraf, Pandey et al. 2009).

[c] Theoretically obtained orientation polarization, $P\mu$, from the calculated dipole moments: $P_{2\mu}^{(0)} = \mu_0^2\ N_A / 9\ \varepsilon_0\ k_B\ T$.(Upadhyayula, Bao et al. 2011)

Scheme 4-1. Origin of the intrinsic dipole moment of anthranilamides.

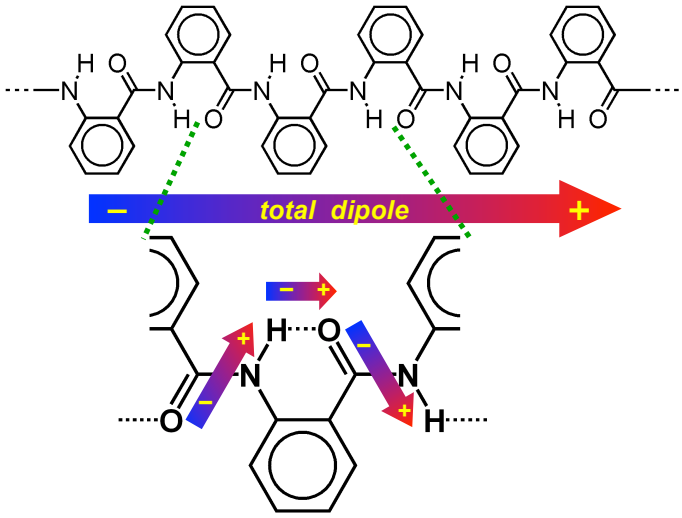

Scheme 4-2. Anthranilamide oligomers with highlighted hydrogen-bonded (red) and non-hydrogen-bonded (blue) protons.

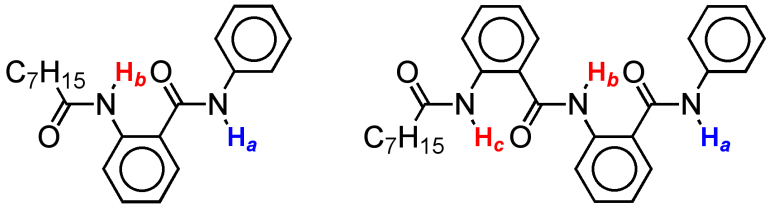

h-A-ph

h-AA-ph

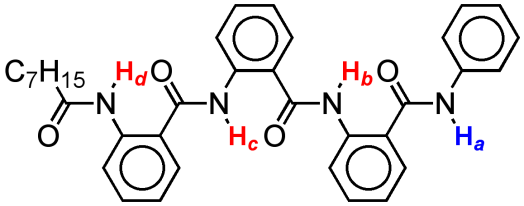

h-AAA-ph

Scheme 4-3. Trianthranilamide, h-AAA-ph, with highlighted protons used for establishing the connectivity patterns in the NMR analysis.

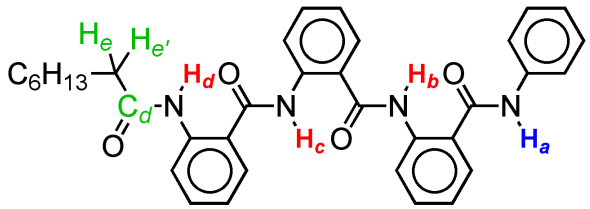

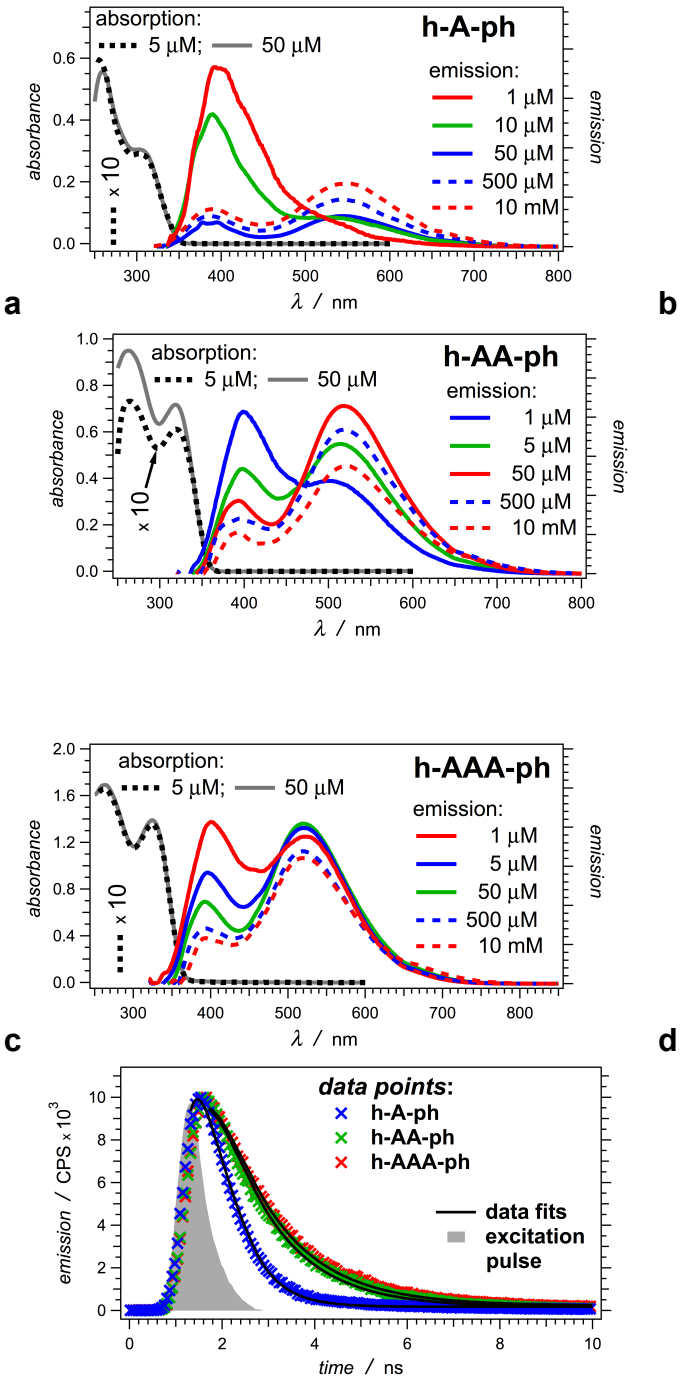
absorption:
5 µM; 50 µM
h-A-ph
emission:
1 µM
10 µM
50 µM
500 µM
10 mM
absorbance
emission
x 10
λ / nm
a
b
absorption:
5 µM; 50 µM
h-AA-ph
emission:
1 µM
5 µM
50 µM
500 µM
10 mM
absorbance
emission
x 10
λ / nm
absorption:
5 µM; 50 µM
h-AAA-ph
emission:
1 µM
5 µM
50 µM
500 µM
10 mM
absorbance
emission
x 10
λ / nm
c
d
data points:
h-A-ph
h-AA-ph
h-AAA-ph
data fits
excitation pulse
emission / CPS x 10^3
time / ns

Figure 4-1

Figure 4-1. Absorption and emission properties of the anthranilamide oligomers. **(a-c)** Steady-state absorption and emission spectra (chloroform solutions; l_{ex} = 305 nm). The absorption spectra for 5 mM concentrations were scaled up by a factor of 10 for comparison with the absorption spectra for 50 mM concentrations. The emission spectra for concentrations exceeding 10^{-4} M were recorded using small-angle fluorescence spectroscopy.(Mayers, Vezenov et al. 2005; Wan, Thomas et al. 2009; Lu, Bao et al. 2010; Thomas, Clift et al. 2010; Ghazinejad, Kyle et al. 2012; Upadhyayula, Quinata et al. 2012) **(d)** Time-resolved emission decays recorded at the low-energy bands, i.e., at 545 nm for h-A-ph, and at 520 nm for h-AAA-ph (l_{ex} = 278 nm, half-height pulse width = 1 ns).

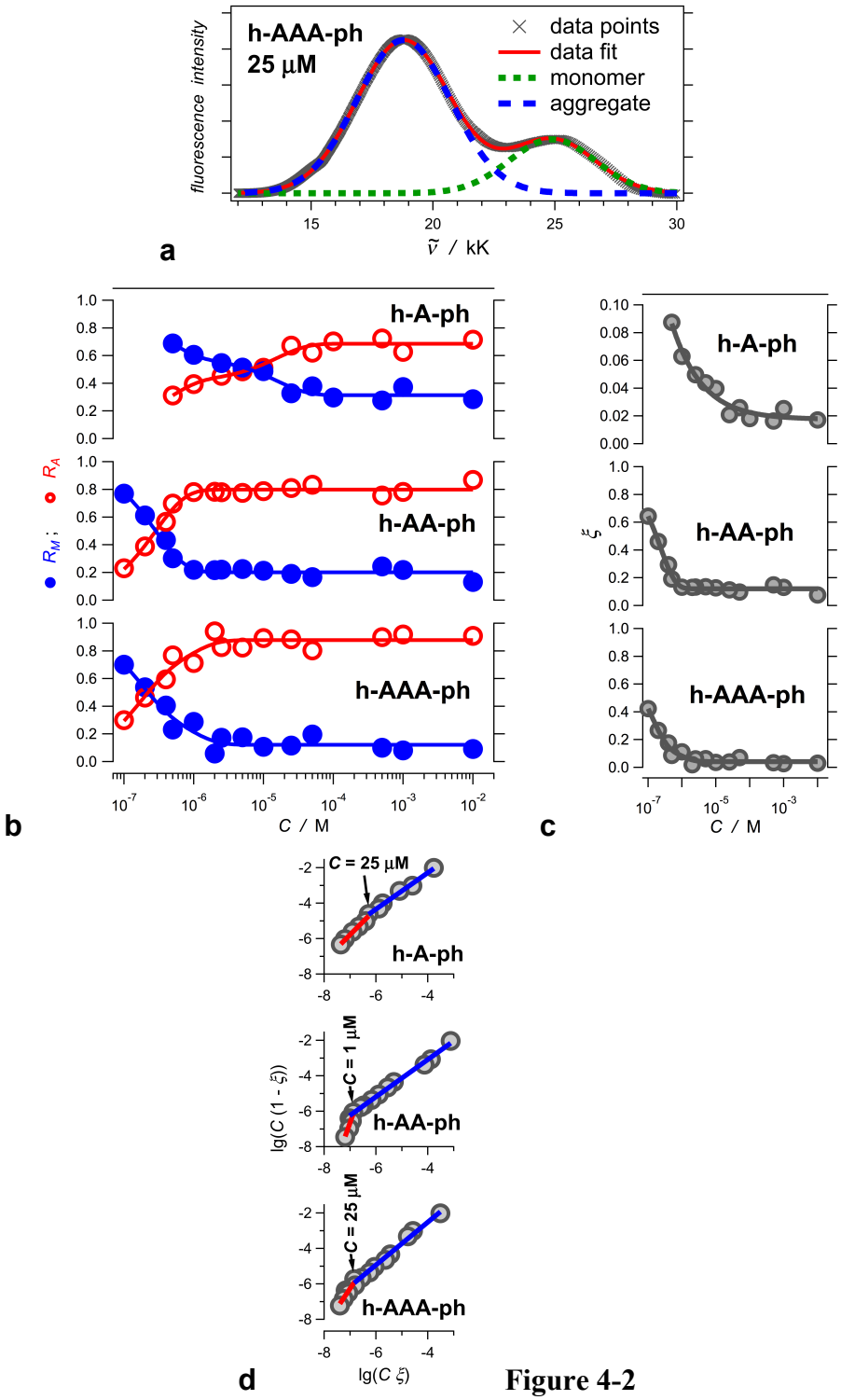
a
h-AAA-ph
25 µM
data points
data fit
monomer
aggregate
fluorescence intensity
15
20
25
30
ν̃ / kK
b
h-A-ph
h-AA-ph
h-AAA-ph
R_M ; R_A
C / M
c
h-A-ph
h-AA-ph
h-AAA-ph
ξ
C / M
d
C = 25 µM
h-A-ph
C = 1 µM
h-AA-ph
C = 25 µM
h-AAA-ph
lg(C (1 - ξ))
lg(C ξ)

Figure 4-2

Figure 4-2. Concentration dependence of the emission properties of the anthranilamide oligomers. **(a)** A representative example of deconvolution of a fluorescence spectrum using a sum of two Gaussian functions. To plot the spectrum versus energy, i.e., vs. wavenumber, $\tilde{\nu}$, instead of vs. wavelength, *l*, we converted the fluorescence intensity accordingly, $F_{\tilde{\nu}}(\tilde{\nu}) = \lambda^2 F_{\lambda}(\lambda)$.(Valeur 2002) **(b)** Concentration dependence of the fractions of the monomer, R_m, and aggregate, R_a, emission (eq. 1). **(c)** Concentration dependence of the monomer fractions, *x* (eq. 2). **(d)** Linear analysis of lg(*C*(1-*x*)) vs. lg(*Cx*) (eq. 3). The gray circles designate the data points; and the red and blue lines – the linear data fits at low and high concentrations, respectively.

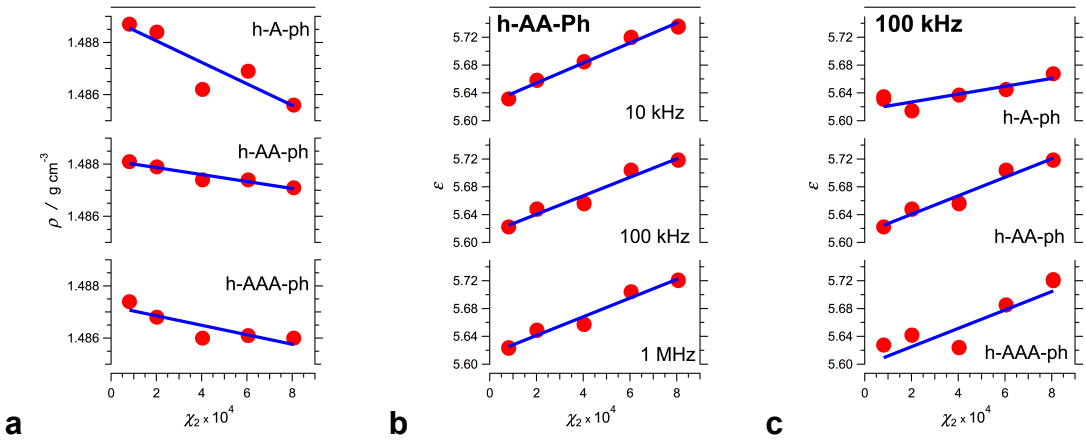
a
b
c
h-A-ph
h-AA-ph
h-AAA-ph
h-AA-Ph
10 kHz
100 kHz
1 MHz
100 kHz
h-A-ph
h-AA-ph
h-AAA-ph
ρ / g cm-3
ε
χ2 x 10^4

Figure 4-3

Figure 4-3. Dependence of **(a)** the density, r, and **(b, c)** the dielectric properties of anthranilamide solutions in chloroform on the oligomer molar fraction, c_2. **(b)** Dielectric constant, e, of h-AA-ph solutions extracted from capacitance measurements at different frequencies. **(c)** e of solutions of the three oligomers extracted from capacitance measurements at 100 kHz.

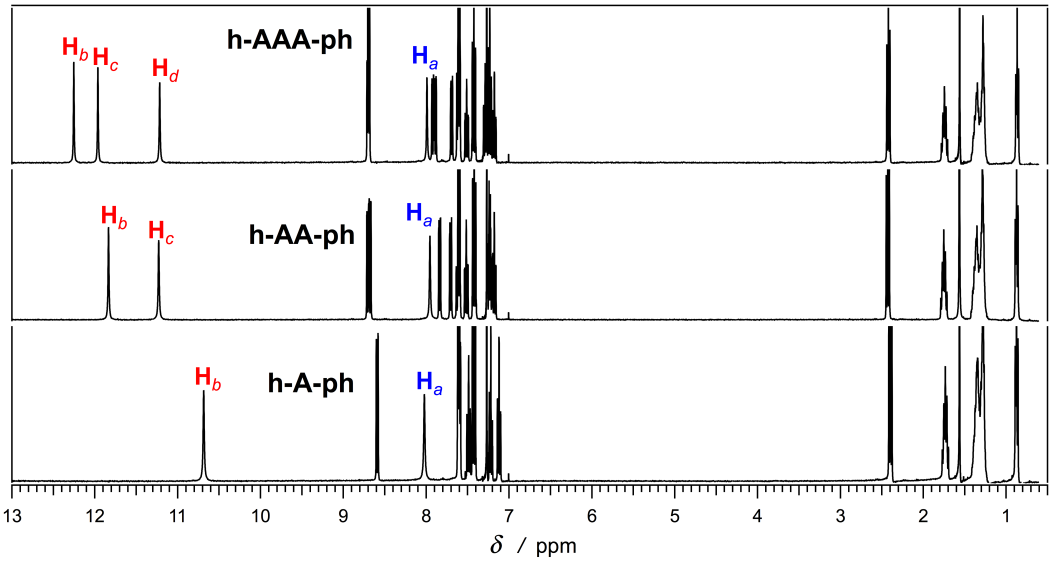
h-AAA-ph
h-AA-ph
h-A-ph
H_b H_c
H_d
H_a
H_b H_c
H_a
H_b
H_a
13 12 11 10 9 8 7 6 5 4 3 2 1
δ / ppm

Figure 4-4

Figure 4-4. ^{1}H-NMR spectra of the three anthranilamide oligomers with assignments of the peaks corresponding to the amide protons. (2 mM in $CDCl_3$; 400 MHz)

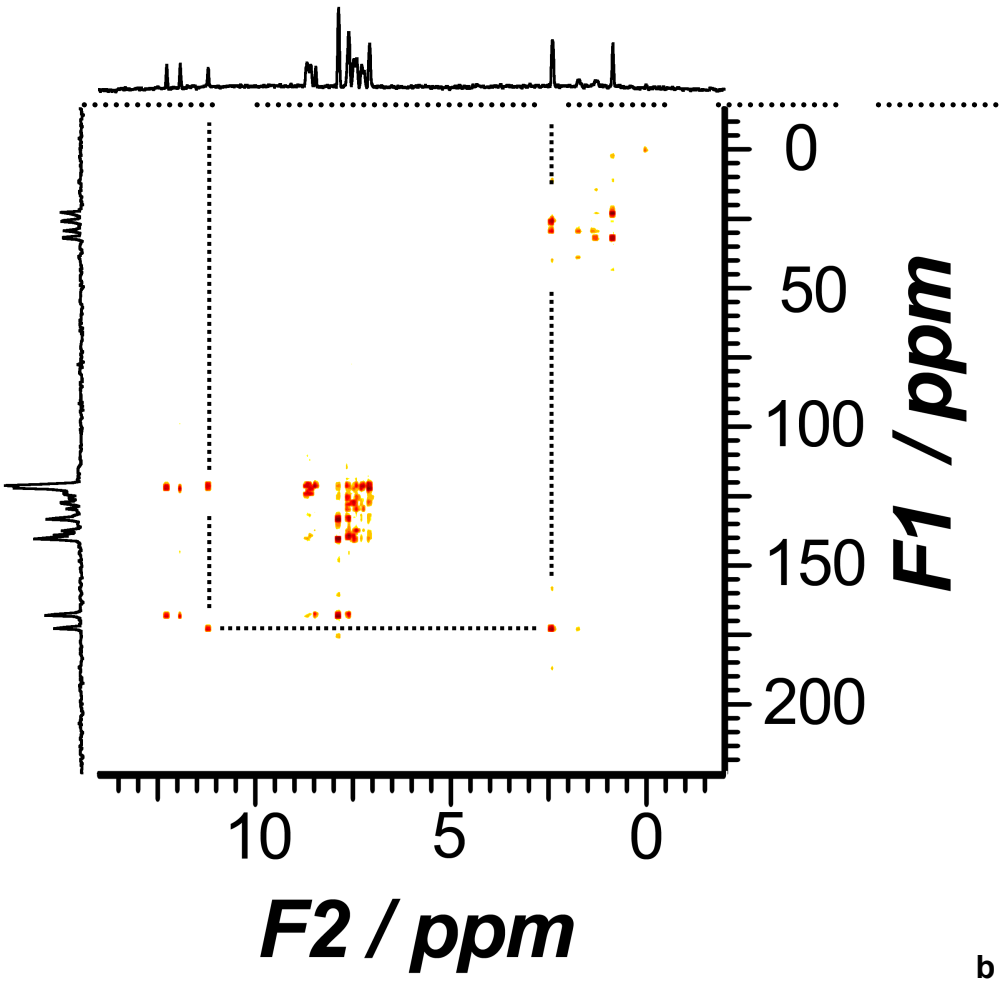

a b

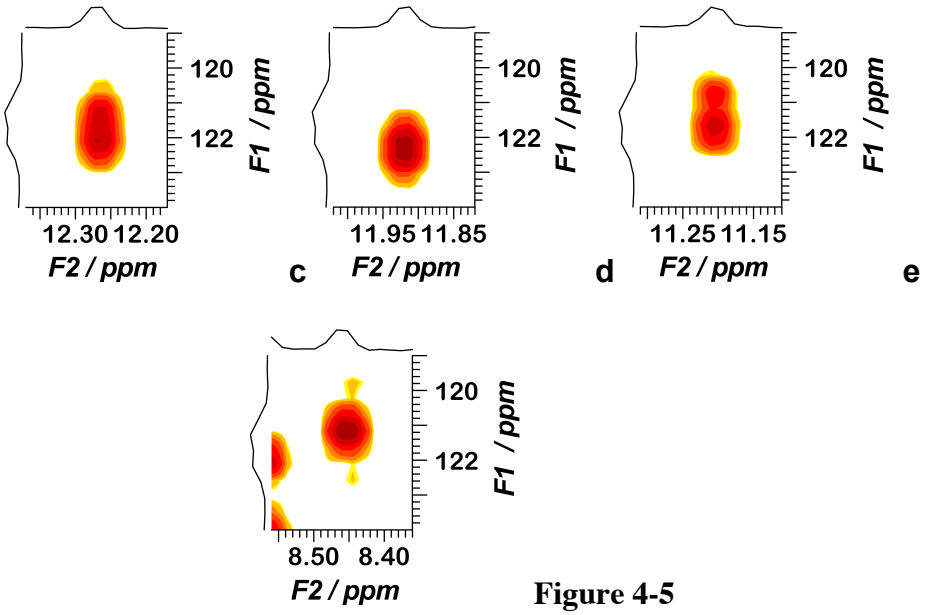

Figure 4-5

Figure 4-5. ^{1}H-^{13}C gHMBC spectrum of h-AAA-ph (2 mM in $CDCl_3$; 400 MHz). **(a)** The full spectral range with ^{2}J correlations (indicated with the gray lines) between $^{1}H_e$/$^{1}H_{e'}$ and $^{13}C_d$ and between $^{13}C_d$ and $^{1}H_d$ (Scheme 4-3). **(b-e)** Zoomed ^{3}J correlation peaks between the amide protons and the carbons three bonds away. The peaks at: **(b)** 12.3 ppm; **(c)** 11.9 ppm; **(d)** 11.2 ppm; and **(e)** 8.45 ppm.

REFERENCES

Araya-Maturana, R., H. Pessoa-Mahana, et al. (2008). "Very long-range correlations (nJC,H n > 3) in HMBC spectra." Nat. Prod. Commun. **3**(3): 445-450.

Ashraf, M. K., R. R. Pandey, et al. (2009). "Theoretical design of bioinspired macromolecular electrets based on anthranilamide derivatives." Biotechnol. Prog. **25**(4): 915-922.

Bahmani, B., S. Gupta, et al. (2011). "Effect of polyethylene glycol coatings on uptake of indocyanine green loaded nanocapsules by human spleen macrophages in vitro." J. Biomed. Opt. **16**(5): 051303/051301-051303/051310.

Bao, D., B. Millare, et al. (2009). "Electrochemical Oxidation of Ferrocene: A Strong Dependence on the Concentration of the Supporting Electrolyte for Nonpolar Solvents." J. Phys. Chem. A **113**(7): 1259-1267.

Bao, D., S. Ramu, et al. (2010). "Electrochemical Reduction of Quinones: Interfacing Experiment and Theory for Defining Effective Radii of Redox Moieties." J. Phys. Chem. B **114**(45): 14467-14479.

Beratan, D. N., J. N. Onuchic, et al. (1992). "Electron-Tunneling Pathways in Proteins." Science **258**(5089): 1740-1741.

Böttcher, C. J. F. (1973). Theory of Electric Polarization, Elsevier Scientific Publishing Company.

Böttcher, C. J. F. and P. Bordewijk (1978). Theory of Electric Polarization, Elsevier Scientific Publishing Company.

Breitung, E. M., W. E. Vaughan, et al. (2000). "Measurement of solute dipole moments in dilute solution: A simple three-terminal cell." Rev. Sci. Instrum. **71**(1): 224-227.

Brouwer, A. M. (2011). "Standards for photoluminescence quantum yield measurements in solution (IUPAC Technical Report)." Pure and Applied Chemistry **83**(12): 2213-2228.

Colombo, S., C. Coluccini, et al. (2010). "Shape selectivity in the synthesis of chiral macrocyclic amides." Tetrahedron **66**(23): 4206-4211.

Coluccini, C., A. Mazzanti, et al. (2010). "Locked chromophores as CD and NMR probes for the helical conformation of tetraamidic macrocycles." Organic & Biomolecular Chemistry **8**(8): 1807-1815.

Dawson, W. R. and M. W. Windsor (1968). "Fluorescence Yields of Aromatic Compounds." J. Phys. Chem. **72**(9): 3251-3260.

Debye, P. J. W. (1945). Polar Molecules, Dover Publications, Inc., NY.

Demas, J. N. and G. A. Crosby (1971). "Measurement of Photoluminescence Quantum Yields - Review." Journal of Physical Chemistry **75**(8): 991-&.

Doyle, D. A., J. M. Cabral, et al. (1998). "The structure of the potassium channel: Molecular basis of K+ conduction and selectivity." Science **280**(5360): 69-77.

Dutzler, R., E. B. Campbell, et al. (2002). "X-ray structure of a CIC chloride channel at 3.0 angstrom reveals the molecular basis of anion selectivity." Nature **415**(6869): 287-294.

Eaton, D. F. (1990). "Recommended methods for fluorescence decay analysis." Pure Appl. Chem. **62**(8): 1631-1648.

Erhard, D. P., D. Lovera, et al. (2010). "Recent advances in the improvement of polymer electret films." Adv. Polym. Sci. **228**(Complex Macromolecular Systems II): 155-207.

Fox, M. A. and E. Galoppini (1997). "Electric Field Effects on Electron Transfer Rates in Dichromophoric Peptides: The Effect of Helix Unfolding." J. Am. Chem. Soc. **119**(23): 5277-5285.

Galoppini, E. and M. A. Fox (1996). "Effect of the Electric Field Generated by the Helix Dipole on Photoinduced Intramolecular Electron Transfer in Dichromophoric alpha - Helical Peptides." J. Am. Chem. Soc. **118**(9): 2299-2300.

Garcia, H. (2011). "Toward Efficient Solar Light Hydrogen Generation from Water. Bioinspiration and Structuring by Zeolites." Journal of Physical Chemistry Letters **2**(5): 520-521.

Ghazinejad, M., J. R. Kyle, et al. (2012). "Non-Invasive High-Throughput Metrology of Functionalized Graphene Sheets." Adv. Funct. Mater. **22**(21): 4519-4525.

Gong, B. (2008). "Hollow Crescents, Helices, and Macrocycles from Enforced Folding and Folding-Assisted Macrocyclization." Accounts of Chemical Research **41**(10): 1376-1386.

Gray, H. B. and J. R. Winkler (2005). "Long-range electron transfer." Proceedings of the National Academy of Sciences of the United States of America **102**(10): 3534-3539.

Hamuro, Y., S. J. Geib, et al. (1996). "Oligoanthranilamides. Non-Peptide Subunits That Show Formation of Specific Secondary Structure." Journal of the American Chemical Society **118**(32): 7529-7541.

Hamuro, Y. and A. D. Hamilton (2001). "Functionalized oligoanthranilamides: modular and conformationally controlled scaffolds." Bioorganic & Medicinal Chemistry **9**(9): 2355-2363.

Hedestrand, G. (1929). "Calculation of the molecular polarization of dissolved substances at infinite dilution." Z. Physik. Chem. **2**(Abt. B): 428-444.

Hill, N. E., W. E. Vaughan, et al. (1969). Dielectric Properties and Molecular Behavior (The Van Nostrand Series in Physical Chemistry), Van Nostrand Reinhold Company Ltd.

Hisamatsu, H. and K. Maekawa (1994). "The Distribution of the Durbin-Watson Statistic in Integrated and near-Integrated Models." Journal of Econometrics **61**(2): 367-382.

Hol, W. G. J., P. T. Van Duijnen, et al. (1978). "The alpha -helix dipole and the properties of proteins." Nature **273**(5662): 443-446.

Hong, C., D. Bao, et al. (2008). "Print-and-Peel Fabrication of Microelectrodes." Langmuir **24**(16): 8439-8442.

Hu, J., B. Xia, et al. (2009). "Long-Lived Photogenerated States of alpha -Oligothiophene-Acridinium Dyads Have Triplet Character." J. Phys. Chem. A **113**(13): 3096-3107.

Jones, G., II, L. N. Lu, et al. (1995). "Photoactive peptides. 6. Photoinduced electron transfer for pyrenesulfonamide conjugates of tryptophan-containing peptides. Mitigation of fluoroprobe behavior in N-terminal labeling experiments." Bioorg. Med. Chem. Lett. **5**(20): 2385-2390.

Jones, G., II, V. Vullev, et al. (2000). "Multistep Photoinduced Electron Transfer in a de Novo Helix Bundle: Multimer Self-Assembly of Peptide Chains Including a Chromophore Special Pair." J. Am. Chem. Soc. **122**(2): 388-389.

Jones, G., II and V. I. Vullev (2001). "Contribution of a Pyrene Fluorescence Probe to the Aggregation Propensity of Polypeptides." Org. Lett. **3**(16): 2457-2460.

Jones, G., II and V. I. Vullev (2001). "Ground- and Excited-State Aggregation Properties of a Pyrene Derivative in Aqueous Media." J. Phys. Chem. A **105**(26): 6402-6406.

Jones, G., II and V. I. Vullev (2002). "Medium effects on the photophysical properties of terbium(III) complexes with pyridine-2,6-dicarboxylate." Photochem. Photobiol. Sci. **1**(12): 925-933.

Jones, G., II and V. I. Vullev (2002). "Medium Effects on the Stability of Terbium(III) Complexes with Pyridine-2,6-dicarboxylate." J. Phys. Chem. A **106**(35): 8213-8222.

Jones, G., II and V. I. Vullev (2002). "Photoinduced Electron Transfer between Non-Native Donor-Acceptor Moieties Incorporated in Synthetic Polypeptide Aggregates." Org. Lett. **4**(23): 4001-4004.

Jones, G., II, D. Yan, et al. (2007). "Photoinduced Electron Transfer in Arylacridinium Conjugates in a Solid Glass Matrix." J. Phys. Chem. B **111**(24): 6921-6929.

Jones, G., II, X. Zhou, et al. (2003). "Photoinduced electron transfer in alpha -helical polypeptides: dependence on conformation and electron donor-acceptor distance." Photochem. Photobiol. Sci. **2**(11): 1080-1087.

Kepler, R. G. (1978). "Piezoelectricity, pyroelectricity, and ferroelectricity in organic materials." Annu. Rev. Phys. Chem. **29**: 497-518.

Lockhart, D. J. and P. S. Kim (1993). "Electrostatic Screening of Charge and Dipole Interactions with the Helix Backbone." Science **260**(5105): 198-202.

Lu, H., D. Bao, et al. (2010). "Pyridine-coated lead sulfide quantum dots for polymer hybrid photovoltaic devices." Adv. Sci. Lett. **3**(2): 101-109.

Martins, J. C., M. Biesemans, et al. (2000). "Tin NMR based methodologies and their use in structural tin chemistry." Prog. Nucl. Magn. Reson. Spectrosc. **36**(4): 271-322.

Mayers, B. T., D. V. Vezenov, et al. (2005). "Arrays and Cascades of Fluorescent Liquid-Liquid Waveguides: Broadband Light Sources for Spectroscopy in Microchannels." Anal. Chem. **77**(5): 1310-1316.

Montalti, M., A. Credi, et al. (2006). Handbook of Photochemistry, CRC Press.

Nad, S. and H. Pal (2001). "Unusual photophysical properties of coumarin-151." Journal of Physical Chemistry A **105**(7): 1097-1106.

Rutledge, D. N. and A. S. Barros (2002). "Durbin-Watson statistic as a morphological estimator of information content." Analytica Chimica Acta **454**(2): 277-295.

Shih, C., A. K. Museth, et al. (2008). "Tryptophan-Accelerated Electron Flow Through Proteins." Science **320**(5884): 1760-1762.

Shin, Y.-G. K., M. D. Newton, et al. (2003). "Distance Dependence of Electron Transfer Across Peptides with Different Secondary Structures: The Role of Peptide Energetics and Electronic Coupling." J. Am. Chem. Soc. **125**(13): 3722-3732.

Suzuki, Y. (2011). "Recent progress in MEMS electret generator for energy harvesting." IEEJ Trans. Electr. Electron. Eng. **6**(2): 101-111.

Thomas, M. S., J. M. Clift, et al. (2010). "Print-and-Peel Fabricated Passive Micromixers." Langmuir **26**(4): 2951-2957.

Thomas, M. S., B. Millare, et al. (2010). "Print-and-peel fabrication for microfluidics: what's in it for biomedical applications?" Ann Biomed Eng **38**(1): 21-32.

Tjahjono, M., T. Davis, et al. (2007). "Three-terminal capacitance cell for stopped-flow measurements of very dilute solutions." Rev. Sci. Instrum. **78**(2): 023902/023901-023902/023906.

Upadhyayula, S., D. Bao, et al. (2011). "Permanent Electric Dipole Moments of Carboxyamides in Condensed Media: What Are the Limitations of Theory and Experiment?" J. Phys. Chem. B **115**(30): 9473-9490.

Upadhyayula, S., T. Quinata, et al. (2012). "Coatings of Polyethylene Glycol for Suppressing Adhesion between Solid Microspheres and Flat Surfaces." Langmuir **28**(11): 5059-5069.

Valeur, B. (2002). Molecular Fluorescence, Principles and Applications, WILEY-VCH.

Vasquez, J. M., A. Vu, et al. (2009). "Fluorescence enhancement of warfarin induced by interaction with beta -cyclodextrin." Biotechnol. Prog. **25**(4): 906-914.

Vullev, V. I. (2011). "From Biomimesis to Bioinspiration: What's the Benefit for Solar Energy Conversion Applications?" J. Phys. Chem. Lett. **2**(5): 503–508.

Vullev, V. I., H. Jiang, et al. (2005). "Excimer sensing." Top. Fluoresc. Spectrosc. **10**(Advanced Concepts in Fluorescence Sensing, Part B): 211-239.

Vullev, V. I. and G. Jones (2002). "Photoinduced electron transfer in alkanoylpyrene aggregates in conjugated polypeptides." Tetrahedron Lett. **43**(47): 8611-8615.

Vullev, V. I. and G. Jones, II (2002). "Photoinduced charge transfer in helical polypeptides." Res. Chem. Intermed. **28**(7-9): 795-815.

Vullev, V. I., J. Wan, et al. (2006). "Nonlithographic Fabrication of Microfluidic Devices." J. Am. Chem. Soc. **128**(50): 16062-16072.

Wan, J., A. Ferreira, et al. (2008). "Solvent dependence of the charge-transfer properties of a quaterthiophene-anthraquinone dyad." J. Photochem. Photobiol., A **197**(2-3): 364-374.

Wan, J., M. S. Thomas, et al. (2009). "Surface-bound proteins with preserved functionality." Ann. Biomed. Eng. **37**(6): 1190-1205.

Wieser, M. E. and T. B. Coplen (2011). "Atomic weights of the elements 2009 (IUPAC Technical Report)." Pure and Applied Chemistry **83**(2): 359-396.

Wu, J., J. Becerril, et al. (2011). "Sequential Transformations to Access Polycyclic Chemotypes: Asymmetric Crotylation and Metal Carbenoid Reactions." Angewandte Chemie-International Edition **50**(26): 5938-5942.

Xia, B., S. Upadhyayula, et al. (2011). "Amyloid histology stain for rapid bacterial endospore imaging." J. Clin. Microbiol. **49**(8): 2966-2975.

Yasutomi, S., T. Morita, et al. (2004). "A Molecular Photodiode System That Can Switch Photocurrent Direction." Science **304**(5679): 1944-1947.

Zhu, J., X.-Z. Wang, et al. (2004). "Hydrogen-Bonding-Induced Planar, Rigid, and Zigzag Oligoanthranilamides. Synthesis, Characterization, and Self-Assembly of a Metallocyclophane." Journal of Organic Chemistry **69**(19): 6221-6227.

Appendix

Appendix: Chapter 5

Microfluidic space-domain time-resolved emission spectroscopy of terbium (III) and europium (III) chelates with pyridine-2,6-dicarboxylate

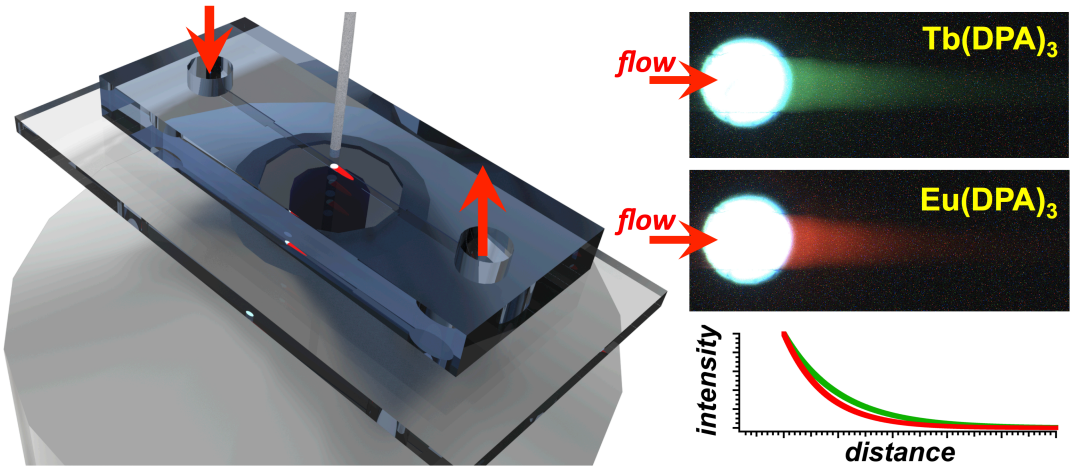

ABSTRACT

This article describes the utilization of laminar microflows for time-resolved emission measurements with steady-state excitation and detection. Passing a laminar flow through a short illuminated section of a microchannel provided a means for pulsed-like photoexcitation of the moieties carried by the fluid. Imaging the microchannel flows carrying thus photoexcited chelates of lanthanide ions allowed us to extract their excited-state lifetimes from the spatial distribution of the changes in the emission intensity. The lifetime values obtained using this space-domain approach agreed well with the lifetimes from time-domain measurements. This validated space-domain microfluidic approach reveals a means for miniaturization of time-resolved emission spectroscopy.

KEYWORDS: laminar flow, flow rate, flow velocity, lanthanides, luminescence, dipicolinic acid

Introduction

Currently, the experimental determination of emission lifetimes requires time-domain or frequency-domain approaches.(Lakowicz 2006; Wróbel, Dudkowiak et al. 2010) Time-domain measurements involve excitation with short pulses and monitoring of radiative decays with fast detectors.(Birch and Imhof 1991) Conversely, frequency-domain measurements yield lifetimes from the phase shifts and the demodulation of emission signals recorded during photoexcitation with radio-frequency-modulated illumination.(Gratton, Jameson et al. 1984)

Extracting temporal information from spatial distribution of optical signals benefited the development of ultrafast time-resolved spectroscopy. Pump-probe and streak-camera techniques utilizing a control of spatial delays for pulses (traveling with the speed of light) provide the means for pico- femto- and atosecond temporal resolution.(Campillo and Shapiro 1983; Beeby 2002; Fushitani 2008; Wan, Ferreira et al. 2008; Nisoli and Sansone 2009) Such ultrafast techniques, however, are unfeasible for nanosecond and longer time domains.

Microfluidics (μFLs) presents an alternative for time-resolved spectroscopy by employing excitation and imaging, both operating solely in a steady-state mode.(Song, Chen et al. 2006; Ristenpart, Wan et al. 2008) Flow velocities in the range of cm s^{-1} to m s^{-1}, readily attainable in μFLs, provide the means for observable spatial displacement that correspond to micro- and millisecond time domains: i.e., time-domains that are too slow for ultrafast spectroscopy and too fast for traditional steady-state techniques.(Beeby

2002; Thomas, Millare et al. 2010) Inherently, μFLs offers venues for miniaturization and for field-deployable technologies.

Fast mixing in microchannels, followed by monitoring the appearance of the microflows down the stream, allows for kinetic measurements with millisecond resolution.(Song and Ismagilov 2003; Bringer, Gerdts et al. 2004; Song, Chen et al. 2006) A control of the flow rates provides a means for converting the distance along an imaged microchannel into time scales.(Song and Ismagilov 2003) The speed of mixing, the flow rates, and the spatial imaging resolution control the limits of the temporal resolution of such space-domain measurements.

Pyridine-2,6-dicarboxylic acid, i.e., dipicolinic acid (DPA) is a natural product present solely in bacterial endospores,(Slieman and Nicholson 2001; Setlow 2011) and has a high affinity for lanthanide ions, Ln^{3+}.(Jones and Vullev 2002; Cable, Kirby et al. 2009) In such Ln^{3+} chelates, the DPA ligands act as photo-sensitizers, allowing access to spin-forbidden radiative-decay transitions of the chelated ions. Thus, the complexation of Tb^{3+}, Eu^{3+} and other lanthanide ions with DPA, which enhances their emission, offers a key handle for biosensing of bacterial endospores.(Rosen, Sharpless et al. 1997; Pellegrino, Fell et al. 1998; Rosen 1998; Hindle and Hall 1999; Rosen 1999; Rosen 2006; Cable, Kirby et al. 2007; Yung, Lester et al. 2007; Yung, Shafaat et al. 2007; Li, Dasgupta et al. 2008; Yung and Ponce 2008; Cable, Kirby et al. 2009; Yang and Ponce 2009; Ammann, Kolle et al. 2011; Yang and Ponce 2011) Furthermore, the emission lifetimes of such complexes strongly depend on the number of ligands chelating the metal ions.(Jones and Vullev 2002)

Herein, we explore the use of laminar microflows for time-resolved emission spectroscopy employing steady-state imaging. Continuous-waveform (CW) illumination of a short stretch of a microchannel caused a pulse-like excitation of chromophores carried by the flow through the illuminated region (Scheme 5-1). Epifluorescence imaging of microflows after such confined CW illumination revealed the progress of the radiative deactivation of the excited states of complexes of terbium, Tb^{3+}, and europium, Eu^{3+}, ions with DPA. Comparison of the obtained space-domain emission lifetimes with previously reported time-domain measurements(Horrocks and Sudnick 1979; Jones and Vullev 2002; George, Golden et al. 2006; Cable, Kirby et al. 2007) revealed the unexplored benefits, as well as the limitations, of this microfluidic approach.

Results

Principles of μFL space-domain spectroscopy. We hypothesized that if continuous-waveform (CW) localized illumination at the beginning of a microchannel photoinitiates radiative processes, their progress can be monitored by imaging the microflows adjacent to the CW excitation. At flow rates, Q, of tens of microliters per minute, fluids move through microchannels in a laminar manner with average flow velocities, $\langle v \rangle$, on the order of decimeters per second (due to the small cross sections, A, of the channels): i.e., $\langle v \rangle = Q A^{-1}$. Therefore, imaging such microflows with lateral resolution of a few micrometers provides the means for temporal resolution in the order of 10^{-5} s.

For the space-domain time-resolved emission measurements, we used print-and-peel (PAP)(Vullev, Wan et al. 2006; Hong, Bao et al. 2008; Thomas, Clift et al. 2010; Thomas, Millare et al. 2010) fabricated μFL devices that were coupled with quartz optical fibers for illuminating small regions of the microchannels with UV light (Scheme 5-1a, c). As laminar flows carried solutions of Ln^{3+} and DPA through CW-illuminated spots, the chromophores experienced pulsed-like excitation (Scheme 5-1). Sufficiently fast flow velocities resulted in short enough effective durations of the flow-induced excitation pulses, ensuring that much of the radiative deactivation of the Ln^{3+} chelates occurred in the non-illuminated regions of the channels (Figure 5-1b). Images of such flows revealed green and red luminescence from the Tb^{3+} and Eu^{3+} solutions, respectively, decaying along the channel lengths after the illuminated spots.

Two approaches allow spectral characterization of the emission-decays images: (1) separating the *red*, the *green* and the *blue* components of RGB images recorded with a color camera; and (2) placing band-pass filters between the μFL devices and a monochromatic camera, and imaging only the spectral features at particular emission wavelength ranges. We used the latter approach because it provided improved selection of the wavelength ranges of interest.

Analysis of time-resolved data in space domain. Because the size of the excitation spots, $S(x, y)$, was comparable with the lengths of the imaged luminescence decays, we deconvoluted the measured emission response, $R^*(x, y)$, to extract the space-domain

lifetimes, τ_S, of the samples (Figure 5-1c, d):(Giurleo and Talaga 2008; Lu, Bao et al. 2010)

$$R^*(x,y) = R(x,y) + \psi S(x,y) \tag{1a}$$

$$\begin{aligned} R(x,y) &= \int_0^h L(x,y,z) \otimes G(x,y,z)\, dz = \\ &= \int_0^h \int_0^x L(x-\xi,y,z)\, G(\xi,y,z)\, d\xi\, dz \end{aligned} \tag{1b}$$

where $R(x, y)$ is the response resultant from the chromophore emission, and the second term of the sum accounts for the imaged autofluorescence from the materials along the pathway of the excitation ultraviolet light. $L(x, y, z)$ is the intensity of the excitation light at coordinates x, y and z, corresponding to the axes oriented along the length, the width, w, and the height, h, of the channel, respectively. $G(x, y, z)$ is an exponential decay function of emission induced by δ-function pulse excitation, i.e., excitation by illumination at a single point with coordinates 0, y, z. This exponential decay function encompasses the conversion of spatial displacement along the channel length, x, to time after the δ-excitation, $t(y, z)$, employing the component of the flow velocity along x, $v_x(x, y, z)$:

$$L(x,y,z)_{0 \le z \le h} = S(x,y)\ 10^{-\varepsilon_{ex} C_{\mathrm{DPA}} (h-z)} \tag{2a}$$

$$G(x,y,z) = G_0 \exp\left(-\frac{t(y,z)}{\tau_S}\right) + g_\infty = \\ = G_0 \exp\left(-\frac{x}{v_x(x,y,z)}\frac{1}{\tau_S}\right) + g_\infty \quad (2b)$$

The vertical z-dependence of L was estimated from the optical density of the samples by accounting for the concentration of DPA, C_{DPA}, i.e., the principal light absorber at 280 nm, and for its molar extinction coefficient at that wavelength, ε_{ex} (equation 2a).(Jones and Vullev 2002) For the image of the excitation spots, $S(x, y)$, we recorded the autofluorescence from the μFL devices without emissive sample in their channels (Figure 5-1a).

Flow-velocity profiles within elastomer microchannels. For flow rates between 10 and 50 ml min^{-1}, the Reynolds numbers, Re, for the aqueous solutions passing through the stretch of the microchannel illuminated with the excitation light, ranged between 0.9 and 4.4. These relatively small values of Re ensured that the flows of the tested samples were laminar. Furthermore, due to the small heights of the channels, the entry lengths for the different flow rates did not exceed 10 μm; i.e., the parabolic velocity profiles of the laminar flows were completely developed by the time they reached the illuminated region of the channels.

The conservation of mass allows for relating the flow-velocity profiles, $v(x, y, z)$, at each position x along the channel, with the flow rate, Q:

$$Q = \int_0^w \int_0^h v(x,y,z)\,dz\,dy \approx \int_0^w \int_0^h v_x(x,y,z)\,dz\,dy \qquad (3)$$

Dividing the *x*-coordinate by the magnitude of the components of the flow velocity vectors along the length of the channel, $v_x(x, y, z)$ provided the time-resolved features from the space-domain dynamics (equation 2b). Assuming parabolic distribution and no-slip conditions, we estimated the velocity-profile distributions across the channel cross-sections from the flow rates (equation 3). Profilometry and fluorescence microscopy provided a means for determining the channel cross sections.

The μFL devices were PAP-fabricated of *poly*-dimethyl-siloxane (PDMS) slabs, permanently adhered to glass slides.(Millare, Thomas et al. 2008; Chau, Millare et al. 2011) Because of the relatively large elasticity of PDMS, pressure-driven flows deform the walls and the ceilings of the microchannels of such devices.(Gervais, El-Ali et al. 2006) Such deformations alter the channel cross-sections and the flow-velocity profiles during the operation of the devices. Therefore, profilometry measurements of the negative-relief imprints on the PDMS slabs (Figure 5-2a), prior to the device assembly, represented only of the channel cross sections with no pressure-drive flows through them.

Employing fluorescence microscopy allowed us to estimate the cross-sections at different flow rates. We imaged the μFL channels as we passed solution of fluorescein at different flow rates. An increase in the flow rate increased the intensity of the recorded emission from the imaged channels (Figure 5-2b, c). Because the dye concentration was constant, we ascribed this increase in the emission intensity to the increase in the

thickness of the channel, i.e., to the increase in the pathway of excitation of the fluorescent sample.

The distribution of the imaged fluorescence intensity across the channels (at 0 μl min^{-1}) does not directly follow the contour of the channel cross-section obtained from profilometry (Figure 5-2a, d, e). Unlike transmission optical microscopy where the recorded pixel intensity is linearly proportional to the height of the channel,(Thomas, Clift et al. 2010) as well as to the concentration and the extinction coefficient of the chromophore, fluorescence intensity has a non-linear dependence on these parameters.(Wan, Thomas et al. 2009; Xia, Upadhyayula et al. 2011) We, therefore, considered this nonlinearity in order to reconstruct the channel cross-sections from the fluorescence images.

For estimating the shapes of the channel cross-sections from the fluorescence images we used data recorded with an objective that had depth of field exceeding ~30 μm, i.e., ensuring that the whole channel, $0 \le z \le h$, was within the depth of field. Therefore, we could represent the imaged fluorescence intensity, $F_{x,y}(h, \lambda_{ex})$, as an addition of the fluorescence from each point along the vertical axis, z, of the channel:

$$F_{x,y}\left(h,\lambda_{ex}\right)=\int_{0}^{h}F_{x,y}\left(z,\lambda_{ex}\right)dz \tag{4a}$$

where λ_{ex} is the excitation wavelength, and $F(z, \lambda_{ex})$ represents the fluorescence from an infinitesimally thin horizontal plane (with thickness $\zeta \rightarrow 0$), located at z. The

fluorescence intensity is proportional to the emission quantum yield of the dye, **Φ**, and the light absorbed by the thin plane at z:

$$F\left(z,\lambda_{ex}\right) \propto \Phi I_0\left(\lambda_{ex}\right)\left(1-10^{-\varepsilon(\lambda_{ex})C\zeta}\right)10^{-\varepsilon(\lambda_{ex})Cz} = I\left(\lambda_{ex}\right)10^{-\varepsilon(\lambda_{ex})Cz} \quad (4b)$$

where $I_0(\lambda_{ex})$ is the light intensity at the bottom of the channel, i.e., at $z = 0$, $\varepsilon(\lambda_{ex})$ is the molar extinction coefficient of the dye, and C is the dye concentration. $I_0\left(\lambda_{ex}\right)10^{-\varepsilon(\lambda_{ex})Cz}$ represents the intensity of the light transmitted through the dye solution from 0 to z, i.e., the intensity of the excitation light reaching the plane at z. The intensity of the absorbed light by the dye within the plane with thickness ζ is proportional to $\left(1-10^{-\varepsilon(\lambda_{ex})C\zeta}\right)$, and $I(\lambda_{ex})$ does not have z-dependence, i.e., $I\left(\lambda_{ex}\right) = \Phi I_0\left(\lambda_{ex}\right)\left(1-10^{-\varepsilon(\lambda_{ex})C\zeta}\right)$. Substituting 4b in 4a and integrating along z provide the dependence of fluorescence on the channel height:

$$F_{x,y}\left(h,\lambda_{ex}\right) \propto I\left(\lambda_{ex}\right)\int_0^h 10^{-\varepsilon(\lambda_{ex})Cz}\,dz = \frac{I\left(\lambda_{ex}\right)\varepsilon\left(\lambda_{ex}\right)C}{\ln(10)}\left(1-10^{-\varepsilon(\lambda_{ex})Ch}\right) \quad (4c)$$

$$F_{x,y}\left(h,\lambda_{ex}\right) = \varphi_{x,y} I\left(\lambda_{ex}\right)\varepsilon\left(\lambda_{ex}\right)\left(1-10^{-\varepsilon(\lambda_{ex})Ch}\right) \quad (4d)$$

The proportionality coefficient, $\varphi_{x,y}$, accounts for the dye quantum yield, for the microscope settings, and for the uneven illumination through the field of view. Because

we employed broadband excitation for the microscopy measurements, we integrated 4b over the excitation wavelength range, between λ_1 and λ_2, in order to relate the imaged fluorescence intensity with the channel height:

$$F_{x,y}(h) = \varphi_{x,y}\Upsilon(h) \tag{5a}$$

where,

$$\Upsilon(h) = \int_{\lambda_1}^{\lambda_2} I(\lambda_{ex})\varepsilon(\lambda_{ex})\left(1-10^{-\varepsilon(\lambda_{ex})Ch}\right)d\lambda_{ex} \tag{5b}$$

We numerically solved the integral $\Upsilon(h)$, using $\varepsilon(\lambda)$ estimated from absorption spectra recorded for aqueous fluorescein solutions. For $I_0(\lambda_{ex})$, needed for calculating $I(\lambda_{ex})$, we used the spectrum of the mercury arc lamp of the fluorescence microscope, recorded through the excitation filter (Figure 5-2h). To calculate the proportionality coefficient, $\varphi_{x,y}$, we used the fluorescence recorded at no flow rate, $Q = 0$, and the channel heights obtained from profilometry measurements:

$$\varphi_{x,y} = \frac{F_{x,y,Q=0}\left(h_{profilometry}\right)}{\Upsilon\left(h_{profilometry}\right)} \tag{5c}$$

Applying equations 4 and 5 to traces from the fluorescence images recorded at different flow rates, we estimated the cross section of the channels (Figure 5-2f, g). For channels with large aspect ratios, i.e., $w >> h$,(Spiga and Morini 1994) the fluorescence image data

and finite element analysis revealed that the displacement and the arching of the channel ceilings (across the channel widths) encompasses the principal deformation that affects the cross sections and the flow-velocity profiles, which was in accordance with the report from Gervais et al.(Gervais, El-Ali et al. 2006)

Within the 2-mm stretch along the μFL channel, where we recorded the emission decays (Figure 5-1b), the difference between cross-sections along the channel length, x, did not exceed ~10% (Figure 5-2f, g), which further justified the approximation $v(x, y, z) \approx v_x(x, y, z)$ in equation 3. Using the channel cross-sections obtained from the fluorescence images, and employing no-slip conditions and parabolic distribution to equation 3, resulted in the flow-velocity profiles, $v_x(x, y, z)$, for different flow rates (Figure 5-2i, j), needed for the space-domain emission-decay analysis (equation 2).

Space-domain time-resolved emission of Ln^{3+} chelates. Using space-domain approach, we investigated the emission decays for mixtures of lanthanide ions and DPA, in which the luminescent species were a *mono*-chelated complex, i.e, Tb(DPA), and *tris*-chelated complexes, i.e., $Tb(DPA)_3$ and $Eu(DPA)_3$. In accordance with previous reports, solutions in which the concentration of the terbium ions, C_{Tb}, exceeded the DPA concentration five-fold, provided predominantly *mono*-DPA chelates.(Jones and Vullev 2002; Jones and Vullev 2002) Conversely, for the *tris*-chelated samples, the C_{DPA} exceeded the concentration of the lanthanide ions, C_{Ln}, five-fold.(Jones and Vullev 2002; George, Golden et al. 2006) The fine structure of the emission spectra of the Ln^{3+}-DPA mixtures revealed that, indeed, for C_{Ln}:C_{DPA} = 1:5 the luminescent species were *tris*-

chelates; and that for C_{Tb}:C_{DPA} = 5:1 – the luminescent species were *mono*-chelates (Figure 5-3a).(Jones and Vullev 2002; George, Golden et al. 2006)

For all samples, the principal light absorber was DPA: at 280 nm, the molar extinction coefficients of Tb^{3+} or Eu^{3+} are considerably smaller than that of DPA.(Jones and Vullev 2002) The photoexcited DPA moieties that ligated the lanthanide ions, Ln^{3+}, undergo fast energy transfer to Ln^{3+}, while the photoexcited free DPA molecules undergo non-radiative deactivation. Thus, the principal luminophores in the Ln^{3+}-DPA solutions were the chelated Tb^{3+} and Eu^{3+}.

For the space-domain emission measurements, we passed the Ln^{3+}-DPA solutions through the illuminated channels with flow rates ranging from 10 to 50 μl min^{-1} (Figure 5-3b). An increase in the flow rate increased the lengths of the emission decays (Figure 5-3b, d), and hence improved the temporal resolution. The backpressure, however, sets the principal limit on the maximum flow rates that were feasibly attainable. Furthermore, at the same flow rate, the lengths of the emission decays from the three chelates differed (Figure 5-3b, c) in accordance with the differences in their luminescence lifetimes.(Horrocks and Sudnick 1979; Latva, Takalo et al. 1997; Jones and Vullev 2002; George, Golden et al. 2006; Cable, Kirby et al. 2007)

From recorded images of $R^*(x, y)$ and $S(x, y)$, we extracted traces along the middle of the channels, reducing the data to a one-dimensional spatial coordinate that provides the time resolution, i.e., $R^*(x)_{y=w/2}$ and $S(x)_{y=w/2}$ (Figure 5-1). Least-square (LS) fits of the $R^*(x)$ traces using equations 1 and 2, and the estimated flow-velocity profiles (Figure 5-2), allowed for extracting the emission decay lifetimes for solutions containing

luminescent lanthanide chelates (Figure 5-1c, d). The fitting parameters encompassed the lifetime, τ_S, along with other quantities, G_0, ψ, and g_∞ (equations 1, 2), that were not available via alternative estimates. For each flow rate, the terbium *tris*-chelate samples exhibited the longest lifetimes and the terbium *mono*-chelate samples – the shortest (Table 5-1). For each chelate, the lifetimes extracted from the emission-decay traces did not manifest statistically significant dependence on the flow rate (Table 5-1, footnote b(Thomas, Millare et al. 2010)). The thus obtained values of τ_S were in good agreement with the previously reported lifetimes of these chelates.(Horrocks and Sudnick 1979; Latva, Takalo et al. 1997; Jones and Vullev 2002; George, Golden et al. 2006; Cable, Kirby et al. 2007)

To further confirm the emission lifetimes obtained from the space-domain image data, we examined the luminescence properties of the same Ln^{3+} samples using time-domain measurements. Illuminating the samples with femtosecond pulses from a modelocked laser source resulted in emission decay signals that extended to a few milliseconds after the excitation (Figure 5-4). The laser pulse-width was orders of magnitude smaller than the measured lifetimes, ensuring that δ-function represented a reasonable approximation for the excitation pulses. Monoexponential fits of these time-domain emission-decay data yielded lifetimes, τ_T, that agreed well with the space-domain measured τ_S (Table 5-1, footnote d).

Discussion

The steady-state mode of operation of this space-domain μFL approach, allowed for a fast acquisition of emission-decay data with relatively large signal-to-noise ratios. Using lanthanide chelates as emission samples, we demonstrated the feasibility of employing facilely fabricated microdevices for measuring lifetimes that range from hundreds of microseconds to milliseconds.

It took seconds to record the emission-decay images using easy-to-fabricate low-cost μFL assemblies. Furthermore, this space-domain approach provides venues for miniaturization, allowing for *in situ* time-resolved spectroscopy measurements on lab-on-a-chip (LoC) setups. In fact, the fluorescence microscope was the "bulkiest" component of the setup needed for these studies. The development of the camera and microscopy field-deployable technologies, however, will address concerns for competitive cost and size of the microscopes needed for the space-domain μFL measurements.(Breslauer, Maamari et al. 2009; Zhu, Isikman et al. 2013) Even in these studies, the cost and the size of the equipment for time-domain measurements (Figure 5-4) exceeded the cost and the size of the space-domain emission microscopy setup. Furthermore, time-domain measurements employing "traditional" time-correlated single-photon counting may take an hour or longer to acquire reasonable counts per channel for decays in the 100s of μs and ms domains. Therefore, space-domain time-resolved emission spectroscopy, which is based on steady-state measurements, has certain unexplored advantages that can prove useful for a range of analytical and LoC applications.

Average flow velocities of decimeters per second provide the means for temporal resolutions of 10 μs or better assuming micrometer optical spatial resolution between neighboring points on the decay images. In the current devices, however, the size of the excitation spot (Figure 5-1a) set the lower limit on the measurable lifetimes. For the flow velocities we attained (Figure 5-2), excitation spanning over 300 μm along the channel prevented the characterization of emission-decay kinetics with lifetimes much smaller than about 100 μs. Therefore, decreasing the area of the excitation spot would not only extend the lower limit of the measureable lifetimes, but also simplify the analysis of emission decays involving relatively long lifetimes by eliminating the need for spatial deconvolution (equation 1b).

An increase in the flow rate lengthened the decay traces (Figure 5-3b), and appeared to provide the means for improving not only the temporal resolution, but also the lower limit of the attainable lifetimes. Such a flow-rate increase, however, also increased the backpressure, which deformed the channels and increased the areas of the cross-sections, decreasing the average flow velocity in comparison with non-deformed channels. Therefore, the elasticity of the polymer composing the devices presented a limitation on the feasibly useful flow-rate range.

As a material for fabricating μFL devices, PDMS has a range of disadvantages, such as pronounced elasticity and oxygen permeability.(Houston, Weinkauf et al. 2002; Mehta, Lee et al. 2009) Indeed, employing non-elastic materials for space-domain devices would not only prevent the deformation of the microchannels, but also considerably simplify the analysis of the flow-velocity profiles and improve the dynamic range for the

measurements, which will make this technique even more attractive than the herein proof-of-concept design.

Nevertheless, the ease of molding, along with the simplicity of assembling microdevices, has made PDMS one of the most widely used material for μFL devices.(McDonald and Whitesides 2002; Gates 2005; Hui, Wang et al. 2005; Teh, Lin et al. 2008; Fiddes, Raz et al. 2010; Pan and Wang 2011) Indeed, PAP-fabricated PDMS microdevices allowed us to demonstrate the concept of space-domain time-resolved spectroscopy.

Conclusions

Simplicity and speed are some of the attractive features of this space-domain microfluidic technique. While probing emission decays in femtosecond to nanosecond time domains is routine for the developed time-resolved spectroscopy techniques, monitoring radiative processes in the microsecond and millisecond scales is challenging for most of these "traditional" approaches. Indeed, custom assemblies of Q-switched pulsed lasers, reasonably fast photodetectors, and oscilloscopes provide access to the μs and ms time domains.(Jones and Vullev 2002; Cable, Kirby et al. 2007) Conversely, the space-domain μFL approach offers accessible means for exploring millisecond and submillisecond photokinetics, i.e., time domains important for biochemical probes(Thomas, Carlsen et al. 1978) and for emerging nanomaterials.(Sykora, Mangolini

et al. 2008) We believe that such space-domain approach will provide key venues for bringing time-resolved spectroscopy to lab-on-a-chip settings.

Experimental

Materials. Terbium (III) chloride hexahydrate (99.999%), europium (III) chloride hexahydrate (99.999%), and pyridine-2,6-dicarboxylic acid were purchased from Sigma-Aldrich. Glacial acetic acid and aqueous ammonium hydroxide solution were obtained from Fisher Scientific. Polydimethylsiloxane (PDMS), prepolymer and curing agent, was obtained from Dow Corning. Microscope glass slides where purchased from Fisher Scientific. Non-radiopaque polyethylene tubing was purchased from BD Medical.

For the chelate solutions, preweighed amounts of DPA and lanthanide salts were separately dissolved in Milli-Q water. Ammonium hydroxide was added drop-wise to the DPA solution to bring the pH close to 7 and to ensure complete dissolution.[9] Acetic acid was added to the lanthanide chloride solutions to bring the pH to 6.5 – 7 and to prevent the formation of precipitates of the metal hydroxide.[9] Each of the lanthanide solutions was mixed with the corresponding DPA solution. Upon the formation of white precipitate, either ammonia solution or acetic acid was added to bring the pH to 7, and hence redissolve the precipitate. The thus prepared DPA-lanthanide solutions were diluted with Milli-Q water to attain the targeted concentrations for the microfluidic time-resolved emission measurements.

Device fabrication. We fabricated the devices using PAP as we have previously described.(Vullev, Wan et al. 2006; Hong, Bao et al. 2008; Thomas, Clift et al. 2010; Thomas, Millare et al. 2010) The CAD pattern of the microchannel was prepared using Adobe Illustrator (v. 14.0.0). Using a laser-jet printer (Hewlett-Packard Laser-Jet 1320), the designed patterns were printed on overhead transparency films to form positive-relief masters. Upon immobilization of the master films to the bottom of polystyrene Petri dishes, polyethylene posts for forming of inlet and outlet vertical channels were immobilized at the termini of the printed channel patterns.(Vullev, Wan et al. 2006; Thomas, Clift et al. 2010) About 0.5 mm film of PDMS prepolymer-curing agent mixture was added and allowed to cure.

To form the well for the excitation source, a polypropylene cylinder was placed on the cured PDMS film above the microchannels for space-domain measurements. Quartz optical fibers, coupled with UV LEDs (FIAlab® LED-Lamp 280 nm), were used for excitation source. Hence, the diameter of the polypropylene-cylinder molds corresponded to the diameter of the termini of the optical fibers. Additional 5 mm layer of PDMS prepolymer mixture was poured over the cured elastomer with posts and cylinders on it, and allowed to cure. Upon curing of the second layer of PDMS, the elastomer slabs were lifted from the printed transparency masters and the polymer posts were removed from the slabs to leave inlet and outlet channels, and a well for the optical fiber over each horizontal microchannel imprint. The slabs were cut into 10×25 mm blocks (each block encompassing one test microchannel with an inlet, an outlet, and a well for an optical-fiber terminus) to form the PDMS components of the devices. The PDMS surfaces with

the negative microchannel imprints were activated with oxygen plasma (50 W, 0.5 mBar)[21-22] and permanently adhered to glass slides to yield the microfluidic devices for space-domain measurements.

The cross-section of the channels was determined prior to adhering the PDMS slabs to the glass, using a benchtop surface profilometer (Dektak 8, Veeco Systems). The 9-mm long test channels under the excitation-illuminated area had 7.5±0.5 μm height and 365±10 μm width. Two 3-mm long 0.7-mm wide channels connected the test channels with the inlet and the outlet (Scheme 5-1a).

Estimating flow-velocity profiles. The estimation of the velocity profiles and especially of the velocity profiles in the middle of the channels, $v_x(x, y=w/2, z)$ needed for analyzing the decay traces (Figures 1b-d and 3b-d), involved: (1) estimation of the cross-sections of the channels in the emission-decay regions; and (2) numerical calculation of $v_x(x, y, z)$ from the cross-sections and the flow rates, Q (equation 3).

For estimating the channel cross-sections in absence of flows, a bench-top surface profilometer (Dektak 8, Veeco Systems), with 12.5-μm radius stylus, was employed for the analysis of the negative-relief channel imprints on the PDMS surfaces. To reconstruct the channel shapes (Figure 5-2a), usually 1.6-mm scans across the channel imprints were performed at every 0.2 mm, 5-mm along the channel length.

For reconstructing the channel cross-sections under flow conditions, 1 mM aqueous fluorescein solution (buffered at pH 8 with 10 mM phosphate buffer) was passed through

the channel at different flow rates and imaged with AcuScope 3031 inverted fluorescence microscope equipped with FITC filter and Spot Insight digital CCD camera.

From the epifluorescence images of the channels, the cross-sections of the channels were reconstructed using equations 4 and 5. For the proportionality coefficient, $\varphi_{x,y}$, we assumed negligible alteration of the excitation illumination intensity across the channel for each cross section, i.e., $\varphi_{x,y} \approx \varphi_x$. Using equation 5c, therefore, we estimated φ_x for each cross section from the profilometry data and the imaged fluorescence values for the middle of the channel, i.e., for $y = w/2$.

Considering the maximum channel height, h_{max}, extracted from the cross-sections and that the principal deformation involved curving of the PDMS ceiling (Figure 5-2f, g), the shape of the deformed cross-sections, in terms of the height of the channels, $h(y)$, at various points y along the width, was estimated:

$$h(y) = h_{max} - r + \sqrt{r^2 - \left(y - \frac{w}{2}\right)^2} \tag{6a}$$

where r is the radius of the circular arc representing the ceiling deformation:

$$r = \frac{4\left(h_{max} - h_0\right)^2 + w^2}{8\left(h_{max} - h_0\right)} \tag{6b}$$

Approximating the shape of the arc from circular to parabolic, allows for simplifying the expression for $h(y)$:

$$h(y) \approx h_0 + (h_{max} - h_0)\left(1 - \left(\frac{2y - w}{w}\right)^2\right) \tag{6c}$$

At each y value (along the width), the flow-velocity profiles were modeled as parabolically distributed $v_x(x, y, z)$ along the height of the channels, z, with maximum velocity in the half-height, and zero velocity at the floor and the ceiling, i.e., $v_x(x, y, z=h/2) = v_{max}(x, y)$, and $v_x(x, y, z=h), = v_x(x, y, z=0) = 0$.(Spiga and Morini 1994) Near the side edges of the flat channels, i.e., $y < h/2$ and $y > w - h/2$, $v_{max}(x, y)$ had parabolic distribution along y;(Spiga and Morini 1994) and in the absence of any deformation $v_{max}(x, y)$ was constant for $h/2 < y < w - h/2$. At each point y for deformed channels, $v_{max}(x, y)$ was increased proportionally with $h(y)$. Using these considerations for the y, z distribution of the flow-velocity values across the cross sections of the deformed channels, for each coordinate x along the flow with different rates, Q, the flow-velocity profiles, v_x, were calculated numerically using equation 3.

Space-domain time-resolved emission measurements. The space-domain emission decays of microflows, containing lanthanide chelates, were imaged using a Nikon Eclipse Ti-S fluorescence microscope equipped with a 10× Nikon CFI Plan Fluor objective lens and a Hamamatsu EM-CCD camera (model C9100-13). Band-pass filters were placed on

the optical pathway between the device and the camera: 510-560 nm for the terbium (III) samples, and 570-620 nm for the europium (III) sample. For the excitation spots (Figure 5-1a), the illuminated region was imaged without band-pass filters and without lanthanide (III) samples in the channels. The photoexcitation was delivered by placing the illumination source (UV LED-coupled optical fiber) in the well.

For recording excitation profiles, $S(x, y)$, the channels were filled with Milli-Q water and the autofluorescence of the assembly was imaged at $Q = 0$ μl min^{-1}. The same $S(x, y)$ profiles were obtained when the channels were filled with aqueous solutions of fluorophores, such as fluorescein, with ns excited-state lifetimes. For recording the emission-response profiles, $R^*(x, y)$, the solution was passed through the microchannel at flow rates, Q, of 10, 20, 30, 40 and 50 μl min^{-1} using a programmable syringe pump (Harvard Apparatus PHD 2000). At each flow rate for each chelate solution, the images of the decay flows were captured with exposure time of 10 s using HCImage Hamamatsu imaging software (the sensitivity gain was set to 0, and the gain was set to 1).

Because the field of view of the objective was 0.5×0.5 mm, several images displaced along the channel were recorded in order to encompass the complete emission decay patterns. Using Photomerge (with Reposition layout, and no photo-correction options selected) as implemented with Adobe Photoshop (v. 11.0; CS4 extended), the monochromatic square images were overlapped and merged together to generate the continuous decay patterns without further manipulations.

Data analysis. From the monochromatic images, the emission-decay traces, $R^*(x, y)$, and the excitation traces, $S(x, y)$, were extracted from the middle of the channels as gray-scale intensity of the pixels vs. the channel length, x (Figure 5-1), as we have previously demonstrated.(Thomas, Clift et al. 2010) Using a least-square data-fitting algorithm, as implemented by Igor Pro (v. 6.02A),(Vullev and Jones 2002; Jones, Yan et al. 2007) the emission lifetimes were extracted from the emission-decay traces using the space-domain deconvolution function (equations 1, 2).

To illustrate the concepts behind the spectral differences of the space-domain emission data recorded through different optical filters, some of the monochromatic images were colored using Adobe Photoshop CS4. A new layer, filled with either red color (RGB value of R:255 G:0 B:0) or green color (RGB value of R:0 G:200 B:0) color to show europium (III) or terbium (III) luminescence, respectively, was created over the original TIFF files and modified using the Overlay layer blending option. These images (Figure 5-1b, 3b) were created solely to demonstrate the concept behind the space-domain spectroscopy and were not used for extracting the decay traces and emission lifetimes.

Time-domain time-resolved emission measurements. The laser source for the pulsed excitation was a SpitFire Pro 35F regenerative amplifier (Spectra Physics / Newport) generating 800-nm pulses (38 fs, 3.5 mJ, 55 nm bandwidth) at 1 kHz repetition rate. The amplifier was pumped with an Empower 30 Q-switched laser ran at 20 W, and a MaiTai SP oscillator provided the seed beam. The 800-nm beam was passed through a second-harmonic and a third-harmonic generator (Minioptic Technology, Inc., Arcadia, CA), and the repetition rate of the 266-nm beam was reduced from 1 kHz to about 33 Hz.

The emission was detected at 90° to the excitation illumination. The liquid samples were placed in a quartz cuvette in front of a Si detector with nanosecond response time equipped with the appropriate band-pass optical filters. The signals from the photodetector were forwarded to a 300-MHz digital oscilloscope (LeCroy 9361) and terminated at 50 Ω, resulting in the recorded emission-decay traces (Figure 5-4).(Jones and Vullev 2002; Vullev and Jones 2005)

Emission spectroscopy. Steady-state emission spectra (Figure 5-3a) were recorded using a FluoroLog-3 spectrofluorometer (Horiba-Jobin-Yvon) equipped with double-grating monochromators and a TBX single-photon-counting detector (λ_{ex} = 280 nm).(Bao, Millare et al. 2009; Hu, Xia et al. 2009; Vasquez, Vu et al. 2009) To suppress the detection of the $2\times\lambda_{ex}$ signal, a longpass filter (λ_{cutoff} = 380 nm) was placed on the optical pathway between the cuvette and the emission monochromator. By adjusting the slit widths, the signal at all wavelengths was kept under 10^6 CPS to ensure that it was within the linear dynamic range of the detector.

Acknowledgment: This research was supported by the U.S. National Science Foundation (CBET 0923408 and CBET 0935995, as well as GRFP 2011081805 for VN), and by the Riverside Public Utilities. We also extend our gratitude to Prof. Victor G. J. Rodgers and Prof. Jerome S. Schultz for assistance with the fluid-dynamics analysis; to Prof. Bahman Anvari for providing access to the imaging equipment in his lab; and to Prof. B. Hyle Park for insightful discussions regarding the image analysis.

Tables:

Table 5-1. Emission lifetimes of Tb^{3+} and Eu^{3+} chelates with DPA.[a]

chelate	τ_S / ms, measured at flow rates Q / ml min^{-1}: [b]					$\langle\tau_S\rangle$ / ms [c]	τ_T / ms [d]
	10	20	30	40	50		
$Tb(DPA)_3$	2.13 ± 0.33	2.16 ± 0.23	1.98 ± 0.23	1.96 ± 0.27	1.99 ± 0.22	2.04 ± 0.26	2.05 ± 0.02
Tb(DPA)	0.581±0.179	0.497±0.183	0.556±0.245	0.570±0.152	0.531±0.19	0.547 ± 0.192	0.528 ± 0.018
$Eu(DPA)_3$	1.77 ± 0.37	1.64 ± 0.31	1.73 ± 0.27	1.56 ± 0.25	1.53 ± 0.31	1.65 ± 0.31	1.51 ± 0.11

[a] Data from four different microfluidic devices. For $Ln(DPA)_3$, C_{Ln} = 20 mM and C_{DPA} = 100 mM; and for Tb(DPA), C_{Tb} = 50 mM and C_{DPA} = 10 mM.

[b] Lifetimes, τ_S, from space-domain measurements. Based on two factor ANOVA test, while the lifetime values were unique for each chelate, they did not depend on the flow rate, Q. The two null hypotheses were: $H_0^{(1)}$: τ does not depend on the chelate; and $H_0^{(2)}$: τ does not depend on Q. The p-values for the two hypotheses, obtained from the ANOVA test, were: $p_{chelate} < 10^{-8}$, $p_Q = 0.57$, and $p_{interaction} = 0.93$. These findings allowed for rejecting $H_0^{(1)}$, but not $H_0^{(2)}$.(Thomas, Millare et al. 2010)

[c] Based on the lack of statistically significant dependence of the lifetimes on the flow rates, for each chelate, $\langle\tau_S\rangle$ is averaged over the five flow rates: $\langle\tau_S\rangle = 5^{-1}\mathbf{\Sigma}_i\,\tau_S(Q_i)$. The error bars, $\Delta\tau_S$, were propagated from the error bars for the different flow rates: $\Delta\tau_S{}^2 = 5^{-1}\mathbf{\Sigma}_i(\Delta\tau_S(Q_i))^2$.

[d] Lifetimes, τ_T, from time-domain measurements (from at least five different measurements for each of the chelates). Based on a Welch's t-test, i.e., a modified Student's t-test, the lifetimes obtained from space-domain, τ_S, and time-domain, τ_T, measurements did not differ within 5% level of statistical significance, i.e., $\alpha = 0.05$. Testing H_0, if τ_S and τ_T are identical for each of the three chelates, yielded $p = 0.87$, $p = 0.67$, and $p = 0.083$ for $Tb(DPA)_3$, Tb(DPA), and $Eu(DPA)_3$.

Scheme 5-1. μFL setup for space-domain measurements.

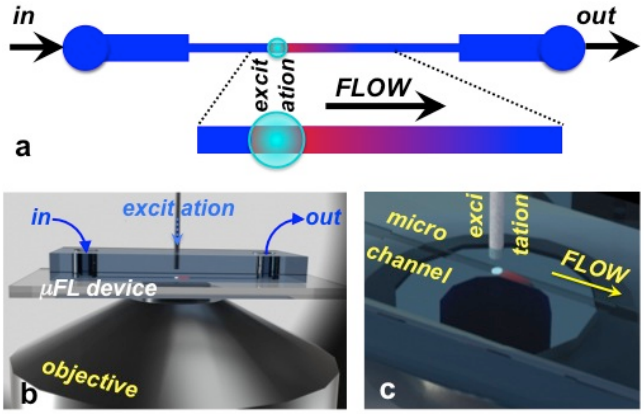

(a) Channel geometry;
(b) Device-microscope assembly;
(c) Close view of the working area of the device.

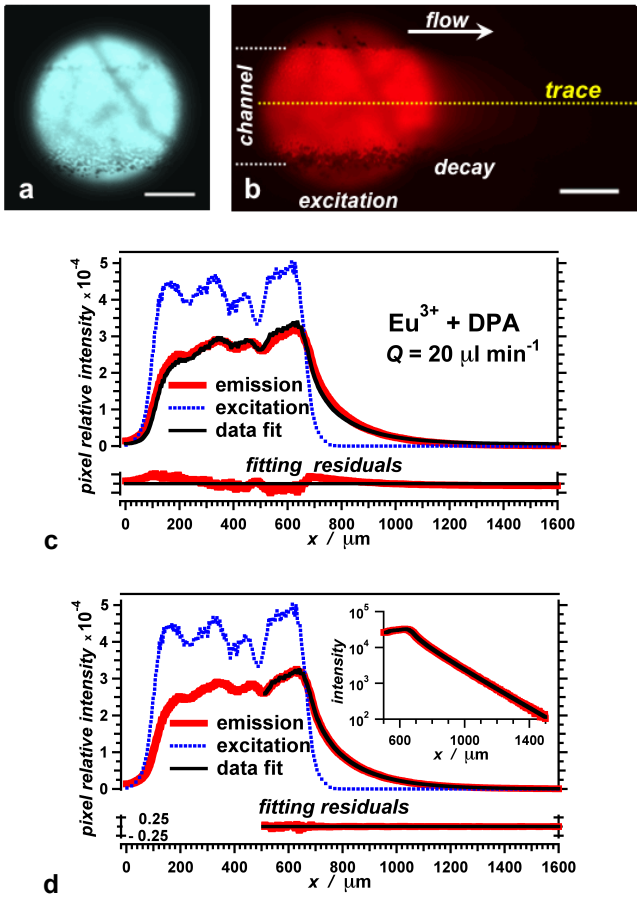
a
b
flow
channel
trace
decay
excitation
pixel relative intensity x 10^-4
Eu3+ + DPA
Q = 20 µl min-1
emission
excitation
data fit
fitting residuals
x / µm
c
intensity
fitting residuals
d

Figure 5-1

Figure 5-1. Space-domain time-resolved emission measurements. **(a)** Microscope image (16 bit) of the region of a microchannel, filled with water, illuminated at 280 nm. The imaged emission originated from autofluorescence. **(b)** Microscope image of the emission decay recorded through a band-pass filter (570-620 nm). Solution of 20 mM Eu^{3+} and 100 mM DPA was flown through the illuminated region of the channel (l_{ex} = 280 nm) at flow rate Q = 20 ml min^{-1}. Scale bars on (a) and (b) correspond to 200 mm. **(c)** Emission trace, $R^*(x)$, extracted from the decay image, (b), along with excitation trace, $L(x)$, extracted from the image of the illumination spot, (a), and the data fit of $R^*(x)$ vs. x using equations 1 and 2. **(d)** The same $R^*(x)$ and $L(x)$ as (c), in which the data fitting was limited to the decay region of the image trace with minimum interference from the autofluorescence from the excitation spot. The difference in the lifetimes from (c) and (d) was less than 10%. The inset represents the decay data and the data fit plotted against logarithmic ordinate. The use of equations 1 and 2 provided adequate data fits for the traces, $R^*(x)$, extracted from images (b). As indicated by the residuals, however, limiting the data fits to the regions of the emission-decay traces, $R^*(x)$, where the autofluorescence from the excitation had minimum to no contribution, improved the quality of the data fits, i.e., (c) vs. (d).

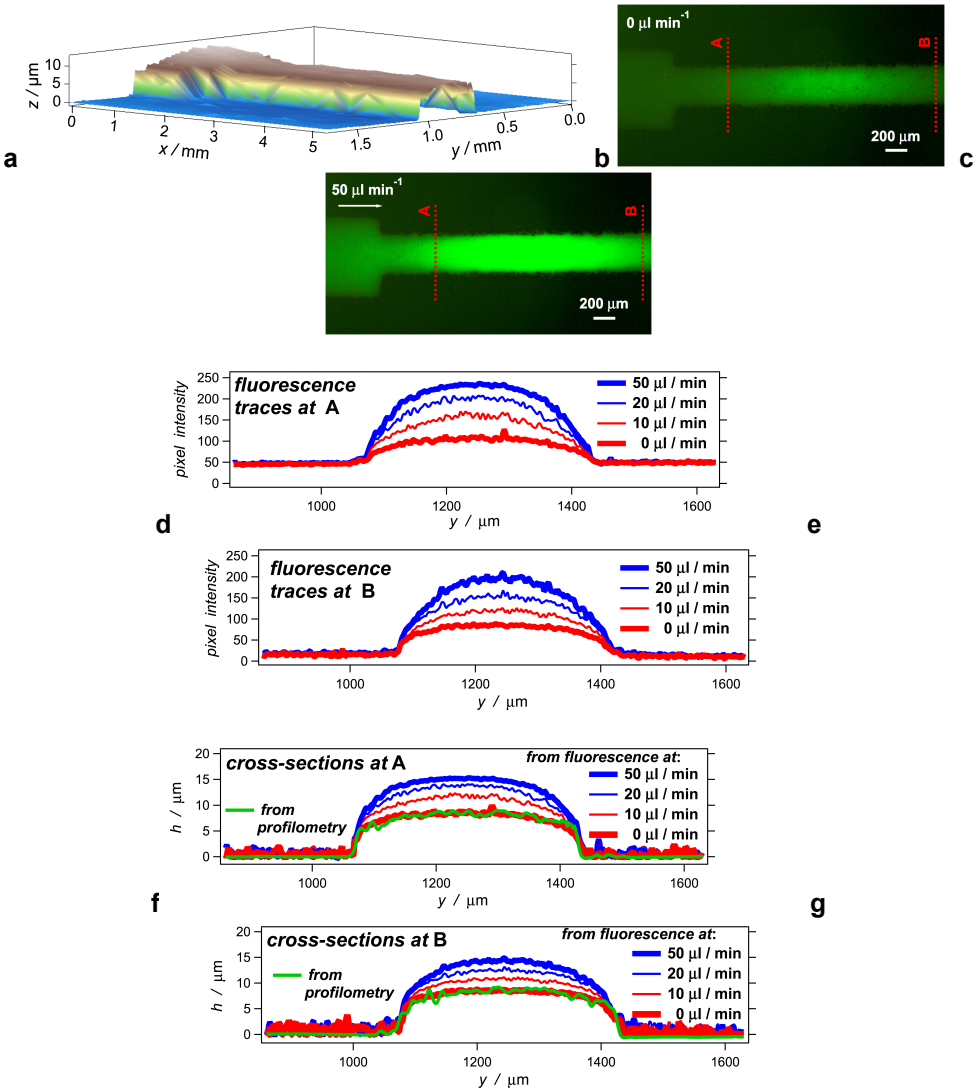
a
z / µm
x / mm
y / mm
b
0 µl min-1
A
B
200 µm
c
50 µl min-1
d
fluorescence traces at A
pixel intensity
50 µl / min
20 µl / min
10 µl / min
0 µl / min
y / µm
e
fluorescence traces at B
f
cross-sections at A
from fluorescence at:
from profilometry
h / µm
g
cross-sections at B

Figure 5-2

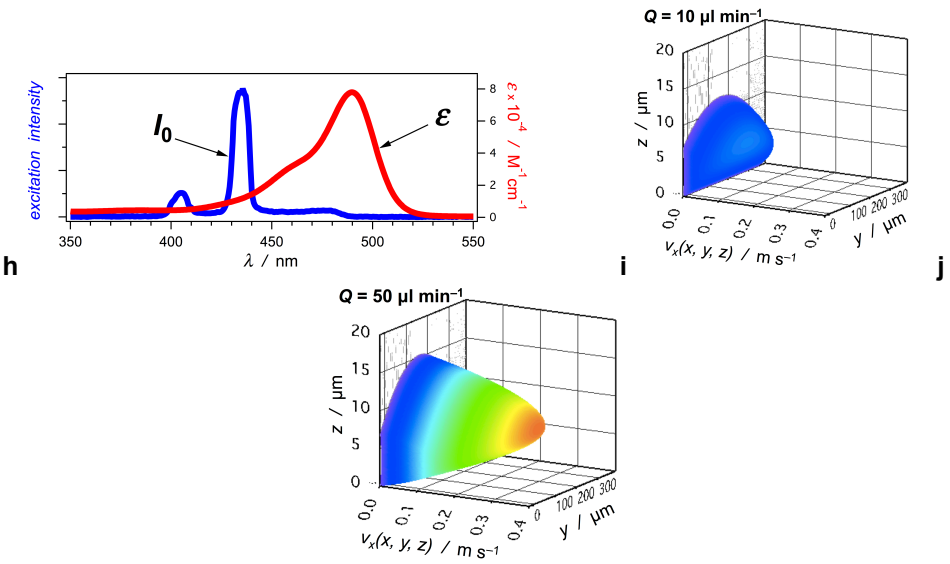
h
excitation intensity
I_0
ε
$\varepsilon \times 10^{-4}$ / M^{-1} cm^{-1}
λ / nm
i
Q = 10 µl min⁻¹
z / µm
$v_x(x, y, z)$ / m s⁻¹
y / µm
j
Q = 50 µl min⁻¹
z / µm
$v_x(x, y, z)$ / m s⁻¹
y / µm

Figure 5-2

Figure 5-2. Channel cross-section and flow-velocity profiles, $v_x(x, y, z)$, estimated from profilometry and fluorescence images for different flow rates, Q. **(a)** Surface plot of the entrance region of a mFL channel from profilometry data. **(b, c)** Uncorrected epifluorescence images (8 bit) of the entrance region of a mFL channel filled with 1 mM aqueous solution of fluorescein buffered at pH 8, at rest and at flow rate of 50 ml min^{-1}. **(d, e)** Uncorrected fluorescence traces across the channels, recorded at different flow rates, as indicated with the dotted red lines on the images, (b) and (c). **(f, g)** Channel cross-sections estimated from the fluorescence traces (d) and (e), using equations 4 and 5. **(h)** Spectral overlap between the fluorescein absorption at pH 8 and the excitation, I_0, obtained from the microscope mercury lamp as a light source, passed through the fluorescein isothiocyanate (FITC) excitation filter used for the recording of the fluorescence images. **(i, j)** Flow-velocity profiles for 10 and 50 ml min^{-1}, obtained using equation 3 and smoothed cross-sections (f) for various flow rates assuming no-slip conditions and parabolic distribution.

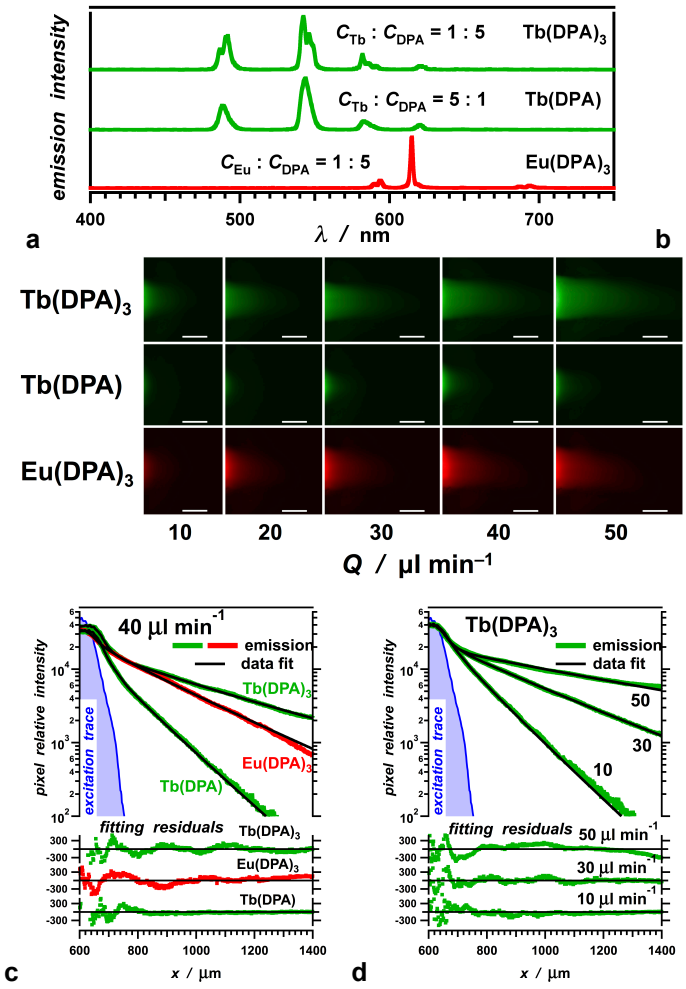
emission intensity
C_{Tb} : C_{DPA} = 1 : 5
Tb(DPA)$_3$
C_{Tb} : C_{DPA} = 5 : 1
Tb(DPA)
C_{Eu} : C_{DPA} = 1 : 5
Eu(DPA)$_3$
400
500
600
700
λ / nm
a
b
Tb(DPA)$_3$
Tb(DPA)
Eu(DPA)$_3$
10
20
30
40
50
Q / µl min^{-1}
40 µl min^{-1}
emission
data fit
Tb(DPA)$_3$
Eu(DPA)$_3$
Tb(DPA)
excitation trace
pixel relative intensity
fitting residuals
x / µm
c
d
50
30
10
50 µl min^{-1}
30 µl min^{-1}
10 µl min^{-1}

Figure 5-3

Figure 5-3. Space-domain emission decays of Tb^{3+} and Eu^{3+} chelated with DPA, recorded for different flow rates. **(a)** Emission spectra of Tb^{3+} and Eu^{3+} in the presence of DPA. **(b)** Images of the emission decays of lanthanide chelates, recorded at different flow rates. The scale bars correspond to 200 mm. The emission-decay images were recorded through band-pass filters: 510-560 nm for the terbium (III) samples, and 570-620 nm for the europium (III) samples. **(c)** Emission-decays traces, $R^*(x)$, of the three lanthanide chelates recorded at flow rate, Q = 40 ml min^{-1}, along with the corresponding data fits and fitting residuals. **(d)** Emission-decay traces of $Tb(DPA)_3$, along with the corresponding data fits and fitting residuals, recorded at flow rates, Q = 10, 30 and 50 ml min^{-1}. The traces were extracted from the middle of the imaged channels, i.e., $y = w / 2$. For $Ln(DPA)_3$, C_{Ln} = 20 mM and C_{DPA} = 100 mM; and for Tb(DPA), C_{Tb} = 50 mM and C_{DPA} = 10 mM (l_{ex} = 280 nm).

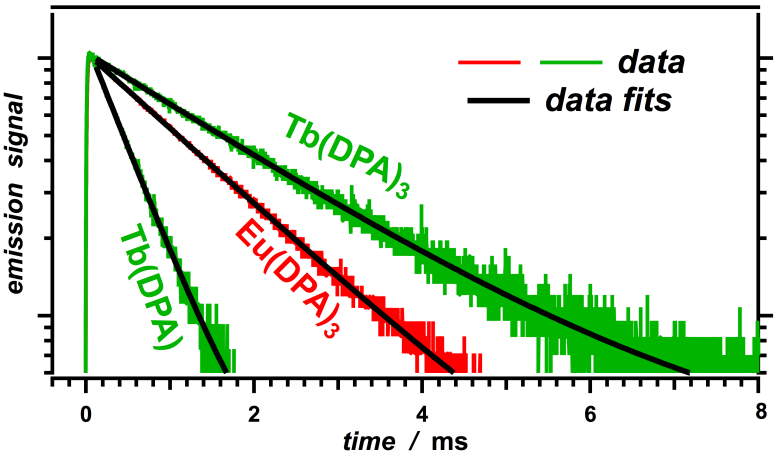
data
data fits
Tb(DPA)3
Eu(DPA)3
Tb(DPA)
emission signal
0
2
4
6
8
time / ms

Figure 5-4

Figure 5-4. Time-domain measurements, with the corresponding monoexponential data fits, of emission decays of Tb^{3+} and Eu^{3+} chelated with DPA, normalized for $t = 0$, which correspond to the timing of the excitation laser pulse, and presented against logarithmic ordinate. For $Ln(DPA)_3$, C_{Ln} = 20 mM and C_{DPA} = 100 mM; and for Tb(DPA), C_{Tb} = 50 mM and C_{DPA} = 10 mM (l_{ex} = 266 nm; 40 fs pulse width at 800 nm prior to the second and third harmonic generators).

References

Ammann, A. B., L. Kolle, et al. (2011). "Detection of bacterial endospores in soil by terbium fluorescence." Int. J. Microbiol.: 435281, 435285 pp.

Bao, D., B. Millare, et al. (2009). "Electrochemical Oxidation of Ferrocene: A Strong Dependence on the Concentration of the Supporting Electrolyte for Nonpolar Solvents." J. Phys. Chem. A **113**(7): 1259-1267.

Beeby, A. (2002). "Pump-probe laser spectroscopy." Introd. Laser Spectrosc. (2nd Ed.): 105-137.

Birch, D. J. S. and R. E. Imhof (1991). "Time-domain fluorescence spectroscopy using time-correlated single-photon counting." Top. Fluoresc. Spectrosc. **1**: 1-95.

Breslauer, D. N., R. N. Maamari, et al. (2009). "Mobile Phone Based Clinical Microscopy for Global Health Applications." Plos One **4**(7): e6320.

Bringer, M. R., C. J. Gerdts, et al. (2004). "Microfluidic systems for chemical kinetics that rely on chaotic mixing in droplets." Philos. Trans. R. Soc. London, Ser. A **362**(1818): 1087-1104.

Cable, M. L., J. P. Kirby, et al. (2009). "Detection of Bacterial Spores with Lanthanide-Macrocycle Binary Complexes." J. Am. Chem. Soc. **131**(27): 9562-9570.

Cable, M. L., J. P. Kirby, et al. (2007). "Bacterial Spore Detection by [Tb3+(macrocycle)(dipicolinate)] Luminescence." J. Am. Chem. Soc. **129**(6): 1474-1475.

Campillo, A. J. and S. L. Shapiro (1983). "Picosecond streak camera fluorometry - a review." IEEE J. Quantum Electron. **QE-19**(4): 585-603.

Chau, K., B. Millare, et al. (2011). "Dependence of the quality of adhesion between poly(dimethylsiloxane) and glass surfaces on the composition of the oxidizing plasma." Microfluid. Nanofluid. **10**(4): 907-917.

Fiddes, L. K., N. Raz, et al. (2010). "A circular cross-section PDMS microfluidics system for replication of cardiovascular flow conditions." Biomaterials **31**(13): 3459-3464.

Fushitani, M. (2008). "Applications of pump-probe spectroscopy." Annu. Rep. Prog. Chem., Sect. C Phys. Chem. **104**: 272-297.

Gates, B. D. (2005). "Nanofabrication with molds and stamps." Materials Today **8**(2): 44-49.

George, M. R., C. A. Golden, et al. (2006). "Modified dipicolinic acid ligands for sensitization of europium(III) luminescence." Inorg. Chem. **45**(4): 1739-1744.

Gervais, T., J. El-Ali, et al. (2006). "Flow-induced deformation of shallow microfluidic channels." Lab Chip **6**(4): 500-507.

Giurleo, J. T. and D. S. Talaga (2008). "Global fitting without a global model: Regularization based on the continuity of the evolution of parameter distributions." J. Chem. Phys. **128**(11): 114114/114111-114114/114118.

Gratton, E., D. M. Jameson, et al. (1984). "Multifrequency phase and modulation fluorometry." Annu. Rev. Biophys. Bioeng. **13**: 105-124.

Hindle, A. A. and E. A. H. Hall (1999). "Dipicolinic acid (DPA) assay revisited and appraised for spore detection." Analyst **124**(11): 1599-1604.

Hong, C., D. Bao, et al. (2008). "Print-and-Peel Fabrication of Microelectrodes." Langmuir **24**(16): 8439-8442.

Horrocks, W. D. J. and D. R. Sudnick (1979). "Time-resolved europium(III) excitation spectroscopy: a luminescence probe of metal ion binding sites." Science **206**(4423): 1194-1196.

Houston, K. S., D. H. Weinkauf, et al. (2002). "Gas transport characteristics of plasma treated poly(dimethylsiloxane) and polyphosphazene membrane materials." Journal of Membrane Science **205**(1-2): 103-112.

Hu, J., B. Xia, et al. (2009). "Long-Lived Photogenerated States of alpha -Oligothiophene-Acridinium Dyads Have Triplet Character." J. Phys. Chem. A **113**(13): 3096-3107.

Hui, A. Y. N., G. Wang, et al. (2005). "Microwave plasma treatment of polymer surface for irreversible sealing of microfluidic devices." Lab on a Chip **5**(10): 1173-1177.

Jones, G., II and V. I. Vullev (2002). "Medium effects on the photophysical properties of terbium(III) complexes with pyridine-2,6-dicarboxylate." Photochem. Photobiol. Sci. **1**(12): 925-933.

Jones, G., II and V. I. Vullev (2002). "Medium Effects on the Stability of Terbium(III) Complexes with Pyridine-2,6-dicarboxylate." J. Phys. Chem. A **106**(35): 8213-8222.

Jones, G., II, D. Yan, et al. (2007). "Photoinduced Electron Transfer in Arylacridinium Conjugates in a Solid Glass Matrix." J. Phys. Chem. B **111**(24): 6921-6929.

Lakowicz, J. R. (2006). Principles of Fluorescence Spectroscopy, Springer Science+Business Media, LLC.

Latva, M., H. Takalo, et al. (1997). "Correlation between the lowest triplet state energy level of the ligand and lanthanide(III) luminescence quantum yield." J. Lumin. **75**(2): 149-169.

Li, Q., P. K. Dasgupta, et al. (2008). "Airborne Bacterial Spore Counts by Terbium-enhanced Luminescence Detection: Pitfalls and Real Values." Environ. Sci. Technol. **42**(8): 2799-2804.

Lu, H., D. Bao, et al. (2010). "Pyridine-coated lead sulfide quantum dots for polymer hybrid photovoltaic devices." Adv. Sci. Lett. **3**(2): 101-109.

McDonald, J. C. and G. M. Whitesides (2002). "Poly(dimethylsiloxane) as a Material for Fabricating Microfluidic Devices." Accounts of Chemical Research **35**(7): 491-499.

Mehta, G., J. Lee, et al. (2009). "Hard Top Soft Bottom Microfluidic Devices for Cell Culture and Chemical Analysis." Analytical Chemistry **81**(10): 3714-3722.

Millare, B., M. Thomas, et al. (2008). "Dependence of the quality of adhesion between polydimethyl siloxane and glass surfaces on the conditions of treatment with oxygen plasma." Langmuir **24**(22): 13218-13224.

Nisoli, M. and G. Sansone (2009). "New frontiers in attosecond science." Prog. Quantum Electron. **33**(1): 17-59.

Pan, T. and W. Wang (2011). "From cleanroom to desktop: emerging micro-nanofabrication technology for biomedical applications." Ann Biomed Eng **39**(2): 600-620.

Pellegrino, P. M., N. F. Fell, Jr., et al. (1998). "Bacterial Endospore Detection Using Terbium Dipicolinate Photoluminescence in the Presence of Chemical and Biological Materials." Anal. Chem. **70**(9): 1755-1760.

Ristenpart, W. D., J. Wan, et al. (2008). "Enzymatic Reactions in Microfluidic Devices: Michaelis-Menten Kinetics." Anal. Chem. **80**(9): 3270-3276.

Rosen, D. L. (1998). "Wavelength pair selection for bacterial endospore detection by use of terbium dipicolinate photoluminescence." Appl. Opt. **37**(4): 805-807.

Rosen, D. L. (1999). "Bacterial endospore detection using photoluminescence from terbium dipicolinate." Rev. Anal. Chem. **18**(1-2): 1-21.

Rosen, D. L. (2006). "Airborne bacterial endospores detected by use of a impinger containing aqueous terbium chloride." Appl. Opt. **45**(13): 3152-3157.

Rosen, D. L., C. Sharpless, et al. (1997). "Bacterial Spore Detection and Determination by Use of Terbium Dipicolinate Photoluminescence." Anal. Chem. **69**(6): 1082-1085.

Setlow, P. (2011). "Resistance of bacterial spores." Bact. Stress Responses (2nd Ed.): 319-332.

Slieman, T. A. and W. L. Nicholson (2001). "Role of dipicolinic acid in survival of Bacillus subtilis spores exposed to artificial and solar UV radiation." Appl. Environ. Microbiol. **67**(3): 1274-1279.

Song, H., D. L. Chen, et al. (2006). "Reactions in droplets in microfluidic channels." Angew. Chem., Int. Ed. **45**(44): 7336-7356.

Song, H. and R. F. Ismagilov (2003). "Millisecond kinetics on a microfluidic chip using nanoliters of reagents." J. Am. Chem. Soc. **125**(47): 14613-14619.

Spiga, M. and G. L. Morini (1994). "A symmetric solution for velocity profile in laminar flow through rectangular ducts." Int. Commun. Heat Mass Transfer **21**(4): 469-475.

Sykora, M., L. Mangolini, et al. (2008). "Size-Dependent Intrinsic Radiative Decay Rates of Silicon Nanocrystals at Large Confinement Energies." Phys. Rev. Lett. **100**(6): 067401/067401-067401/067404.

Teh, S.-Y., R. Lin, et al. (2008). "Droplet microfluidics." Lab Chip **8**(2): 198-220.

Thomas, D. D., W. F. Carlsen, et al. (1978). "Fluorescence energy transfer in the rapid-diffusion limit." Proc. Natl. Acad. Sci. U. S. A. **75**(12): 5746-5750.

Thomas, M. S., J. M. Clift, et al. (2010). "Print-and-Peel Fabricated Passive Micromixers." Langmuir **26**(4): 2951-2957.

Thomas, M. S., B. Millare, et al. (2010). "Print-and-peel fabrication for microfluidics: what's in it for biomedical applications?" Ann Biomed Eng **38**(1): 21-32.

Vasquez, J. M., A. Vu, et al. (2009). "Fluorescence enhancement of warfarin induced by interaction with beta -cyclodextrin." Biotechnol. Prog. **25**(4): 906-914.

Vullev, V. I. and G. Jones (2002). "Photoinduced electron transfer in alkanoylpyrene aggregates in conjugated polypeptides." Tetrahedron Lett. **43**(47): 8611-8615.

Vullev, V. I. and G. Jones, II (2005). "Nanosecond laser flash photolysis: Dealing with dynamic-range and response-time limitations of the detection system." J. Appl. Sci. **5**(3): 517-526.

Vullev, V. I., J. Wan, et al. (2006). "Nonlithographic Fabrication of Microfluidic Devices." J. Am. Chem. Soc. **128**(50): 16062-16072.

Wan, J., A. Ferreira, et al. (2008). "Solvent dependence of the charge-transfer properties of a quaterthiophene-anthraquinone dyad." J. Photochem. Photobiol., A **197**(2-3): 364-374.

Wan, J., M. S. Thomas, et al. (2009). "Surface-bound proteins with preserved functionality." Ann. Biomed. Eng. **37**(6): 1190-1205.

Wróbel, D., A. Dudkowiak, et al. (2010). "Fluorescence spectroscopy in optoelectronics photomedicine, and investigation of biomolecular systems." Rev. Fluoresc. **5**: 237-275.

Xia, B., S. Upadhyayula, et al. (2011). "Amyloid histology stain for rapid bacterial endospore imaging." J. Clin. Microbiol. **49**(8): 2966-2975.

Yang, W.-W. and A. Ponce (2009). "Rapid endospore viability assay of Clostridium sporogenes spores." Int. J. Food Microbiol. **133**(3): 213-216.

Yang, W.-W. and A. Ponce (2011). "Validation of a Clostridium endospore viability assay and analysis of Greenland ices and Atacama Desert soils." Appl Environ Microbiol **77**(7): 2352-2358.

Yung, P. T., E. D. Lester, et al. (2007). "An automated front-end monitor for anthrax surveillance systems based on the rapid detection of airborne endospores." Biotechnol. Bioeng. **98**(4): 864-871.

Yung, P. T. and A. Ponce (2008). "Fast sterility assessment by germinable-endospore biodosimetry." Appl. Environ. Microbiol. **74**(24): 7669-7674.

Yung, P. T., H. S. Shafaat, et al. (2007). "Quantification of viable endospores from a Greenland ice core." FEMS Microbiol. Ecol. **59**(2): 300-306.

Zhu, H. Y., S. O. Isikman, et al. (2013). "Optical imaging techniques for point-of-care diagnostics." Lab Chip **13**(1): 51-67.

Srigokul Upadhyayula

Ph.D. Candidate; *Department of Biochemistry and Molecular Biology*
University of California, Riverside, Material Science & Engineering 233
(951) 732 8424; supad003@ucr.edu; www.vullevgroup.org

Employment:

University of California, Riverside, California (Oct. 2007 – June 2013)
Graduate student researcher, Department of Bioengineering, June 2008 – June 2013
Graduate student researcher, Department of Plant Pathology, Oct 2007 – June 2008
Teaching assistant, Fall 2008 – Spring 2012

Education:

Harvard University, Boston, Massachusetts (accepted)

June 2013	Post-Doctoral Fellow at the Harvard Medical School; Program in Cellular and Molecular Medicine at Children's Hospital Boston

University of California, Riverside, California

July 2008 – June 2013	Ph.D. Candidate, Biochemistry and Molecular Biology
Jan 2012 – Sept 2012	M.S., Bioengineering (Awarded Fall 2012)
Sept. 2007 – June 2008	M.S., Biochemistry and Molecular Biology (Awarded March 2009)

University of California, Irvine, California

Sept. 2005 – June 2007	B.S., Biological Sciences (Awarded June 2007)

Riverside Community College, Riverside, California (2003 – 2005)

Awards and Recognitions:

2012 **Best Graduate Student Talk** presented by the Department of Biochemistry, UCR, for an outstanding presentation at the 25th Annual Biochemistry Symposium

2012 **Earle C. Anthony Research Travel Award** presented by the Academic Senate Faculty Committee, UCR to present research at a top tier National/International professional conference

2012 **Demonstration of Energy-Efficient Developments** awarded by the American Public Power Association for research contributing to energy innovation: improving efficiencies and lowering costs

2012 **Dissertation Year Fellowship** awarded by the Graduate Division, UCR, competitively selected based on academic and research merit

2012 **NSF sponsored Biophotonics Summer Program** accepted to attend the prestigious Biophotonics summer program at University of Illinois at Urbana-Champaign

2012 **James and Margaret Lesley Annual Prize** awarded by the Committee on Honors and Scholarships, College of Natural and Agricultural Sciences, UCR, for original research in microfluidic biosensing

2012, 2011 **Randolph T. and Mary K. Wedding Travel Award** awarded by the Department of Biochemistry, UCR

2012, 2011 **Outstanding Teaching Assistant** awarded by the Department of Biochemistry and Graduate Division, UCR, for excellence in teaching

2011 **Walton B. Sinclair Award** presented by the Department of Biochemistry, UCR, for excellence in teaching

2011 **Randolph T. and Mary K. Wedding Prize** awarded by the Department of Biochemistry, UCR, for significant contribution to the peer reviewed scientific literature in biochemistry and molecular biology

2011 **University Teaching Certificate** awarded by the Graduate Dean and Teaching

Assistant Developmental Program, UCR

2011 **Graduate Dean's Dissertation Research Grant** awarded by the Graduate Council's Fellowship Committee, UCR, for a competitive dissertation proposal

2010 **Telemedicine & Advanced Technology Research Center Grand Challenge** recognized as a finalist at the UC-systemwide Bioengineering symposium

2007 **Excellence in Research** awarded by the University of California, Irvine, for outstanding undergraduate research in Neuropharmacology

2005 **Dean's List** awarded by the Dean of Biological sciences, UC Irvine, for academic excellence

2005 **Transfer Award** awarded by Riverside Community College for successfully transferring to a 4-year university

Research Experience*:*

Single molecule surface chemistry, Photoinduced charge transfer (2008–2013)

University of California Riverside, Department of Bioengineering, Riverside, CA

Using surface chemistry methodologies and *in vitro* solid phase peptide synthesis (SPPS) we study the biophysical dissociation properties of Leucine zippers on a single molecule level. In parallel, using the SPPS along with nontraditional amino acids we produce oligomers with enhanced charge transfer properties for use in photovoltaic devices and characterize them using ultrafast spectroscopic techniques (such as femtosecond TAS).

Microfluidic Biosensing (2009–2013)

University of California Riverside, Department of Bioengineering, Riverside, CA

Developing utilitarian tools by incorporating microfluidics for magnetic biosensing applications that are practical for laboratory use as well as immensely valuable for field deployment. Moreover, optimize the tools to decrease the ambiguity with which medical professionals currently treat infections by emphasizing simplicity, expedience and versatility.

Viral coat protein-replicase interaction and packaging studies (2007 – 2008)

University of California Riverside, Department of Plant Pathology, Riverside, CA

Using bimolecular fluorescence studies with enhanced yellow fluorescent protein genes fused to Bromo Mosaic Virus (BMV) coat protein genes and BMV replicase in various conformations, we examined the essential interactions between coat proteins and viral RNA packaging by the replicase.

***In situ* hybridization of GPCR and ligand mRNA during development** (2005 – 2007)

University of California Irvine, Department of Neuropharmacology, Irvine, CA

Demonstrated the localization of GPR7 and its ligands, neuropeptide B (NPB) and neuropeptide W (NPW) during development. Sections were incubated with radiolabeled cRNA probes for GPR7, NPB precursor, or NPW precursor during the *in situ* hybridization process and exposed to MR-1 Kodak films.

Teaching Experience:

University of California, Riverside, California (Sept. 2008 – 2012)

Teaching assistant Fall 2008 - Present

Elementary Biochemistry (BCH 100), **Fall 2008, Winter 2010 & Winter 2011**

Microbiology Laboratory (MCBL 121L), **Winter 2009, Spring 2009, Spring 2010, Spring 2011, Winter 2012 & Spring '12**

Biochemistry (BCH 110A), **Fall 2009, Fall 2010 & Fall 2011**

Bioengineering Senior Design (BIEN 175 A&B), **Winter 2010 & Spring 2010**

BRITE Mentorship, **Summer 2009**

MY BEST Mentorship, **Summer 2009 - Present**

Computer Experience:

Molecular Modeling: SwissPDB, RasTop, MolMol, Chimera
Animation and 3D Design: SolidWorks, Maya 3D, Google Sketchup
Microsoft Office products: Word, Excel, PowerPoint, Publisher, Access, Outlook
Adobe products: Photoshop, Illustrator, Acrobat, Flash, Dreamweaver, Indesign, After Effects
Web design: created and manage research group website: www.vullevgroup.org
Interactive learning: Animated educational video production and editing for *Journal of Physical Chemistry Letters*

Peer Reviewed Publications: Journal Articles & Conference Proceedings

17. Lock, J. Y.; Wyatt, E.; **Upadhyayula, S**.; Whall, A.; Nuñez, V.; Vullev, V.; Liu, H. "Degradation and Antimicrobial Properties of Magnesium Alloys in Artificial Urine for Potential Resorbable Ureteral Stent Applications," *Journal of Biomedical Materials Research: Part A* **2013**, accepted.

16. Guo, S.; Bao, D.; **Upadhyayula, S.**; Wang, W.; Guvenc, A. B.; Kyle, J. R.; Bay, H.; Bozhilov, K.;Vullev, V.; Ozkan, C.; Ozkan, M. "Photoinduced Electron Transfer between Pyridine-Coated Cadmium Selenide Quantum Dots and Single-Sheet Graphene," *Adv. Funct. Mat.* **2013**, accepted.

15. Nuñez, V.; **Upadhyayula, S.**; Millare, B.; Hadian, Ali.; Shin, S.; Vandrangi, P.; Gupta, S.; Xu, H.; Lin, A.; Larsen, J.; Georgiev, G.; Vullev, V. I. "Microfluidic space-domain time-resolved emission spectroscopy of terbium (III) and europium (III) chelates with pyridine-2,6-dicarboxylate," *Analytical Chemistry* **2013**, 85(9) 4567-4577.

14. Xia, B.; Bao, D.; **Upadhyayula, S.**; Jones, G.; Vullev, V. I. "Anthranilamides as Bioinspired Molecular Electrets: Experimental Evidence for Permanent Ground-State Electric Dipole Moment," *Journal of Organic Chemistry* **2013**, 78(5) 1994-2004.

13. Lock, J. Y.; Dragonov, M.; Whall, A.; Dhillon, S.; **Upadhyayula, S**.; Vullev, V.; Liu, H. "Antimicrobial Properties of Biodegradable Magnesium for Next Generation Ureteral Stent Applications," *Proc. IEEE-EMBS* **2012**, Paper WeC20.5.

12. **Upadhyayula, S.**; Lam, S.; Ha, A.; Malik-Chaudhry, H. K.; Vullev, V. "Dynamic Staining of Bacilli Endospores with Thioflavin T," *Proc. IEEE-EMBS* **2012**, Paper WeB06.1.

11. **Upadhyayula, S.**; Quinata, T.; Bishop, S.; Gupta, S.; Johnson, N.; Bahmani, B.; Bozhilov, K.; Stubbs, J.; Jreij, P.; Nallagatla, P.; Vullev, V. "Coatings of Polyethylene Glycol for Suppressing Non-specific Interactions between Solid Microspheres and Flat Surfaces," *Langmuir* **2012**, 28 (11), 5059-5069.

10. **Upadhyayula, S**.; Bao, D.; Millare, B.; Sylvia, S.; Habib, K. M. M.; Ashraf, M.; Ferreira, A.; Bishop, S.; Bonderer, R.; Baqai, S.; Jing, X.; Penchev, M.; Ozkan, M.; Ozkan, C.; Lake, R.; Vullev, V. "Permanent Electric Dipole Moments of Carboxyamides in Condensed Media: What Are the Limitations of Theory and Experiment?," *J. Phys. Chem. B* **2011**, 115(30), 9473-9490.

8. Xia, B.; **Upadhyayula, S.**; Nunez, V.; Landsman, P.; Lam, S.; Malik, H.; Gupta, S; Sarshar, M.; Hu, J.; Anvari, B.; Jones, G.; Vullev, V. I. "Amyloid Histology Stain for Rapid Bacterial Endospore Imaging," *Journal of Clinical Microbiology* **2011**, 49(8), 2966-2975.

8. Nuñez, V.; **Upadhyayula, S.**; Lin, A.; Chau, K.; Vullev, V. "Dynamic staining of bacteria at a single-cell level," *Proc. SPIE* 8018, 80180A **2011**; doi:10.1117/12.884186

7. Bahmani, B.; Gupta, S.; **Upadhyayula, S.**; Vullev, V.; Anvari, B. "Effect of Polyethylene Glycol Coatings on Uptake of Indocyanine Green Loaded Nanocapsules by Human Spleen Macrophages In-Vitro," *Journal of Biomedical Optics* **2011,** 16(5) 051303.

6. Chau, K.; Millare, B.; Lin, A.; **Upadhyayula, S.**; Nunez, V.; Xu, H.; Vullev, V. I. "Dependence of the Quality of Adhesion between Poly(dimethylsiloxane) and Glass Surfaces on the Composition of the Oxidizing Plasma," *Microfluidics and Nanofluidics* **2011**, 10(4), 907-917.

5. Bao, D.; Ramu, S.; Contreras, A.; **Upadhyayula, S.**; Vasquez, J.M.; Beran, G. and Vullev, V. I. "Electrochemical Reduction of Quinones: Interfacing Experiment and Theory for Defining Effective Radii of Redox Moieties," *J. Phys. Chem. B* **2010**, 114, 14467-14479.

4. Thomas, M. S.; Nunez, V.; **Upadhyayula, S.**; Zielins, E.; Bao, D.; Vasquez, J.M.; Bahmani, B. and Vullev, V. I. "Kinetics of Bacterial Fluorescence Staining with 3,3'-Diethylthiacyanine," *Langmuir* **2010**, 26 (12), 9756-9765.

3. **Upadhyayula, S.;** Nuñez, V.; Wan, J.; Vullev, V.; "Bacterial-Spore Assay Based on Fluorescence-Enhancement Kinetics as a Platform for Lab-on-a-Chip Setting," *Proc. of the 11th Annual UC Bioengineering Meeting* **2010** UCBioE-19-21

2. Nuñez, V.; Thomas, M.; Zielins, E.; **Upadhyayula, S.;** Vullev, V.; "Rapid Bacterial Identification Using Kinetics of Fluorescence Staining," *Proc. of the 11th Annual UC Bioengineering Meeting* **2010** UCBioE-3-5

1. **Upadhyayula, S.**, Jackson, V., Civelli, O. "Differential expression of GPR7 receptor, Neuropeptide B, and Neuropeptide W, in the brains of postnatal Sprague-Dawley rats during development," *Journal of Undergraduate Research in the Biological Sciences, University of California, Irvine, Volume 3*7 **2007**

Oral & Poster Presentations:

15. (August 2012) **Upadhyayula, S.**, Nunez, V., Lam, S., Ha, A., Vullev, V. "Dynamic Staining of *Bacillus* Endospores with Thioflavin T," 2012 **IEEE – Engineering in Medicine & Biology Conference**: San Diego CA (Paper/*Poster Presentation*)

14. (July 2012) **Upadhyayula, S.**, Bishop, S., Johnson, N., Quinata, T., Nallagatla, P., Gupta, S., Vullev, V. "Suppressing non-specific interactions between solid surfaces used for single-molecule force measurements," 2012 **Gordon Research Conference**: Single Molecule Approaches to Biology, West Dover, VT (*Poster Presentation*)

13. (June 2012) **Upadhyayula, S.**, Bonderer, R., Ashraf, K., Bao, D., Millare, B., Ferreira, A., Lake, R., Vullev, V. "Bioinspired electrets for solar energy conversion," 2012 **UC Systemwide Bioengineering Symposium**, University of California, Berkeley, CA (*Oral Presentation*)

12. (May 2012) **Upadhyayula, S.**, Nunez, V., Lam, S., Ha, A., Vullev, V. "Fluorescence-Enhancement Based Dynamic Staining: Applications For Vegetative Bacterial and

Bacterial-Spore Detection," 2012 **Imaging at Illinois Conference**: Urbana-Champaign IL (*Poster Presentation*)

11. (July 2011) **Upadhyayula, S.**, Nunez, V., Lam, S., Ha, A., Vullev, V. "Fluorescence-Enhancement Based Dynamic Staining: Applications For Vegetative Bacterial and Bacterial-Spore Detection," 2011 **Gordon Research Conference**: Photochemistry, Easton MA (*Poster Presentation*)

10. (October 2010) **Upadhyayula, S.**, Bishop, S., Johnson, N., Quinata, T., Nallagatla, P., Gupta, S., Vullev, V. "Suppressing non-specific interactions between solid surfaces used for single-molecule force measurements," 2010 **Biomedical Engineering Society** Annual Meeting, Austin TX (*Poster Presentation*)

9. (August 2010) **Upadhyayula, S.**, Bonderer, R., Ashraf, K., Bao, D., Millare, B., Ferreira, A., Lake, R., Vullev, V. "Bioinspired electrets for solar energy conversion," 2010 **Gordon Research Conference**: Electron Donor Acceptor Interactions, Newport RI (*Poster Presentation*)

8. (August 2010) **Upadhyayula, S.**, Bonderer, R., Ashraf, K., Bao, D., Millare, B., Ferreira, A., Lake, R., Vullev, V. "Bioinspired electrets for solar energy conversion," 2010 **American Chemical Society**, Annual Fall Meeting: PHYS: Division of Physical Chemistry, Boston MA (*Poster Presentation*)

7. (August 2010) **Upadhyayula, S.**, Johnson, N., Bishop, S., Gupta, S., Vullev, V. "Suppressing non-specific interactions between solid surfaces used for single-molecule force measurements," 2010 **American Chemical Society**, Annual Fall Meeting: COLL: Division of Colloid and Surface Chemistry, Boston MA (*Oral Presentation*)

6. (July 2010) **Upadhyayula, S.**, Nunez, V., Wan, J., Vullev, V.I. "Bacterial-Spore Assay Based on Fluorescence-Enhancement Kinetics as a Platform for Lab-on-a-Chip Setting," US ARMY - TATRC Grand Challenge Oral presentation at the 2010 **UC Systemwide Bioengineering Symposium**, University of California, Davis, CA (*Oral Presentation*)

5. (Feb 2010) **Upadhyayula, S.**, Johnson, N., Bishop, S., Gupta, S., Vullev, V. "Suppressing non-specific interactions between solid surfaces used for single-molecule force measurements," 2012 **Biophysical Society** 54th Annual Meeting: Biotechnology and Bioengineering Track, San Francisco, CA (*Poster Presentation*)

4. (Oct 2009) **Upadhyayula, S.**, Ashraf, K., Bao, D., Millare, B., Ferreira, A., Lake, R., Vullev,V. "Bioinspired Electrets for Solar Energy Conversion," 2009 **Biomedical Engineering Society** Annual Meeting: Bridging the 3 Rivers of Biology, Engineering and Medicine, Pittsburgh, PA (*Poster Presentation*)

3. (September 2009) **Upadhyayula, S.**, Bao, D., Vullev,V. "Synthesizing oligo-*ortho*-anthranilic acids for improved Charge-Transfer properties in photovoltaic cells," 2009 **UC Riverside Biochemistry and Molecular Biology Symposium**, Riverside CA (*Oral Presentation*)

2. (June 2009) **Upadhyayula, S.**, Bao, D., Vullev,V. "Solid-Phase Peptide synthesis of Bioinspired Electrets Based on Non-Traditional Amino Acids," 10th Annual **UC systemwide Bioengineering Symposium**: Molecular and Cellular Engineering Track, University of California, Merced CA (*Oral Presentation*)

1. (September 2008) **Upadhyayula, S.**, Jackson, V., Civelli, O. “Differential expression of GPR7 receptor, Neuropeptide B, and Neuropeptide W, in the brains of postnatal Sprague-Dawley rats during development,” 2008 **UC Riverside Biochemistry and Molecular Biology Symposium**, Riverside CA (*Oral Presentation*)